EINDHOVEN UNIVERSITY OF TECHNOLOGY

Understanding quantitative DCE-MRI of the breast : towards meaningful clinical application

Citation for published version (APA):
Heisen, M. (2010). *Understanding quantitative DCE-MRI of the breast : towards meaningful clinical application*. [Phd Thesis 1 (Research TU/e / Graduation TU/e), Biomedical Engineering]. Technische Universiteit Eindhoven. https://doi.org/10.6100/IR690662

DOI:
10.6100/IR690662

Document status and date:
Published: 01/01/2010

Document Version:
Publisher's PDF, also known as Version of Record (includes final page, issue and volume numbers)

Please check the document version of this publication:

• A submitted manuscript is the version of the article upon submission and before peer-review. There can be important differences between the submitted version and the official published version of record. People interested in the research are advised to contact the author for the final version of the publication, or visit the DOI to the publisher's website.
• The final author version and the galley proof are versions of the publication after peer review.
• The final published version features the final layout of the paper including the volume, issue and page numbers.

Link to publication

General rights
Copyright and moral rights for the publications made accessible in the public portal are retained by the authors and/or other copyright owners and it is a condition of accessing publications that users recognise and abide by the legal requirements associated with these rights.

• Users may download and print one copy of any publication from the public portal for the purpose of private study or research.
• You may not further distribute the material or use it for any profit-making activity or commercial gain
• You may freely distribute the URL identifying the publication in the public portal.

If the publication is distributed under the terms of Article 25fa of the Dutch Copyright Act, indicated by the "Taverne" license above, please follow below link for the End User Agreement:

www.tue.nl/taverne

Take down policy
If you believe that this document breaches copyright please contact us at:

openaccess@tue.nl

providing details and we will investigate your claim.

Download date: 04. Oct. 2023

Understanding quantitative DCE-MRI of the breast

Towards meaningful clinical application

A catalogue record is available from the Eindhoven University of Technology Library

ISBN: 978-90-386-2356-6

Cover design: Evelinda Baerends and Douwe Hoendervanger
www.douwehoendervanger.nl

Printed by Universiteitsdrukkerij TU Eindhoven, Eindhoven, The Netherlands.

Financial support for the publication of this thesis was kindly provided by the Advanced School for Computing and Imaging (ASCI), Eindhoven University of Technology, and Philips Healthcare.

Travel grants were awarded by Philips Healthcare, Niemans-Schootemeijer Fund, KWF Kankerbestrijding, Vereniging voor Biofysica en Biomedische Technologie, and International Society for Magnetic Resonance in Medicine.

Advanced School for Computing and Imaging

This work was carried out in the ASCI graduate school. ASCI dissertation series number 200.

Copyright © 2010 by M. Heisen

All rights reserved. No part of this book may be reproduced, stored in a database or retrieval system, or published, in any form or in any way, electronically, mechanically, by print, photo print, microfilm or any other means without prior written permission by the author.

Understanding quantitative DCE-MRI of the breast

Towards meaningful clinical application

PROEFSCHRIFT

ter verkrijging van de graad van doctor aan de
Technische Universiteit Eindhoven, op gezag van de
rector magnificus, prof.dr.ir. C.J. van Duijn, voor een
commissie aangewezen door het College voor
Promoties in het openbaar te verdedigen
op maandag 15 november 2010 om 16.00 uur

door

Marieke Heisen

geboren te Nijmegen

Dit proefschrift is goedgekeurd door de promotor:

prof.dr.ir. B.M. ter Haar Romeny

Copromotoren:
dr.ir. J. Buurman
en
dr.ir. N.A.W. van Riel

Contents

Summary		**III**
Chapter 1	General introduction	**1**
Chapter 2	Introduction to pharmacokinetic modeling	**15**
Chapter 3	Data-imposed limitations on pharmacokinetic models for DCE-MRI of the breast	**57**
Chapter 4	Patient-specific calibration for breast MRI: development and use of a breast-coil insertable reference phantom	**77**
Chapter 5	The influence of temporal resolution in determining pharmacokinetic parameters from DCE-MRI data	**129**
Chapter 6	The use of a reference tissue arterial input function with low-temporal-resolution DCE-MRI data	**143**
Chapter 7	Multi-parametric assessment of the anti-angiogenic effects of liposomal glucocorticoids	**159**
Chapter 8	General discussion	**179**
References		**186**
Samenvatting		**203**
Dankwoord		**205**
Curriculum vitae		**207**
List of publications		**208**

Summary

Understanding quantitative DCE-MRI of the breast

Towards meaningful clinical application

In most industrialized countries breast cancer will affect one out of eight women during her lifetime. In the USA, after continuously increasing for more than two decades, incidence rates are slowly decreasing since 2001. Since 1990, death rates from breast cancer have steadily decreased in women, which is attributed to both earlier detection and improved treatment. Still, it is second only to lung cancer as a cause of cancer death in women. In this work we set out to improve early detection of breast cancer via quantitative analysis of magnetic resonance images (MRI).

Screening and diagnosis of breast cancer are generally performed using X-ray mammography, possibly in conjunction with ultrasonography. However, MRI is becoming an important modality for screening of women at high-risk due to for instance hereditary gene mutations, as a problem-solving tool in case of indecisive mammographic and / or ultrasonic imaging, and for anti-cancer therapy assessment. In this work, we focused on MR imaging of the breast. More specifically, the dynamic contrast-enhanced (DCE) part of the protocol was highlighted, as well as radiological assessment of DCE-MRI data.

The T_1-weighted (T_1: longitudinal relaxation time, a tissue property) signal-versus-time curve that can be extracted from the DCE-MRI series that is acquired at the time of and after injection of a T_1-shortening (shorter T_1 results in higher signal) contrast agent, is usually visually assessed by the radiologist. For example, a fast initial rise to the peak (1-2 minutes post injection) followed by loss of signal within a time frame of about 5-6 minutes is a sign for malignancy, whereas a curve showing persistent (slow) uptake within the same time frame is a sign for benignity. This difference in contrast agent uptake pattern is related to physiological changes in tumorous tissue that for instance result in a stronger uptake of the contrast agent. However, this descriptive way of curve type classification is based on clinical *statistics*, not on *knowledge* of tumor physiology.

We investigated pharmacokinetic modeling as a quantitative image analysis tool. Pharmacokinetics describes what happens to a substance (e.g. drug or contrast agent) after it has been administered to a living organism. This includes the mechanisms of absorption and distribution. The terms in which these mechanisms are described are physiological and can therefore provide parameters describing the functioning of the

tissue. This physiological aspect makes it an attractive approach to investigate (aberrant) tissue functioning. In addition, this type of analysis excludes confounding factors due to inter- and intra-patient differences in the systemic blood circulation, as well as differences in the injection protocol.

In this work, we discussed the physiological basis and details of different types of pharmacokinetic models, with the focus on compartmental models. Practical implications such as obtaining an arterial input function (AIF, the input to the pharmacokinetic model) and model parameter estimation were taken into account as well. A simulation study of the data-imposed limitations – in terms of temporal resolution and noise properties – on the complexity of pharmacokinetic models led to the insight that only one of the tested models, the basic Tofts model, is applicable to DCE-MRI data of the breast. For the basic Tofts model we further investigated the aspect of temporal resolution, because a typical diagnostic DCE-MRI scan of the breast is acquired at a rate of about 1 image volume every minute; whereas pharmacokinetic modeling usually requires a sampling time of less than 10 s. For this experiment we developed a new downsampling method using high-temporal-resolution raw k-space data to simulate what uptake curves would have looked like if they were acquired at lower temporal resolutions. We made use of preclinical animal data. With this data we demonstrated that the limit of 10 s can be stretched to about 1 min if the arterial input function is inversely derived from a healthy reference tissue, instead of measured in an artery or taken from the literature.

An important precondition for the application of pharmacokinetic modeling is knowledge of the relationship between the acquired DCE-MRI signal and the actual concentration of the contrast agent in the tissue. This relationship is not trivial because with MRI we measure the indirect effect of the contrast agent on water protons. To establish this relationship via calculation of $T_1(t)$, we investigated both a theoretical and an empirical approach, making use of an in-house (University of Chicago) developed reference object that is scanned concurrently with the patient. The use of the calibration object can shorten the scan duration (an empirical approach requires less additional scans than an approach using a model of the acquisition technique), and can demonstrate if theoretical approaches are valid. Moreover we produced concentration images and estimated tissue proton density, also making use of the calibration object.

We studied therapy assessment as well. Via pharmacokinetic modeling and other MRI-derived measures we partly revealed the actions of a novel therapeutic in a preclinical study. In particular, the anti-tumor activity of a single dose of liposomal prednisolone phosphate was investigated, which is an anti-inflammatory drug that has demonstrated tumor growth inhibition.

The work presented in this thesis contributes to a meaningful clinical application and interpretation of quantitative DCE-MRI of the breast.

Chapter 1

General introduction

In most industrialized countries breast cancer will affect one out of eight women during her lifetime (Berg 2009). Prevalence of male breast cancer is about 90 times lower. In the USA, after continuously increasing for more than two decades, incidence rates are slowly decreasing since 2001. Since 1990, death rates from breast cancer have steadily decreased in women, which is attributed to both earlier detection and improved treatment. Still, it is second only to lung cancer as a cause of cancer death in women. In this work we set out to improve early detection via quantitative analysis of magnetic resonance images (MRI).

In the present chapter the formation of breast cancer will be described in relationship to breast cancer imaging. Screening and diagnosis of breast cancer are generally performed using X-ray mammography, possibly in conjunction with ultrasonography. As a screening modality, MRI is only used for women at high risk – among other reasons – because of its superior sensitivity in young women. In this work, we will focus on MR imaging of the breast. More specifically, the dynamic contrast-enhanced (DCE) part of the protocol will be highlighted, as well as radiological assessment of DCE-MRI data. The current standard of care will be reviewed and directions for improvement will be pointed out.

1.1 Oncogenesis

Cancer can be defined as uncontrolled malignant cell growth. As the number of neoplastic cells increases, their demand for oxygen and nutrients outgrows the capacity of interstitial diffusion. The consequent local hypoxia is a trigger for angiogenesis, which is the sprouting of new blood vessels from pre-existing vessels. The angiogenic cascade, regulated by pro-angiogenic factors such as vascular endothelial growth factor, involves proliferation, migration, and differentiation of endothelial cells to form new capillaries. In the tumor environment this process is however not well-controlled, resulting in structural and functional abnormalities; an important one being high vessel-wall permeability due to incomplete endothelium lining and an interrupted basement membrane. In addition, the smooth muscle layer that assures vasoreactivity is often underdeveloped or lacking.

The onset of angiogenesis adds to the malignant potential of the tumor because it enables (rapid) tumor growth and provides access to the blood circulation, thereby increasing the risk of metastases. However, the increased vasculature also provides access to the tumor, such that contrast materials and drugs can be delivered, to, respectively, detect and treat it. High-grade tumors tend to present higher vascular disorganization and permeability than low-grade tumors (Daldrup et al. 1998). Tumor grade is defined as the histological degree of cell abnormality; the less the cells are differentiated into normal cells, the higher the grade and the faster the cells grow and spread. Monitoring tumor vascularization could therefore potentially help to predict tumor aggressiveness and to design a tailored treatment (Brix et al. 1999).

As cancer is a heterogeneous disease, not all types of breast cancer develop as a single clump of growing cells. In radiological terminology a fairly large (about 5 mm or larger, American College of Radiology 2003) single clump of cancer cells is called a mass, which is defined as a space-occupying lesion that distorts the surrounding tissue. Other cancers develop as a more diffuse pattern. They are categorized as non-mass-like enhancement (NMLE). 'Enhancement' refers to the increased MR signal in these areas (as will be described in Section 1.3). Ductal carcinoma *in situ* (DCIS) is an example of a non-obligate precursor of cancer that frequently presents as NMLE. In DCIS, abnormal cells have accumulated in the milk duct but have not spread to other tissues in the breast. Since it is a non-obligate precursor, it is of special interest to detect and characterize DCIS. Image-based evidence of the absence or presence of malignant potential could prevent unnecessary treatment.

1.2 Breast cancer imaging

Most breast cancers are diagnosed using (X-ray) mammography, which is the standard screening modality. The introduction of population screening programs in the late 1980's has decreased the death rate from breast cancer, despite an increased incidence. Although mammography is the only screening test proven to reduce breast cancer mortality, there is increased awareness that mammography alone may not be adequate to screen certain subpopulations (Berg 2009). Those subpopulations consist for instance of women with a genetic predisposition to develop breast cancer – such as carrying one of the BRCA mutations – women with a personal history of cancer, or women who have undergone chest radiation. As they are at high-risk (aggregate lifetime risk of more than 20%, Saslow et al. 2007), these women should start screening at a relatively young age, when breast tissue is often mammographically dense. A high density arises from a high calcium concentration causing a high background signal on mammography, possible obscuring microcalcifications that can be a sign of cancer. Moreover, a high density is also a risk factor in itself (Berg 2009). For women at high risk, the addition of either MRI or ultrasound to mammography results in a higher detection yield than achieved with mammography alone, as can be seen in Table 1.1. Therefore, for these women, additional screening beyond annual mammography has been advised by the American Cancer Society since 2007 (Saslow et al. 2007). Preferably MRI is used, because the combination of MRI with standard mammography gives the highest detection rate. For women at normal risk, MRI can be used in case of a suspicious but inconclusive mammogram. However, ultrasound is more commonly used as a second-look modality. Over the past ten years, in the USA the number of breast MRI studies has increased with nearly 40% per year (Newell et al. 2010).

Table 1.1 *High-risk screening, percentage of cancers found listed per modality and per combination of modalities, after Berg 2009.*

Modality	% of cancers found
Mammography	36
Ultrasound	40
Mammography + Ultrasound	52
Magnetic resonance imaging	81
Mammography + magnetic resonance imaging	93

If diagnosis calls for treatment, MRI could be used to assess the extent of disease. However, this use of MRI, as well as the use of MRI for (contralateral) screening, is currently vehemently debated as it may (unnecessarily) increase recall and intervention rates. An increase of the false positive ratio has been reported (Houssami et al. 2008), although others state that the specificity – i.e. the probability of a negative test in women without breast cancer – of MRI is similar to that of mammography (Kuhl et al. 2007). The reported range in specificity is therefore large (37-97%). On the part of sensitivity – i.e. the probability of a positive test in women with breast cancer – there is consensus that it is higher for MRI (77-100%) than for mammography (25-59%). Possibly, improvements in standardization can contribute to a higher and more uniform specificity. The above figures hold for women at high risk (Kuhl et al. 2005b, Leach et al. 2005a, Lehman et al. 2005, Lord et al. 2007, Newell et al. 2010, Sardanelli et al. 2007, Warner et al. 2004).

During the treatment phase, MRI can be used to monitor the response to (neoadjuvant) chemotherapy or other therapies. For agents acting on the tumor vasculature it can be crucial to use MRI for therapy assessment, because it can provide information about the degree of vascularization and the quality of the vessels. More on this topic in **Chapter 7**.

1.3 MRI and tissue contrast

MR contrast emerges from differences in relaxation properties of tissue hydrogen nuclei after undergoing radio-frequency excitation. In the classical view, the excitation tilts the magnetic spin vectors of the hydrogen nuclei from their alignment with the main (static) magnetic field. After the excitation they return to equilibrium (alignment with the main field) due to relaxation processes. The time constants of these relaxation processes are used to generate image contrast. The longitudinal relaxation time constant T_1 tells us how quickly the spins return to equilibrium, the transverse relaxation time constant T_2 how quickly the spins de-phase due to fluctuations in precession frequency. If field inhomogeneities play a role, the transverse relaxation

time constant is shorter than T_2, which is then referred to as T_2^*. A third property adding to tissue contrast is proton density (PD), which is a measure of mobile hydrogen nuclei. Acquisition sequences can be tuned in such a way that one of the tissue properties dominantly determines the contrast, resulting in T_1-weighted, $T_2^{(*)}$-weighted, or PD-weighted imaging.

Only a limited percentage of malignant breast tumors can be detected – as well as distinguished from benign tumors – using the intrinsic T_1- / T_2- / PD-weighted MR contrast (Bottomley et al. 1987). Therefore, during a standard clinical MR breast examination, a T_1-shortening contrast agent is intravenously injected. The most common agents are low-molecular-weight (weight < 1kDa) complexes of the lanthanide gadolinium (Gd^{3+}). The unpaired electrons of this paramagnetic metal ion create a locally fluctuating magnetic field causing water nuclei in its close proximity to relax more rapidly through dipole-dipole interactions. Due to the process of angiogenesis, more of the contrast agent ends up in the tumor area than in the surrounding normal tissue. The T_1-shortening in the tumor area causes a bright signal, resulting in an increased contrast between the tumor and its environment. Here we emphasize that the presence of the contrast agent can only be indirectly detected through measurements of tissue water relaxation. This is a fundamental difference with contrast agents used in nuclear medicine. To allow for quantification of the contrast agent concentration (Section 1.6), the native tissue T_1 (T_{10}) has to be measured, requiring additional scans (**Chapter 4**). The ΔR_1 ($R_1 = 1/T_1$) caused by the presence of the contrast agent is related to its concentration in the following way

$$\Delta R_1(t) = R_1(t) - R_{10} = r_1 \cdot C(t), \qquad [1.1]$$

in which r_1 (mM^{-1} s^{-1}) is the longitudinal relaxivity; C (mM) the contrast agent concentration; and t (min) is time. A similar relationship holds for ΔR_2^*, which is exploited in dynamic susceptibility-weighted MRI (DSC). In DCE-MRI this effect is suppressed in the signal due to T_1-weighting.

The acquisition of MR data takes place in k-space, which is the spatial-frequency domain. Application of the inverse Fourier transform on the (complex) k-space data results in the corresponding image data. In Figure 1.1 we show an example taken from rat data (**Chapters 5 and 6**), both in k-space and in the image domain. We stress that MRI is not a 'snapshot tool'. The excitation and subsequent signal readout cannot happen for every spatial frequency at the same time, otherwise it would be unknown where the acquired signal came from, and thereby it would be impossible to reconstruct the image. The fact that acquisition of a single k-space data volume can take more than a minute is important in the context of quantifying temporal aspects of contrast agent uptake; i.e., during the acquisition of a single volume the local contrast agent concentration varies due to the ongoing processes of flow and extravasation which

makes it difficult to obtain measures of these processes. We will discuss this in more detail in **Chapters 5 and 6**.

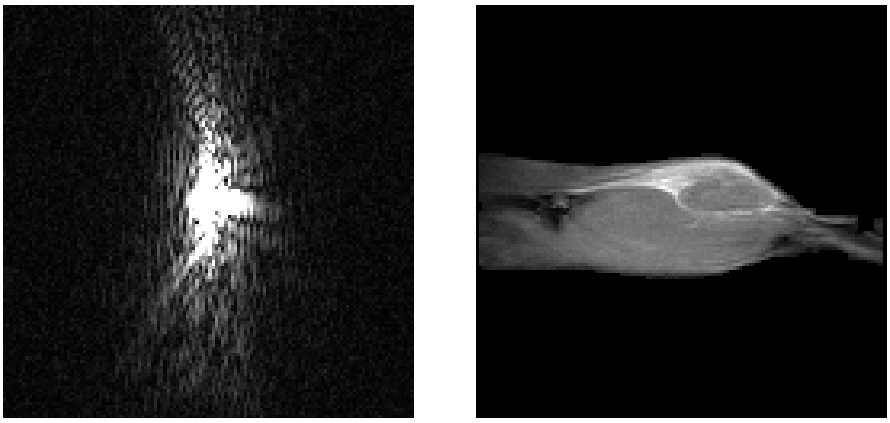

Figure 1.1 *Left: acquired k-space data (taken absolute), and right: the corresponding image.*

1.4 Dynamic contrast-enhanced MRI

DCE-MRI of the breast was first performed by Heywang et al. (1989), and Kaiser and Zeitler (1989). 'Dynamic' reflects that the acquisition is repeated multiple times, before as well as after contrast agent administration. Nearly all clinical DCE-MRI is performed at 1.5 T, although 3.0 T is gaining popularity (Kuhl 2007a). The data have a typical spatial resolution of a cubic millimeter; this to achieve an acceptable signal-to-noise ratio while covering the volume of both breasts within an acceptable amount of time. The acquisition is repeated as rapidly as possible continuing for 5 to 10 minutes after injection. As peak enhancement in breast tissue is expected within the first 2 minutes after contrast injection, a temporal resolution of at least 60 s – 120 s is specified in the guidelines from the European Society of Breast Imaging (Mann et al. 2008). A commonly used T_1-weighted acquisition is the spoiled gradient echo sequence, with a repetition time of 3 to 10 ms, an echo time under 5 ms, and a variety of choice of flip angle (Jackson et al. 2007). The spoiled gradient echo signal model is given by

$$S(t) = M_0 \cdot e^{-TE/T_2^*(t)} \frac{\sin\theta\left(1-e^{-TR/T_1(t)}\right)}{1-\cos\theta \cdot e^{-TR/T_1(t)}}, \qquad [1.2]$$

in which $S(t)$ is the measured signal intensity; M_0 is a scaling factor that depends on scanner gain and proton density; θ (°) is the flip angle; TE (ms) is the echo time; TR (ms) is the repetition time; and t (min) is time. To obtain ΔR_1 (see Eq. 1.1), needed to calculate contrast agent concentration, the measured signal S has to be converted to T_1, for instance using the signal model given in Eq. 1.2. More on this matter in **Chapter 4**.

The tissue characteristics that are exploited by MRI to detect malignant lesions are fundamentally different from those used in (X-ray) mammography. Whereas in

mammographic imaging certain patterns of calcium deposits (microcalcifications) are seen as signs of increased cell activity and possibly cancer; in the T_1-weighted dynamic contrast-enhanced part of the MRI protocol it is the tumor microvasculature that is probed. Both an increased blood supply and increased vessel wall permeability will cause more of the contrast agent to end up in the tumor region than in the surrounding healthy tissue. The observed enhancement pattern is used to assess both tissue morphology and contrast agent uptake kinetics.

Clinical MRI protocols for the breast often also contain a T_2-weighted imaging sequence performed before injection of the contrast agent. This to exclude certain benign conditions, like cysts, that may appear alarming on T_1-weighted images, but can often be excluded from suspicion in case of a bright T_2-weighted signal. Recently, diffusion-weighted imaging is gaining popularity in diagnostic MRI of the breast (Partridge et al. 2009). However, it is not (yet) part of most clinical protocols. Although we provided a general description of a clinical MR breast exam, we should stress that acquisition protocols vary to a great extent; there is only limited standardization.

1.5 Radiological assessment

Most breast MR practices will assess the acquired MRI data according to the BI-RADS guidelines (Breast Imaging-Reporting and Data System, American College of Radiology 2003, update expected end of 2010). These guidelines distinguish three main lesion types: focus, mass, and non-mass-like enhancement. A focus is so small – smaller than 5 mm but this may change as the achievable spatial resolution is currently higher than in 2003 – that it cannot otherwise be characterized. A mass is a space-occupying lesion that comprises a single process. Non-mass-like enhancement presents as areas of normal glandular tissue or fat interspersed between the abnormally enhancing components. In radiological assessment, these types of lesions are each treated differently. A focus can only be characterized as being present. Mass lesions can be characterized by their 'shape', 'margin', and 'internal enhancement pattern'; e.g. a round lesion with a smooth margin and a homogeneous enhancement pattern is much more likely to be benign than a lesion with an irregular shape and margin showing heterogeneous enhancement. The descriptors for NMLE are slightly different; they are 'distribution' and 'internal enhancement pattern'. For instance, a diffuse distribution showing homogeneous enhancement is more likely to be benign than a segmental distribution showing heterogeneous enhancement. Especially in case of NMLE, an important characteristic is also the degree of symmetry between the two breasts; if both breasts show the same enhancement pattern, it is more likely that we are seeing (strong) enhancement in the healthy glandular tissue.

The above-described characteristics are morphologic, usually assessed by looking at the (baseline-subtracted) image volume that shows most enhancement in the lesion. However, the guidelines also describe how the temporal contrast agent uptake pattern

can be assessed, so making use of the whole dynamic series. The so-called kinetic curves are usually inspected as relative enhancement (RE in percentage) curves:

$$RE = \frac{S(t)-S_0}{S_0} \times 100\%, \qquad [1.3]$$

in which $S(t)$ is the dynamic signal; $S_0 = S(t = 0)$ the precontrast signal; and t (min) time. Normalization with respect to S_0 deals to a large extent with inhomogeneous coil sensitivity, but it does not make RE protocol-independent (see **Chapter 4**). The obtained curves are classified as (i) steady enhancement, (ii) plateau of signal intensity, or (iii) wash-out, see Figure 1.2 (Kuhl et al. 1999). A typical malignant lesion will show a fast initial rise and wash-out (signal decay) after reaching peak enhancement. This classification scheme may seem basic, but at a temporal resolution of 1 – 2 min, there are only a few T_1-weighted image volumes acquired (series duration 5 – 10 min). Moreover, this classification scheme has statistically been proven to add to lesion differentiation (Kuhl et al. 1999).

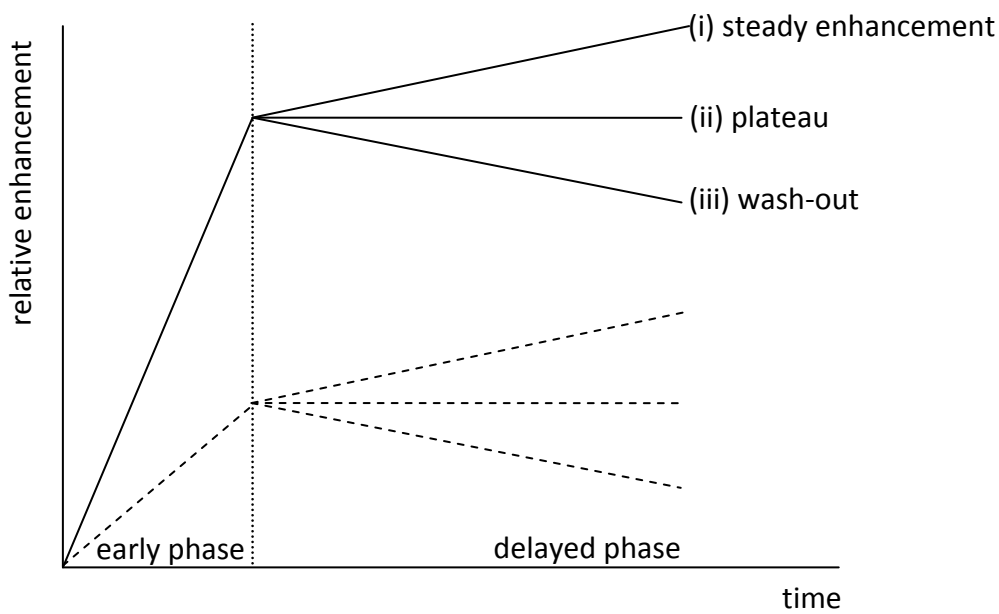

Figure 1.2 *Descriptive curve-type classification of relative enhancement curves. Steady enhancement is associated with benignity, washout with malignancy. The intermediate pattern (plateau) is suspicious.*

To accurately track the distribution of the injected contrast agent over time, temporal resolution has to be increased. However, there is a direct trade-off between sampling time and spatial resolution / image volume. As stated in the European guidelines (Mann et al. 2008), temporal resolution should not compromise spatial resolution. Indeed, it was shown that an increase in spatial resolution results in higher diagnostic confidence, even when the temporal resolution is slightly sacrificed (Kuhl et

al. 2005a). Also, in the BI-RADS guidelines kinetic assessment is considered an adjunct to morphologic assessment, as morphology overrules kinetics: suspicious morphologic features should prompt biopsy regardless of curve kinetics (American College of Radiology 2003). Moreover, several papers have stated that kinetic assessment is of limited relevance for NMLE (Kuhl 2007b, Newell et al. 2010, Yabuuchi et al. 2010), restricting its role to the differentiation of mass lesions. But is this 'secondary' role of kinetic analysis justified? For example, in a multi-center study using an automatic feature selection method, kinetic features were preferred over morphologic features (Heywang-Kobrunner et al. 2001). Besides, the added value of kinetic analysis can probably not be fully assessed at temporal resolutions typical for DCE-MRI of the breast.

As pointed out by Schabel et al. (2010), in the previously mentioned study by Kuhl et al. (2005a) a decrease in temporal resolution from 69 s to 116 s may not have caused a loss of crucial kinetic information as both resolutions are too low to provide an accurate description of kinetics. This thesis is supported by the work of El Khouli et al. (2009) which showed a significant increase in the area under the receiver-operatoring-characteristic curve when increasing the temporal resolution from 60 s to 15 s. Yet, according to Kuhl (2007b), there is no relevant additional diagnostic information attainable by reducing sampling times to below 60 s, because studies using high-temporal-resolution DCE-MRI in combination with advanced kinetic modeling – as will be discussed in the next section – did not demonstrate superiority, compared to a standard protocol that allowed detailed morphologic assessment. Certainly, the cited work by Schorn et al. (1999) demonstrated that considerably sacrificing spatial resolution (factor of 5) to gain high-temporal resolution (factor of 44) does not result in higher diagnostic confidence, because kinetic analysis cannot replace morphologic analysis. Interestingly, other cited references in Kuhl 2007b are milder in their judgment and speak of a useful functional imaging technique that needs to be standardized (Choyke et al. 2003); and issues that must be addressed to move this methodology into routine clinical practice, such as the needed kinetic model complexity (a simple model might suffice), and the most rational and reliable data collection procedure (Taylor et al. 1999). It is likely too early to state that a gain in diagnostic performance can only be expected from an increase in spatial resolution, as the temporal aspects appear to not have been fully exploited yet. Nonetheless, current consensus lies at a temporal resolution of 1 – 2 min in combination with a (sub)millimeter in-plane spatial resolution at a slice thickness of 1 – 3 mm (Kuhl 2007b). It is therefore also important to study if more kinetic information can be extracted from 'low' temporal resolution data (a temporal resolution of 1 min is not considered low in the context of DCE-MRI of the breast, but very low in the context of, for instance, DCE-MRI of the prostate). We will therefore discuss pharmacokinetic modeling of low-temporal-resolution data as an alternative to descriptive curve-type modeling. In the future, acquisition protocols may head for a combination of high-temporal / high-spatial resolution as a result of faster

scan techniques, or smart alternation between high-temporal-resolution sampling (during the first phase) and high-spatial-resolution sampling (during the second phase). In the work by Veltman et al. (2008) the latter approach significantly improved diagnostic performance.

1.6 Quantitative image analysis

Despite the fact that relative enhancement curves not only reflect a change in contrast agent concentration, but also depend on scan parameters such as repetition time and flip angle (Hittmair et al. 1994) and other factors such as the native T_1 of the tissue and the patient's systemic blood circulation, still, descriptive modeling of RE curves adds considerable diagnostic value (Kuhl et al. 1999). With the use of more quantitative methods, the aim is to remove these unwanted dependencies so that the derived parameters only reflect local tissue properties. The removal of irrelevant factors can potentially boost the diagnostic value of kinetic analysis.

Two factors that should not affect diagnostics are the patient's systemic circulation and the applied injection protocol. Together, they dictate the shape of the arterial input function (AIF). The AIF describes the bolus of contrast agent passing through the blood circulation. As the contrast agent is exchanged between the blood plasma and the tissue, the shape of the AIF can influence the enhancement seen in the tissue. In a pharmacokinetic model (thoroughly explained in **Chapter 2**), for example a two-compartment model, the input of contrast agent material (AIF) is taken into account in assessing the response, i.e. the uptake of contrast agent material in the tissue. By deconvolving the response with the input function, variations in systemic circulation or injection protocol are excluded from the assessment of the contrast agent uptake. To arrive at tissue parameters with a physiological meaning, the pharmacokinetic model has to be fitted to contrast agent uptake curves represented in contrast agent concentration. We therefore have to convert the measured signal intensities to $T_1(t)$. The change in $T_1(t)$ with respect to the precontrast $T_1(t = 0)$ can then be used to derive contrast agent concentration (see Eq. 1.1). The background and details of pharmacokinetic modeling will be thoroughly discussed in **Chapter 2**. In **Chapter 4** we will deal with signal calibration, i.e. the conversion from signal intensity to contrast agent concentration.

A conversion from signal intensity to contrast agent concentration can also be applied as a preprocessing step for descriptive curve-type classification, but this is rarely seen; it is usually applied to relative enhancement. The native-T_1 dependency that is present in RE curves is nicely illustrated in Galbraith 2006, Figure 2, as well as in Vincensini et al. 2007, Figure 2. This dependency mainly affects the assessment of the initial uptake: the same uptake results in a higher RE in tissues with a long native T_1 than in tissues with a short native T_1.

Several studies have demonstrated high diagnostic performance using pharmacokinetic modeling. Schabel et al. (2010) arrived at a sensitivity of 91% and a specificity of 85%, using a three-parameter pharmacokinetic model and automatic thresholding. In comparison, a large multi-center trial (Bluemke et al. 2004) using similar eligibility criteria but a standard (BI-RADS) protocol and analysis reached a sensitivity of 88% at a specificity of 68%. Eliat et al. (2004) reached a sensitivity of 95% at 85% specificity using a combination of descriptive kinetic and pharmacokinetic parameters. Moreover, as pharmacokinetic modeling is physiology-based, the parameters have potential application not only in diagnostics, but also in determining prognosis, in predicting (non)responders, and in evaluating treatment effect (Henderson et al. 2000). This also means that lesions with a distinct physiology, like DCIS, may be characterized by looking at a different combination of pharmacokinetic parameters than for 'typical' mass lesions. Pharmacokinetic modeling is not a 'one-size-fits-all' approach.

Even though introduction of quantitative pharmacokinetic modeling should overcome the issues caused by a lack of standardization in data acquisition, pharmacokinetic model selection and parameter estimation methods are also non-standardized. There are few guidelines describing which model is applicable in which context. We will address this in **Chapters 2 and 3**. In **Chapter 3** we will provide a practical guideline for model selection.

In this section we have discussed quantitative kinetic analysis, but there is no reason to restrict quantitative analysis to kinetics only. The assessment of morphologic features using concentration images instead of signal intensity (subtraction) images, can potentially improve diagnostic standardization and reproducibility as well. In addition, morphologic features are quite subjective if a lesion does not show a distinct 'shape', 'distribution', 'margin', or 'internal enhancement pattern' (Kose et al. 2010). Computer-aided calculation of morphologic features (Gilhuijs et al. 2002) could therefore also improve the reproducibility of diagnostics.

1.7 Rationale and outline

The aim of this work is to provide understanding of quantitative techniques to analyze DCE-MRI data of the breast, as well as guidance on how to apply these techniques and under which conditions. Quantitative analysis of DCE-MRI data will only provide meaningful parameters that can contribute to diagnostics in case it is applied in a sensible way.

In **Chapter 2** we will discuss and explain pharmacokinetic modeling starting from the physiological basis. The focus lies on compartmental models. In addition to the theoretical background we also deal with the practical implications of applying a pharmacokinetic model, such as obtaining an arterial input function and parameter estimation. We will answer questions such as: 'in what way do pharmacokinetic models

describe contrast agent uptake in a lesion?', 'there are many pharmacokinetic models, in what sense do they differ?' and 'what are the practical implications of applying a pharmacokinetic model?'

As the relatively low temporal resolution of DCE-MRI breast data forms a major challenge to the application of pharmacokinetic models, we continue in **Chapter 3** with a simulation study that should answer the question: 'given these specific data properties, which pharmacokinetic model can I apply?' In this simulation study we investigated for a range of temporal resolutions and noise levels the applicability of the basic Tofts model (2 parameters), the extended Tofts model (3 parameters), and the shutter-speed model (3 parameters). (The details of these models are explained in Chapter 2.) The results of this study suggest that the use of models more complex than the basic Tofts model require data of very high quality, currently rarely obtained for clinical breast MRI. So, even though the basic Tofts model assumptions may be an oversimplification of the underlying physiology in some scenarios, we will investigate the use of this model in the remainder of this work.

An important relationship to establish in the framework of quantitative analysis of DCE-MRI data is the one between the acquired signal and the actual concentration of the contrast agent in the tissue. We will therefore look into signal calibration in **Chapter 4**. For this purpose, we developed a breast-coil insertable reference phantom that can be concurrently scanned with the patient. With the use of this phantom we investigated patient-specific signal calibration, answering questions as: 'Can I assume a theoretical relationship between contrast agent concentration and signal intensity?' and 'Can I still calibrate the signal if there is no applicable theoretical model?' The advantage of concurrent scanning is that variations introduced by the presence of the patient, as well as variations in scanner performance can be taken into account. We used the phantom to estimate a flip angle correction factor for variable flip angle precontrast T_1-mapping under assumption of the spoiled gradient echo signal model (Eq. 1.2). We also demonstrate a more empirical approach. Moreover, we produced concentration images and estimated tissue proton density, making use of the calibration phantom.

In Chapters 5 and 6 we will further explore the use of pharmacokinetic modeling in combination with low-temporal-resolution data. For this purpose, we used raw k-space rat data acquired at high-temporal resolution. First (**Chapter 5**), we investigated a realistic downsampling strategy to mimic the acquisition of low-temporal-resolution data, in which we incorporated the non-instantaneous nature of MR acquisition techniques: 'How can I simulate DCE-MRI data acquisition at low-temporal resolution?' In a comparison, we demonstrated that downsampling by omitting intermediate time points does not realistically reflect a low-temporal-resolution acquisition. In the same chapter, we estimated the error in the pharmacokinetic parameter estimates as a function of temporal resolution while making use of the true AIF (high-temporal-

resolution standard AIF): 'Using a standard AIF, how accurately can I estimate pharmacokinetic parameters from low-temporal-resolution data?'

Since in reality the high-temporal-resolution AIF would be unknown for data acquired at low-temporal resolution, in **Chapter 6** we estimated the AIF from the contrast agent uptake in a reference tissue present in the low-temporal-resolution data (data-derived AIF). Again, we investigated the error in the parameter estimates as a function of temporal resolution: 'Given low-temporal-resolution data, can I improve pharmacokinetic parameter estimation by making use of a data-derived AIF?' With the data under study, temporal resolution had no significant impact on parameter accuracy up to a sampling time of 60 s using the data-derived AIFs, whereas the use of a standard AIF resulted in a progressive error in the pharmacokinetic parameter estimates.

In **Chapter 7** we will discuss preclinical therapy assessment of an anti-cancer therapeutic in a mouse model. More specifically, we investigated the anti-tumor activity of a single dose of liposomal prednisolone phosphate. This anti-inflammatory agent has demonstrated to inhibit tumor growth. To investigate the mechanisms through which it acts on the tumor and its vasculature we studied multiple *in vivo* MRI-derived parameters as well histological parameters: 'Can I assess treatment response with MRI-derived parameters?'

In the concluding **Chapter 8** we will provide a general discussion as well as implications for future research resulting from this work.

Chapter 2

Introduction to pharmacokinetic modeling

This chapter contains work adapted from:

G.J.S. Litjens, M. Heisen, J. Buurman, B.M. ter Haar Romeny (2009). "Pharmacokinetic modeling in breast cancer MRI" Master's thesis, Eindhoven University of Technology, Eindhoven, The Netherlands, nr. 09/05

M. Heisen, J. Buurman, A. Vilanova, T. Twellmann, F.A. Gerritsen (2007). "Impact of the arterial input function on the classification of contrast-agent uptake curves in dynamic contrast-enhanced (DCE) MR images based on heuristic shape modeling" Proceedings ECR 2007, Vienna, Austria, 284

M. Heisen, J. Buurman, A. Vilanova, T. Twellmann, F.A. Gerritsen, B.M. ter Haar Romeny (2006). "Considerations regarding pharmacokinetic analysis of DCE-MR breast images" Master's thesis, Eindhoven University of Technology, Eindhoven, The Netherlands, nr. 06/05

In the present chapter we provide an overview of pharmacokinetic models, covering the most-applied models in the field of oncology. We describe their common ground and the ways in which they differ, both from a theoretical as well as a practical point of view. Moreover, we discuss methods to obtain an arterial input function and describe the parameter estimation methods applied in this work.

The application of the discussed models and methods is not limited to the context of dynamic contrast-enhanced magnetic resonance imaging (DCE-MRI) of the breast. However, we did write this chapter with that perspective in mind; i.e. strengths and limitations are addressed with the focus on DCE-MRI of the breast. An issue that is specific for this context is the relatively low-temporal resolution at which diagnostic DCE-MRI data of the breast is often acquired. We will touch upon this matter towards the end of this chapter, and discuss it in more detail in Chapters 3, 5, and 6. In this chapter it is assumed that uptake curves are available as contrast agent concentration curves. In Chapter 4 we will address the conversion from measured signal intensity data to contrast agent concentration.

2.1 Physiology in the framework of compartment modeling

Pharmacokinetics describes what happens to a substance, e.g. drug or contrast agent, after it has been administered to a living organism. This includes the mechanisms of absorption and distribution. The terms in which these mechanisms are described are physiological and therefore provide parameters describing the functioning of the organism's tissue. This physiological aspect makes it an attractive approach to investigate (aberrant) tissue functioning, and to diagnose diseased tissue.

In the field of DCE-MRI, pharmacokinetics is mainly studied by means of compartment modeling. 'Compartment' is a modeling concept and does not necessarily describe a singular physical location. A compartment can be defined as an amount or volume of material. The interconnected compartments that are involved in the distribution of the substance define the system. A compartment by itself is assumed to be kinetically homogeneous, i.e. the kinetic behavior is the same across the compartment. It is also assumed to be well-mixed, i.e. a single concentration is expected within the compartment. A physiological process can be modeled at different levels of detail, depending on the necessity to capture the complexness of the specific process. Different model systems, i.e. differing in the number of simplifying model assumptions, can therefore describe the same physiological process.

A basic pharmacokinetic model is the two-compartment model, in which the first compartment serves as input to the second compartment. The offered amount of substance, $u_1(t)$ – where t represents time – to the first compartment (with volume V_1) results in a dynamic concentration $C_1(t)$. The dynamic concentration of the responding compartment (with volume V_2), $C_2(t)$, changes as a result of exchange between the two

compartments. The exchange from compartment 1 to compartment 2 is governed by exchange rate k_{21}, whereas the reverse is governed by k_{12}. The loss of substance from the system is modeled by the excretion rate f_{01}. This example model is shown in Figure 2.1.

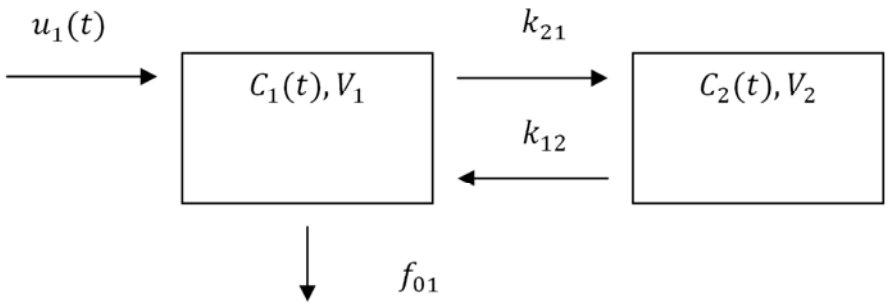

Figure 2.1 *Basic two-compartment model. Influx of substance into and efflux of substance out of the system takes place in compartment 1. Compartment 2 receives (k_{21}) substance from and returns (k_{12}) substance to compartment 1.*

The mass balance equations representing this system are

$$V_1 \frac{dC_1(t)}{dt} = u_1(t) - (k_{21} + f_{01}) \cdot C_1(t) + k_{12} \cdot C_2(t), \text{ and} \quad [2.1]$$

$$V_2 \frac{dC_2(t)}{dt} = k_{21} \cdot C_1(t) - k_{12} \cdot C_2(t). \quad [2.2]$$

In the context of DCE-MRI, $u_1(t)$ represents an intravenous (bolus) injection of a gadolinium-based contrast agent; compartment 1 represents the distribution volume in the capillary blood, which is the capillary blood plasma space V_c; and compartment 2 represents the distribution volume in a specific tissue, which is the extravascular extracellular space (EES) V_e. The EES is the space within the tissue, outside the microvessels, and outside the tissue cells. These two distribution volumes are specific for contrast agents that can exit the blood circulation but cannot enter cells. The latter currently holds for all clinically approved gadolinium-based contrast agents. In addition, the contrast particles are not actively transported across the microvascular membrane and therefore the exchange is symmetric, i.e. only passive, concentration-gradient-based, exchange takes place. This happens in the capillary bed, because only microvessels have a porous vessel wall. Schematically, the capillary bed is shown in Figure 2.2, connecting the arterial (C_p) to the venous (C_v) side of the main blood circulation. At this level, the contrast particles (small spheres) can leave the blood plasma and enter the EES. Excretion (f_{01} in Fig. 2.1) takes place in the kidneys.

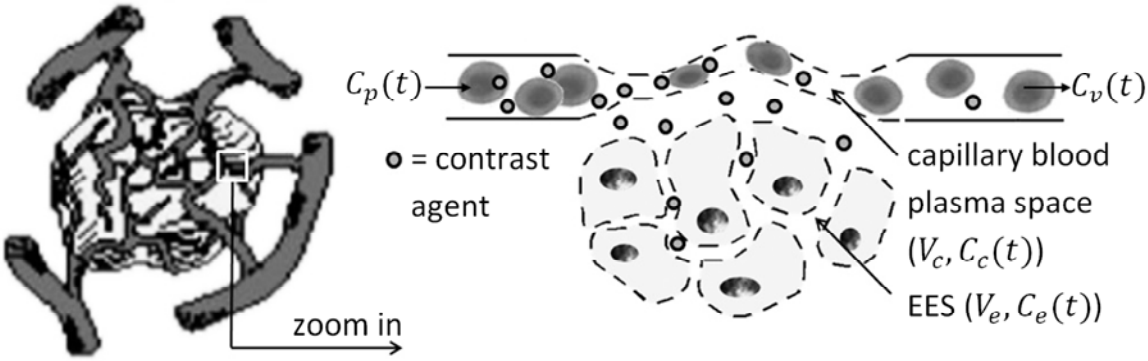

Figure 2.2 *Schematic representation of an imaging voxel relative to the size of a medium-sized tumor and the contrast agent exchange process taking place on the microvessel scale.*

Probing the microvasculature with MRI is a great challenge due to a discrepancy in scale. Microvessels range from 5 to 10 µm in diameter, whereas MRI images are acquired on a millimeter scale – a more than hundredfold difference in scale. The implication is that the signal that is measured at the millimeter scale contains contributions of several compartments, and therefore is a measure of the bulk concentration. For example, the single 1 mm^3 voxel, as depicted in Fig. 2.2 (white box), contains microvessels, cells, and extravascular extracellular space. This difference in scale, and the fact that the MR signal is an indirect measure of the contrast agent concentration, necessitates assumptions about the underlying physiological tissue behavior. Because current pharmacokinetic models differ in the level of assumptions and thereby resulting simplifications, the differences and overlap between several models will be discussed in Section 2.2.

In terms of tissue functioning, it is interesting to know what changes occur in the course of cancer development. As discussed in Chapter 1, hypoxia triggers the process of angiogenesis. Due to the poorly regulated sprouting and growth of the tumor-feeding microvessels, they exhibit structural (for impressive scanning electron microscopic images see: McDonald and Choyke 2003) and functional abnormalities; an important one being high vessel-wall permeability due to incomplete or lacking endothelium lining, and an interrupted basement membrane (Brix et al. 2004). The extent of microvascular disorganization and permeability can even be related to malignant tumor grade, i.e. becoming worse for higher grade (less differentiated) tumors. Tumor grade might therefore (partly) determine the organization and maturation of newly recruited microvessels (Daldrup et al. 1998). The increased microvascular density and permeability cause a rapid inflow of contrast agent into malignant tissue, resulting in the characteristic fast initial rise. Moreover, the same properties enable quick diffusion back into the capillary space; resulting in the other malignant characteristic, wash-out.

Another factor contributing to wash-out can be understood by separating the tissue bulk concentration into its blood plasma and EES components. If the plasma component contributes dominantly to the tissue bulk concentration the tissue will display wash-out, whereas a dominant EES contribution leads to a persistent uptake curve (Brix et al. 2004). Care should be taken not to overlook non-mass-like enhancements, which usually do not display this typical enhancement pattern, but a slower and often persistent uptake (Jansen et al. 2007, Newell et al. 2010). Take for example ductal carcinoma *in situ* (DCIS); the governing pharmacokinetics are in that case probably fundamentally different from those in mass-like lesions. Likely, an additional intraductal compartment is involved (Jansen et al. 2009a). Moreover, masses might not display a fast initial rise due to high interstitial pressure caused by increased permeability and lack of lymphatic drainage. For this type of tumor the EES is increased and therefore an important tissue property to determine (Vincensini et al. 2007, Vos et al. 2008).

2.2 Common ground and differences between compartment models

2.2.1 Common ground

The compartment models that will be further discussed in this work have the basic shape of an open two-compartment model in common (Fig. 2.3). The models are 'open' because the main blood circulation, which could be seen as the third compartment, is not modeled as such, but as supplying input to the system and taking up its output. Input and output are governed by the apparent plasma flow $\tilde{F}$. The exchange between the capillary blood plasma compartment and the EES is governed by K_{PS}, which is a measure of the permeability surface area product ($P \cdot S$). Excretion (f_{01} in Fig. 2.1) reduces the amount of contrast agent in the main blood circulation and is therefore not explicitly present in the diagram. The mass balance equations representing this system are

$$V_c \frac{d\bar{C}_c(t)}{dt} = \tilde{F}\left(C_p(t) - \bar{C}_c(t)\right) - K_{PS}\left(\bar{C}_c(t) - \bar{C}_e(t)\right), \text{ and} \qquad [2.3]$$

$$V_e \frac{d\bar{C}_e(t)}{dt} = K_{PS}\left(\bar{C}_c(t) - \bar{C}_e(t)\right), \qquad [2.4]$$

in which $\bar{C}_c$ (mmol/L = mM) is the concentration in the capillary plasma volume, V_c (mL); and $\bar{C}_e$ (mM) in the EES, V_e (mL). C_p (mM) is the concentration entering the capillary bed on the arterial side, and C_v (mM) the concentration exiting on the venous side. $\tilde{F}$ (mL/min) is the apparent plasma flow, and K_{PS} (mL/min) is the capillary transfer coefficient. (Note, the use of liters as well as milliliters in one equation is due to conventions.) Although it is common to use the notations '$C_c(t)$' and '$C_e(t)$', as we did in the previous section, we will use the notations '$\bar{C}_c(t)$' and '$\bar{C}_e(t)$' in Section 2.2 to reflect that these concentrations are (spatial) mean concentrations in the capillary space and the EES, respectively.

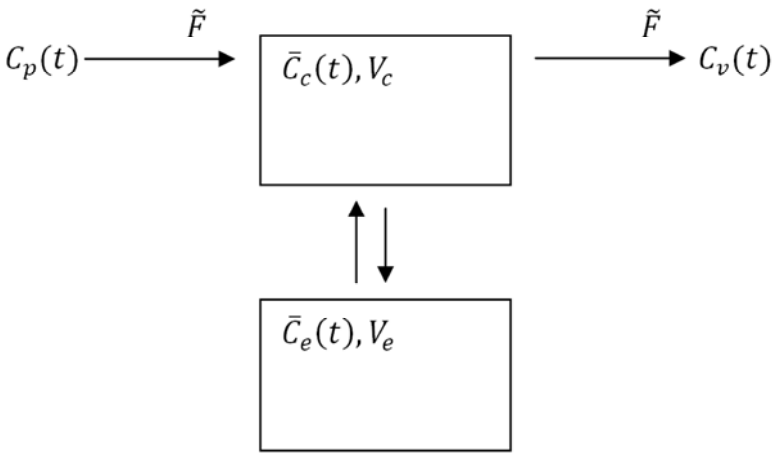

Figure 2.3 *General open two-compartment model, after (Brix et al. 1999). $\bar{C}_c(t)$ and $\bar{C}_e(t)$ respectively denote the mean concentration in the capillary compartment and the mean concentration in the extravascular extracellular volume.*

All models have to cope with the fact that the scale of MRI is too large to measure $\bar{C}_c(t)$ and $\bar{C}_e(t)$ independently. The measured tissue bulk concentration, $\bar{C}_t(t)$, represents $\bar{C}_c(t)$ as well as $\bar{C}_e(t)$,

$$V_t \cdot \bar{C}_t(t) = V_c \cdot \bar{C}_c(t) + V_e \cdot \bar{C}_e(t) \rightarrow \bar{C}_t(t) = v_c \cdot \bar{C}_c(t) + v_e \cdot \bar{C}_e(t), \qquad [2.5]$$

in which the concentrations in the contributing compartments are weighted by their respective volume fractions ($v_c = V_c/V_t$, $v_e = V_e/V_t$, V_t = tissue volume). In Figure 2.4, we show four $\bar{C}_t(t)$ curves. The dashed lines show the separate contributions of the capillary compartment and the EES. We used the system as described by Eqs. 2.3 and 2.4 and a literature input function (Yang et al. 2007) to simulate these curves. In Fig. 2.4(a), $\bar{C}_t(t)$ is simulated for pectoralis muscle with $v_e/v_c = 0.09/0.04 = 2.25$ (Brix et al. 2004). The curve shape is persistent uptake / plateau. In Fig. 2.4(b) we increased v_c from 0.04 to 0.20, resulting in a ratio $v_e/v_c = 0.09/0.20 = 0.45$. Interestingly, the dominant capillary contribution in (b) does not result in a wash-out type of enhancement pattern. A mere increase in v_c, decreasing the ratio v_e/v_c, is not the sole cause of a wash-out pattern (as mentioned in Section 2.1). Its increase does, however, cause a steeper initial rise. To obtain a wash-out curve, the input of contrast agent into the capillary space cannot stay at the basic level: at low flow, the larger space v_c will follow the input function $C_p(y)$ more slowly, and will not resemble its 'spike' shape. Only if we scale F with v_c, so times five in comparison to (a) and (b), we obtain a wash-out curve (Fig. 2.4(c)). Scaling K_{PS} with v_c as well (Fig.2.4(d)) enhances the wash-out feature because in that case the contrast agent can more easily enter and exit the EES.

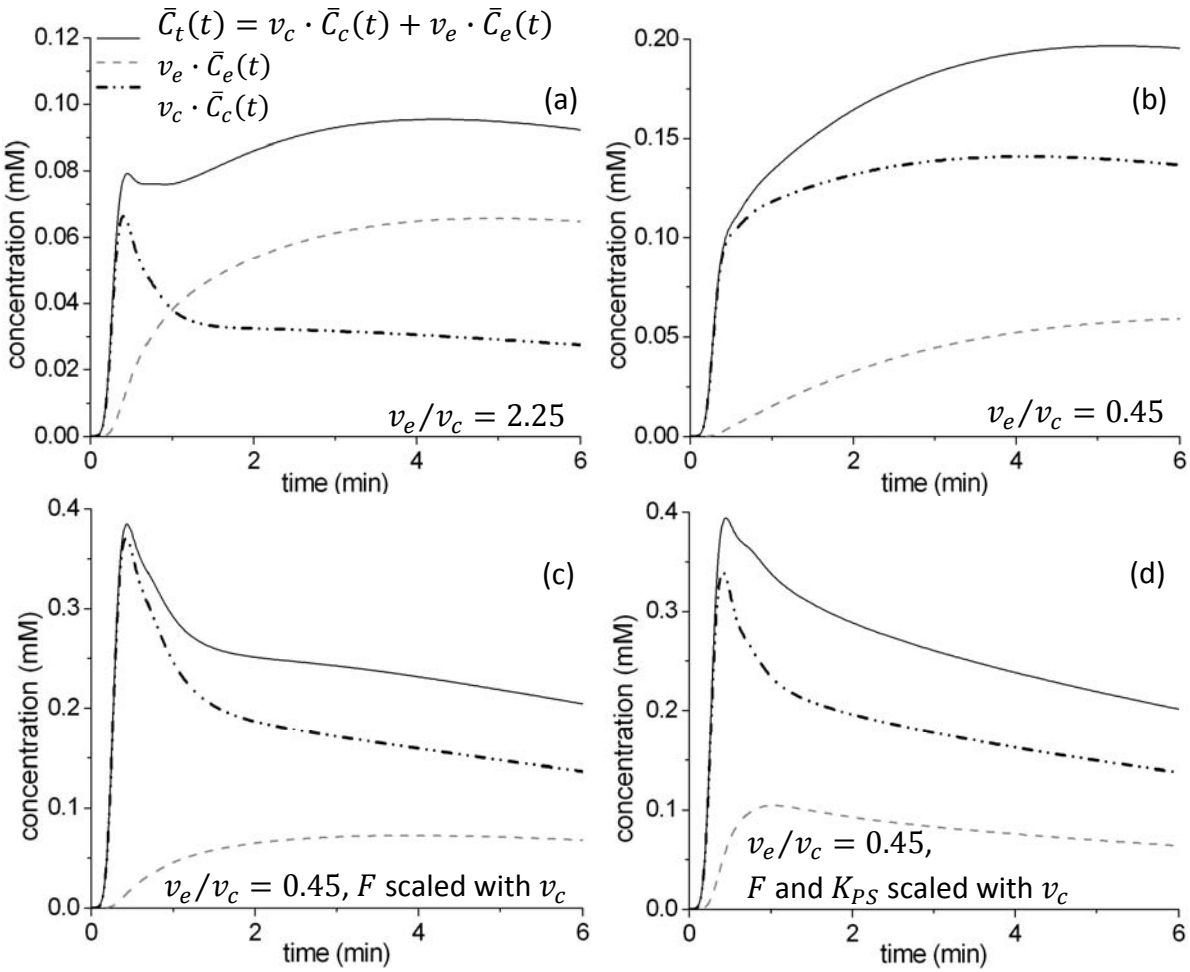

Figure 2.4 *Simulated contrast agent uptake curves in the tissue, showing the separate contributions of the EES (weight: v_e) and the capillary space (weight: v_c). (a) Relatively large contribution of v_e, as found in pectoralis muscle; (b) increased v_c; (c) increased v_c and F; and (d) increased v_c, F and K_{PS}. The latter two combinations cause a wash-out curve type.*

As explained above, $\bar{C}_c(t)$ plays a double role; it inputs contrast agent to the EES, and contributes to $\bar{C}_t(t)$ as a direct throughput. To extract pharmacokinetic parameters from a tissue measurement $\bar{C}_t(t)$, we therefore need to know $\bar{C}_c(t)$. Because it is impossible to measure at the scale of the capillary bed, $\bar{C}_c(t)$ has to be estimated. The difficulty with estimating $\bar{C}_c(t)$ is that while passing through the capillary bed, contrast agent is exchanged with the EES. This implicates a spatial dependency in addition to a temporal dependency. That is why in Eq. 2.3 flow is called the apparent flow ($\tilde{F}$). This issue is addressed in Panel A by looking at the transport of a contrast agent through a single capillary.

Panel A

Suppression of spatial variations to arrive at compartmental description of contrast agent exchange

The following description of transport of a contrast agent through a single capillary is largely based on the appendix in Brix et al. 1999 and Chapter 27 in Principles of Nuclear Medicine by Wagner, Szabo, and Buchanan (Gjedde 1995). We assume that within the tissue of interest all capillaries demonstrate identical behavior. The solubility of the contrast agent is assumed to be the same in the EES as in the blood plasma. We make use of the general definition of a compartment as a tracer state that varies in time only (Rescigno and Beck 1972):

$$\frac{dm}{dt} = j - k \cdot m, \qquad \text{[A.1]}$$

in which m (mmol) is the quantity of tracer that belongs to the compartment, k (min^{-1}) is the rate constant (m is depleted at rate $k \cdot m$), and j (mmol/min) is the rate at which m is replenished.

To investigate the spatial dependency of contrast agent concentration we look at a small time interval dt during which we assume an instantaneous concentration gradient between the capillary space and the EES. The replenishing rate (j) can in that case be described by Fick's first law of unidirectional diffusion:

$$j = -D \cdot A \frac{\partial c(t,x)}{\partial x}, \qquad \text{[A.2]}$$

in which D (mL cm^{-1} min^{-1}) is the diffusion coefficient, A (cm^2) is the cross-sectional area through which the diffusion occurs, x (cm) marks the position, and $\partial c(t,x)/dx$ is the concentration gradient. The negative sign takes into account that diffusive flow is in the opposite direction of increasing concentration, i.e. the flow runs from the compartment with the highest concentration to the compartment with the lowest concentration.

In the context of a single capillary j can be described as

$$j = -F \cdot L \frac{\partial C_c(t,x)}{dx}, \qquad \text{[A.3]}$$

in which L (cm) is the length of the capillary. The dimensions of $[D \cdot A] =$ mL cm min^{-1} are the same as those of $[F \cdot L] =$ mL min^{-1} cm. The depletion rate ($k \cdot m$) can be described as

$$k \cdot m = K_{PS}\big(C_c(t,x) - C_e(t,x)\big), \qquad \text{[A.4]}$$

in which K_{PS} is the capillary transfer coefficient. For dm/dt holds

Panel A (continued)

$$\frac{dm}{dt} = V_c \frac{\partial C_c(t,x)}{dt}. \quad [A.5]$$

Using Eqs. A.3 – A.5, we can write the following pair of mass balance equations for the capillary compartment and the EES:

$$V_c \frac{\partial C_c(t,x)}{\partial t} = -F \cdot L \frac{\partial C_c(t,x)}{\partial x} - K_{PS}\big(C_c(t,x) - C_e(t,x)\big), \text{ and} \quad [A.6]$$

$$V_e \frac{\partial C_e(t,x)}{\partial t} = K_{PS}\big(C_c(t,x) - C_e(t,x)\big), \quad [A.7]$$

in which $C_c(t,x)$ is the plasma concentration at time t at point x along the capillary, $C_e(t,x)$ the concentration in the EES at time t at point x along the capillary, and F is the plasma flow through the capillary. The first term in Eq. A.6 represents diffusive flow along the capillary, the second exchange with the EES.

Because a compartment is assumed to be kinetically homogeneous and well-mixed, we can suppress spatial variation from inlet ($x = 0$) to outlet ($x = L$) by an approximation of the integral:

$$\int_0^L C_c(t,x)dx = L \cdot \bar{C}_c\,(t), \quad [A.8]$$

$$\int_0^L C_e(t,x)dx = L \cdot \bar{C}_e(t), \quad [A.9]$$

$$\int_0^L \frac{\partial C_c(t,x)}{\partial x} dx = C_c(t, x = L) - C_c(t, x = 0), \quad [A.10]$$

in which $\bar{C}_c(t)$ and $\bar{C}_e(t)$ reflect the mean concentration in the capillary plasma and the EES, respectively. Because $C_c(t, x = 0)$ equals $C_p(t)$, and $C_c(t, x = L)$ equals $C_v(t)$, instead of Eqs. 2.3 and 2.4 we can write:

$$V_c \frac{d\bar{C}_c(t)}{dt} = F\left(C_p(t) - C_v(t)\right) - K_{PS}\big(\bar{C}_c(t) - \bar{C}_e(t)\big), \quad [A.11]$$

$$V_e \frac{d\bar{C}_e(t)}{dt} = K_{PS}\big(\bar{C}_c(t) - \bar{C}_e(t)\big). \quad [A.12]$$

In brief, via the assumptions of (i) identical capillaries in the tissue of interest, (ii) equal solubility of the contrast agent in the EES and the blood plasma, and (iii) kinetic homogeneity and well-mixedness in the compartments, the system that was described by Eqs. 2.3 and 2.4 can now be described by

$$V_c \frac{d\bar{C}_c(t)}{dt} = F\left(C_p(t) - C_v(t)\right) - K_{PS}\big(\bar{C}_c(t) - \bar{C}_e(t)\big), \text{ and} \quad [2.6]$$

$$V_e \frac{d\bar{C}_e(t)}{dt} = K_{PS}\left(\bar{C}_c(t) - \bar{C}_e(t)\right), \qquad [2.7]$$

in which F (mL/min) is the true flow instead of the apparent flow. However, as a consequence of using the true flow, $C_v(t)$ is introduced in Eq. 2.6. Whereas it is possible to measure $C_p(t)$, i.e. the passage of contrast agent material before arrival in the capillary bed, the exiting material, $C_v(t)$, is hard to measure. The specific assumptions involved to exclude $C_v(t)$ from the pair of mass balance equations are dealt with in Sections 2.2.2 and 2.2.3.

2.2.2 Independent measures of flow and permeability

Two characteristics that can point out a malignant type of growth are flow (F) and permeability (K_{PS}); one being a measure of the amount of functional vessels, the other of microvessel wall quality. Especially in the assessment of therapeutic effects of agents acting on the vasculature, it can be crucial to obtain independent estimates of these two parameters.

Morales and Smith

Morales and Smith (1948) developed an approach to allow independent estimation of flow and permeability. The main idea being that there is a constant factor r between $C_p(t) - C_v(t)$ and $C_p(t) - \bar{C}_c(t)$, so that

$$r\left(C_p(t) - C_v(t)\right) = C_p(t) - \bar{C}_c(t), \qquad \text{for } 0 \leq r \leq 1. \qquad [2.8]$$

It gives a weight to the influence of $C_p(t)$ and $C_v(t)$ on $\bar{C}_c(t)$. For example: $r = 1 \rightarrow C_p(t) - C_v(t) = C_p(t) - \bar{C}_c(t) \rightarrow \bar{C}_c(t) = C_v(t)$, which means that there is ample loss of contrast agent to the EES, enough to have $\bar{C}_c(t)$ match $C_v(t)$. Or: $r = 0 \rightarrow 0 = C_p(t) - \bar{C}_c(t) \rightarrow \bar{C}_c(t) = C_p(t)$, which means that there is minor loss of contrast agent to the EES, and $\bar{C}_c(t)$ remains at the level of $C_p(t)$. Using this factor r, Eqs. 2.6 and 2.7 become

$$V_c \frac{d\bar{C}_c(t)}{dt} = \frac{F}{r}\left(C_p(t) - \bar{C}_c(t)\right) - K_{PS}\left(\bar{C}_c(t) - \bar{C}_e(t)\right), \text{ and} \qquad [2.9]$$

$$V_e \frac{d\bar{C}_e(t)}{dt} = K_{PS}\left(\bar{C}_c(t) - \bar{C}_e(t)\right). \qquad [2.10]$$

Via the assumption of a fixed slope (r) of the concentration gradient from inlet to outlet of the capillary bed, we have removed $C_v(t)$ from the equations. The apparent plasma flow $\tilde{F}$, as introduced in Section 2.2.1, equals

$$\tilde{F} = \frac{F}{r} \geq F, \quad \text{for } 0 \leq r \leq 1. \qquad [2.11]$$

It follows from Eq. 2.11 that the apparent flow $\tilde{F}$ is an overestimation of the true flow F.

As a final step, we express Eqs. 2.9 and 2.10 per unit of tissue volume ($v_c = V_c/V_t$, $v_e = V_e/V_t$) to meet the convention as proposed by Tofts et al. (1999). We first multiply with the tissue density ρ (M_t/V_t):

$$M_t \frac{V_c}{V_t} \frac{d\bar{C}_c(t)}{dt} = \frac{F \cdot \rho}{r} \left(C_p(t) - \bar{C}_c(t) \right) - K_{PS} \cdot \rho \left(\bar{C}_c(t) - \bar{C}_e(t) \right), \qquad [2.12]$$

in which $V_c/V_t = v_c$. Then we divide by M_t again, changing the unit of both F and K_{PS} from mL/min to mL/min/g. In addition, we drop the '$\bar{C}$' notation to denote the use of a spatial mean:

$$v_c \frac{dC_c(t)}{dt} = \frac{F\rho}{r} \left(C_p(t) - C_c(t) \right) - K_{PS} \cdot \rho \left(C_c(t) - C_e(t) \right), \qquad [2.13]$$

$$v_e \frac{dC_e(t)}{dt} = K_{PS} \cdot \rho \left(C_c(t) - C_e(t) \right), \text{ and} \qquad [2.14]$$

$$C_t(t) = v_c \cdot C_c(t) + v_e \cdot C_e(t). \qquad [2.15]$$

Note that in the proposed convention F represents whole blood flow, not plasma flow. In that case, F has to be corrected for the hematocrit factor, H_{ct}:

$$F_{whole\ blood} = F_{plasma}(1 - H_{ct}). \qquad [2.16]$$

A typical range of hematocrit in large vessels is 0.4 (Lammertsma et al. 1984) to 0.45 (Brix et al. 2004). In Henderson et al. (2000) it is proposed to scale the hematocrit factor from large to small vessels, because the red blood cell content in small vessels is lower. The factor $(1 - H_{ct})$ then changes into $(1 - w \cdot H_{ct})$, with $w \approx 0.7$ (Lammertsma et al. 1984). Note that the hematocrit level is often lower in cancer patients (Yang et al. 2009). Here, we did not adopt the use of F as marking whole blood flow.

We will refer to the above-described type of model, which gives us independent estimates of (apparent / true) flow and permeability-surface area product, as the *full two-compartment model* (Brix et al. 2009). Recent publications using this type of model are Bains et al. 2010, Brix et al. 2004, Brix et al. 2009, and Donaldson et al. 2010. In De Bazelaire et al. 2005, this type of model is used under the assumption of negligible reflux of the contrast agent from the EES back into the capillary space; which means that no estimate of v_e is obtained. This assumption is appropriate for macromolecular contrast agents with a slow trans-membrane leakage rate, and / or a DCE-MRI acquisition of short duration.

St. Lawrence and Lee

The approach as proposed by St. Lawrence and Lee (1998) to solve the open two-compartment model is not purely compartmental. It is an adiabatic approximation to the tissue homogeneity model (Johnson and Wilson 1966). In the tissue homogeneity model spatial variation in contrast agent concentration along the capillaries is taken into

account. Although Garpebring et al. (2009) recently showed promising results via calculations in Fourier space, parameter estimation with the tissue homogeneity model is unstable. For this reason, Morales and Smith (1948) averaged the capillary concentration (see Panel A), which reduces the capillary space to a compartment. Here, a different approach is chosen (the 'common ground' as described in 2.2.1 only holds for purely compartmental models). The tissue enhancement is divided into two phases: the initial vascular phase (from $t = 0$ to $t = T_c$, T_c: mean capillary transit time), and the secondary extravascular phase. In contrast to the capillary space, the EES is modeled as a compartment. The approach is called adiabatic because the AIF is assumed to not change appreciably during the mean capillary transit time (Brix et al. 2010), which implies the assumption of negligible exchange during the initial phase. This assumption is motivated by the fact that concentration changes in the EES are slow relative to those in the capillary space. Therefore, for a small time interval, the rate of change of $C_e(t)$ can be considered to be at steady state while the fast change of $C_p(t)$ is taking place. The equation describing $C_t(t)$ (Buckley 2002b),

$$C_t(t) = F \cdot \rho \int_0^{T_c} C_p(t-u)du + F \cdot E \cdot \rho \int_{T_c}^{t} C_p(u)\, e^{-F \cdot E \cdot \rho / v_e (t-u-T_c)} du, \qquad [2.17]$$

is a closed-form solution of the tissue homogeneity model in the time domain (St Lawrence and Lee 1998), leading to estimates of F, E, v_e, and T_c. The unit step function is denoted as u.

The newly introduced parameter E represents the initial extraction fraction during first pass, $\left(C_p(t) - C_v(t)\right)/C_p(t)$, and, using the Renkin-Crone assumption (Crone 1963, Renkin 1959), can be described by

$$E = 1 - e^{-P \cdot S/F}. \qquad [2.18]$$

The discontinuity between the intravascular phase and the extravascular phase at $t = T_c$, occurs as a fraction $(1 - E)$ of the contrast agent leaves the tissue. It is assumed that first-pass exchange of contrast agent is unidirectional, and that the concentration decreases exponentially along the capillary as a result of loss of contrast agent to the EES. Therefore, the higher the permeability (P) and the surface area for exchange (S), the closer E is to 1. The extraction fraction is inversely related to the plasma flow, because at high flow rates the capacity of the capillary bed for transferring the contrast agent approaches a maximum. The constant $P \cdot S$ describes the loss of contrast agent from the capillary space to the EES in case the concentration gradient between the two compartments would be constant, i.e. if capillary concentration was maintained almost at the arterial level throughout the length of the capillary (Peters 1998). Because F is present in both the first and the second term of Eq. 2.17, we can obtain independent estimates of F and $P \cdot S$.

The St. Lawrence and Lee approach is reasonable in brain tissue because of the blood-brain barrier (limited permeability), but may be less applicable to other tissues (St Lawrence and Lee 1998). The applicability can be tested by simultaneously measuring changes in T_1-relaxation (affected by flow and permeability) and T_2^*-relaxation (affected by flow only) as a function of contrast agent concentration. Modeling approaches similar to the St. Lawrence and Lee approach described in this section have been applied by for instance Henderson et al. (2000), Koh et al. (2001), Buckley (2002b), and Kershaw et al. (2009). We will refer to this type of model as the *adiabatic approximation to the tissue homogeneity model*. In case the mean capillary transit time (T_c) is negligible (physically or relative to the sampling interval of the measurement), the first term equals zero and the second term can be recognized as the integral form of the model described in the next section.

2.2.3 Composite measure of flow and permeability

Although it is valuable to obtain independent measures of flow and permeability, instead, the most commonly applied pharmacokinetic models deliver a composite measure. The models as described in Section 2.2.2 are demanding in terms of data quality. Because of their level of detail and thus large number of fitting parameters (full two-compartment model: F, K_{PS}, v_c, v_e; St. Lawrence and Lee model: F, T_c, E, v_e from which $P \cdot S$ and v_c can be derived), they require a high temporal-sampling rate and a high signal-to-noise ratio. The fact that the 'less demanding' models as described in this section are more commonly applied, reflects the gap that exists between modeling theory and practical data acquisition. In Section 2.3 we will further compare the different types of models and their use.

Vascular component neglected

We can think of two scenarios in which the contribution of the capillary compartment to the measured signal is negligible, and $\bar{C}_t(t) \approx v_e \cdot \bar{C}_e(t)$. One, in case the capillary fraction (v_c) is negligibly small (Tofts and Kermode 1991), and two, in case the capillary concentration ($\bar{C}_c(t)$) cannot be distinguished from the extravascular extracellular concentration ($\bar{C}_e(t)$) due to very high permeability (Gjedde 1995), see Figure 2.5.

The first scenario is mainly applicable to brain diseases, because in normal brain tissues the capillary volume fraction is about 2-4% (Tofts 2003). The approach was first suggested by Kety (1951). It is assumed that the loss of contrast agent from the capillary space to the EES does not deplete the capillary contrast agent concentration (Tofts and Kermode 1991). A small vascular volume (V_c) in combination with limited permeability ($F \gg P \cdot S$), implies that the changes in mean tissue concentration during the time of passage of an element of blood through the tissue are negligible:

$$V_t \frac{d\bar{C}_t(t)}{dt} = V_c \frac{d\bar{C}_c(t)}{dt} + V_e \frac{d\bar{C}_e(t)}{dt} \approx V_e \frac{d\bar{C}_e(t)}{dt}. \qquad [2.19]$$

Using Eq. 2.19, we can reduce Eq. 2.6 to

$$0 = F\left(C_p(t) - C_v(t)\right) - K_{PS}\left(\bar{C}_c(t) - \bar{C}_e(t)\right), \qquad [2.20]$$

which we can use in 2.7:

$$V_e \frac{d\bar{C}_e(t)}{dt} = F\left(C_p(t) - C_v(t)\right). \qquad [2.21]$$

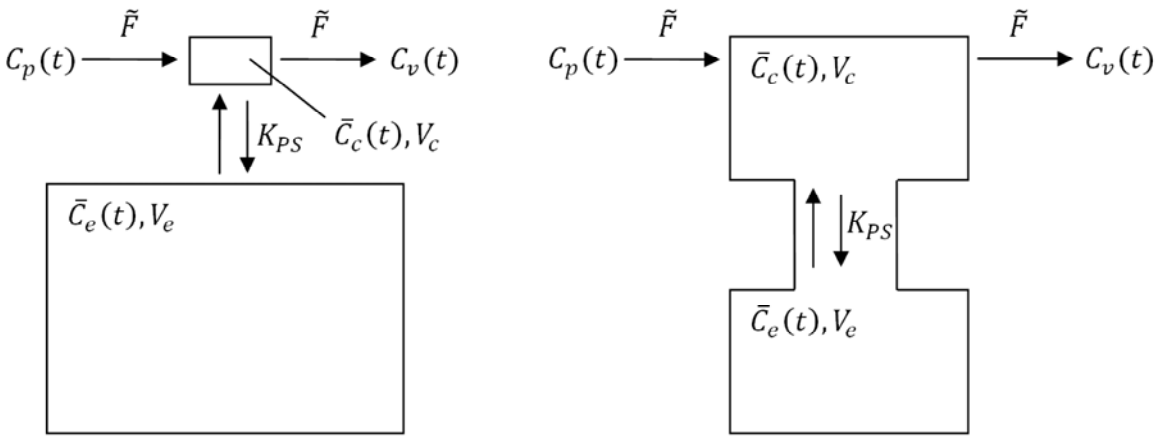

Figure 2.5 *Left: scenario 1, permeability-limited (large flow); right: scenario 2, flow-limited (large permeability).*

In the second scenario ($P \cdot S \gg F$), the contrast agent concentration in the capillary compartment is identical to the concentration in the EES, as it exits from the tissue. Such a high-permeability scenario is for instance applicable to high-grade tumors with aggressive angiogenesis, resulting in an extensive network of highly permeable vessels. In that case, the only limitation for $\bar{C}_e(t)$ to directly follow $\bar{C}_c(t)$ is the blood plasma flow (F). The increase in $\bar{C}_e(t)$ thereby becomes directly proportional to the difference between the entering concentration ($C_p(t)$) and the exiting concentration ($C_v(t)$), which makes it impossible to obtain a measure of the permeability surface area product, K_{PS}. In addition, the distribution volume V_e includes both, V_e and V_p. We again obtain Eq. 2.21.

Even though the underlying tissue compositions and behavior are very distinct, the two scenarios (see Fig. 2.5) lead to the same approximation (Eq. 2.21). This single equation is a reduced version of the system described by Eqs. 2.6 and 2.7. A detailed derivation of how the unknown $C_v(t)$ is removed from Eq. 2.21 is given in Panel B. The outcome is that, assuming uniformity of $C_e(t)$ along the capillary, we can write $C_p(t) - C_v(t)$ in terms of $C_p(t) - C_e(t)$:

$$C_p(t) - C_v(t) = \left(1 - e^{-P \cdot S/F}\right)\left(C_p(t) - C_e(t)\right), \qquad [2.22]$$

in which we can recognize the Renkin-Crone model (Eq. 2.18).

Combining Eqs. 2.21 and 2.22, we arrive at

$$V_e \frac{dC_e(t)}{dt} = F\left(1 - e^{-PS/F}\right)\left(C_p(t) - C_e(t)\right) = F \cdot E\left(C_p(t) - C_e(t)\right). \qquad [2.23]$$

To meet the convention as proposed by Tofts et al. (1999), we first multiply with the tissue density ρ (M_t/V_t):

$$M_t \frac{V_e}{V_t} \frac{dC_e(t)}{dt} = F \cdot E \cdot \rho\left(C_p(t) - C_e(t)\right), \qquad [2.24]$$

in which $V_e/V_t = v_e$. Then we divide by M_t again, changing the unit of F from mL/min to mL/min/g:

$$v_e \frac{dC_e(t)}{dt} = F \cdot E \cdot \rho\left(C_p(t) - C_e(t)\right). \qquad [2.25]$$

Because the contribution of the capillary compartment to the signal is assumed to be negligible, $C_e(t)$ can be replaced by $C_t(t)/v_e$ (see Eq. 2.5), leading to

$$v_e \frac{dC_e(t)}{dt} = F \cdot E \cdot \rho\left(C_p(t) - \frac{C_t(t)}{v_e}\right), \text{ and} \qquad [2.26]$$

$$C_t(t) \approx v_e \cdot C_e(t). \qquad [2.27]$$

In case of the first scenario, in which $F >> P \cdot S$, we can see that the term $F \cdot E \cdot \rho$ can be reduced to represent the permeability surface area product, using a first order Taylor expansion:

$$F \cdot E \cdot \rho = F\left(1 - e^{-P \cdot S/F}\right)\rho \approx F \cdot P \cdot S/F \cdot \rho = P \cdot S \cdot \rho, \qquad [2.28]$$

whereas in the second scenario, in which $F << P \cdot S$, the same term represents flow, because E approaches a value of 1:

$$F \cdot E \cdot \rho = F\left(1 - e^{-P \cdot S/F}\right)\rho \approx F \cdot 1 \cdot \rho = F \cdot \rho. \qquad [2.29]$$

Panel B

Introduction of the extraction fraction into the reduced two-compartment model

The following description is largely based on the derivation given in Kety 1951, and uses the same single capillary model as in Panel A. We start with the general definition of a compartment as a tracer state that varies in time only (Rescigno and Beck 1972):

$$\frac{dm}{dt} = j - k \cdot m. \qquad [B.1]$$

Using Eq. 2.6, repeated over here,

$$V_c \frac{d\bar{C}_c(t)}{dt} = F\left(C_p(t) - C_v(t)\right) - K_{PS}\left(\bar{C}_c(t) - \bar{C}_e(t)\right), \qquad [B.2]$$

we can describe the loss of contrast agent from the capillary space to the EES ($-k \cdot m$, i.e. the second term in Eq. B.2) for a unit amount of contrast agent (dm_c) as it moves from x through dx, during a unit time interval dt as:

$$dm_c(t,x) = -P \cdot s' \cdot dx\left(C_c(t,x) - C_e(t,x)\right)dt, \qquad [B.3]$$

in which P (L cm^{-2} min^{-1}) is the permeability per unit area per unit time, s' (cm) is the surface area per unit length, dx (cm) is a unit length, $C_c(t,x)$ (mM) is the concentration in the capillary space at position x and time t, $C_e(t,x)$ (mM) is the concentration in the EES at position x and time t, and dt (min) is a unit time.

The left-hand side of Eq. B.3 can be expressed as

$$dm_c(t,x) = dC_c(t,x) \cdot v' \cdot dx, \qquad [B.4]$$

in wich v' (cm^2) is the volume per unit length. If we introduce f (cm min^{-1}) as the average linear plasma velocity in the capillary, it holds that

$$dx = f \cdot dt, \qquad [B.5]$$

which can be used in Eq. B.4:

$$dC_c(t,x) \cdot v' \cdot dx = dC_c(t,x) \cdot v' \cdot f \cdot dt. \qquad [B.6]$$

Combining Eqs. B.3 and B.6, we obtain

$$dC_c(t,x) \cdot v' \cdot f \cdot dt = -P \cdot s' \cdot dx\left(C_c(t,x) - C_e(t,x)\right)dt, \qquad [B.7]$$

which can be rearranged as:

$$\frac{dC_c(t,x)}{dx} = -\frac{P \cdot s'}{v' \cdot f}\left(C_c(t,x) - C_e(t,x)\right). \qquad [B.8]$$

Panel B (continued)

Assuming that $C_e(t,x)$ is approximately uniform along the capillary, it is only a function of time, i.e. $C_e(t)$. In that case, the solution of this differential equation is given by

$$C_c(t,x) - C_e(t) = A \cdot e^{-\frac{P \cdot s\prime}{v\prime \cdot f} x}, \qquad [B.9]$$

where A is an integration constant. Application of the boundary conditions that $C_c(t,x) = C_p(t)$ at $x = 0$, and that $C_c(t,x) = C_v(t)$ at $x = L$, gives

$$C_c(t,0) - C_e(t) = C_p(t) - C_e(t) = A, \text{ and} \qquad [B.10]$$

$$C_c(t,L) - C_e(t) = C_v(t) - C_e(t) = A \cdot e^{-\frac{P \cdot s\prime}{v\prime \cdot f} L} = \left(C_p(t) - C_e(t)\right) e^{-\frac{P \cdot s\prime}{v\prime \cdot f} L}. \qquad [B.11]$$

Because $P \cdot s' \cdot L$ can be written as $P \cdot S$, and $v' \cdot f$ as F, Eq. B.11 is equivalent to

$$C_v(t) - C_e(t) = \left(C_p(t) - C_e(t)\right) e^{-P \cdot S/F}. \qquad [B.12]$$

Using the above result, we can now write $C_p(t) - C_v(t)$ in terms of $C_p(t) - C_e(t)$:

$$\left(C_p(t) - C_e(t)\right) - \left(C_v(t) - C_e(t)\right) = \left(C_p(t) - C_e(t)\right) - \left(C_p(t) - C_e(t)\right) e^{-P \cdot S/F}, \qquad [B.13]$$

thus:

$$C_p(t) - C_v(t) = \left(1 - e^{-P \cdot S/F}\right)\left(C_p(t) - C_e(t)\right). \qquad [B.14]$$

Eq. 2.28 represents the permeability-limited regime, whereas Eq. 2.29 represents the flow-limited regime. In reality, a tissue might show intermediate behavior, which is called the mixed regime. Because of the potentially ambiguous meaning of $F \cdot E \cdot \rho$ (in case it is unknown which regime the tissue obeys), the transfer coefficient K^{trans} is introduced:

$$K^{trans} = F \cdot E \cdot \rho. \qquad [2.30]$$

Sometimes, K^{trans} and v_e are reported as the ratio K^{trans}/v_e, which equals the rate constant between the EES and the capillary plasma fraction, k_{ep} (Tofts et al. 1999). The use of k_{ep} has the advantage of providing a measure with unit min^{-1}, even without conversion from signal intensity to contrast agent concentration. This does not hold for K^{trans}, which has in that case an arbitrary unit.

Similar implementations of this type of model have been suggested by Tofts and Kermode (1991), Brix et al. (1991), and Larsson et al. (1990). In Larsson and Tofts 1992 it was shown that the differences between the approaches suggested by Tofts, Brix, and Larsson are mainly due to differences in the respective measurement schemes, and can be largely removed by making use of precontrast T_1 estimates and independent AIF measurements. In Zwick et al. 2010 it was shown that if the originally proposed measurement schemes are used, the K^{trans}/v_e obtained with the Tofts approach does not match well with k_{ep} obtained with the Brix approach. This was attributed to differences in modeling the AIF – respectively, assuming a standard (predefined) rapid-bolus injection, and modeling a short-time constant-rate infusion – signal calibration, and model implementation. Because we use the Tofts version of this type of model, we will refer to it as the *basic Tofts model*.

Vascular contribution

The above-described model that ignores a vascular contribution to the signal can only roughly characterize tissue composition and behavior, because it does not reflect all main components of the system. In many tissues outside the brain, the capillary volume fraction is too large to be neglected; especially in case of cancer. This rules out scenario 1, as described above (Fig. 2.5). Also, many tissues contain non-exchange vessels (Gjedde 1995). The contrast agent concentration in these (micro)vessels can be seen as a direct throughput of $C_p(t)$ into $C_t(t)$. Therefore, the reduction of the capillary space and the EES to a single compartment (scenario 2, Fig. 2.5) often leads to an incomplete description of contrast agent exchange. In both cases, both $C_c(t)$ and $C_e(t)$ significantly contribute to $C_t(t)$. For $C_c(t)$ and $C_e(t)$ to be distinguishable, the loss of contrast agent from the capillary space to the EES can only happen at a moderate rate, i.e. obeying the permeability-limited regime. In that case

$C_c(t) \approx C_p(t)$, and [2.31]

$$C_t(t) = v_c \cdot C_c(t) + v_e \cdot C_e(t) = v_p \cdot C_p(t) + v_e \cdot C_e(t), \quad [2.32]$$

in which v_p has the same meaning as v_c (v_p is more common in use than v_c) and $C_e(t)$ is described by Eq. 2.25. We will refer to this type of model as the *extended Tofts model* (Tofts 2003).

Reflux neglected

To obtain a reliable estimate of v_e, data acquisition has to be long enough for $C_t(t)$ to no longer be rising (Donaldson et al. 2010). If this is not the case – note that persistent uptake is a commonly observed curve type – for instance due to limited scan time and / or the use of a macromolecular contrast agent, it is wise to use a model that assumes unidirectional exchange, i.e. from the capillary plasma to the EES (Patlak et al. 1983). The reflux from the EES back into the capillary plasma space is assumed to be

negligible. This assumption only holds under the permeability-limited regime. In Eq. 2.33, K^{trans} is therefore a measure of permeability:

$$v_e \frac{dC_e(t)}{dt} = F \cdot E \cdot \rho \cdot C_p(t) = K^{trans} \cdot C_p(t), \text{ and} \quad [2.33]$$

$$C_t(t) = v_p \cdot C_p(t) + v_e \cdot C_e(t). \quad [2.34]$$

We will refer to this type of model as the *Patlak model*. Examples of publications in which this type of model is applied are Li et al. 2000 and Vonken et al. 2000.

2.2.4 Well-mixedness revisited

For all the models we have touched upon, we tracked the path of the contrast agent particles from entering the capillary bed on the arterial side, possibly leaving the blood plasma and entering the EES, and exiting the capillary bed on the venous side. What is crucial to underscore, is that with (^1H_2O) MRI it is not the contrast agent that generates the positive signal (T_1 shortening), but the water protons that the contrast agent acts upon. Whereas the contrast agent cannot enter cells because it cannot pass their membranes, water molecules can. This transcytolemmal (across cell membrane) water exchange necessitates a closer look at the intracellular space. Note that in most tissues most water is intracellular (Yankeelov et al. 2003). In addition, just as the contrast agent, water molecules pass the microvessel wall. This transendothelial water exchange may also affect contrast agent concentration quantification (Donahue et al. 1997, Kim et al. 2002). We have added both types of water exchange to the schematic representation of contrast agent exchange at the microvessel scale (Fig. 2.6).

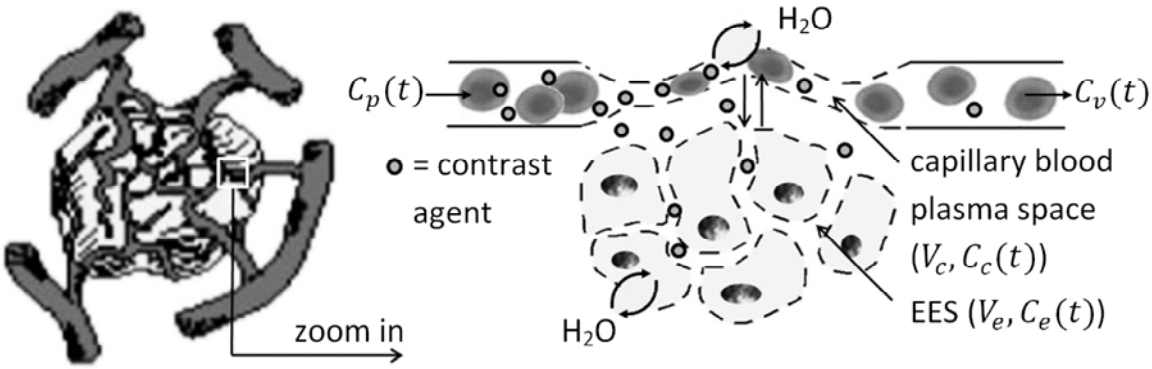

Figure 2.6 *Transendothelial (top) and transcytolemmal (bottom) water exchange added to the schematic representation of contrast agent exchange.*

If water exchange is not modeled explicitly, it is assumed to be 'infinitely' fast (on the time scale of the water T_1), which is equal to assuming that the contrast agent acts on all water molecules in the tissue. This situation is called the *fast-exchange limit* (FXL); a single relaxation rate is assumed in each compartment. Whereas there is some

evidence that the FXL assumption holds in normal tissues, there is no data available to substantiate its validity for a broad range of pathological tissues (Brix et al. 2010). Especially at high contrast agent concentrations, the FXL assumption may not hold; i.e. not all contrast agent particles may have access to all water. The *shutter-speed model* was developed to add the effect of a finite water exchange rate to a compartment model. It replaces the assumption of a linear relationship between the longitudinal relaxation rate (R_1) and the contrast agent concentration, as described in Eq. 1.1 in Chapter 1.

Considering transcytolemmal water exchange, there are two different R_1 values in each compartment, of which the population ratio is determined by the exchange rate of

$$[H_2O]_i \leftrightarrows [H_2O]_o, \qquad [2.35]$$

in which 'i' stands for intracellular and 'o' stands for outside. In principle, this holds for both the EES as well as the blood (about half the water in blood is contained in red blood cells). However, because red blood cells are smaller and more water-permeable than tissue cells, the transcytolemmal exchange in the blood is usually assumed to be in the FXL (Faranesh et al. 2006: transcytolemmal water exchange rate red blood cell ≈ 100 s^{-1}, transcytolemmal water exchange rate muscle cell ≈ 0.8 s^{-1}). The transendothelial water exchange process can be described in the same way (Eq. 2.35), replacing 'i' with 't' (tissue) and 'o' with 'b' (blood).

In case the capillary fraction is small, transendothelial water exchange is negligible, and the shutter-speed model is a combination of the basic Tofts model and the above-described transcytolemmal water exchange in the tissue. Besides K^{trans} and v_e, the mean intracellular lifetime of a water molecule, τ_i (s), is obtained. We will refer to this model as the *first generation shutter-speed model*. In case of a significant capillary fraction, the transendothelial water exchange could be included. The compartment model of choice would in that case be the extended Tofts model, leading to estimates of K^{trans}, v_e, v_p, τ_i, and τ_b; with τ_b (s) representing the mean lifetime of a water molecule in a capillary if there was no flow. This model we will refer to as the *second generation shutter-speed model* (Li et al. 2005). The latter model is only relevant for tissue with a large capillary fraction and a low K^{trans} (Yankeelov et al. 2003).

For modeling details we refer to the following papers. In Landis et al. 1999 and Landis et al. 2000 incorporation of the shutter-speed effect is extensively described. In response to these papers, Buckley (2002a) expressed his concerns about the appropriateness of assuming the *fast-exchange regime* (FXR), thereby neglecting the slow component (with smaller T_1). In Yankeelov et al. 2003, a thorough comparison of the applicability of the FXL, FXR, and the *slow-exchange regime* (SXR) was given. According to this paper, there is a range of contrast agent concentrations (Landis et al.

1999: up to 10 mM) wherein the slow component is not directly detectable. At higher concentrations, the slow component can no longer be neglected, and the system has entered the *slow-exchange regime* (SXR). The second generation shutter-speed model is well-explained in Li et al. 2005. Recent publications using the shutter-speed model are Buckley et al. 2008, Huang et al. 2008, Kim et al. 2007, and Yankeelov et al. 2008.

2.3 Summary comparison of discussed models

In Section 2.2 we have discussed a selection of commonly used pharmacokinetic models; one model representing the underlying physiology in a more simplified way than the other. Please note that the application of a specific model in a specific context is not standardized. Besides different 'tastes' in models, e.g. compartmental versus non-compartmental, the same data can be fitted with a varying level of complexity. In general, the more compartments a model has, the harder it becomes to discriminate between those compartments. In addition, the transfer coefficients can be distinguished only when they are not too different or too similar. Thus, if we measure the tissue bulk concentration $C_t(t)$, only a limited number of compartments and transfer coefficients can be identified (Gjedde 1995). This brings us to the bias versus variance trade-off; with too few model parameters we are likely to introduce a bias in our parameter estimates, while with too many model parameters we are likely to obtain poor precision. A possible way of dealing with this trade-off is to analyze data by means of competing models (Brix et al. 2010). Moreover, not all pharmacokinetic parameters are equally difficult to estimate. In Brix et al. 1999 it is mentioned that the volume fractions v_e and v_p can be determined with greater accuracy than the functional parameters F and $P \cdot S$. In our own experience, in the context of the extended Tofts model, the above holds for v_e but not for v_p. The latter is often difficult to estimate due to its small scale. As a critical note, we should consider that all described models are based on the fundamental idea that the capillary bed consists of capillaries of equal length and volume, each supplying nutrients to a cylinder-shaped volume of tissue. This neatly ordered and parallel conception might not be representative of the capillary bed of most tumors, because those capillary beds are often greatly disorganized (Kety 1951). Further reviewing of the different types of pharmacokinetic models applied to DCE-MRI data can be found in Brix et al. 2009, Brix et al. 2010, Buckley 2002b, Jackson et al. 2005, Parker and Tofts 1999, Tofts 1997, Tofts et al. 1999, and Tofts 2003. Below, we will review the major differences between the discussed models and their limitations.

2.3.1 K^{trans} versus independent measures of flow and permeability

In the basic Tofts model the composite measure K^{trans} is both affected by changes in flow (F) and permeability surface area product ($P \cdot S$). In the extended Tofts model K^{trans} should be representative of $P \cdot S$, but the model is often applied to non-permeability-limited problems. In those cases, the physiological meaning of K^{trans} is difficult to interpret. Data presented in Brix et al. 2004 show that the distinction between F and $P \cdot S$ can be crucial, because in that study the enhancement of breast

carcinoma hot spots was permeability-limited, whereas the enhancement of most benign lesions was flow-limited. With the composite measure K^{trans} it would not have been possible to make this distinction. In contrast with this study, Henderson et al. (2000) point out that measurements of K^{trans} and F are of the same magnitude in at least some human breast tumors, which implies a large extraction fraction and thereby K^{trans} being a measure of F (flow-limited regime). Subtle differences in permeability are in that case unidentifiable. It was shown by Fan and Karczmar (2009) that the basic Tofts model assumption of a mono-exponential impulse response holds for muscle tissue, but not for tumor tissue. As a result, the basic Tofts model often finds unrealistically large values of v_e in tumor tissue.

The ambiguous meaning of K^{trans} makes it hard to compare values found in one study / patient / tumor type / model implementation to another. And, in studying treatment effects, what if F and $P \cdot S$ change in opposite directions, how would that be reflected in K^{trans}? It is clear that we would obtain much more insight into tumor physiology if we would estimate flow and permeability separately. However, this comes at a price. To measure flow separate from permeability, as well as the capillary fraction v_p, sampling times have to be in the order of a few seconds (Donaldson et al. 2010, Henderson et al. 1998). Only in cases of very limited permeability the contrast agent uptake may take several minutes, and sampling times up to the order of 1 minute may be appropriate (Buckley 2010a). High sampling rates usually result in compromised image quality because temporal resolution is exchanged for spatial resolution, and / or signal-to-noise ratio (SNR), and / or imaging field of view.

2.3.2 Vascular component

In the basic Tofts model the contribution of the vascular component to the tissue bulk concentration is neglected. In case this model is applied under the flow-limited regime, it should be recognized that v_e represents both v_e and v_p. Neglection of v_p can also bias K^{trans}. Beside the possible introduction of biases in v_e and K^{trans} (for more on this matter see Chapter 3), neglecting the vascular contribution also limits the utility of the basic Tofts model for diagnostics or therapy assessment. The capillary fraction v_p is likely to be an important parameter to assess, because it directly relates to microvessel angiogenesis. As mentioned in Section 2.1, a large vascular contribution can lead to a wash-out curve shape, which is associated with malignancy.

2.3.3 Capillary transit time

Both the basic and extended Tofts model assume that the capillary transit time is negligible (at least shorter than the data sampling interval), which is equivalent to the assumption of no dispersion of the AIF in the tissue; i.e. $C_c(t)$ equals $C_p(t)$. This assumption can lead to biases in the parameter estimates. However, the capillary transit time can only be estimated in case of adequate temporal resolution during the initial enhancement phase, i.e. the sampling time has to be smaller than the mean

transit time (MTT) of the contrast agent particles passing through the capillary bed. After the initial phase, sampling requirements are less stringent (Brix et al. 2010). In addition to rapid sampling, the separation of the flow-dominated phase from the permeability-dominated phase requires a rapid bolus injection. There is evidence to suggest that the MTT is often non-negligible. Donaldson et al. (2010) estimated an MTT of 22 s for cervix carcinoma. It is mentioned that cervix carcinomas are known to be highly vascular with a long MTT. Kershaw and Buckley (2006) found an MTT of 19 s in prostate tumor, of 60 s in healthy prostate tissue, and of 41 s in muscle tissue. Henderson et al. (2000) supply an educated guess of an MTT of 20 s for breast tumors. On the contrary, in white and gray matter, MTTs are in the order of seconds (Sourbron et al. 2009). In the latter case, MTT could be negligible relative to the temporal sampling interval, and modeling with the extended Tofts model could be appropriate. In case of negligible v_p, the model could be further reduced to the basic Tofts model.

2.3.4 Fast-exchange limit versus fast-exchange regime

To date, most applications of pharmacokinetic modeling are under the assumption of the fast-exchange limit (FXL). There is an ongoing debate about the issues of water exchange (Buckley 2002a). In case of non-negligibly short water lifetimes, the consequence of the FXL assumption is underestimation of v_p and overestimation of K^{trans} (Cao et al. 2005, Donahue et al. 1996, Faranesh et al. 2006). In case the vascular fraction is neglected, inappropriately assuming FXL results in underestimation of K^{trans} (Yankeelov et al. 2003). The consideration we have to make in case of adequate data quality and temporal resolution to add an additional parameter to the basic Tofts model, i.e. v_p or τ_i, is discussed in Chapter 3. Table 2.1 provides an overview of the different properties of the discussed pharmacokinetic models. The need for high-temporal resolution (last row Table 2.1) is not always clear – how high is high enough? This will be further investigated in Chapter 3.

Table 2.1 *Six pharmacokinetic models and their properties summarized.*

	Full two-compartment	**St. Lawrence and Lee**	**Basic Tofts**	**Extended Tofts**	**Patlak**	**Shutter-speed**
Purely compartmental	Yes	No	Yes	Yes	Yes	Yes
Independent estimates of flow and permeability	Yes: - Apparent flow - True flow (Morales and Smith)	Yes	No	No	No	No
Assumption of negligible vascular component	No	No	Yes	No	No, but v_e not estimated	- First generation: Yes - Second generation: No
Assumption of limited permeability	No	Yes	- Scenario 1: Yes - Scenario 2: No (v_e: $v_e + v_p$)	Yes	Yes	- First generation: see basic Tofts - Second generation: see extended Tofts
Assumption of infinitely fast water exchange	Yes	Yes	Yes	Yes	Yes	No
Need for high temporal resolution (sample period < 5 s)	Yes	Yes	No?	Yes?	See extended Tofts	Yes?

2.4 Applied models in current work

Not all the above-discussed models will be applied in the remainder of this work. We focused on models based on compartment theory; therefore we did not further investigate the adiabatic approximation to the tissue homogeneity model. Because our aim is to apply pharmacokinetic modeling to diagnostic DCE-MRI data of the breast, which is often acquired at relatively low temporal resolution, we first obtain an indication of the suitability of the full two-compartment model, the extended Tofts model, and the basic Tofts model in this section. The addition of the shutter-speed effect will be discussed in Chapter 3; as well as a more thorough investigation on temporal sampling requirements.

We qualitatively assessed how well the models can fit the pharmacokinetic parameters via the analysis of sensitivity functions (Henderson et al. 1998). If sensitivity functions of two parameters are very similar, a parameter estimation method will have difficulty to distinguish those two parameters. A sensitivity function (SF) is defined as

$$SF_i(t) = \partial C_t(t)/\partial p_i, \qquad [2.36]$$

in which p_i is the ith parameter of a model. It means that if the ith parameter is changed by Δp_i, then $C_t(t)$ will change by $\Delta p_i \cdot SF_i(t)$. We used a forward Euler approach to approximate the sensitivity functions (Mattheij and Molenaar 2002). In Figure 2.7 we show the sensitivity functions as relative contributions ($SF_i(t) \cdot p_i$) to the contrast agent uptake in the tissue. The first column shows the contrast agent concentration curve in the tissue ($C_t(t)$) simulated with the basic Tofts model and its relative contributions (v_e, K^{trans}); the second column shows the same for the extended Tofts model (v_e, K^{trans}, v_p); and the third column for the full two-compartment model (v_e, K_{PS}, v_p, F). For the first row we used parameter values for pectoralis muscle: $v_p = 0.04$, $v_e = 0.09$, $F/V_p = 2.4$ min^{-1}, $P \cdot S/V_p = 1.2$ min^{-1} (Brix et al. 2004). F is here the apparent plasma flow. To calculate K^{trans} from these parameters we used: $E = 1 - e^{-P \cdot S/F}$ (Eq. 2.18), and $K^{trans} = F \cdot E \cdot \rho$ (Eq. 2.30). We assumed ρ equal to 1 g/mL. Using the same settings, but multiplying K_{PS} with a factor of 4, we obtained the curves shown on the second row. An additional multiplication of F with a factor of 4 resulted in the curves shown on the last row.

An interesting difference between the three models is the contribution of v_p; there is no contribution in the basic Tofts model, whereas in the extended model we see a direct throughput of the AIF, causing a high and narrow peak. With the full two-compartment model the AIF is dispersed in the tissue; therefore most of the narrow spike is lost. Moving from the first to the second row, the contributions to the curve simulated with the full two-compartment model nicely show that with $K_{PS} > F$ we move towards the flow-limited regime, i.e. the influence of F increases whereas the influence of K_{PS} becomes very small. If we now also increase F (third row), the

contributions of K_{PS}, F, and v_p are very similar in the early enhancement phase. It is not unlikely that a parameter estimation method would not be able to identify the separate contributions in such a scenario. Indeed, a Monte Carlo simulation study (high-temporal resolution, no noise) using the full two-compartment model confirmed that parameters were often unidentifiable from the data (G.J.S. Litjens, personal communication). Here, unidentifiable means that there are different sets of parameter values that describe the measured data equally well, with equal likelihood (Lopata et al. 2007). To us, these observations indicate that studying the use of the full two-compartment model in combination with data at relatively low temporal resolution would be in vain. So, we did not study the use of the full two-compartment model in this work, despite of its benefits from a theoretical point of view. Parameter estimation will be further discussed in Section 2.6.

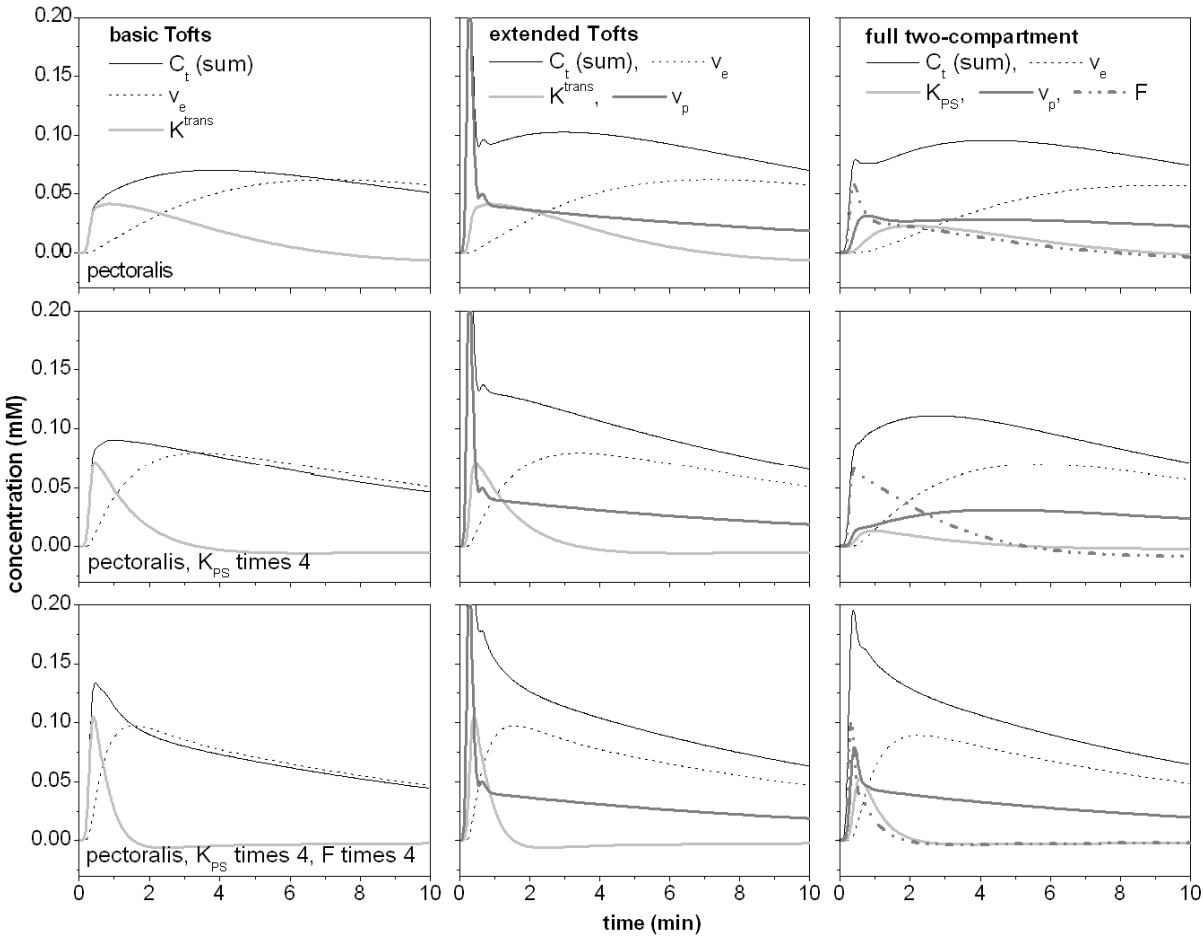

Figure 2.7 *Sensitivty functions shown as relative contributions. Columns (left to right): basic Tofts model, extended Tofts model, full two-compartment model. Rows (top to bottom): pectoralis muscle (v_p= 0.04, v_e = 0.09, F/V_p = min^{-1}, $P \cdot S/V_p$ = 1.2 min^{-1}), 4 times higher K_{PS} than in pectoralis muscle, 4 times higher K_{PS} and F than in pectoralis muscle.*

2.5 The arterial input function

2.5.1 Obtaining the arterial input function

To fit a pharmacokinetic model to DCE-MRI data, we need both the tissue bulk concentration $C_t(t)$, as well as the arterial input function $C_p(t)$. Measurement or estimation of the AIF has proven to be difficult, which makes it a major source of error in pharmacokinetic parameter estimates (Yang et al. 2004). Several approaches to obtain the AIF have been proposed, of which 5 are discussed below.

Blood sampling

The first method is to draw blood samples during the DCE-MRI experiment (e.g., Larsson et al. 1990). Due to its invasiveness and inherently low temporal resolution, this method is rarely put to practice.

Direct AIF measurement in artery

The second approach is direct measurement of the bolus passage in an artery (in the DCE series); preferably, a tumor-feeding artery. In case of DCE-MRI of the breast, due to a lack of other options, the aorta is often used, which is quite remote from the tissue of interest. A remotely measured AIF can be substantially different from the AIF that arrives at the tissue of interest due to delay and dispersion effects (Yang et al. 2004). A recent publication extracted the AIF from a nearby artery, i.e. the axillary artery (Huang et al. 2010). However, this measurement could not be performed in all patients.

A direct measurement in an artery faces several challenges. To mention a few, for the high contrast agent concentrations encountered in arteries, conversion from signal intensity to concentration may be problematic due to nonlinearities and T_2^*-effects; furthermore, the measured signal can be distorted by artifacts arising from effects such as inflow, dephasing, partial volume, and pulsatility (Zhang et al. 2009). To capture the rapid dynamics of the bolus passage in an artery, a sampling interval of approximately 1 s is required (Henderson et al. 1998).

The measurement can be performed by ROI placement if a large artery is available, or automatic arterial voxel selection. The latter method is usually applied in the brain (e.g., Simonetti et al. 2007), because of less disturbing background enhancement in healthy brain tissue than in healthy body tissues due to the blood-brain-barrier. Rijpkema et al. (2001) showed that arterial voxel selection can also be applied outside the brain, for instance in the prostate. Note that, after conversion from signal intensity to contrast agent concentration, the extracted curve represents the whole arterial blood concentration and has to be corrected for the hematocrit factor (see Section 2.2) to represent the plasma concentration.

Standard AIF

The third method is to use a standard AIF. This could be an AIF published in literature, such as the bi-exponential AIFs by Weinmann et al. (1984), by Fritz-Hansen et al. (1996) – recently combined with the Weinmann AIF to form the modified Fritz-Hansen AIF (Walker-Samuel et al. 2006) – and by Tofts and Kermode (1991); the simplified mono-exponential AIF by Vincensini et al. (2007); the gamma-variate AIF by Starmer and Clark (1970); the population-averaged AIF by Parker et al. (2006); or adapted versions of the latter AIF (Orton et al. 2008, Yang et al. 2007). The use of a standard AIF can reduce random sources of error, but, in case it is based on direct measurements, may not correct systematic artifacts such as inflow and partial volume effects (Zhang et al. 2009). Furthermore, the standard AIF can mismatch with the specific patient's hemodynamics (cardiac output, blood volume), and with the specific injection protocol. The latter problem could be overcome by constructing a population-averaged AIF from an (independent) group of patients that underwent exactly the same protocol as the patients under study. Still, according to Port et al. (2001), peak signal enhancement and the area under the AIF can, respectively, vary 2.5- and 3.7-fold between patients.

In a small experiment we investigated the effects of such inter-patient AIF variability on descriptive curve-shape classification (Heisen et al. 2007a). The results are reproduced in Panel C. In descriptive curve-shape classification, the AIF is not considered and thus implicitly assumed to vary little between patients. This is similar to the assumption of a standard AIF in pharmacokinetic modeling.

Simultaneous estimation of the AIF and pharmacokinetic properties

The fourth method does not involve a measured or assumed AIF. It is assumed that the AIF can be described by a family of functions with adjustable parameters. The AIF parameters and the pharmacokinetic parameters are simultaneously fit, only using the tissue bulk concentration $C_t(t)$. The AIF parameters are adapted in such a way that the best fit to $C_t(t)$ is provided. In Hoffmann et al. 1995 a mono-exponential function was chosen to characterize the shape of the AIF. According to Yang et al. (2004) this oversimplification may introduce significant errors in pharmacokinetic parameter estimates. However, usage of an AIF model with many parameters may hinder dissociation of the AIF parameters from the pharmacokinetic parameters.

Panel C

Effect of not taking inter-patient AIF variation into account on descriptive curve-type classification

According to Port et al. (2001), peak signal enhancement and the area under the AIF can, respectively, vary 2.5- and 3.7-fold between patients. The effect of this intra-patient variability of the AIF shape on descriptive curve shape classification was investigated using two types of AIF variation, i.e. dispersion and scale. To simulate a difference in dispersion, the adapted Parker AIF (Yang et al. 2007) was convolved twice with a transport function

$$h(t) = \frac{\rho^{-\sigma}(t-t_0)^{\sigma-1}\, e^{-(t-t_0)/\rho}}{\Gamma(\sigma)}, \qquad [C.1]$$

in which ρ (min) is the scale of the transport function and σ the order; t (min) is time; t_0 (min) is the bolus arrival time; and Γ denotes the complete Gamma function. Once, we used a scale (ρ) of 0.02 min, and once a scale of 0.05 min. The order (σ) was fixed at 4, and t_0 at 0 min. After convolution, a time lag of 25 s was added. This, to simulate a protocol in which the acquisition of the first postcontrast volume is timed to start at the same time as the contrast injection. The obtained AIFs, having the same area under the curve, are displayed in Fig. C.1(a). A difference in scale was obtained by applying the same transport function $h(t)$ to the adapted Parker AIF with a scale of 0.03 min, and subsequently multiplying it with a factor of 3. In comparison to before multiplication, the difference in AUC is now a factor of 3. This combination of AIFs is shown in Fig. C.1(b).

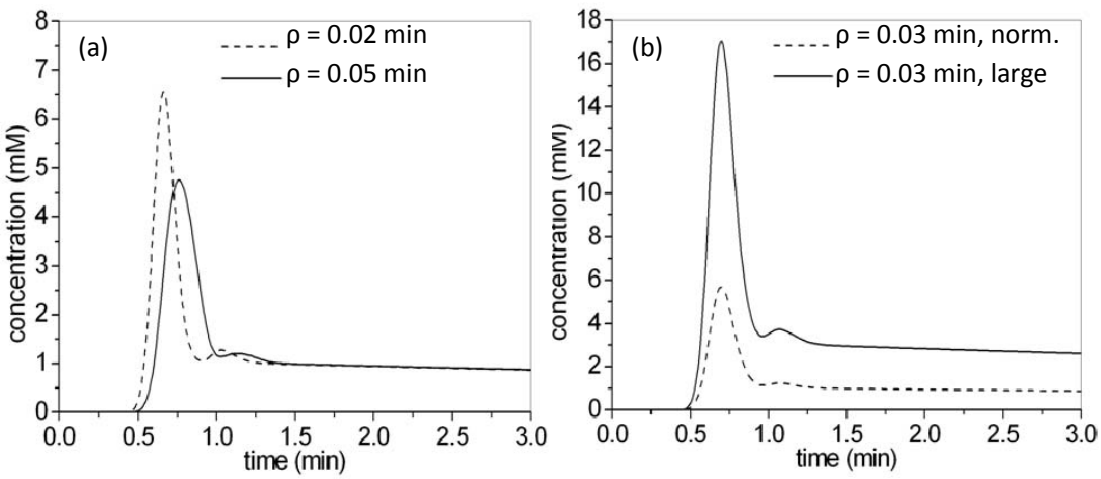

Figure C.1 *(a) Two simulated AIFs with different dispersion; i.e., ρ = 0.02 min (dashed), ρ = 0.05 min (solid). The areas under the curves are the same. (b) Two simulated AIFs with the same dispersion, ρ = 0.03 min, but a different scale. The area under the large AIF (solid) is three times as large as the area under the normal AIF (dashed).*

Panel C (continued)

To simulate tissue response curves to these four AIFs we used the extended Tofts model and the following parameter ranges: K^{trans} = [0.1 – 1.3 min^{-1}] and v_e = [0.1 – 8]. The vascular fraction v_p was fixed at 0.01. Then, acquisition parameter settings representative of a clinical protocol (repetition time / echo time = 4.53/2.2 ms, θ = 10°) were used to convert the generated contrast agent concentration curves to signal intensity curves, afterwards converted to relative enhancement curves (Eq. 1.3). Subsequently, the relative enhancement curves were downsampled to a typical temporal resolution of 1 min by averaging over the acquisition period. Finally, the 1 min resolution relative enhancement curves were classified according to descriptive curve shape modeling. The signal enhancement ratio (SER) was defined as the relative enhancement at the early (2 min) postcontrast time point divided by the relative enhancement at the late (6 min) postcontrast time point. The applied rules to distinguish the three types of curve shape were: (i) if the SER is smaller 0.9 the curve shows steady uptake (blue, probably benign); (ii) if the SER is larger than 1.1 the curve shows wash-out (red, probably malignant); and (iii) intermediate SER is descriptive for plateau enhancement (green, suspicious). The color-coded results are shown in the K^{trans}-versus-v_e plane. In Figure C.2 we see on the left the classification corresponding to the small-dispersion AIF, and on the right to the large-dispersion AIF. The difference in classification is marginal. In Figure C.3 the classifications corresponding to the normal-AUC AIF (left), and the large-AUC AIF (right) are shown. Here, the difference in classification is substantial. It implicates, for instance, that it is less likely that a tumor (certain combination of K^{trans}, v_e, v_p) in a patient with a large AIF will be classified as probably malignant than in a patient with a normal AIF, only due to a difference in AIF. As an example, a K^{trans} above 0.8 min^{-1} is always considered a sign for malignancy, except for the case of the large-AUC AIF.

AIF differences are partly due to variation in patient systemic circulation such as cardiac output, blood volume, and vessel wall stiffness. However, the cause of a large-AUC AIF can also be dosage. Although a dosage of 0.1 mmol gadolinium-based contrast agent/ kg body-weight is fairly standard, some institutes may use a different dose. This is usually not taken into account in automatic classification systems that apply rules similar to the ones described above. Moreover, an obese patient will receive a larger amount of contrast agent because the dose is calculated per kg of body-weight. However, in case of obesity, the increase in weight is not proportional to the increase in blood volume. This is because fatty tissue is poorly perfused.

Panel C (continued)

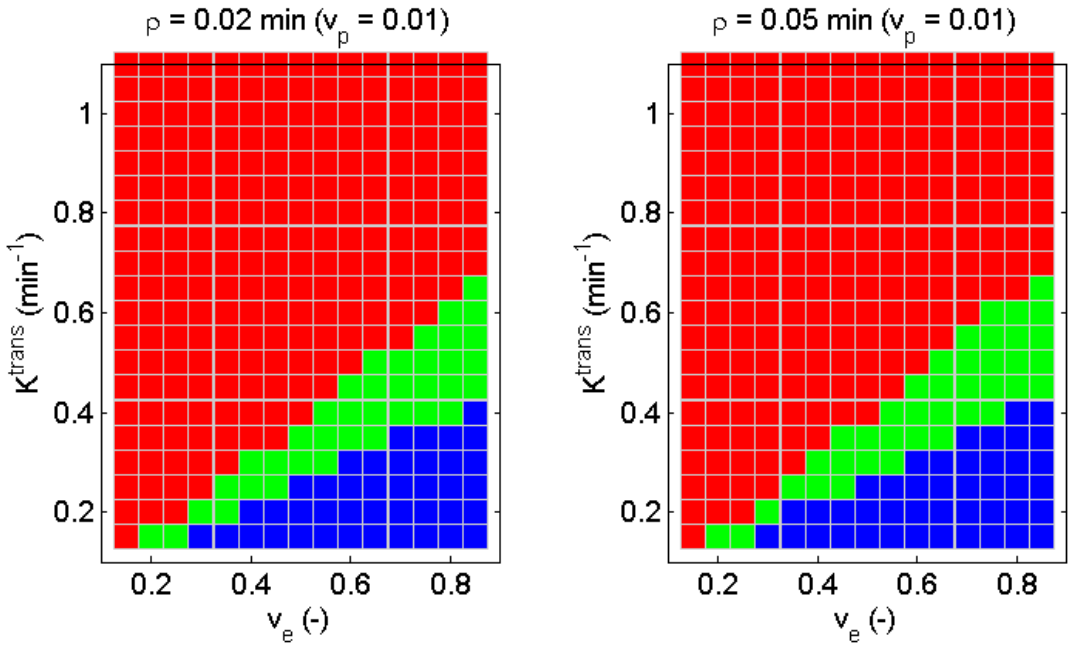

Figure C.2 *Color-coded combinations of Ktrans and ve, corresponding to three curve types; probably malignant (red), probably benign (blue), and suspicious (green). On the left, a low-dispersion AIF was used, on the right a large-dispersion AIF. Little difference in classification.*

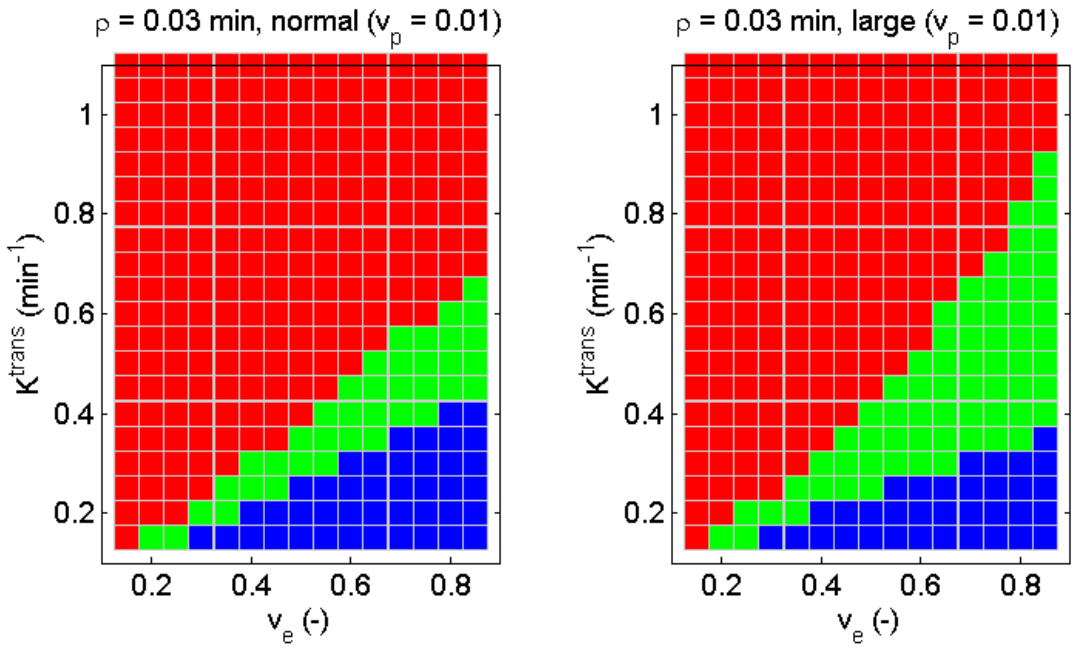

Figure C.3 *On the left, a normal-AUC AIF was used; on the right a large-AUC AIF. Both curves had normal dispersion. With the large AIF, more curves are classified as suspicious (green), less as benign (blue) or malignant (red).*

Reference tissue AIF

The fifth approach is to derive the AIF from a reference tissue (Kovar et al. 1998, Yankeelov et al. 2005). This method does not involve a measured or assumed AIF either. The most basic form uses the assumption of known pharmacokinetic parameter values for a single healthy reference tissue. The AIF can then be inversely derived from the contrast agent uptake curve in the reference tissue.

The reference tissue AIF method shows good correlation with direct AIF measurement (Kovar et al. 1998, Yankeelov et al. 2007). But, in a study by Yang et al. (2010), it was found that the reference tissue AIF had a much higher and wider first-pass peak than the directly measured AIF. Also, the directly measured AIF showed the second pass, whereas this detail could not be seen in the reference tissue AIF. The wider shape can be partly explained by the fact that the reference tissue AIF is more local than the directly measured AIF, and thus has travelled further along smaller vessels experiencing more dispersion. Dispersion might also explain why the second pass could not be seen.

An inherent assumption of this method is that the AIF is the same for the reference tissue as for the tumor. This is not necessarily true, although the reference tissue is usually nearer to the tumor tissue than the feeding artery, in which a direct AIF measurement can be performed. Moreover, recent research has demonstrated that the reference tissue AIF can be adjusted to produce a local tumor AIF (Fan and Karczmar 2009).

The assignment of literature values to healthy tissue ignores that there is a natural range of pharmacokinetic tissue properties; for human skeletal muscle, see for instance Padhani et al. 2002). In addition, systemic or local therapy could also affect healthy tissue. This assignment of literature values is not a necessity; but, additional degrees of freedom in the fitting routine entail a greater potential variability. Alternatively, the pharmacokinetic parameters of the tissue of interest could be reported relative to the pharmacokinetic parameters of the reference tissue (Yankeelov et al. 2005). Using relative parameter values, assuming literature values for the reference tissue is no longer necessary.

The use of multiple reference tissues (Yang et al. 2007, Yang et al. 2010) could improve AIF accuracy, and, if enough reference tissues are used, this method does not require the assignment of literature values to the reference tissues either (so-called blind identification); it only requires an estimate of the AIF scale. The scale could be obtained by combining the (multiple) reference tissue method with a post-peak measurement in an artery (Fan et al. 2010b). Since with multiple reference tissues it is unnecessary to assign literature values, there is no reason to not use the tumor itself. It can even be advantageous to use the tumor, because it can often be split up into several

clusters of different enhancement patterns due to tumor heterogeneity, providing more than one reference tissue. In addition, the produced AIF is in that case a truly local tumor AIF (Yang et al. 2007).

The choice of a specific pharmacokinetic model to represent reference tissue behavior can affect parameter estimation for the tissue of interest, i.e. in case the tissue of interest demonstrates more complex behavior than encompassed in the reference tissue model (Faranesh and Yankeelov 2008, Chapter 3). Inclusion of more than one reference tissue, possibly described by different models, could offer a solution. The uptake in skeletal muscle tissue is usually described by the basic Tofts model, which suits its pharmacokinetic properties (Fan and Karczmar 2009).

2.5.2 Arterial input function shape

Several approaches to obtain the AIF include assumptions about the AIF shape. It is important to note that some of these approaches might match better with a certain kind of injection and scan protocol, than with another kind. Currently, a rapid intravenous bolus injection (duration < 10 s) (Tofts 2003) is the most-applied method to administer the contrast agent, but a constant-rate infusion injection is also in use (duration ≈ 30 s) (Brix et al. 2004). According to Brix et al. (2010), good mixing of the injected contrast agent in the blood pool is achieved when injection time is comparable with the blood circulation time, which is in the human body about 20-25 seconds. These two injection protocols result in different AIF shapes. Papers comparing the use of different standard AIF shapes are for instance Orton et al. 2008 and Cheng 2008. In Port et al. 2001, the inter-patient variability in AIF shape was investigated. It is remarked by Yang et al. (2004) that a bi-exponential standard AIF cannot describe the high first-pass peak that is characteristic of rapid bolus injection. It may only be suitable for data acquired with a relatively low temporal resolution, thereby only capturing the effects of the second pass.

In case a patient-specific AIF is extracted from the data itself, a first order check of its shape can be performed by measuring the area under the first-pass part of the curve (whole blood contrast agent concentration). (In Yang et al. 2009, a gamma-variate function was fit to the AIF to exclude the second pass.) Because the rate at which the agent is diluted reflects the cardiac output (CO), this area under the curve is inversely related to the CO via (Hamilton et al. 1948)

$$CO = \frac{Q}{\int_{first\ pass} C_a(t)dt}, \qquad [2.37]$$

in which C_a (mM) represents the whole arterial blood contrast agent concentration, and Q (mmol) the dose of injected contrast agent. For instance, the cardiac output corresponding to the Parker AIF (Parker et al. 2006) was approximated at 10.5 L/min (Yang et al. 2009), which is much higher than the average adult cardiac output of 6.5

L/min (Wade and Bishop 1962). The multiple reference tissue method applied in the same paper (Yang et al. 2009) produced an average AIF that corresponded to a cardiac output of 6.1 L/min.

2.5.3 Temporal resolution and bolus arrival time

As briefly mentioned, if a standard AIF is used, it should match the temporal resolution of the data at hand. Interestingly, a common reason for using an – often high-temporal-resolution (!) – standard AIF is that the temporal resolution of the data at hand is too low to directly measure an AIF. In that case, the use of a high-temporal-resolution standard AIF results in, respectively, under- and overestimation of K^{trans} and v_e (see Chapter 5, Heisen et al. 2010a). This temporal-resolution-dependent bias cannot be easily accounted for. According to Cheng 2008, in case of low temporal resolution, it is better to use a standard bi-exponential AIF. With such an AIF, the vascular fraction cannot be estimated. However, accurate estimation of v_p is not expected – not even with the use of a high-temporal-resolution standard AIF – due to the low temporal resolution of the data at hand.

To obtain a patient-specific AIF directly measured in an artery, temporal resolution has to be around 1 s. For DCE-MRI data at lower temporal resolution – almost always the case for DCE-MRI of the breast – extracting a patient-specific AIF via a reference tissue presents as an attractive alternative. A reference tissue with gradual enhancement can be sampled relatively slowly. In this approach, it is not the AIF that sets the necessary temporal resolution, but the contrast uptake curve in the lesion. We will investigate the use of the reference tissue AIF approach in Chapter 6. Several papers have already shown that this method works well for low temporal resolution data (Heisen et al. 2010b, Planey et al. 2009, Yankeelov et al. 2005), even at sampling intervals of 88 s (Li et al. 2009).

The effect of temporal resolution is intertwined with the effect of bolus arrival time. In case of a long sampling interval the switch from precontrast (no contrast agent present) to postconstrast (contrast agent present in the tissue) will likely take place during the acquisition of an image volume. The volume before this specific image will be seen as the last precontrast volume, and the volume itself will be seen as the first postcontrast volume. However, a large part of the first postcontrast volume may have been acquired before bolus arrival. If a standard AIF is subsequently aligned with this time frame, K^{trans} can be seriously underestimated. The reference tissue AIF method suffers less from not knowing the exact bolus arrival time because the reference tissue and the tissue of interest are imaged in the same way, in the same volume. Approximate temporal alignment is guaranteed, as long as the reference tissue is not very remote. Note that in the multiple reference tissue method the difference in bolus arrival time is included as a model parameter (Yang et al. 2010). In case the AIF is obtained via direct measurement in an artery, it is advisable to include the time lag

between bolus arrival in the artery and in the tissue of interest as an additional parameter in the pharmacokinetic model (e.g. time lag between aorta and breast tissue ~ 12 s, Brix et al. 2010). The intricate matter of bolus arrival time is only briefly touched upon in this work in Chapter 6. Publications considering bolus arrival time are Henderson et al. 1998, Kershaw and Buckley 2006, and Laue et al. 2007.

2.5.4 Standard versus patient-specific AIF

In pharmacokinetic modeling, the reason for deconvolving the contrast agent uptake in the tissue of interest with the AIF is to separate systemic effects from local effects. The obtained pharmacokinetic parameters therefore describe local tissue properties. With this in mind, ideally, the AIF is patient-specific, leading to more accurate parameter estimates relative to a standard AIF (Port et al. 2001, Rijpkema et al. 2001). As mentioned, the inter-patient – and even intra-patient – differences in AIF can be large. Moreover, it has been demonstrated that in diagnostics the use of a patient-specific AIF results in a larger area under the receiver-operator curve, and thus performs better, than the use of a standard AIF (Huisman et al. 2006, Vos et al. 2009). On the other hand, Parker et al. (2006) showed an improved reproducibility in a longitudinal patient study when using a standard AIF (matching the same group of patients). A possible reason may be that sampling resolution was not high enough to measure the first-pass peak with high precision (Henderson et al. 1998). In case the peak was not captured in one of the visits, a standard – i.e. constant – AIF would give better reproducibility. Despite this possible shortcoming of the study, Walker-Samuel et al. (2007b) as well found a better reproducibility with a standard AIF. Rijpkema et al. (2001), however, found the opposite, i.e. better reproducibility with a patient-specific AIF.

The choice of a certain type of AIF depends on the possibilities – e.g., is it possible to obtain a patient-specific AIF? – and on the purpose of the study. In a longitudinal study, it may be more important to capture a change in the parameters than capturing them with high accuracy. In a cross-sectional study (comparing patients group), the use of a standard AIF could mask treatment effects acting on the AIF itself, thereby influencing the difference in pharmacokinetic parameter estimates between the patient groups (Parker et al. 2006).

2.6 Parameter estimation

There are many techniques available to fit a pharmacokinetic model to the combination of the tissue bulk concentration $C_t(t)$ and the arterial input function $C_p(t)$. To estimate the pharmacokinetic parameters, a merit function has to be defined that provides a measure of agreement between the acquired data and the model with a particular choice of parameters. Once a parameter set has been found that minimizes / maximizes the merit function, the 'quality' of the set can be assessed with a goodness-of-fit measure. Having found a good fit, however, may not mean that we have found the

best fit, or that there are no other parameters sets of comparable quality. An error estimate on the found parameter values, for instance the standard deviation, can tell us how likely the estimate is: if K^{trans} is estimated at 0.20 ± 0.15 min^{-1}, it means that there is a fairly large range of K^{trans} values with comparable likeliness of matching the data representation of the underlying process. An optimal fitting procedure therefore provides (i) parameter estimates, (ii) error estimates on the parameters, and (iii) a statistical measure of goodness-of-fit (Flannery and Teukolsky 1992). To prevent the event of finding a good fit in one area of parameter space (local optimum), whereas the best solution lies in a different area (global optimum), one can use global optimization techniques that search the whole solution space spanned by the model parameters. Even though the solution space is searched in a clever way, global techniques are usually computationally expensive.

A popular local optimization technique is nonlinear least-squares, often using Levenberg-Marquardt (Di Giovanni et al. 2010), repeated with several (e.g. N = 500, Lopata et al. 2007) randomly selected initializations. The use of several initializations increases the chance of finding the global optimum. If the measurement errors are independent and normally distributed with constant standard deviation, least-squares fitting gives a maximum-likelihood estimation of the fitted parameters (Flannery and Teukolsky 1992). It can also provide an error estimate on the parameters making use of the Fisher information matrix (Raue et al. 2009): the variance on the parameters is inversely proportional to the 'visibility' of the parameters in the residuals (residual: difference between the measured data point and the model value); i.e. if the residuals can be characterized as white noise, the variance on the parameter estimate is very small (Damen 2003).

Another local optimization technique is golden section search (GSS), e.g. used in Fan et al. 2010b. It is the analog of the bisection method for finding roots, optimized for function optimization (Press et al. 2007). Because it is a bracketing technique, selecting a smaller interval in which the optimum is expected at each step, it does not require several initializations. The appeal of this method is that it is fast, which is important in fitting 3D (x, y, time) or even 4D (x, y, z, time) image data. Note that a disadvantage of this method is that it does not provide an error estimate on the parameters. Usually, GSS is applied to 1D problems. To solve a 2D problem, as in fitting the basic Tofts model, the bracketing has to be alternated between parameters (K^{trans}, v_e). Here, we investigated its suitability for this specific context.

2.6.1 Using golden section search to fit the basic Tofts model

The golden section search fitting approach was tested for its robustness against local optima. As merit function we used R^2 (coefficient of determination)

$$R^2 = 1 - \frac{SS_{residuals}}{SS_{total}}, \qquad [2.38]$$

in which the sum of squared residuals is defined as

$$SS_{residuals} = \sum_{i=1}^{N}(y_i - f_i)^2, \quad [2.39]$$

and the total sum of squares as

$$SS_{total} = \sum_{i=1}^{N}(y_i - \bar{y})^2, \quad [2.40]$$

where y_i are the observed values modeled with f_i, and $\bar{y}$ is the mean of the observed data. The closer R^2 is to 1, the better the fit follows the trend of the data. In alternating between K^{trans} and v_e we started off with bracketing v_e. K^{trans} followed in each step, providing a K^{trans} range for both the lower and upper bound of v_e. This order was chosen because v_e is a more stable parameter than K^{trans}. As an example we used DCE-MRI rat data that will be further discussed in Chapters 5 and 6. Here, we show the algorithm being tested for two types of tissue, i.e. muscle and tumor tissue, at two temporal resolutions, i.e. 5 s and 60 s resolution. The AIF that we used in fitting the basic Tofts model was derived from the uptake in muscle tissue under the assumption of known K^{trans} and v_e (0.11 min^{-1}, 0.20, Kovar et al. 1998). It matched the data sets in temporal resolution. Figure 2.8 shows the AIF (left axis), a single-voxel uptake curve in muscle tissue (right axis, circles), and a single-voxel uptake curve in tumor tissue (right axis, squares), at 5 s resolution. Figure 2.9 shows the same curves, but extracted at 60 s resolution. The details of downsampling from 5 s to 60 s resolution will be discussed in Chapter 5. Note that the scale of the AIF extracted at 60 s resolution is smaller than the one extracted at 5 s resolution.

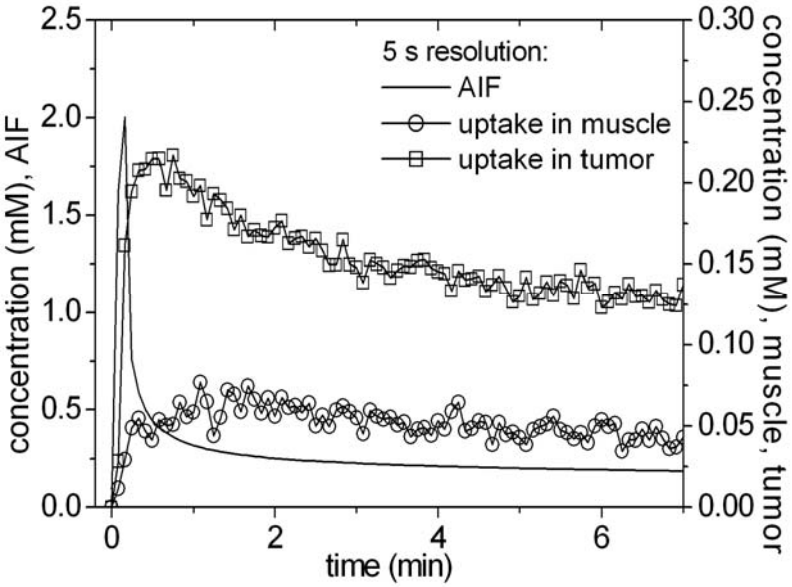

Figure 2.8 *AIF derived from uptake in muscle tissue at 5 s resolution (left axis), single-voxel uptake curve in muscle tissue (right axis, circles), and single-voxel uptake curve in tumor tissue (right axis, squares).*

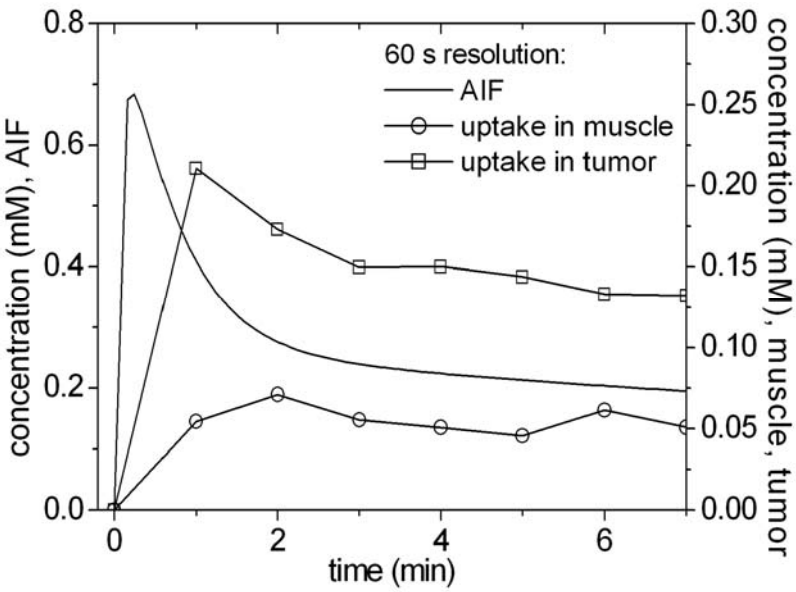

Figure 2.9 *AIF derived from uptake in muscle tissue at 60 s resolution (left axis), single-voxel uptake curve in muscle tissue (circles), and single-voxel uptake curve in tumor tissue (squares). The curves are extracted from the same locations as at 5 s resolution.*

To find the global solution we applied a brute force approach of calculating R^2 values over all combinations of K^{trans} and v_e covering a large range. Subsequently, we applied the GSS fitting algorithm. We did this for both tissues, at both temporal resolutions. The results are displayed in Tables 2.2 (muscle tissue) and 2.3 (tumor tissue). For both tissues, and at both temporal resolutions, the parameter estimates obtained with GSS were very similar to the best-R^2 results. Convergence was mostly reached within less than 20 iterations, as shown in Figure 2.10 for the 5 s resolution contrast agent uptake curve in muscle. The stopping criterion for both K^{trans} and v_e was a distance of $1{\cdot}10^{-4}$ between the upper and lower bound.

Table 2.2 *Positions of best-R^2 and GSS optimal R^2 in K^{trans}-versus-v_e space: contrast agent uptake in muscle tissue.*

K^{trans} (min^{-1})	Global optimum	GSS optimum
5 s resolution	0.14	0.14
60 s resolution	0.14	0.14

v_e	Global optimum	GSS optimum
5 s resolution	0.22	0.21
60 s resolution	0.23	0.22

Table 2.3 *Positions of best-R^2 and GSS optimal R^2 in K^{trans}-versus-v_e space: contrast agent uptake in tumor tissue.*

K^{trans} (min^{-1})	Global optimum	GSS optimum
5 s resolution	0.56	0.53
60 s resolution	0.52	0.52

v_e	Global optimum	GSS optimum
5 s resolution	0.61	0.61
60 s resolution	0.61	0.61

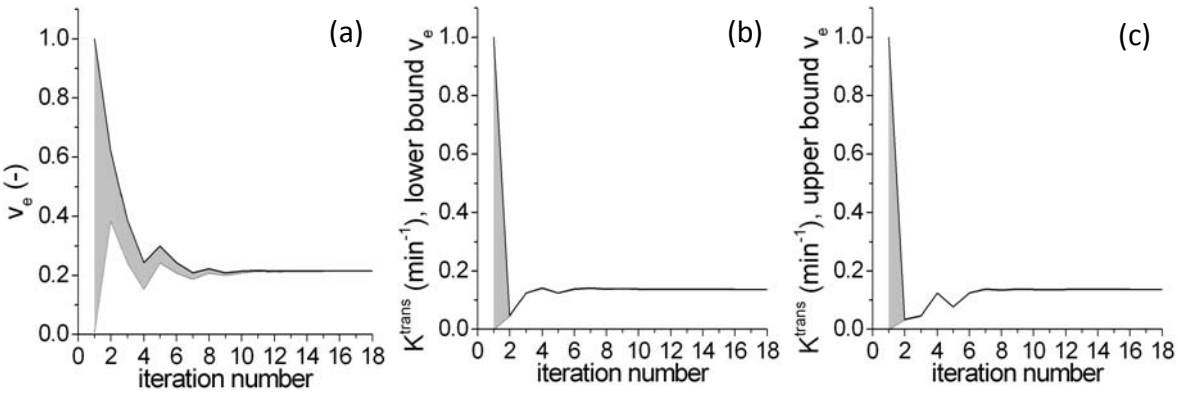

Figure 2.10 *Example of convergence of GSS method for the uptake in muscle tissue at 5 s resolution. (a) v_e, (b) K^{trans} corresponding to the lower bound of v_e, (c)K^{trans} corresponding to the upper bound of v_e.*

In Figures 2.11 (5 s resolution) and 2.12 (60 s resolution) we show the best-R^2 solution and the GSS solution together with the acquired data. The difference between the best-R^2 solution and the GSS solution is hard to see. What we can see is that the curves fitting the tumor data do not display the same shape as the measured data; the decay after the peak is slower and the end phase is lower. This holds both for the best-R^2 as well as for the GSS fit. It therefore appears to be a limitation of the assumed model (more on this matter in Chapter 3). The GSS fitting approach therefore appears robust against local optima.

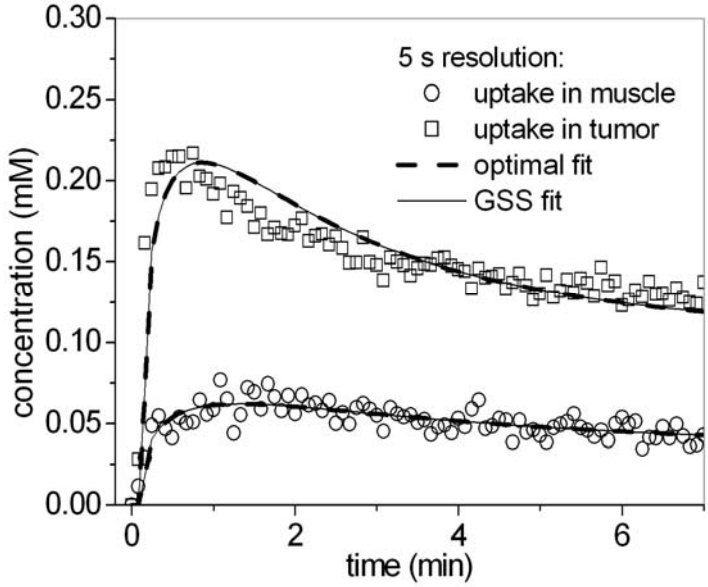

Figure 2.11 *Single-voxel uptake in muscle tissue (circles) and in tumor tissue (squares), at 5 s resolution. For both measured curves the dashed line reflects the global best-R^2 fit, whereas the continuous line reflects the optimal-R^2 GSS fit.*

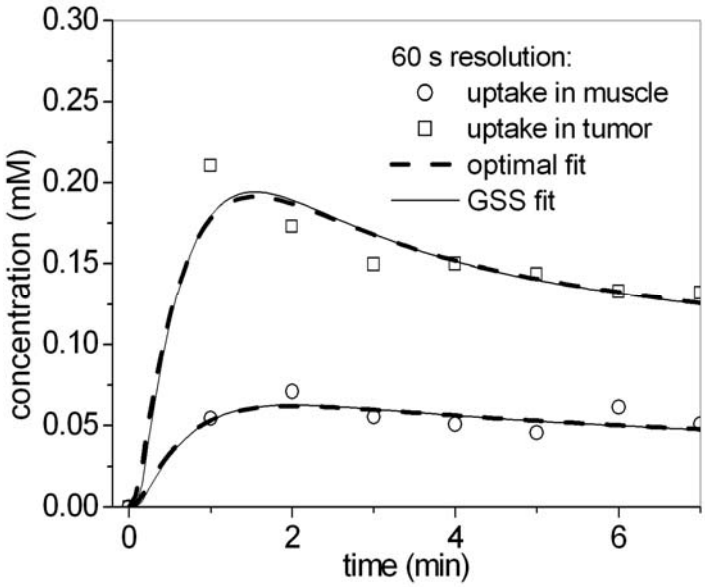

Figure 2.12 *The same measured curves and fits as in Fig. 2.11, this time at 60-second resolution.*

To test for robustness against noise, we used the best-R^2 solution and added noise in the signal intensity domain. We determined the noise level in these data in air (outside imaged object) and corrected for the Rician distribution (Kaufman et al. 1989).

In muscle, baseline SNR was about 40, and peak signal SNR was about 50. Using 200 random noise realizations, we transformed the curves back to contrast agent concentration and fitted the basic Tofts model with the GSS fitting routine. As can be seen in Figs. 2.13 (5 s resolution) and 2.14 (60 s resolution), the GSS solutions are all found within a narrow range (slightly larger at lower temporal resolution). The figures show the contour plots of the R^2 landscape with v_e on the x-axis and K^{trans} on the y-axis. The cross marks the best-R^2 solution, whereas the black stars mark the optimal-R^2 GSS solutions. For tumor tissue we do see a bias in K^{trans} (3.7% at 5 s and 11.4% at 60 s resolution) introduced by the fitting routine, i.e. the best solution lies just outside the collection of GSS solutions. As a temporal resolution of 60 s (bias of 11.4% for tumor tissue) is towards the limit in terms of temporal resolutions suitable to fit the basic Tofts model – which we will further discuss in Chapters 3, 5, and 6 – we conclude that the GSS fitting approach is robust against noise. Taken as a whole, we can conclude that the golden section search fitting algorithm is appropriate for fitting the basic Tofts model. The method does provide a goodness-of-fit measure R^2, but no error estimate on the parameters.

The fairly flat landscape surrounding the best-R^2 solution (Figs. 2.13 and 2.14) results in a range of solutions having a comparable likelihood. A nonlinear least-squares approach can provide the likelihood of the found solution. The merit function is in that case the sum of squared differences. The method looks at the steepness of the merit function surrounding the solution with a quadratic approximation. This tells us how 'easy' it is to end up at the wrong solution. The steeper the 'valley', the higher the cost of being wrong, so the likelier it is that we have ended up at the right position. Because in the approximation the 'valley' is assumed to be ellipsoidal, this error estimate gives a lower bound of the error (Lopata et al. 2007). An estimate of the error on the parameters tells us if the parameters are identifiable from the data, whereas a goodness-of-fit measure alerts for erroneous fits. Both can be caused by erroneous model assumptions. Note that both R^2 and the sum of squared differences not only depend on the quality of the model fit but also on the random noise contained in the data. Alternative merit functions, less influenced by noise, are proposed by Balvay et al. (2005).

2.6.2 Fitting complex pharmacokinetic models

In Chapter 3, the basic Tofts model, the extended Tofts model, and the shutter-speed model will be compared. The extended Tofts model and the shutter-speed model both have three parameters. With three parameters, the use of the golden section search method may become problematic, e.g. the order in which the parameters are alternated might start to play a role. Therefore, in that chapter, the models are all fit with a robust global search method, i.e. the Downhill Simplex method (Nelder and Mead 1965). Simplex fitting is an accepted approach in the field of pharmacokinetic modeling (Bonate 2006, Harmatz and Greenblatt 1987). The method requires only function

evaluations, not derivatives (Press et al. 2007). As a final note, we would like to encourage adding information about the applied fitting routine to (clinical) publications on pharmacokinetic modeling. As the fitting routine can be one of the factors contributing to inter-institute differences, it is important to know its details.

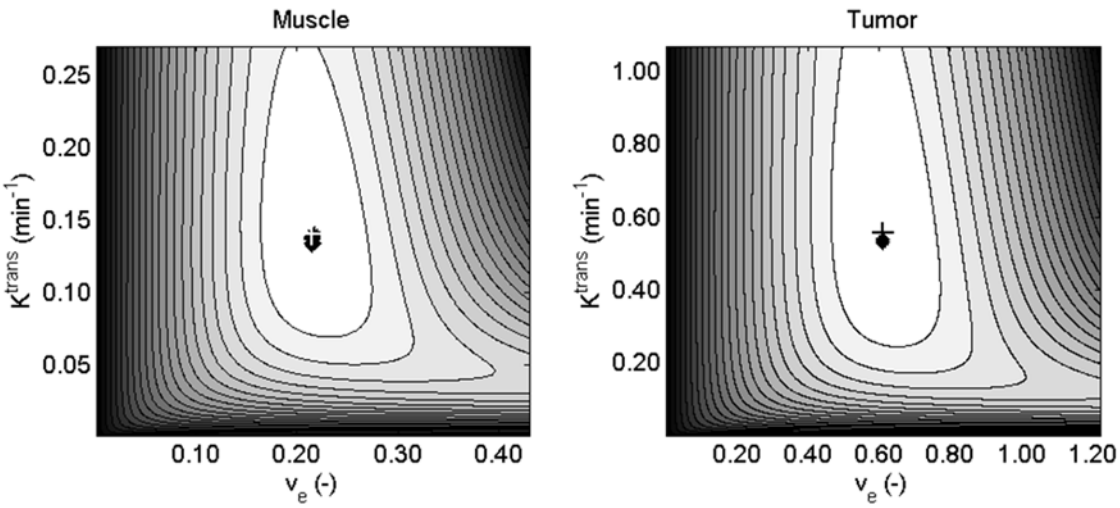

Figure 2.13 *Contour plots of the R^2 landscape for the basic Tofts model, grey levels scaled between 0 and 1. Left: uptake in muscle tissue, right: uptake in tumor tissue. Temporal resolution is 5 s.*

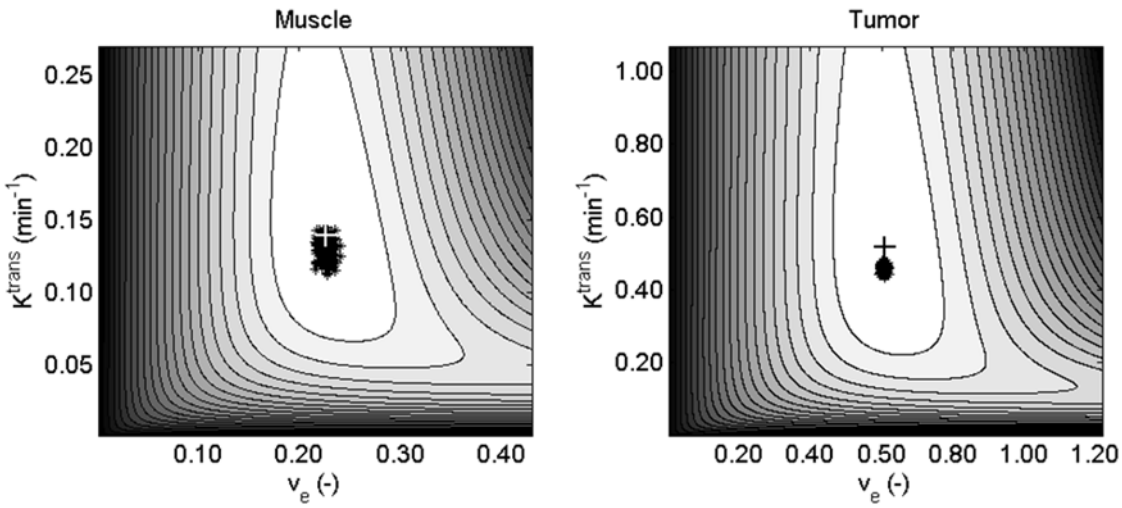

Figure 2.14 *Contour plots of the R^2 landscape for the basic Tofts model. Temporal resolution is 60 s.*

Chapter 3

Data-imposed limitations on pharmacokinetic models for DCE-MRI of the breast

This chapter is based on:

G.J.S. Litjens, M. Heisen, J. Buurman, B.M. ter Haar Romeny (submitted). "Data-imposed limitations on pharmacokinetic models for DCE-MRI of the breast"

G.J.S. Litjens, M.Heisen, J. Buurman, B.M. ter Haar Romeny (2010). "Pharmacokinetic models in clinical practice: What model to use for DCE-MRI of the breast?" Proceedings IEEE ISBI 2010, Rotterdam, The Netherlands, 1727

Abstract

Fitting a pharmacokinetic model to dynamic contrast-enhanced magnetic resonance imaging (DCE-MRI) data of the breast may improve diagnosis of breast cancer by providing higher specificity. For the analysis of diagnostic breast data, the most prominent challenge in using pharmacokinetic modeling is the sampling time, which can exceed 1 minute. In this simulation study, three pharmacokinetic models – i.e. basic Tofts, extended Tofts, and shutter-speed – were tested for their robustness against low-temporal resolution (1 s – 20 s) and noise (0% – 16%); assessing both accuracy and precision for a large range of pharmacokinetic parameter combinations. In addition, the robustness of the basic Tofts model was tested for the presence of a non-negligible vascular fraction, or non-negligibly-short water lifetimes (i.e. inappropriate assumption of the fast-exchange limit). The arterial input function (AIF) was obtained via a reference tissue, whose contrast uptake curve was simulated under the same conditions as the uptake of the lesion. It was found that, within the context of breast imaging (~8% noise, usually sampling time ≥ 20 s), the extended Tofts and shutter-speed model are not useable within a 20% error margin, whereas the basic Tofts model demonstrated adequate robustness (~20% error margin). However, if a non-negligible vascular fraction is present, ignoring it – both in extracting the AIF and in fitting the uptake in the lesion – leads to large errors in the estimated parameters, even for high-quality data. In case the intracellular lifetime of water is longer than 0.2 s, neglecting the shutter-speed effect also leads to unacceptably large errors (> 20%). When using a reference tissue AIF approach, a high signal-to-noise-ratio is more important than a short sampling time. Provided proper model selection, i.e. while considering data quality and the nature of the tissue under study, pharmacokinetic modeling of DCE-MRI breast data is feasible within an acceptable error margin.

3.1 Introduction

Dynamic contrast-enhanced magnetic resonance imaging (DCE-MRI) has shown to be a valuable tool in the diagnosis of breast cancer (Kuhl et al. 1999). During an MR exam, a gadolinium-based contrast agent is injected and T_1-weighted scans are made over time (duration < 10 min), usually on a 1.5 T MRI scanner using a radio-frequency-spoiled gradient echo sequence. In addition to morphologic features of enhancing regions, the kinetics of the contrast agent uptake have diagnostic potential (Kuhl 2007b). However, descriptive kinetic features like signal enhancement ratio (as a measure of wash-out) are subject to large inter- and intra-patient variability, in addition to inter-protocol variability; the former due to variations in systemic circulation, the latter due to variations in injection protocol (Aerts et al. 2008) and scan protocol (Hittmair et al. 1994). To remove these dependencies and obtain tumor-specific parameters, pharmacokinetic models were developed.

Over the past two decades several pharmacokinetic models (e.g. the early models by Brix et al. 1991, Larsson et al. 1990, and Tofts and Kermode 1991) have become available for the analysis of DCE-MRI tissue response curves. These models describe the contrast agent exchange between the blood plasma and the extravascular extracellular space; each using different assumptions and simplifications of the true physiological process. In the context of diagnostic DCE-MRI of the breast, the most prominent constraint for using these models is the sampling time with which clinical images are acquired; it can exceed 1 minute. The sampling time is important because of the Nyquist-Shannon sampling criterion; i.e., if it is too large, rapid kinetics cannot be captured and the pharmacokinetic parameters are unidentifiable from the data (Lopata et al. 2007). In image acquisition a balance has to be found between image quality – i.e. signal-to-noise-ratio (SNR) and spatial resolution – and sampling time, to allow concurrent assessment of morphologic (as described in the BI-RADS lexicon, American College of Radiology 2003) and kinetic features.

The purpose of the current simulation study was to investigate which pharmacokinetic models can be reliably used in the diagnostic breast MRI setting. Three pharmacokinetic models, being the basic Tofts (Tofts et al. 1995), extended Tofts (Tofts 1997), and shutter-speed model (Yankeelov et al. 2003), were tested for their robustness against low-temporal resolution and noise. Both accuracy and precision were assessed for a large range of pharmacokinetic parameter combinations. The arterial input function (AIF) was obtained via simulation of a reference tissue approach. In addition, we also investigated the effect of simplifying model assumptions about the underlying physiological process on pharmacokinetic parameter estimation, i.e. neglecting the vascular contribution, or assuming infinitely fast water exchange.

3.2 Materials and methods

3.2.1 Contrast agent distribution

In oncology, contrast agent exchange is usually modeled with two compartments: an input compartment and a response compartment. The input compartment is the blood plasma and the response compartment is the lesion. Because of the scale of MRI, the imaged lesion voxels consist of intracellular space (IS), extravascular extracellular space (EES), and capillary space (CS). The common gadolinium-based contrast agents cannot access the IS, only the CS and EES. The contrast agent enters the capillary bed on the arterial side from where it diffuses into the EES. Here, the contrast agent influences the relaxation rate of the surrounding water protons, causing a T_1-shortening and thereby a signal increase. It is important to note that the contrast agent can only directly influence the water protons in the CS and EES. The water protons in the IS are only influenced through water exchange between the IS and the EES. A schematic overview is given in Figure 3.1.

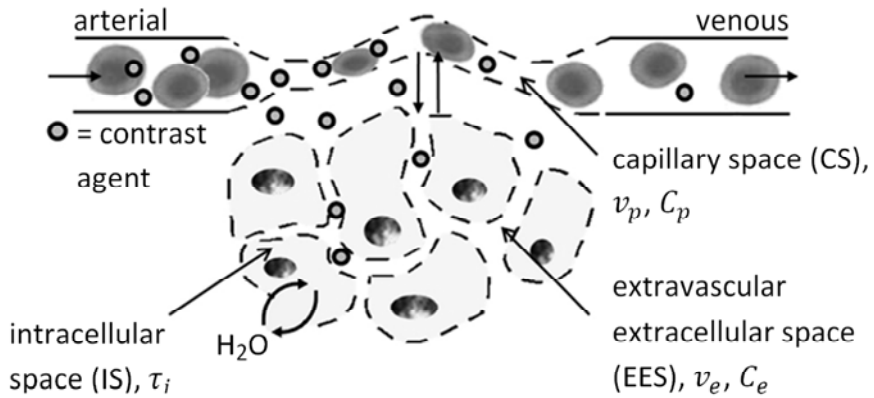

Figure 3.1 *Contrast agent diffusion from the blood plasma into the EES. The water protons inside the cells are only influenced due to water exchange between the IS and EES.*

3.2.2 Pharmacokinetic models

Common pharmacokinetic models for DCE-MRI are the basic Tofts model, the extended Tofts models, and the shutter-speed model. There are many more models available. Recently, models using an adiabatic approximation to the tissue homogeneity model are gaining popularity (Donaldson et al. 2010, Henderson et al. 2000). These models incorporate an estimate of the mean transit time (MTT) of the contrast agent particles passing through the capillary bed of the tissue to obtain separate estimates of blood flow and permeability. In this paper, we focus on the models that are based on Kety compartment theory (Kety 1951) and use the simplification of a negligibly short MTT.

The basic and extended Tofts models are defined by two and three parameters, respectively. In the basic Tofts model, defined as

$$C_t(t) = K^{trans} \int_0^t e^{-K^{trans}(t-s)/v_e} \cdot C_p(s)ds, \qquad [3.1]$$

K^{trans} (min^{-1}) is a combined measure of blood flow and capillary wall permeability, whereas it only represents permeability in the extended model (under the assumption of fast blood flow):

$$C_t(t) = K^{trans} \int_0^t e^{-K^{trans}(t-s)/v_e} \cdot C_p(s)ds + v_p \cdot C_p(t). \qquad [3.2]$$

In both models, v_e is the volume fraction of extravascular extracellular space (EES) within a voxel; C_p (mM) is the concentration of contrast agent in the blood plasma; C_t (mM) the concentration in the tissue of interest; and t (min) is the time that has passed since contrast agent injection. The additional parameter used in the extended Tofts model is v_p, i.e. the fraction of blood plasma within a voxel. In the basic Tofts model this fraction is assumed to be negligible.

The (first generation) shutter-speed model (Eq. 3.3) is different in that it incorporates the effect of water exchange between the IS and EES on the MR signal amplitude. For a thorough derivation the reader is referred to Yankeelov et al. 2003. This effect of transcytolemmal water exchange is combined with the basic Tofts model, which represents the pharmacokinetic part of the equation. The Tofts models themselves assume the water exchange between the IS and EES to be infinitely fast, essentially stating that the contrast agent can influence all water. In the shutter-speed model the extra parameter τ_i (s) is introduced, which is the mean time that a water proton is in the IS. The non-infinitely fast water exchange affects the MR longitudinal magnetization, and thus the shutter-speed part of the model provides a relationship between contrast agent concentration $C_t(t)$ and R_1 (s^{-1}), the longitudinal relaxation rate:

$$R_1(t) = \frac{1}{2}\left(r_1 \cdot C_t(t) + R_{10,i} + \frac{1}{\tau_i} + A_1 + A_2\right)$$

$$-\frac{1}{2}\sqrt{\left(-r_1 \cdot C_t(t) + R_{10,i} + \frac{1}{\tau_i} - A_1 - A_2\right)^2 + A_3}, \qquad [3.3]$$

$$A_1 = \frac{R_{10}-(1-p_e)R_{10,i}}{p_e}, \quad A_2 = \frac{1-p_e}{p_e \cdot \tau_i}, \quad A_3 = \frac{4(1-p_e)}{p_e \cdot \tau_i^2},$$

in which r_1 (mM^{-1} s^{-1}) is the relaxivity of the contrast agent; R_{10} (s^{-1}) and $R_{10,i}$ (s^{-1}) are the relaxation rates in the absence of contrast agent of, respectively, the entire tissue and the IS; and p_e denotes the fractional water population of the EES. Time t in this model is expressed in seconds. In our simulations we assumed r_1 equal to 3.8 mM^{-1} s^{-1}, which corresponds to the relaxivity of gadopentetate dimeglumine (Gd-DTPA,

Magnevist, Schering, Berlin, Germany) at 1.5 T, and p_e equal to $0.8 \cdot v_e$ (Yankeelov et al. 2003).

Fundamental to pharmacokinetic modeling of DCE-MRI data is the use of an arterial input function (AIF) which describes the bolus of contrast agent passing through the blood circulation, and serves as input to the contrast agent uptake in the tissue of interest. It is difficult to extract an accurate AIF from data acquired with modest temporal resolution via direct measurement in an artery. Therefore, reference tissue AIF approaches (Kovar et al. 1998, Yankeelov et al. 2005) were developed to estimate the AIF from a reference tissue; i.e. inversely using a pharmacokinetic model to estimate the input curve from the response curve of a tissue with known properties. Diagnostically, the use of a patient-specific (reference tissue) AIF results in a larger area under the ROC curve, and thus performs better than the use of a standard AIF (Vos et al. 2009). In addition, use of a standard AIF can lead to large errors in parameter estimation (Yang et al. 2007).

In a diagnostic setting there are usually no expectations beforehand about the tissue physiology; i.e. it is unknown what degree of model complexity is necessary to describe it. However, parameter estimation errors, as investigated for the three models addressed in this study, depend on the significance of several contributions to the contrast agent uptake. So, for each type of contrast agent uptake we could find a different error. To obtain a general estimate of model performance, we performed forward-backward simulations for a large range of pharmacokinetic parameter combinations – i.e. fitting the lesion response curve with the same model as with which it was generated – as described in the next section.

3.2.3 Simulation setup

We performed a simulation study to estimate model accuracy and precision under different conditions. First, a reference tissue response curve was generated using a standard AIF (sampling time of 5 s, Parker et al. 2006) and one of the three pharmacokinetic models. Skeletal muscle was chosen to serve as reference tissue, because in DCE-MRI of the breast the pectoralis muscles are often visible within the imaging field of view. The assumed parameter values for muscle were K^{trans} = 0.12 min^{-1}, v_e = 0.10, v_p = 0.08 (in the basic Tofts and shutter-speed model: $v_p \approx 0$), and τ_i = 1.00 s (in the Tofts models $\tau_i \approx 0$) (Faranesh and Yankeelov 2008, Yankeelov et al. 2005, Yankeelov et al. 2008). Subsequently, the reference tissue curve was downsampled and noise was added. The obtained curve was then used as input for the estimation of the pharmacokinetic parameters of the downsampled lesion response curve without explicit calculation of the AIF (Yankeelov et al. 2005). In simulating the reference tissue curve, the same pharmacokinetic model was selected as was used for simulating the lesion response curve. We assume that the same model is applicable to both the reference tissue and the lesion. One simulation cycle consists of:

1. Selecting lesion pharmacokinetic parameter values from a predefined range;
2. Generating tissue response curves for both the reference tissue and the tissue of interest using a standard AIF, one out of three pharmacokinetic models, and the selected parameter values in step 1;
3. Downsampling both tissue response curves (reference and tissue of interest) and adding noise;
4. Fitting the downsampled tissue of interest curve with the model selected in step 2, or, alternatively, with a more simplified model, using the reference tissue curve and its assumed parameters as input;
5. Calculating the error between the fitted lesion parameter values and those used to generate the lesion response curve.

In step 1, using Latin hypercube sampling (Iman et al. 1981), a set of lesion parameter values was selected from a predefined range and a lesion response curve was simulated using one of the three models. For K^{trans} we used values ranging from 0.00 to 1.50 min^{-1}, for v_e from 0.10 to 0.80 (Aerts et al. 2008, Eliat et al. 2004, Veltman et al. 2008), for v_p from 0.00 to 0.30 (Faranesh et al. 2006, Henderson et al. 1998), and for τ_i from 0.00 to 1.50 s (Yankeelov et al. 2003). After simulating the tissue response curves (step 2), they were downsampled (Planey et al. 2009) and Gaussian noise was added (Aerts et al. 2008, Lopata et al. 2007) to represent concentration uncertainty (step 3). In our simulation study the investigated sampling times ranged from 1 s to 20 s per data point (1, 2, 4, 6, 8, 10 and 20 s), which is comparable to the sampling times investigated in other studies (Faranesh and Yankeelov 2008, Henderson et al. 1998, Yankeelov et al. 2008). Noise was added in multiples of 1/3 (varying between 0 and 2) times the typical level of uncertainty in clinical data. In our experience, this level is around 8% of the concentration maximum of a curve, which is similar to values reported in literature (Aerts et al. 2008, Yankeelov et al. 2005). This uncertainty is not only based on image noise but also on uncertainties in T_1-estimation, which is needed to convert signal intensity to contrast agent concentration. In step 4, the selected model was fitted to the simulated curves using the downhill Simplex method (Nelder and Mead 1965), which is relatively robust to local maxima, with a random initialization. Finally (step 5), the resulting parameter estimates were compared to the ones used to generate the lesion response curve. The percentage of error was defined as:

$$error = \left|\frac{P_i^{ori} - P_i^{fit}}{P_i^{ori}}\right| \cdot 100\%, \qquad [3.4]$$

in which P_i is the ith pharmacokinetic parameter. For each model, and for every combination of sampling time and uncertainty level, 500 simulations were performed using different pharmacokinetic parameter values in a Monte-Carlo fashion. The medians and median deviations of the obtained error distributions were determined, as well as the 95%-confidence intervals on the 90th-percentiles (Conover 1980).

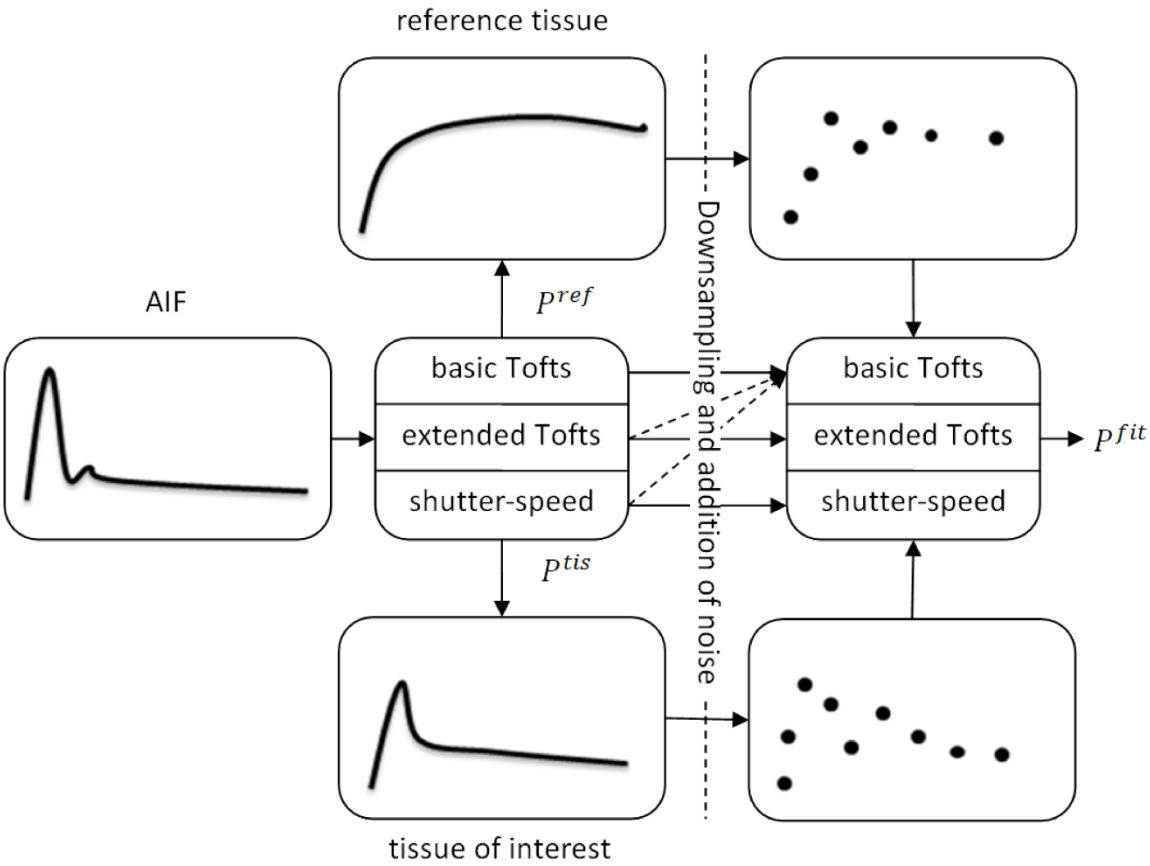

Figure 3.2 *Overview of one simulation cycle. A standard AIF is used as input. Two sets of pharmacokinetic parameters, one for the reference tissue (P^{ref}) and one for the tissue of interest (P^{tis}) are used in conjunction with a model to generate two response curves. After downsampling and addition of noise either the same model is used to fit the lesion response curve (solid arrows), or the basic Tofts model is used to fit the lesion response curve generated with a more complex model (dashed arrows). The fitted parameter values (P^{fit}) can be compared to the simulation parameter values ($P^{tis} = P^{ori}$).*

In addition to the experiments in which we assume that the preconditions for the use of a specific model are fulfilled (forward-backward simulations), we also investigated the effect of using the basic Tofts model when the underlying assumptions are incorrect, i.e. 'undermodeling'. For example, when v_p or τ_i is not small enough to be neglected. The basic Tofts model was chosen because it is the most-simplified representation of the contrast agent distribution process. These experiments were performed with sampling times of 4, 10 and 20 s per data point and an added noise levels equal to 0 and 2.67% (= 1/3·8%) of the concentration maximum. These sampling times and noise levels were chosen to get an indication of the effects of incorrect model assumptions on the parameter estimation errors as a function of temporal resolution and noise. Lesion response curves were simulated using either the extended Tofts or the shutter-speed

model with different values of, respectively, v_p and τ_i. The generated curves were fitted with the basic Tofts model and the errors in K^{trans} and v_e were determined. For both the basic Tofts / extended Tofts and the basic Tofts / shutter-speed combination 1000 simulations were performed. A schematic overview of the complete simulation setup is presented in Figure 3.2.

3.3 Results

For each model and each model parameter, using the error measure specified in Eq. 3.4, contour plots were made of the median absolute error and the median deviation of the absolute error distribution (medians taken over 500 simulations) as a function of sampling time and noise level. Absolute errors were used because otherwise a median error of 0 could give the false impression that the error is low, whereas error is an absolute quantity. The median error and median deviation were preferred over the mean error and mean deviation to limit the influence of outliers. Showing these measures as contour plots provides, respectively, insight into model accuracy (bias) and model precision (variability). In general, a large error variation is worse than a bias; because a *known* stable bias could be corrected for. If the bias is unstable, thus implying a large variation, this is not possible.

In Figure 3.3 the estimation errors in K^{trans} and v_e for the forward-backward simulation with the basic Tofts model are shown as contour plots, with the vertical axis representing the sampling time and the horizontal axis representing the noise level. The almost vertical lines in plots 3.3(a)-(d) indicate that the noise level greatly affects model accuracy and precision, much more so than the sampling time. This can be explained by the fact that noise is present in the input (via uptake in muscle) as well as in the response (uptake in lesion), thereby having a double effect.

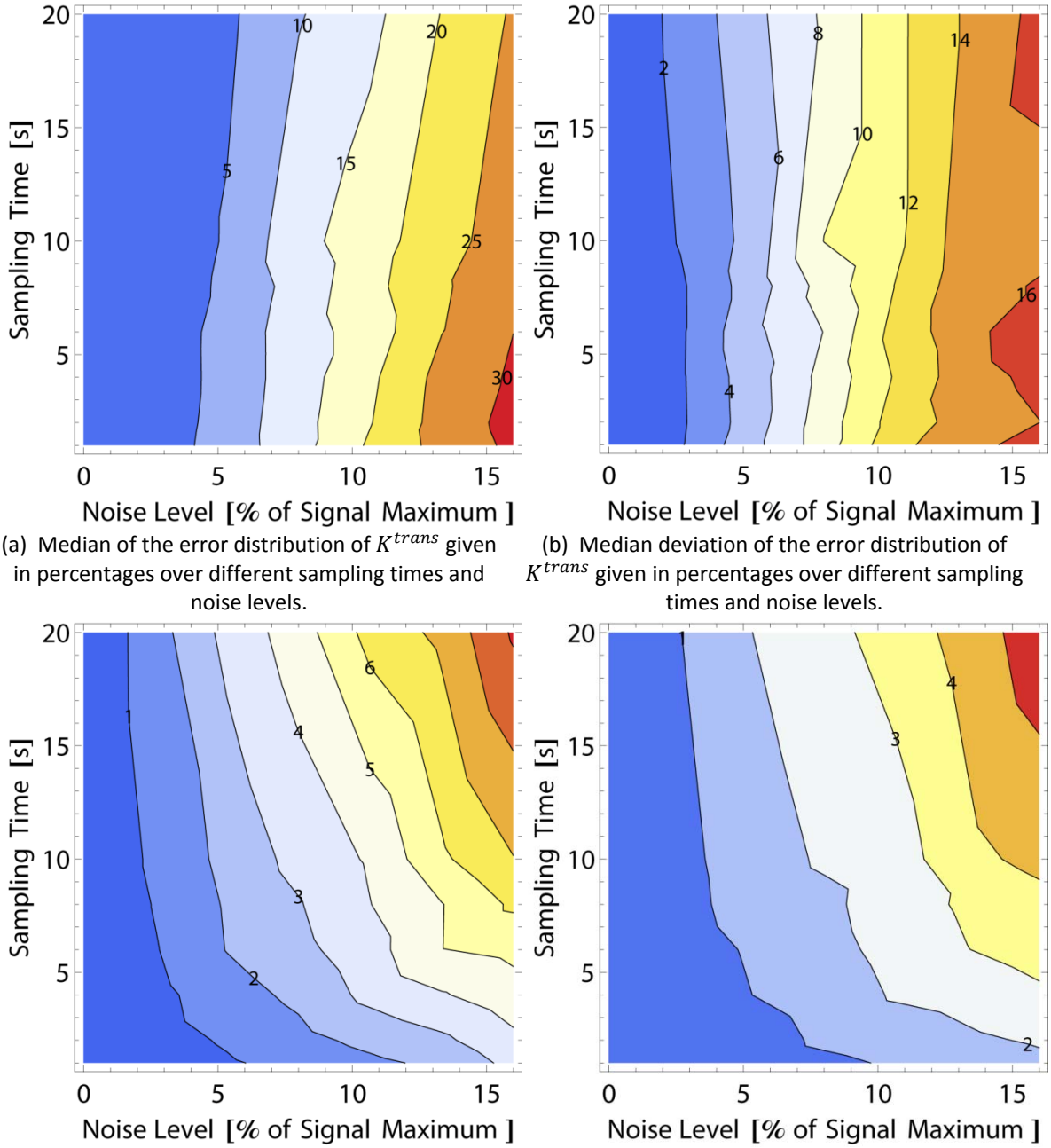

(a) Median of the error distribution of K^{trans} given in percentages over different sampling times and noise levels.

(b) Median deviation of the error distribution of K^{trans} given in percentages over different sampling times and noise levels.

(c) Median of the error distribution of v_e given in percentages over different sampling times and noise levels.

(d) Median deviation of the error distribution of v_e given in percentages over different sampling times and noise levels.

Figure 3.3 *Basic Tofts model: contour plots of the median error (left column) and median deviation of the error (right column) in parameter estimates, as a function of sampling time and noise level. The contour lines represent the values (%) of the median error and median deviation. High values are red, low values are blue. The somewhat unsmooth appearance of the contour lines is due to fairly coarse sampling.*

In Figure 3.4 the results of the forward-backward simulations with the extended Tofts model are shown. The errors are, on average, larger than for the basic Tofts model. As expected, these results demonstrate that the use of more complex models requires more stringent demands on data quality and temporal resolution. In addition, these contour plots show that for the use of the extended Tofts model the sampling time appears much more important than for the use of the basic Tofts model, as the contour lines are much more horizontal.

The results of the forward-backward simulations with the shutter-speed model are shown in Figure 3.5. Here, it can be seen that this model is very sensitive to noise, as the contour lines are almost vertical and sharply rising for all parameters. To allow correct estimation of pharmacokinetic parameters, a very high SNR seems to be required.

Figure 3.4 (next page) *Extended Tofts model: contour plots (%) of the median error (left column) and median deviation of the error (right column) in parameter estimates, as a function of sampling time and noise level.*

Figure 3.5 (page after next) *Shutter-speed model: contour plots (%) of the median error (left column) and median deviation of the error (right column) in parameter estimates, as a function of sampling time and noise level.*

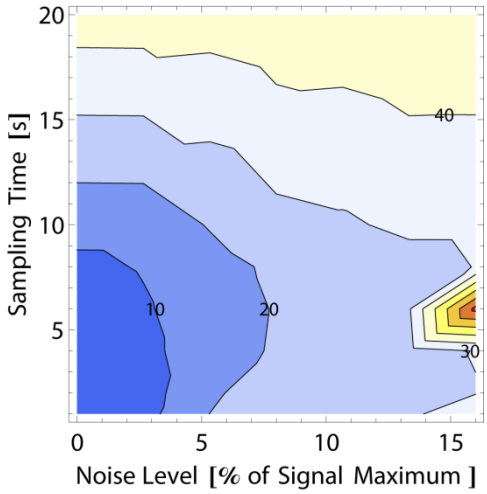

(a) Median of the error distribution of K^{trans} given in percentages over different sampling times and noise levels.

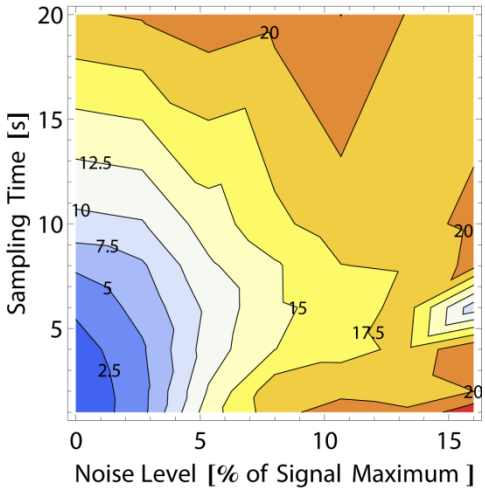

(b) Median deviation of the error distribution of K^{trans} given in percentages over different sampling times and noise levels.

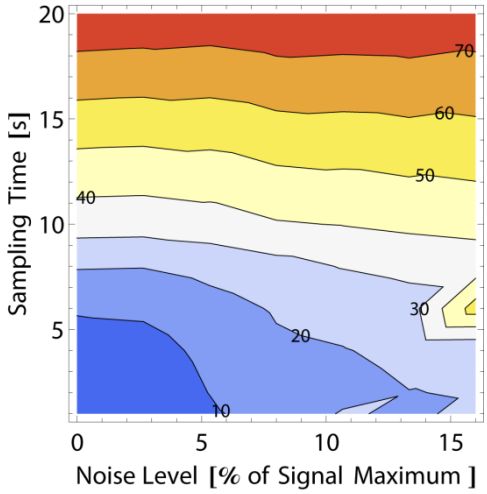

(c) Median of the error distribution of v_e given in percentages over different sampling times and noise levels.

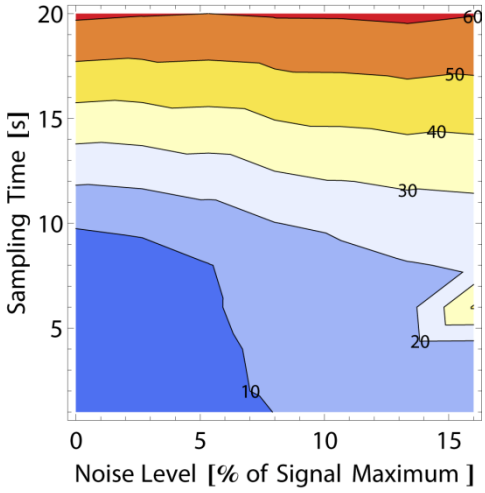

(d) Median deviation of the error distribution of v_e given in percentages over different sampling times and noise levels.

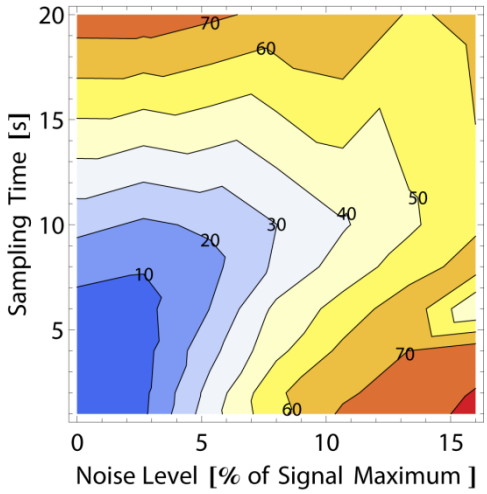

(e) Median of the error distribution of v_p given in percentages over different sampling times and noise levels.

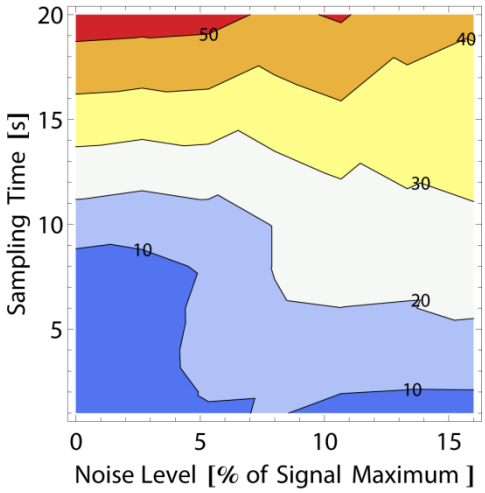

(f) Median deviation of the error distribution of v_p given in percentages over different sampling times and noise levels.

Figure 3.4 *(Extended Tofts)*

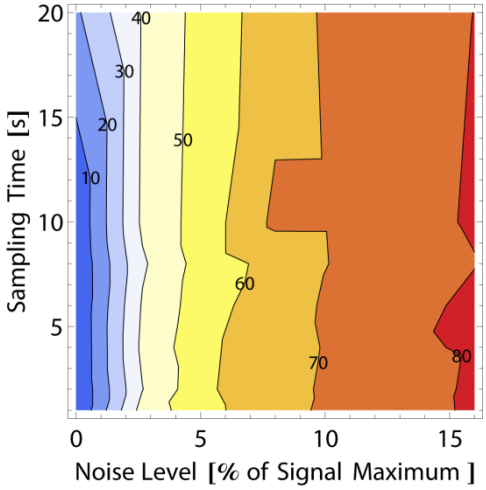

(a) Median of the error distribution of K^{trans} given in percentages over different sampling times and noise levels.

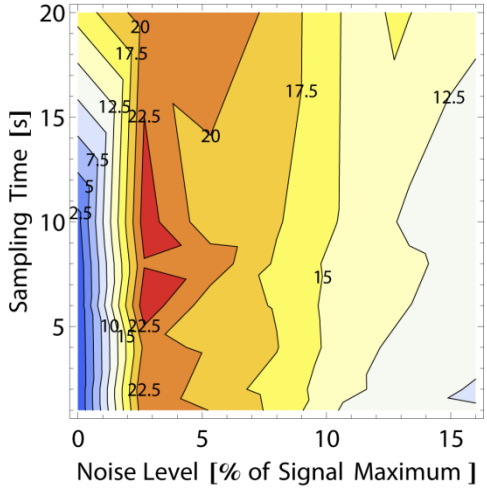

(b) Median deviation of the error distribution of K^{trans} given in percentages over different sampling times and noise levels.

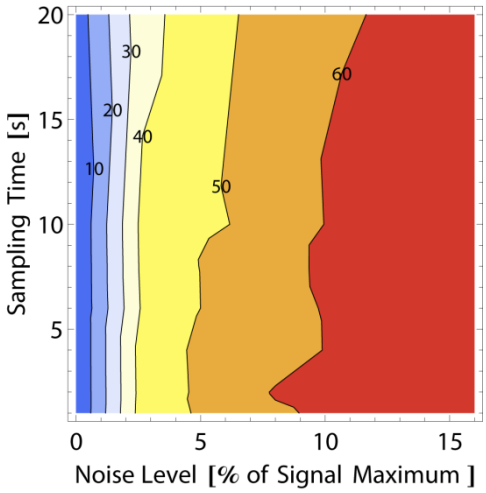

(c) Median of the error distribution of v_e given in percentages over different sampling times and noise levels.

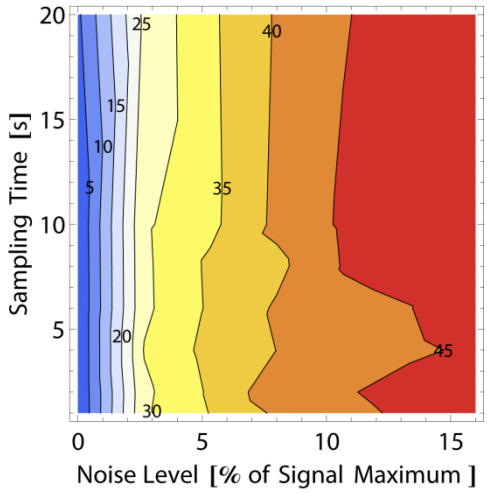

(d) Median deviation of the error distribution of v_e given in percentages over different sampling times and noise levels.

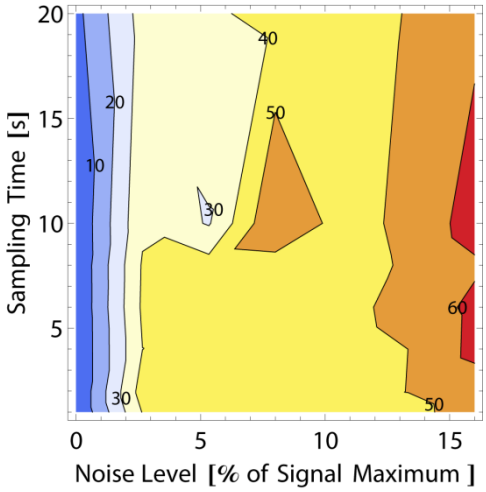

(e) Median of the error distribution of τ_i given in percentages over different sampling times and noise levels.

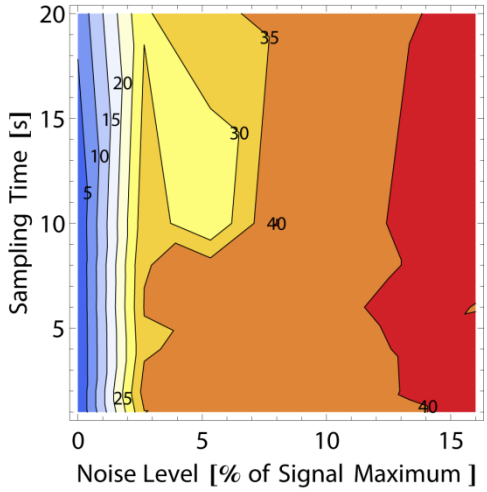

(f) Median deviation of the error distribution of τ_i given in percentages over different sampling times and noise levels.

Figure 3.5 *(Shutter-speed)*

With use of the 95%-confidence interval on the 90th-percentile of the error distribution we can state with 95% confidence that 90% of the error will be below the upper value of the confidence interval. In comparison to the median error ± one median deviation, the influence of outliers is more prominent on the 95%-confidence interval on the 90th-percentile. The specific use of pharmacokinetic parameter estimates in a diagnostic setting will dictate acceptable error margins; i.e. error margins that do not result in a large overlap between the parameter estimates corresponding to a benign uptake pattern and those corresponding to a malignant uptake pattern. In literature we find that separating benign and malignant clusters in pharmacokinetic parameter space is possible up to an error margin of approximately 20% (Eliat et al. 2004, Hulka et al. 1995, Planey et al. 2009, Yankeelov et al. 2008).

In Tables 3.1-3.3 the 95%-confidence interval on the 90th-percentile of the error distribution is shown for the parameters of, respectively, the basic Tofts, the extended Tofts, and the shutter-speed model. For all three models the 90th-percentile increases rapidly for increasing noise levels, whereas temporal resolution is less critical. In the tables we highlighted the results that indicate diagnostic usability (90th-percentile 95%-confidence interval on the error below 20%) in light grey. Borderline cases are indicated with dark grey. Interestingly, the results presented in Tables 3.1-3.3 imply much stricter data-requirements than those presented in Figures 3.3-3.5, likely indicating the impact of the tails of the error distribution. For instance, looking at the median ± one median deviation, the basic Tofts model (Figure 3.3) performs adequately (i.e. for K^{trans}< 1.5 min^{-1}, v_e < 0.8) at a sampling time of 20 s and a noise level of 8%; but looking at the 90th-percentile confidence interval (Table 3.1) the allowed noise level is 2.7% instead. This underlines the importance of a high SNR.

Table 3.1 *Basic Tofts model: 95%-confidence interval on the 90th-percentile of the error (%) in K^{trans} and v_e. Light grey: within 20% error.*

sampling time (s)	K^{trans}							v_e						
	noise level (% of signal maximum)													
	0	**2.67**	**5.35**	**8**	**10.67**	**13.34**	**16**	**0**	**2.67**	**5.35**	**8**	**10.67**	**13.34**	**16**
1	0.0 - 0.0	8.8 - 14.2	26.7 - 37.7	40.0 - 54.9	51.6 - 60.8	58.5 - 66.9	62.1 - 72.0	0.0- 0.0	1.2 - 2.0	2.5 - 4.1	4.1 - 5.8	5.1 - 6.5	6.7 - 9.6	7.7 - 9.3
2	0.1 - 0.2	8.2 - 12.6	24.7 - 39.0	41.4 - 53.5	51.4 - 64.1	57.3 - 69.2	64.1 - 72.4	0.0 - 0.0	1.5 - 2.2	3.1 - 4.2	4.7 - 7.0	6.2 - 7.9	7.8 - 10.9	9.4 - 12.6
4	0.3 - 0.6	8.1 - 12.1	24.2 - 38.4	38.2 - 51.8	50.6 - 62.8	58.8 - 67.1	60.0 - 71.0	0.0 - 0.0	2.1 - 2.9	4.2 - 5.5	6.3 - 8.3	8.6 - 11.3	9.3 - 12.2	12.0 - 15.8
6	0.7 - 1.7	7.9 - 11.3	34.4 - 52.1	40.1 - 52.9	56.2 - 63.1	58.9 – 68.0	64.4 - 73.2	0.0 - 0.0	2.7 - 3.5	6.3 - 11.9	7.1 - 9.2	9.8 - 14.5	12.6 - 16.0	17.3 - 22.7
8	0.7 - 1.9	8.9 - 11.9	26.1 - 39.1	40.8 - 56.8	49.1 - 62.7	58.6 - 69.8	63.1 - 73.4	0.0 - 0.1	2.8 - 3.7	6.0 - 7.7	8.2 - 10.1	10.6 - 14.6	13.6 - 17.4	15.8 - 19.9
10	2.7 - 5.5	9.3 - 12.4	26.2 - 37.6	43.3 - 55.2	49.9 - 60.0	59.0 - 67.4	63.5 - 74.0	0.1 - 0.1	3.0 - 4.5	6.2 - 9.4	9.4 - 12.3	11.5 - 14.3	14.6 - 18.0	18.7 - 22.8
20	5.2 - 7.2	13.7 - 19.6	26.8 - 33.6	38.4 - 50.6	48.5 - 59.1	58.7 - 69.9	63.1 - 74.1	0.4 - 0.5	4.2 - 6.1	8.0 - 10.9	11.9 - 14.5	14.8 - 19.3	18.9 - 25.2	22.2 - 28.1

Table 3.2 *Extended Tofts model: 95%-confidence interval on the 90th-percentile of the error (%) in K^{trans}, v_e, and v_p. Light grey: within 20% error, dark grey: slightly larger error.*

sampling time (s)	K^{trans}							v_e							v_p						
	noise level (% of signal maximum)																				
	0	**2.67**	**5.35**	**8**	**10.7**	**13.3**	**16**	**0**	**2.7**	**5.4**	**8**	**10.7**	**13.3**	**16**	**0**	**2.7**	**5.4**	**8**	**10.7**	**13.3**	**16**
1	0.4 - 2.3	17.6 - 28.3	48.3 - 74.2	77.3 - 122.8	91.3 - 128.3	83.7 - 134.3	98.1 - 162.8	0.4 - 0.9	8.9 - 12.3	25.8 - 36.7	38.6 - 49.9	44.5 - 61.6	51.2 - 67.8	51.9 - 66.6	0.9 - 4.9	15.8 - 20.9	48.7 - 53.3	69.8 - 73.7	80.6 - 85.2	86.0 - 89.7	88.5 - 91.5
2	1.9 - 5.9	21.1 - 27.1	62.6 - 89.2	64.5 - 111.5	95.3 - 135.9	112.8 - 166.1	104.5 - 168.3	1.5 - 3.4	11.4 - 15.5	37.0 - 46.1	40.2 - 53.3	56.5 - 72.9	61.7 - 77.2	64.9 - 91.5	4.1 - 11.4	17.9 - 20.8	50.9 - 57.2	71.4 – 78.0	81.6 - 86.5	88.6 - 92.5	94.3 - 97.5
4	6.7 - 9.7	21.8 - 31.5	52.5 - 67.2	76.7 - 108.5	86.0 - 129.4	98.1 - 149.2	98.9 - 142.2	6.1 - 7.0	15.4 - 21.5	35.8 - 46.2	46.8 - 59.1	58.4 - 76.5	72.1 - 84.0	74.0 - 86.6	14.3 - 27.8	19.3 - 26.4	52.1 - 60.1	71.6 - 78.6	88.0 - 91.7	91.7 - 96.2	95.3 - 98.3
6	15.7 - 22.7	24.0 - 33.0	47.9 - 64.3	67.2 - 85.6	77.3 - 97.7	82.2 - 118.2	91.5 - 94.0	14.9 - 17.3	19.8 - 23.7	37.5 - 46.2	53.4 - 68.2	65.2 - 87.3	70.2 - 83.2	175.6 - 269.1	42.7 - 63.1	23.4 - 39.4	47.7 - 64.3	73.3 - 81.3	81.7 – 91.0	93.7 - 97.9	74.9 – 133.0
8	25.2 - 33.4	30.8 - 42.5	53.2 - 67.5	71.5 - 104.6	75.8 - 104.5	81.6 - 115.8	83.3 - 116.4	27.9 - 32.0	32.6 - 37.0	41.9 - 53.1	58.9 - 75.4	73.0 - 88.1	83.4 - 101.8	86.4 - 104.5	63.1 - 95.1	48.4 - 62.8	49.5 - 70.2	70.2 - 84.3	82.7 - 93.4	90.0 - 95.5	96.6 - 98.6
10	42.9 - 53.9	43.7 - 65.7	63.9 - 77.4	69.2 - 96.0	76.3 - 104.8	89.1 - 116.4	83.4 - 111.0	50.0 - 55.9	52.9 - 59.9	61.2 - 72.4	77.9 - 97.6	100.9 - 115.3	96.6 - 119.3	108.2 - 137.4	119.3 - 227.9	91.4 - 165.1	82.8 - 121.4	89.2 - 122.2	86.5 - 98.4	95.9 - 99.2	96.6 - 99.0
20	138.5 - 235.2	142.4 - 226.5	137.2 - 215.8	128.8 - 205.4	114.0 - 200.5	137.4 - 207.9	122.1 - 217.1	297.0 - 382.2	297.0 - 382.9	297.1 - 383.0	293.7 - 383.0	296.5 - 375.2	293.9 - 380.0	293.9 - 378.2	283.1 - 388.5	286.5 - 413.6	262.2 - 413.8	260.8 - 358.5	228.7 - 382.3	248.3 - 421.9	218.4 - 322.1

Table 3.3 *Shutter-speed model: 95%-confidence interval on the 90th-percentile of the error (%) in K^{trans}, v_e, and τ_i. Light grey: within 20% error, dark grey: slightly larger error.*

sampling time (s)	K^{trans}							v_e							τ_i						
	noise level (% of signal maximum)																				
	0	**2.67**	**5.35**	**8**	**10.7**	**13.3**	**16**	**0**	**2.7**	**5.4**	**8**	**10.7**	**13.3**	**16**	**0**	**2.7**	**5.4**	**8**	**10.7**	**13.3**	**16**
1	0.2 - 1.2	73.2 - 79.5	82.4 - 85.9	86.0 - 88.5	87.4 - 90.2	90.3 - 92.2	93.4 - 95.4	0.0 - 2.9	124.2 - 151.0	151.0 - 187.8	168.8 - 214.9	185.2 - 231.9	203.8 - 236.2	204.8 - 251.3	0.1 - 7.3	315.2 - 519.8	348.8 - 501.3	341.8 - 557.4	305.2 - 633.5	288.7 - 593.9	281.3 - 532.3
2	1.0 - 3.7	75.2 - 80.2	81.3 - 85.6	85.5 - 88.5	88.3 - 90.2	90.8 - 93.7	93.8 - 96.1	0.2 - 7.0	114.9 - 137.4	147.4 - 185.1	162.8 - 208.5	174.8 - 221.9	204.4 - 246.4	205.6 - 266.3	0.9 - 22.1	298.3 - 440.4	327.3 - 587.0	348.0 - 570.9	307.2 - 594.3	295.1 - 584.1	265.5 - 498.3
4	3.7 - 12.7	76.0 - 80.9	81.9 - 86.4	85. – 89.0	88.9 - 91.6	91.5 - 93.8	94.7 - 96.3	0.6 - 14.4	117.7 - 142.2	151.0 - 194.8	164.7 - 206.2	179.5 - 236.2	194.0 - 254.5	204.9 - 264.6	3.8 - 34.0	312.8 - 521.0	325.9 - 575.4	353.1 - 528.7	315.8 - 558.2	264.7 - 512.8	244.2 - 495.7
6	14.2 - 20.2	77.2 - 81.3	82.3 - 85.5	86.5 - 89.3	89.0 - 91.7	92.7 - 94.5	95.3 - 96.7	2.5 - 18.9	127.0 - 155.7	150.4 - 195.8	174.6 - 218.3	193.6 - 249.5	204.9 - 260.7	213.1 - 287.1	7.6 - 32.8	305.6 - 546.0	343.6 - 540.8	327.3 - 551.3	293.3 - 548.5	252.2 - 458.9	228.3 - 457.3
8	19.6 - 30.9	74.3 - 82.2	83.0 - 87.2	86.3 - 89.5	88.9 - 91.9	93.5 - 95.4	94.9 - 96.3	3.9 - 16.2	119.2 - 147.4	145.8 - 185.1	164.7 - 203.0	202.5 - 262.1	204.9 - 250.3	209.7 - 286.1	12.7 - 47.9	324.4 - 519.8	337.6 - 547.1	324.4 - 586.3	299.6 - 649.0	270.2 - 551.0	278.1 - 570.9
10	23.3 - 61.3	77.7 - 80.6	81.0 - 88.3	92.8 - 95.4	89.7 - 93.4	93.1 - 94.7	95.2 - 96.6	8.6 - 32.6	114.1 - 158.2	130.8 - 205.7	213.9 - 283.5	199.4 - 252.1	215.1 - 265.4	232.1 - 299.2	21.5 - 79.8	309.3 - 558.8	203.4 - 845.5	203.5 - 425.8	315.8 - 633.4	283.4 - 631.4	265.8 - 487.3
20	57.1 - 66.7	77.9 - 83.7	84.2 - 87.6	88.2 - 91.3	92.1 - 94.7	94.5 - 96.2	95.9 - 97.1	31.2 - 56.6	121.4 - 156.1	159.3 - 214.5	181.3 - 237.0	200.2 - 257.3	222.7 - 303.0	244.3 - 309.8	65.4 - 99.5	287.0 - 553.5	336.9 - 640.7	310.7 - 646.2	328.0 - 642.3	246.1 - 576.6	273.5 - 474.5

Now that we have seen that the basic Tofts model is robust against long sampling times and fairly robust against noise, it is illustrative to look at the results when the specific preconditions are no longer satisfied; i.e. when v_p or τ_i is non-negligible. These results are shown in Figure 3.6. In subfigures 3.6(a) and 3.6(b) the errors in K^{trans} and v_e are plotted (± one median deviation) versus v_p for the basic Tofts / extended Tofts combination (both reference tissue and tissue of interest). We see the error (y-axis) versus an increasing v_p fraction (x-axis). For the basic Tofts / extended Tofts combination the median error ± one median deviation on K^{trans} is too high (> 20 %) immediately from the start, where v_p is still very low. This is probably caused by the fact that it is assumed that the reference tissue does not contain a significant vascular fraction v_p while it does. The error increases for increasing v_p in the tissue of interest. For v_e we still obtain fairly good estimates (median error ± one median deviation < 20%) for very small fractions of v_p (< 0.1) in the tissue of interest. Temporal resolution and SNR are less important than the assumptions about the underlying physiology, because the curves show little variation between sampling times of 4, 10, and 20 s, with or without added noise. In subfigures 3.6(c) and 3.6(d) similar results are shown for the basic Tofts / shutter-speed combination; the errors in K^{trans} and v_e are plotted versus τ_i. However, for small values of τ_i (τ_i < 0.20 s for K^{trans}, τ_i < 0.50 s for v_e) these estimates are still reasonable (error < 20%). For this combination of basic Tofts / shutter-speed we do see some differences between the two noise levels (no noise

versus 2.7%), implying that at higher noise levels neglecting τ_i has a larger effect. The different sampling times caused little variation in the error.

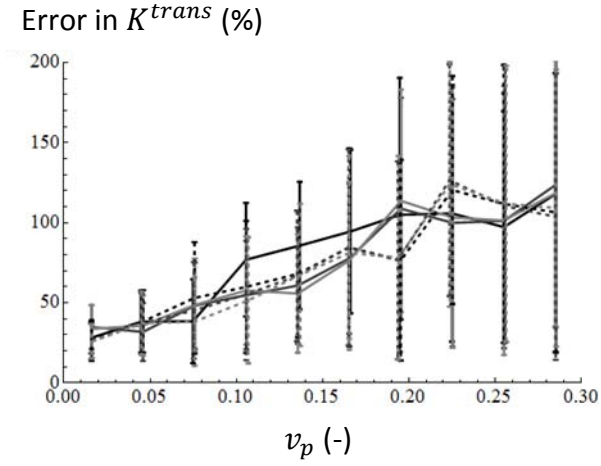

(a) Error distribution (median ± one median deviation) of K^{trans} for different values of v_p.

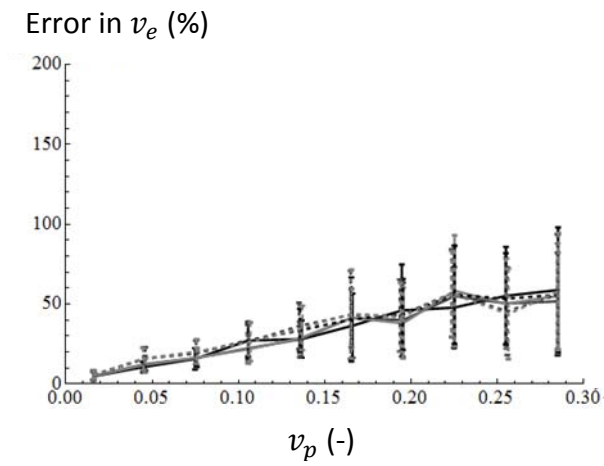

(b) Error distribution (median ± one median deviation) of v_e for different values of v_p.

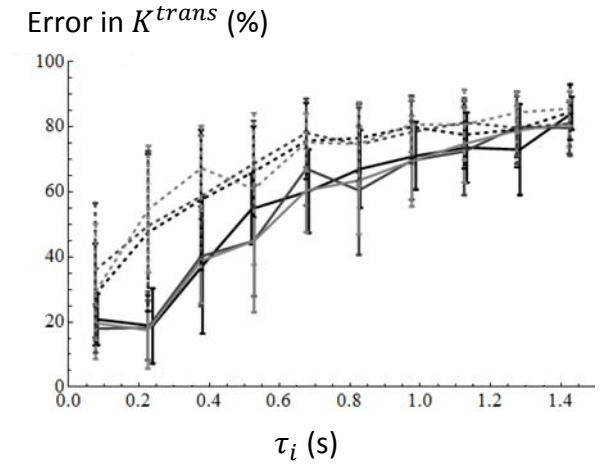

(c) Error distribution (median ± one median deviation) of K^{trans} for different values of τ_i.

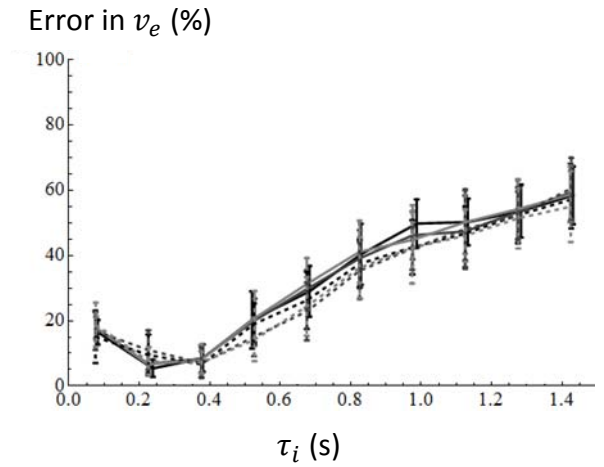

(d) Error distribution (median ± one median deviation) of v_e for different values of τ_i.

Figure 3.6 *Median error in the basic Tofts parameters for different values of v_p (a, b) and τ_i (c, d). The black, dark gray, and light gray lines represent sampling times of 4, 10 and 20 s, respectively. Solid lines are without noise and dashed with 2.7% noise.*

3.4 Discussion

In this paper we have shown that the use of pharmacokinetic models in a diagnostic setting for breast cancer is feasible if sampling times can be reduced to 20 s, or less. However, careful consideration is required in selecting a model and interpreting its results. As expected, the basic Tofts model is most robust against long sampling times and noise, but its estimates can have large errors if the specific preconditions, being a negligible v_p and τ_i are not met. We also explored the use of two more complex models, i.e. the extended Tofts model and the shutter-speed model, which we demonstrated to have high demands in terms of data quality. But, if these demands are met, the models provide additional and more accurate (oversimplification leads to biases in the parameters) information regarding the underlying physiology. In case of adequate data quality, the choice for either of these complex models depends on the expected degree of tumor vascularization: if the tumor is highly vascular the extended Tofts model gives a better representation of the true process than the shutter-speed model, because use of the extended Tofts model would result in more accurate estimates of K^{trans} and v_e. When the vascular fraction is assumed negligible we recommend the use of the shutter-speed model in case of high-SNR data. To provide some concrete limits: if the noise level is significantly lower than 2.7% and the vascular fraction is negligible, one should use the shutter-speed model. If the noise level is about 2.7% or lower and the vascular fraction is non-negligible the extended Tofts model should be used for sampling times of 2 s or shorter. In other cases the basic Tofts model should be used; but note that under the strict measure of the 95%-confidence interval on the 90th-percentile of the error distribution the typical noise level of 8% is fairly high.

In the scenario where we fitted the basic Tofts model to data simulated with the extended Tofts model (Figs. 3.6(a) and (b)), both the reference tissue and the tissue of interest were simulated with a significant vascular fraction. In a practical setting one could also encounter a situation in which the reference tissue v_p is negligible whereas the lesion v_p is significant. If in that case we use a sampling time of 4 s (no noise added), the median error in both K^{trans} and v_e is below 20% up to a lesion v_p of 0.1. In comparison to the results presented in Figs. 3.6(a) and (b), this shows that neglect of a non-negligible reference tissue v_p has a large impact.

An interesting aspect of the results presented in this study is the prominent role of the signal-to-noise ratio. In contrast to an earlier study in which we assumed a standard (known) AIF (Litjens et al. 2010) and found that temporal resolution was more important than SNR, we showed in this work that a low noise level is very important when using a reference tissue AIF approach. This can be explained by the fact that noise propagates both into the input (via the reference tissue) and into the response (tissue of interest) when using a reference tissue method. In our view, the scenario simulated in this paper mimics diagnostic practice in a more realistic way than the use of a standard

AIF, because in practice a perfectly matching AIF (forward-backward simulation with standard AIF) would not be available. To reduce noise propagation in low-SNR situations, a prefitting of the contrast agent uptake curves with an empirical function might be considered (Fan et al. 2007).

In previous research by Henderson et al. (1998) temporal resolution requirements for the basic and extended Tofts models were estimated. In this simulation study a lower-temporal-resolution AIF (sampling time of 10 s) was used as a standard input. The AIF was not derived from the data. In addition, the simulated range of noise levels was smaller than in our study. The main finding of this paper was that for use of the basic Tofts model the sampling time should be below 16 s in case the AIF is sampled every second; for use of the extended Tofts model the sampling time should be below 4 s. Using a reference tissue AIF approach, we found higher temporal requirements for use of the extended Tofts model, whereas we found lower temporal requirements for use of the basic Tofts model. The required temporal resolution for use of the basic and extended Tofts models was also investigated in a series of papers that used the reference tissue AIF approach as well (Faranesh and Yankeelov 2008, Yankeelov et al. 2005). However, in these papers the simulation setup (parameter range, AIF, temporal resolution, analysis method) was not the same for the basic Tofts model and the extended Tofts model, making a comparison difficult. The main findings were that the basic Tofts model in combination with a reference tissue AIF approach required a sampling time of roughly 32 seconds (Yankeelov et al. 2005), which is similar to what we found in our study. We found that for a sampling time of 20 s and a low noise level the error on the parameter estimates is within 20%. Because, the influence of temporal resolution is limited (see Fig. 3.3), a sampling time of approximately 30 s appears within reach. For the extended Tofts model they also observed that accurate parameter estimation depends heavily on high-temporal resolution. Faranesh and Yankeelov (2008) obtained accurate results (error ≈ 0%) with a sampling time of approximately 1 s without added noise, while with our criterion (error < 20%) we found that a sampling time of approximately 6 s is allowed, provided a low noise level (< 2.7%).

In the current work, we focused on the models most commonly in use. The adiabatic approximation to the tissue homogeneity model, which includes separate estimates of blood flow and capillary permeability, was not considered. The investigation of temporal requirements for this model – and a comparison with more simplified models – would be challenging because of the complicated interplay between temporal resolution and the mean transit time. Besides variations in the MTT, variations in the sampling grid relative to bolus arrival (Henderson et al. 1998) also form an interplay with temporal resolution. We did not take the latter into account either. To assess model performance we studied the accuracy and precision with which pharmacokinetic parameters could be estimated. Accurate retrieval of the true parameter values is not necessarily crucial in a diagnostic setting; a systematic error

does not have to result in a poorer separation of malignant and benign clusters in parameter space. If both are shifted with 20% in a certain direction, their separation is still intact. Biases are often the result of oversimplification. In applying the basic Tofts model to curves generated with the extended Tofts model we found that neglect of v_p causes overestimation of K^{trans} and underestimation of v_e. Fitting contrast agent uptake curves characterized by a non-negligibly short τ_i with the basic Tofts model resulted in τ_i-dependent underestimation of both K^{trans} and v_e. In both cases the degree of over- / underestimation was temporal-resolution dependent. These observations imply that the error in the parameters results from the interplay between temporal resolution, noise level, and model choice. The co-occurrence of a large vascular fraction and a non-negligibly short τ_i was not investigated in this study. It probably deserves a closer look because a highly vascularized tumor often displays large contrast agent uptake, and at high concentration levels it is less likely that the agent has access to all water.

Current diagnostic DCE-MRI of the breast is performed with a temporal resolution of approximately 1 minute. In this work we investigated higher temporal resolutions (1 s – 20 s) for several reasons. As was shown, a comparison of the more complex models with the basic Tofts model would be meaningless at 1 min resolution; even at a sampling time of 20 s the more complex models are unusable. In addition, it has been shown previously in prostate cancer that pharmacokinetic modeling at these temporal resolutions (< 20 s) can have an added diagnostic value (Vos et al. 2009), and we also see this trend in breast cancer research (Veltman et al. 2008). Technical developments will allow shorter sampling times while still achieving high image quality in the near future. This paper thus shows what could be achieved using these methods in combination with such data.

Summarizing, we demonstrated that the basic Tofts model is robust to lower quality data, but large errors in parameter estimates can be expected when the specific preconditions are not met. In addition, we have shown that the use of more complex models is feasible with very high data quality. At this point in time, these requirements are very difficult to meet in the diagnostic breast MRI setting, making the basic Tofts model the model of choice. In conclusion, when proper care is taken in analyzing the data, it is possible to reliably estimate pharmacokinetic parameters within an error margin of 20% for diagnostic DCE-MRI of the breast. Based on the above-presented results, we will use the basic Tofts model in the remainder of this work, because the sampling times of the data in Chapters 5, 6, 7 do not allow for the use of more complex models.

Chapter 4

Patient-specific calibration for breast MRI: development and use of a breast-coil insertable reference phantom

This chapter contains work adapted from:

M. Heisen, B. Peng, A.M. Wood, D. Mustafi, J. Buurman, G.M. Newstead, G.S. Karczmar (2010). "Patient-specific calibration for breast MRI: breast-coil insertable reference phantom" Proceedings ISMRM 18, Stockholm, Sweden, 2493

M. Heisen, A.M. Wood, J. Buurman, D. Mustafi, B. Peng, G.M. Newstead, C. Yang, M.K. Ivancevic, G.S. Karczmar (2009). "Standardization and calibration for breast MRI: The use of a unique air bubble free agar phantom" Proceedings RSNA 2009, Chicago, USA, 421

G.J.S. Litjens, M. Heisen, J. Buurman, A.M. Wood, M. Medved, G.S. Karczmar, B.M. ter Haar Romeny (2009). "T_1 quantification: Variable flip angle method vs. use of reference phantom" Proceedings RSNA 2009, Chicago, USA, 422

D. Mustafi, B. Peng, M. Heisen, A.M. Wood, J. Buurman, G.S. Karczmar (2009). "World of phantoms: Reference standards for bench to breast MRI" Proceedings ISMRM 17, Honolulu, USA, 2104

4.1 Introduction

Currently, most clinical sites follow the BI-RADS (Breast Imaging-Reporting and Data System, American College of Radiology 2003) guidelines in assessing contrast agent concentration curves in a descriptive way, i.e. assigning one of three curve types (persistent, plateau, wash-out; see Chapter 1, Fig. 1.2) to the uptake pattern in a lesion. Before doing so, the measured curves are converted to relative – with respect to the native signal intensity – enhancement. Whereas inspection of the relative change in signal may be less protocol-dependent than inspection of the absolute signal in arbitrary units, it is far from protocol-independent. The relative signal does not only reflect a change in contrast agent concentration, but also depends on scan parameters such as the repetition time and flip angle (Hittmair et al. 1994); and other factors such as the native T_1 (longitudinal) relaxation time of the tissue, and the arterial input function (as was shown in Chapter 2, Panel C). In fact, the division by the native signal intensity increases the dependency on the native T_1 relaxation time (Hittmair et al. 1994). A more thorough form of calibration is the conversion from signal intensity to $T_1(t)$, which can be related to contrast agent concentration $C(t)$. This conversion will be the topic of this chapter.

In a recent study, Jansen et al. (2009b) demonstrated that the influence of scanner / protocol dependencies on relative enhancement curves can actually impact diagnostic practice. The objective of their study was to compare dynamic contrast-enhanced (DCE) MRI breast data acquired with three different MRI systems. The kinetic curve data of malignant lesions showed large differences in initial contrast uptake and curve type between systems. As rapid initial enhancement and wash-out curve type are both considered important signs of malignancy (Kuhl et al. 1999), these discrepancies in malignant lesion presentation adversely impact the diagnostic sensitivity and specificity of kinetic analysis. To provide all women undergoing DCE-MRI of the breast with an adequate and consistent diagnosis, we therefore need improved standardization. However, since scan protocol variation is wide due to differences in scanner capabilities, local preferences, and the fact that protocols are tailored to the specific purpose of each type of exam, protocol standardization is unrealistic. Instead, we should standardize the measured dynamic contrast-enhanced data via quantification of the contrast agent concentration. We can attain this by adding a few – at least one – additional scans to the protocol, leaving freedom to variation in the DCE-MRI series.

Pharmacokinetic curve type modeling has long been the promise to provide quantitative, reproducible, tissue parameters. However, to deal with native T_1 and scan parameter dependencies – here as well – a precondition is that the signal intensity data is converted to contrast agent concentration. The most popular conversion method includes precontrast T_1-mapping, often performed via a variable flip angle approach (Buckley et al. 2004), and the assumption of a theoretical signal model, usually the spoiled gradient echo model (Heilmann et al. 2006). This conversion step frequently

results in a large uncertainty on the contrast agent concentration curves due to noise propagation from the T_1-map, plus a position-dependent bias due to imperfect flip angle profiles. Moreover, clinical scan protocols are fine-tuned to provide high-contrast low-noise images at a fast rate. Smart acquisition schemes and filter techniques may affect the dynamic data in such a way that the often-assumed theoretical signal models do not describe the actual data. For example, it is difficult to predict how various fat saturation methods affect the signal. Straight-forward application of 'old' conversion techniques to 'new' data can result in non-reproducible, and, yet again, scan-protocol dependent outcomes.

Both types of kinetic analysis, i.e. descriptive and pharmacokinetic, could benefit from validated signal calibration to minimize the influence of the MR system and the applied imaging protocol on lesion assessment. To provide patient-specific calibration, we propose the use of a reference phantom that is scanned concurrently with the patient. An advantage of concurrent scanning is that variations induced by the presence of the patient can be incorporated into the calibration.

Several studies describe the use of reference phantoms to calibrate the relationship between contrast agent concentration and signal intensity. In 1994, Hittmair et al. (*sequence: 2D spoiled gradient echo*) introduced their 'enhancement factor' which scales linearly with contrast uptake and is independent of native tissue T_1 and sequence parameters. The method requires a proton-density weighted (low-flip-angle) image, and calibration of the enhancement factor for the applied acquisition sequence. This calibration was performed with a series of phantoms varying in T_1 and proton density. This procedure was also applied in Walker-Samuel et al. 2007a. The mismatch between acquisition theory and acquisition practice was nicely demonstrated by Parker et al. (1997) (*sequence: 2D spoiled gradient echo*), who calibrated a T_1-mapping procedure – based on the ratio between the T_1-weighted series and a precontrast PD-weighted image volume, under assumption of the spoiled gradient echo signal model – with gels doped with various amounts of contrast agent. A similar procedure was reported in Galbraith et al. 2002, and in Liney et al. 1999. In the latter study (*sequence: 3D fast spoiled gradient echo*), it was pointed out that a dual-flip angle T_1-estimation method (Fram et al. 1987, Wang et al. 1987) can reproduce T_1 values between 125 ms and 600 ms fairly accurately (with less than 10% error), but for longer T_1 values the error increases dramatically. Typically, T_1 values of normal breast parenchyma and breast lesions are longer than 600 ms; they can even be longer than 900 ms (Bottomley et al. 1987). With an empirical calibration, however, they obtained a small error (within 4%) in T_1 both for short (140 ms) and long T_1 values (925 ms). Henderson et al. (2000) (*sequence: 2D saturation-prepared spoiled gradient echo*) showed a mismatch between theory and practice as well. Via calibration using a series of reference phantoms, they found a match between theory and practice if the nominal flip angle applied during the T_1-weighted dynamic series was divided by a factor of 1.5.

In this context, is it worth mentioning the Quantitative Imaging Biomarkers Alliance (QIBA, Radiological Society of North America), as the DCE-MRI section of this alliance has set out to reduce variation in parameters characterizing tumor vascular functioning due to differences between patients (systemic circulation), scanners, scan protocols, and institutions. A special phantom was designed and built to rotate between institutions. Data acquired from prescribed phantom-only experiments are centrally analyzed and factors resulting in different outcomes are investigated.

In the above-mentioned studies, calibration is performed 'offline': a calibration factor or look-up table is derived from a phantom-only experiment and applied to all patient data acquired with the calibrated sequence. It is not tested whether calibration translates well from patient to patient. Also, if the acquisition protocol is changed, the phantom-only experiment has to be repeated. A few studies considered concurrent scanning of the subject and a reference phantom.

Although for the Hittmair approach (Hittmair et al. 1994) reference phantoms within the field of view are not necessary, it was recommended to use a single reference phantom to prevent drift. If two reference phantoms are present, the enhancement factor can be determined for each acquisition. The calibration used by Pradel et al. (2003) (*sequence: 2D spoiled gradient echo*) is based on a phantom-only scan performed at the end of each experiment; however, one of the phantom tubes is also present while scanning the animal. In a later study from the same group (De Bazelaire et al. 2005) (*sequence: 2D spoiled gradient echo*) sixteen phantom tubes with different contrast agent dilutions were scanned concurrently with the animal. Via assumption of the spoiled gradient echo signal model, proton density and scanner gain were eliminated from the calibration. Eliat et al. (2004) (*sequence: 2D spoiled gradient echo*) placed five calibration phantoms (T_1 between 120 ms and 2174 ms at 1.5 T) next to the breast in the coil. They used the ratio between the T_1-weighted (high-flip-angle) image series and a precontrast PD-weighted (low-flip-angle) image to estimate T_1 in the tissue. Here, it is not assumed that scanner gain is the same between the different types of acquisitions. To obtain an estimate of the scanner gain ratio, a single reference phantom is used with known T_1. The complete set of reference phantoms is subsequently used to calibrate the signal model. In this paper it is explicitly mentioned that the calibration is not reproducible from experiment to experiment.

In this chapter we will discuss the development and characterization of a reference phantom that fits easily into a standard breast coil; as well as its use to improve quantitative measurements of T_1, contrast agent concentration, and proton density. In the "Materials" section we will mainly address the trial-and-error process to arrive at the final design of the reference phantom (Section 4.2.2). The "Methods" section consists of three main parts. In the first part we will discuss three approaches to quantify native T_1 ($= T_{10}$): (i) a time-consuming approach making use of variable-

inversion-time inversion recovery imaging, which will provide us with gold standard phantom T_1 values (Section 4.3.1); (ii) a fast approach making use of variable-flip-angle spoiled gradient echo imaging including a reference-phantom-based correction (Section 4.3.2); and (iii) another fast approach based on empirical signal calibration (Section 4.3.3). As they are fast, approaches (ii) and (ii) can be performed as an addition to a clinical DCE-MRI exam. In the second part of the "Methods" section we will briefly discuss tissue proton density mapping (Section 4.4). The "Methods" section ends with a discussion of different ways to convert from signal intensity to contrast agent concentration (Section 4.5). In the "Results" section we will return to the same three main topics as in the "Methods" section. First, the native T_1 quantification methods are addressed (Sections 4.6.1, 4.6.2, and 4.6.3). Subsequently, tissue apparent proton density maps and concentration images will be shown and discussed in Sections 4.7 and 4.8, respectively. In Section 4.9 we will briefly touch upon imaging artifacts observed in the clinically applied DCE-MRI series. At the end of this chapter (Section 4.10) we will discuss and compare all the proposed quantification methods.

Note: The results shown in this chapter may differ from previously published results because we re-analyzed some of the data using improved routines. All experiments were performed at 1.5 T on a Philips Achieva scanner. As relaxation times and relaxivity depend on field strength (Lerski and de Certaines 1993), the proposed methods cannot be transferred to other field strengths without further investigation. All patients (contrast agent administered) and healthy volunteers (no contrast agent administered) that participated in this study were scanned under University of Chicago Institutional Review Board approval.

To summarize the investigated approaches to obtain T_{10} and subsequent contrast agent concentration for clinical practice, we show a schematic representation of the two main pathways in Figure 4.1. The parallelograms represent acquired or calculated data, whereas the rectangles define actions. We also pointed out in which steps the calibration phantom is of use. The concentration series that are obtained at the end can be used for quantitative kinetic, as well as morphologic, image analysis.

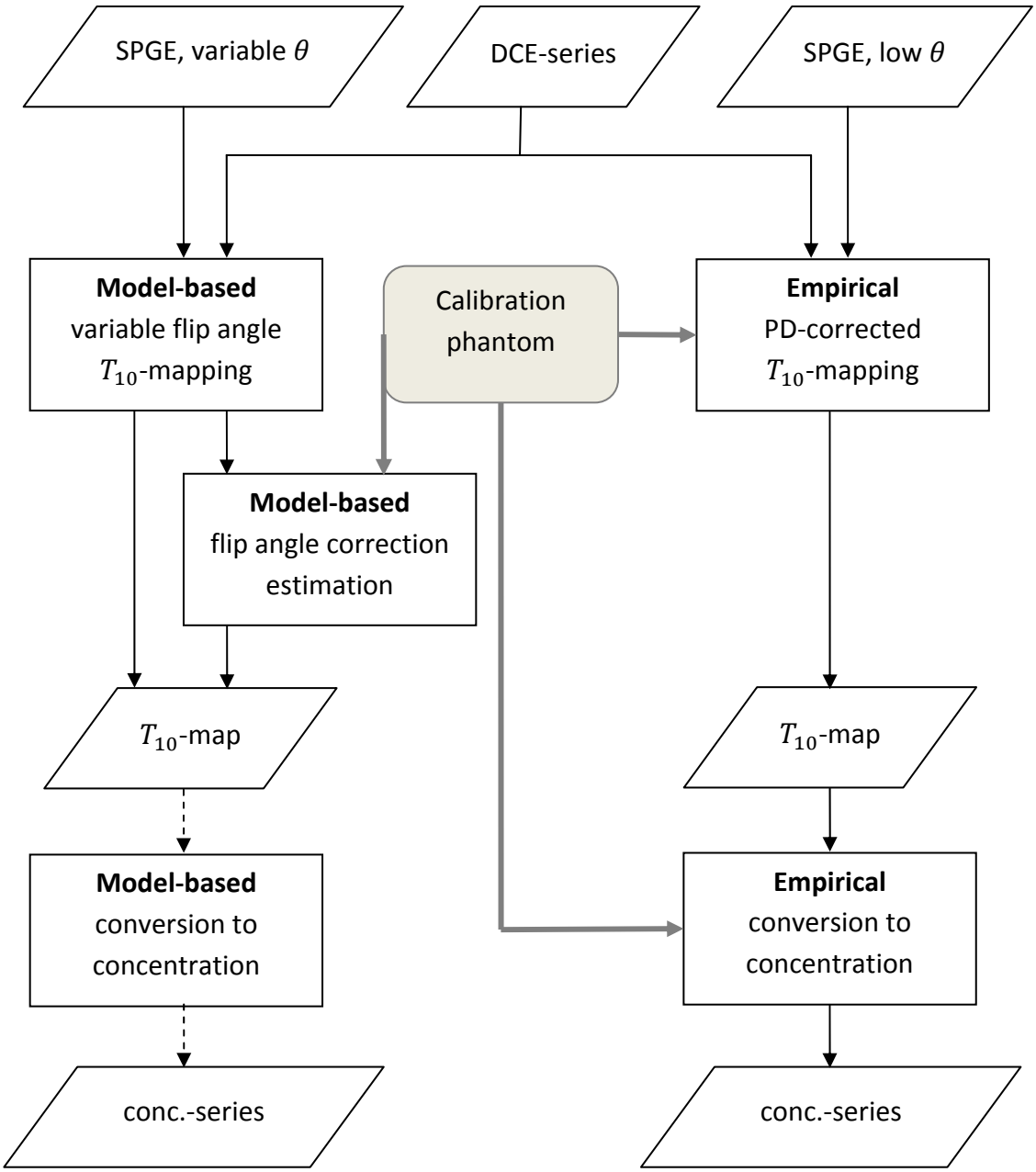

Figure 4.1 *Schematic overview of signal quantification, it is pointed out in which steps the breast-coil insertable reference phantom is of use. SPGE: spoiled gradient echo, T_{10}: precontrast T_1, θ: flip angle, and PD: proton density. Solid arrows: performed in this study, dashed arrows: possible, but not performed.*

4.2 Materials

In studying signal calibration we made use of two different phantoms. Protocols were often first tested with a commercial phantom, i.e. the Eurospin phantom (Diagnostic Sonar, Livingston, UK), with known properties. For concurrent scanning with patients we developed a new – breast-coil insertable – reference phantom; its development will be described in Section 4.2.2.

4.2.1 Eurospin phantom

The Eurospin set of phantoms was developed to provide a general tool for scanner performance assessment and quality control. It consists of five objects designed to test, for instance, image uniformity and resolution. Their use is thoroughly described in Lerski and De Certaines 1993. In this study we made use of test object # 5 (TO5), which consists of eighteen gel phantoms and is meant for assessing T_1- and T_2-mapping procedures. The T_1 values of the gel phantoms were measured using a spectroscopic inversion recovery sequence at manufacture, providing a gold standard (within 3% error). Table 4.1 lists the gold standard T_1 and T_2 values at room temperature (292 K), at 1.5 T. Figure 4.2 shows the phantom tubes together with the Perspex disc in which they can be placed to facilitate scanning.

Table 4.1 *Gold standard T_1 and T_2 values of the Eurospin TO5 at room temperature (292 K),at 1.5 T.*

Tube #	T_1 (ms)	T_2 (ms)
1	199	52
2	298	73
3	295	113
4	455	53
5	446	94
6	442	154
7	597	95
8	592	136
9	745	116

Tube #	T_1 (ms)	T_2 (ms)
10	739	157
11	892	137
12	1440	390
13	959	223
14	1023	167
15	1149	214
16	1261	204
17	1246	183
18	1392	174

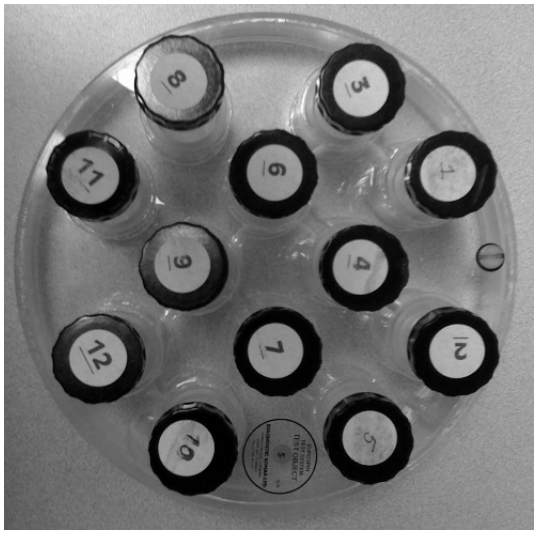

Figure 4.2 *Eurospin TO5, twelve out of eighteen tubes can be placed in the Perspex disc.*

4.2.2 Breast-coil insertable reference phantom

Ring-shaped phantom

The development of a practical and comfortable reference phantom went through several phases. The first design considered a ring-shaped tube (inner diameter of 10 mm) that could be placed around the breast. It contained several gel compartments, separated by Teflon plugs. The ultra-pure agar (1%) gel compartments covered the following range of contrast agent concentrations: 0.0 mM, 0.1 mM, 0.2 mM, 0.5 mM, 1.0 mM (Omniscan, GE Healthcare, Piscataway, NJ, USA). The gel was flushed with helium under vacuum suction to remove air bubbles (Mustafi et al. 2009), because their presence causes susceptibility gradients. Food coloring was used to color-code the different compartments. In Figure 4.3 we show a photo of the actual phantom, a schematic drawing of how the phantom is positioned around the breast, and its appearance on a T_2- and a T_1-weighted MR image.

Using the ring-shaped phantom during several volunteer scans, it turned out to be too delicate. To place the ring around the breast and to make sure it would not drop to the bottom of the coil, the MRI technologist had to slightly squeeze the soft tubing. This caused cracks in some of the gel compartments. Note that the use of rigid tubing would compromise patient comfort. The color-coding was useful in enabling a reproducible protocol, i.e. with always the same compartment at the same side of the breast. However, in the practical setting, this turned out to not be very convenient and the phantom was usually scanned at an arbitrary angle. Retracing which compartment corresponded to which contrast agent concentration in the MRI data was doable (based on expected order of signal intensities), but cumbersome. In addition, the phantom

geometry did not suit all scan orientations. A coronal scan could capture all the compartments in a single slice, although usually the phantom was slightly tilted. In this orientation, the phantom therefore does not help to calibrate inter-slice variation. In an axial or transverse scan, cross-sections of tube segments are imaged across slices. In these orientations, you have a reference in a fair amount of slices, but at maximum two compartments can be imaged in the same slice (as shown in Fig. 4.3), which is not optimal to construct a calibration curve.

Cup-shaped phantom

The second prototype considered a larger phantom, consisting of a plastic cup mounted with six circumferential and six vertical tubes (inner diameter of 4.8 mm). Every tube was completely filled with a single aqueous solution containing Omniscan at the following concentrations: 0.0 mM, 0.1 mM, 0.2 mM, 0.3 mM, 0.4 mM, 0.5 mM. We lowered the maximum concentration level from 1.0 mM to 0.5 mM for several reasons: (i) it is not expected that the contrast agent concentration in breast tissue greatly exceeds 0.5 mM; (ii) it is more important to have an extra measurement in between 0.2 mM and 0.5 mM than at 1.0 mM, and the number of tubes is limited; (iii) at a concentration level of about 1.0 mM or higher, T_2^*-effects may start to play a significant role; and (iv) the presence of a very bright object (1.0 mM tube) in the T_1-weighted MR images affects the automatic windowing level on the diagnostic work station, making the breast look very dark. Note that T_2^*-effects cannot be easily accounted for with either theoretical signal modeling or empirical signal calibration. Of course, in arteries, the contrast agent concentration can exceed 1.0 mM. However, the phantom is not developed for the purpose of calibrating a directly measured arterial input function.

Several attempts to water-tight sealing led to the use of rubber stoppers. The tubes could be easily removed, switched, and reattached to the plastic cup due to the use of Velcro. Because of its fragility we did not proceed with gel solutions. This means that the phantom compartments could suffer from air bubbles and should not be shaken. The specific arrangement of phantom compartments was chosen to have a range of references present in most slices, irrespective of scan orientation. A coronal scan shows cross-sections of the vertical tubes, whereas axial and transverse scans cut through the circumferential tubes. This enables the construction of a calibration curve, and adjustment of this calibration curve to inter-slice variation. A photo of the phantom and a schematic drawing of how it is placed inside the breast coil, together with a T_2- and T_1-weighted image are shown in Figure 4.4.

Figure 4.4 (next page) *The cup-shaped color-coded calibration phantom. The upper edge of the cup is slid between the breast coil (dark grey) and the soft padding (light grey). The two cups are identical. In the schematic representation we show the circumferential tubes as well as the vertical tubes.*

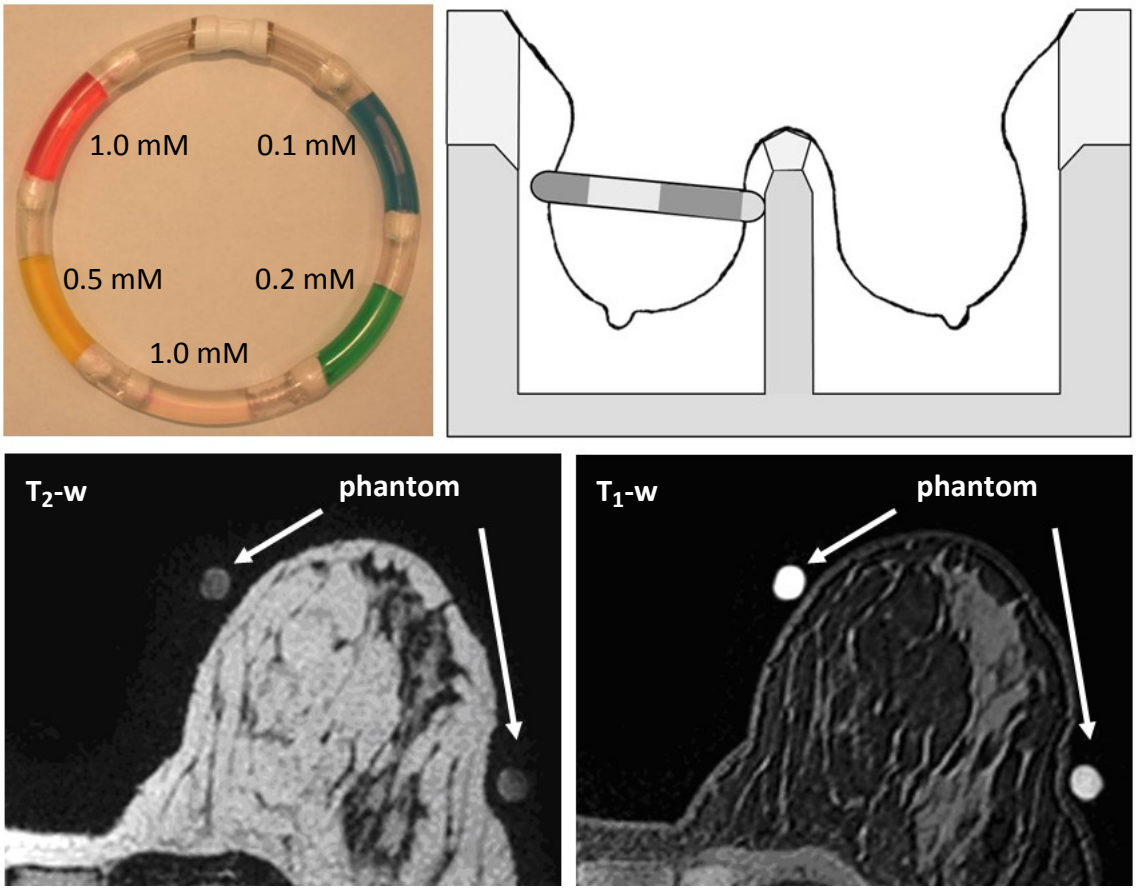

Figure 4.3 *The ring-shaped color-coded calibration phantom.*

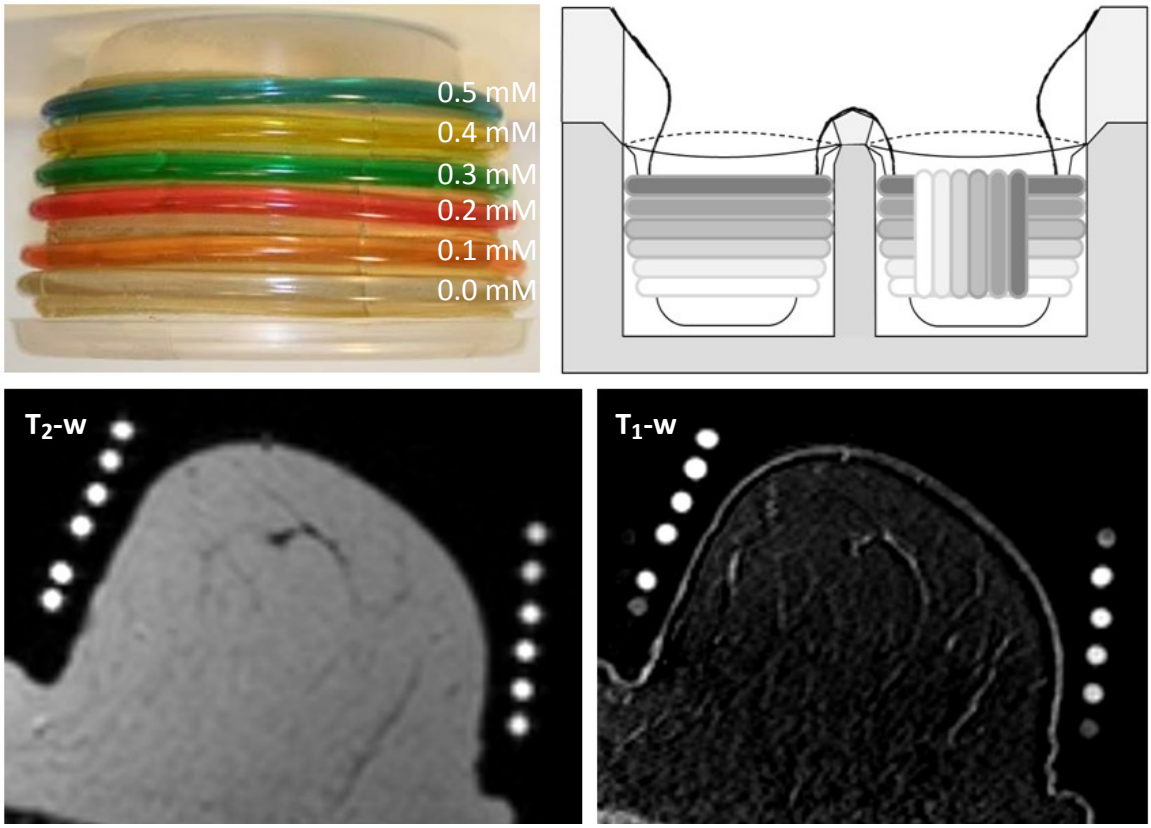

During data acquisition the breast is hung in the phantom cup. Because there is some space needed to add the phantom cup in the coil, this phantom is not appropriate for large-size patients. We attempted to make the phantom as thin as possible. However, as it turned out in analyzing data acquired with this reference phantom (voxel size: 1.3 x 1.3 x 1.5 mm), the tubes were slightly too narrow to perform good region-of-interest (ROI) measurements, i.e. the ROI had to be very small to avoid partial-volume effects. With a small ROI noise may not be averaged out. We therefore switched to tubing with a slightly larger inner diameter of 6.4 mm, and later on also to smaller imaging voxels. We will refer to the first version (inner diameter of 4.8 mm) as phantom "A" and to the second version (inner diameter of 6.4 mm) as phantoms "B1" and "B2", as we made two of those; one for each side. Ultimately, the phantom could be incorporated into the detector.

While testing the cup phantom with several volunteers, we noticed that during the fast spin echo T_2-weighted sequence (specific absorption rate, SAR: high) there was mild heat dissipation in the breast area. This turned out to be caused by the specific scanner / receiver coil combination (Philips 1.5 T Achieva plus 7-channel Invivo phased-array biopsy breast coil), as it was only marginal with a different combination (Philips 1.5 T Achieva plus 16-channel Philips MammoTrak phased-array breast coil), and did not differ in absence / presence of the phantom. Still, to increase ventilation, we drilled holes in the bottoms of the plastic cups. As the latter scanner / receiver coil combination is used for patient scanning, patient comfort was not compromised.

4.3 Methods: T_{10}-mapping

4.3.1 Gold standard T_{10} quantification: inversion recovery with variable TI

To use a phantom for calibration, the T_1 values of its compartments have to be accurately measured. We used a variable-TI (inversion time) inversion recovery (IR) sequence for this purpose, which is well-accepted as a gold standard measurement (Tofts 2003). This sequence takes too long to be applied in a clinical setting (e.g. the data presented in Section 4.3.1 took about an hour to acquire) and was therefore applied in a phantom-only setting.

The spin-echo IR signal model is defined as:

$$S = M_0\left(1 - 2 \cdot e^{-TI/T_1} + e^{-TR/T_1}\right). \qquad [4.1]$$

This model was fitted to the data using an internal nonlinear least squares routine in Matlab (Mathworks, Natick, MA, USA) which is based on a trust-region reflective Newton minimization (global search method, Coleman and Li 1992). The sign of the data was taken into account because use of the absolute signal would complicate estimating uncertainty on the fitted parameters. To know the sign of the data, both the real and

imaginary part of the image data have to be available. In our experiments this was not the case and the sign was estimated afterwards.

As we extracted each measurement on the signal-versus-TI curve from an ROI, we also obtained the standard deviation of each sample. Plotting the standard deviation, as well as the residuals ($S_{measured} - S_{modeled}$) of a non-weighted fit of the model, revealed that the measurement uncertainty on the samples is not constant (i.e. hetereoscedastic, Kirkup 2002), as can be seen in Figure 4.5. With non-constant measurement uncertainty, weighted fitting is required. Weighting was incorporated according to the χ^2-criterion which is a maximum likelihood estimator:

$$\chi^2 = \sum_{i=1}^{N} \left(\frac{S_{measured} - S_{modeled}}{\sigma_i} \right)^2, \qquad [4.2]$$

in which N is the number of inversion times applied and σ_i the standard deviation corresponding to each ROI measurement. Measurements with a high precision receive a large weight, while measurements with a large uncertainty receive a small weight. Using the χ^2-criterion, we can approximate the uncertainty on the obtained parameter estimates quadratically (Bevington and Robinson 2003):

$$\sigma_j^2 = 2 \left(\frac{\partial^2 \chi^2}{\partial^2 a_j} \right)^{-1}, \qquad [4.3]$$

in which a_j are the model parameters and σ_j the standard deviations on these parameters, in our case M_0 and T_1. This uncertainty estimate is based on the same principle as mentioned in Section 2.6 (Fisher information matrix), except here we know the standard deviation of the samples.

For the phantom compartments with a short T_1, the long-TI measurements at the end do not provide additional information about T_1 (flat phase, e.g. see 0.5 mM curve in Figure 4.5), but do add noise (largest standard deviation at longest TI) and therefore uncertainty on the parameter estimates. For both experiments presented in Section 4.6.1 we estimated T_1 without these 'tail' points.

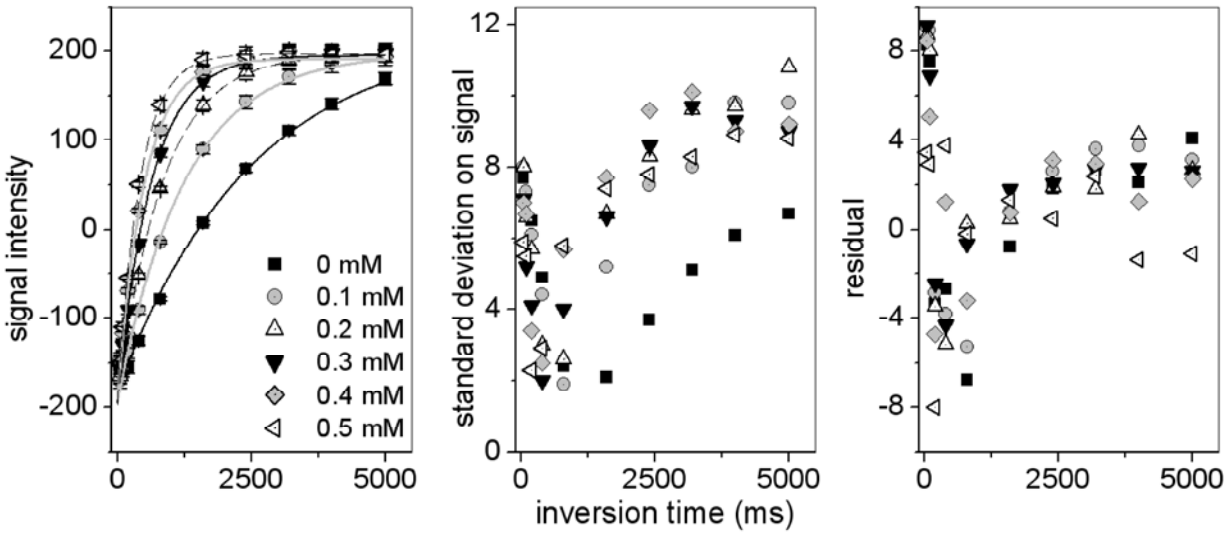

Figure 4.5 *Measurements in phantom compartments (symbols) and non-weighted least-squares fits (lines). The standard deviation on the measured samples as well as the residuals after fitting show a pattern of an initial decrease followed by an increase.*

4.3.2 Clinical T_{10} quantification: fast spoiled gradient echo with variable flip angle

The first method we discuss to obtain precontrast T_1 in a patient scan (available additional time ~ 5 min) is based on knowledge about the applied acquisition sequence, i.e. signal-model based. The second method is empirical, i.e. calibration via the reference phantom, and will be discussed in the next section. In this section, we will explain how the phantom can be used to verify / correct deviations from model-behavior. The acquisition concerns a fast spoiled gradient echo series with a varying flip angle (θ). The signal model for this sequence is as follows:

$$S = M_0 \frac{\sin\theta\left(1-e^{-TR/T_1}\right)}{1-\cos\theta\cdot e^{-TR/T_1}}, \qquad [4.4]$$

in which S is the measured signal intensity; M_0 is a scaling factor that depends on scanner gain and proton density; θ (°) is the flip angle; TR (ms) is the repetition time; and T_1 (ms) is the longitudinal relaxation time. In this equation we neglected T_2^*-attenuation (see Eq. 1.2); however, in a heavily T_1-weighted regime ($TE \ll T_2^*$), this term approximates a value of one and varies little (~5%) for tissues outside the brain (Medved et al. 2004).

Below, we will discuss the different steps that we perform in estimating T_1 from a variable flip angle series. We start with a linear fit to a rearranged version of Equation 4.4. Subsequently, we will discuss a repetition-time- and T_1-dependent selection of the optimal flip angle range. Finally, we will fit the nonlinear model (Eq. 4.4) to the signal-

versus-angle curves, using the parameter estimates from the linear fit as starting values. The data that will be used to illustrate this approach concerns two Eurospin phantom tubes, one with a short T_1 (199 ms) and one with a long T_1 (1392 ms). For this phantom-only experiment we used more flip angles, a higher number of averages, and larger voxels than in case the phantom would be scanned concurrently with a patient (see "Additional scans for quantification in practice" towards the end of this subsection). The acquisition settings were: repetition time / echo time = 25/1.11 ms, flip angle = 3, 5, 10, 15, 20, 25, 30, 35, 40, 50°, NA (number of averages) = 4, acquisition matrix = 88 x 87, pixel spacing = 2.60 mm x 2.60 mm, thickness = 4 mm, spacing 4 mm.

Linearization

We start with a linear regression of a linearized version of the variable flip angle data because linear regression is less error-prone than fitting the signal versus the flip angle according to Eq. 4.4. The latter is for example sensitive to the choice of starting values, whereas the former is not.

Linear fitting is especially popular in combination with a dual-flip angle approach. This is a 'minimalistic' version of the variable flip angle approach. With only two samples available, it makes more sense to fit a straight line than a curve. A common way to reduce the number of additional scans needed for quantification even more, is to acquire one flip angle before the start of the dynamic sequence, the other during the dynamic series. The precontrast part of the dynamic sequence can then be used to fit T_1 in conjunction with the first flip angle data. In this study, however, a variable flip angle sequence consists of 6 flip angles or more. In the "Signal-versus-angle curve fitting" part of this section we will show that more than two flip angles are needed in case the expected variation in tissue T_1 is large.

Via rearrangements of the terms, Eq. 4.4 can be written as (Fram et al. 1987, Wang et al. 1987):

$$\frac{S}{\sin\theta} = e^{-TR/T_1}\frac{S}{\tan\theta} + M_0\left(1 - e^{-TR/T_1}\right), \qquad [4.5]$$

$$y = a \cdot x + b,$$

with $y \equiv \frac{S}{\sin\theta},\ x \equiv \frac{S}{\tan\theta},\ a \equiv e^{-TR/T_1},\ b \equiv M_0\left(1 - e^{-TR/T_1}\right).$

Alternatively, the terms can also be rearranged in the following way (S. Lobregt, personal communication):

$$\frac{S}{\sin\theta} - \frac{S}{\tan\theta} = \left(e^{-TR/T_1} - 1\right)\frac{S}{\tan\theta} + M_0\left(1 - e^{-TR/T_1}\right), \qquad [4.6]$$

$$y' = a' \cdot x + b,$$

with $y' \equiv \frac{S}{\sin\theta} - \frac{S}{\tan\theta},\ x \equiv \frac{S}{\tan\theta},\ a' \equiv e^{-TR/T_1} - 1,\ b \equiv M_0\left(1 - e^{-TR/T_1}\right).$

In Figure 4.6 we show the originally measured curves, S versus θ; the curves after Fram-Wang linearization, $S/\sin\theta$ versus $S/\tan\theta$; as well as after the alternative linearization proposed in this work, $(S/\sin\theta - S/\tan\theta)$ versus $S/\tan\theta$. Note that after linearizarion the samples corresponding to high flip angles end up at the lower end of the x-axis and vice versa. The uncertainty in the measured signal (± one standard deviation) is displayed with an error bar. Here, the flip angles are assumed equal to the nominal values (as set on the scanner console) and uniform across the slice. Their uncertainty (at a fixed position) is assumed to be relatively small. Because after linearization the signal is present on both the y- and x-axis, Figs. 4.6(b) and (c) display error bars along both axes (difficult to see because they are small). We see two interesting differences between the two types of linearization. First, in (b) the straight lines that could be fit to the data sets would be fairly similar, whereas in (c) the data sets look very different. Secondly, in (c) the data corresponding to the long-T_1 tube do not seem to display a linear patter, whereas this deviation from the expected (model-based) shape is invisible in (b). We will address this deviation from model-behavior next.

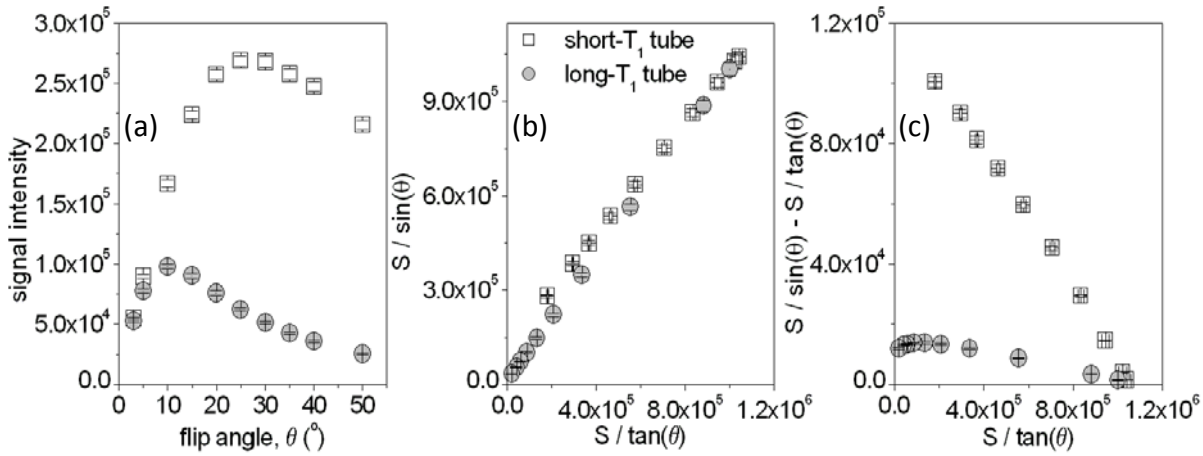

Figure 4.6 *Variable flip angle data for a short-T_1 (199 ms, squares) and a long-T_1 (1392 ms, circles) phantom tube. (a) S versus θ, (b) $S/\sin\theta$ versus $S/\tan\theta$, (c) $S/\sin\theta - S/\tan\theta$ versus $S/\tan\theta$.*

Selection of flip angle range

The deviation from the linear pattern, as seen in Fig. 4.6(c), points out that possibly some flip angles should not be included in fitting certain T_1 values. In case of the above example, the large flip angles do not display 'model behavior' for the long-T_1 tube. Because the alternative linearization displays such deviations from the model more clearly than the Fram-Wang linearization, we chose the former over the latter.

To demonstrate the need for flip angle selection more clearly, we fitted the T_1 of the long-T_1 tube (T_1 = 1392 ms) from the above experiment using linear regression with

a χ^2 merit function (Flannery and Teukolsky 1992). In Fig 4.7(a) we see the linear fit to the alternative linearization (Eq. 4.6) of the data. As you can see, the initial rise of the curve (high-flip angle measurements) causes a bias in the linear regression of the downward slope. If we plot the same fit on top of the signal-versus-angle data (b), we can see that the peak of the data is underestimated because of this effect.

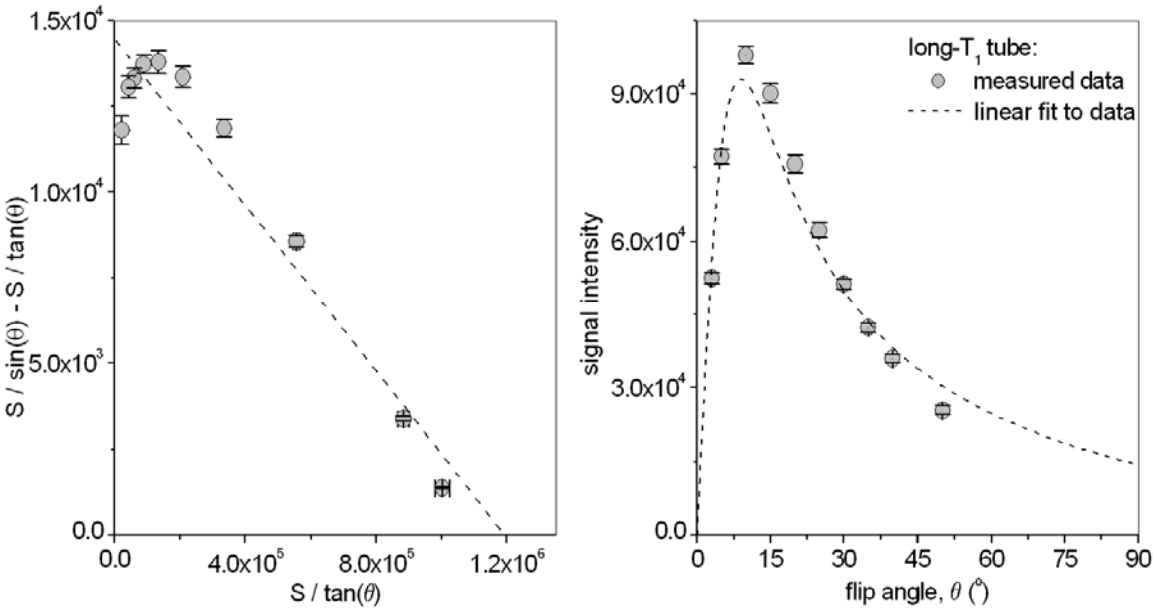

Figure 4.7 *Linear fit, (a) visualized on top of alternative linearization, and (b) on top of S versus θ.*

To obtain a better fit, we would like to use a criterion to exclude certain flip angles from the T_1-mapping procedure. Such a criterion has been defined by Deoni et al. (2003). Although they defined their criterion to select two optimal flip angles for a dual-flip angle approach, we found that it also serves the purpose of selecting a range of flip angles to be included in the fitting procedure. We will refer to this range as the Deoni range. The criterion is based on balancing the distance from the midpoint (peak signal) of the linearized data with the measurement uncertainty. A large distance between the outer angles provides a better fit than a short distance, however, the uncertainty in the measurements increases moving away from the midpoint. For the equations defining this tradeoff we refer to the original paper. Interestingly, we find not only a larger measurement uncertainty moving away from the midpoint, but also a bias from model-behavior. The Deoni criterion usually adequately excludes such biased samples.

The proposed flip angle selection, as described in Deoni et al. 2003, depends on the repetition time and T_1. Since T_1 is the parameter we are fitting, we apply the flip angle selection in an iterative way. We first use all the flip angles to fit T_1. Using this T_1 value we estimate the Deoni range. Subsequently, we repeat the fitting procedure, this

time excluding flip angles outside the Deoni range. In case the found T_1 is very different from the initial T_1, repetition(s) of the fitting cycle may be necessary to find a stable solution. In Figure 4.8 we demonstrate this selection procedure for the same example as in Fig. 4.7. For this example the Deoni range is defined by $\theta_1 = 3.9°, \theta_2 = 22.2°$. In Fig. 4.8(a) this range is marked by the black bars. In both (a) and (b) the dashed line shows the linear fit using all data points, whereas the solid line shows the linear fit only using the data points within the Deoni range. By excluding the flip angles outside the Deoni range, the T_1 estimate for the long-T_1 phantom tube (linearized) changes from 2053 ms to 1659 ms, which is an improvement if we compare these T_1 values to the gold standard T_1 value of 1392 ms. The new Deoni range is defined by $\theta_1 = 4.1°, \theta_2 = 23.6°$. This new range does not lead to a different inclusion of flip angle data, so another iteration is not needed.

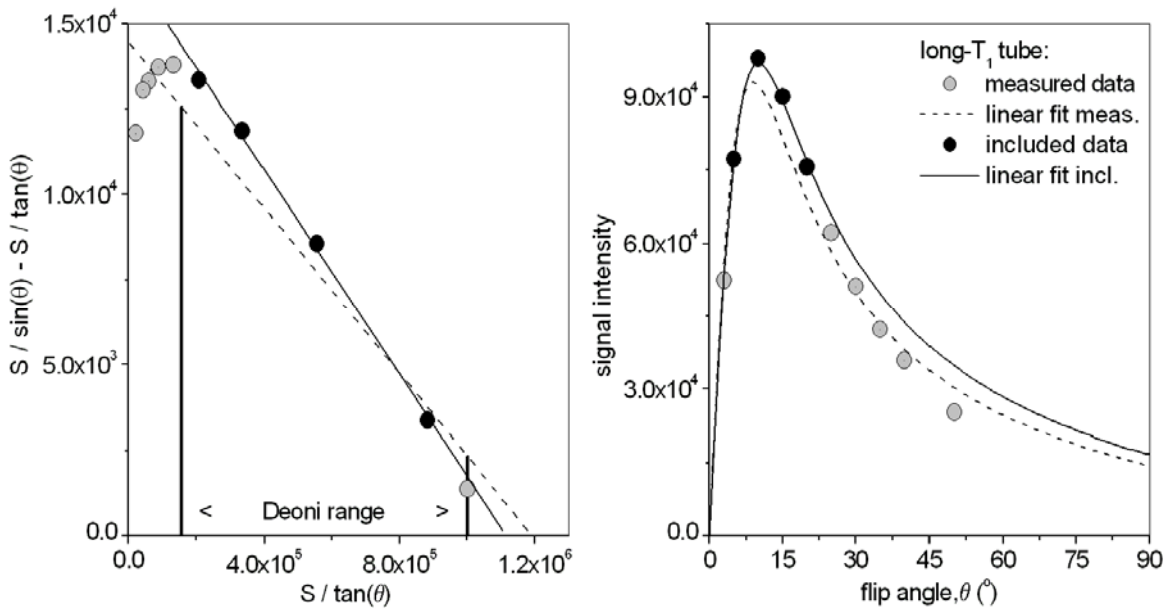

Figure 4.8 *(a) Alternative linearization, the dashed line represents the linear fit using all data points, the solid line using only the data points within the Deoni range (as marked with vertical bars). (b) The same fits as in (a), drawn as S versus θ.*

Looking at the dual-flip angle protocol applied in Liney et al. 1999 as mentioned in the introduction, we can verify that with the applied repetition time of 10.9 ms and angles of 6° and 35°, it is indeed not possible to cover a range from 125 ms (Deoni angles: 9.9° and 53.2°) to 900 ms (Deoni angles: 3.7° and 21.2°). It is in fact surprising that they obtained fairly accurate estimates for a T_1 as short as 125 ms. This also illustrates that with only two angles, the range of estimable T_1 values is limited.

Signal-versus-angle curve fitting

We could have performed a linear fit with data from just two flip angle acquisitions – i.e. with a dual-flip angle approach – instead of ten acquisitions (or, in case of patient data 6 – 7 acquisitions). So, what would be a reason to use more than two flip angles? The most important one would be to cover the full native-T_1 range in the breast. Using the Deoni method, we can calculate that with a repetition time of 25 ms, the two optimal flip angles to measure the T_1 in fatty tissue, which is approximately 260 ms (Stark and Bradley 1999), would be 10.4° and 55.5°. Tumors, on the other hand, can have T_1 values as high as 1300 ms (Bottomley et al. 1987). In that case, we would need flip angles of 4.7° and 26.5°. To cover the whole 260 ms – 1300 ms T_1 range, we would need flip angles spanning from 4.7° to 55.5°. Another reason is that due to linearization of the spoiled gradient echo model, we have the measured signal – and its uncertainty – present on both axes. This makes a calculation of the uncertainty on the estimated parameters complex; even more so, because the properties of the noise are affected by the transformation to a linear function. That is why a linear fit does not give the same result as a signal-versus-angle fit. We therefore do not provide standard deviations for T_1 values estimated with a linear fit. When we fit the measured signal-versus-angle data (according to the χ^2-criterion, Eq. 4.2, because of heteroscedasticity), the measurement noise is only present on the y-axis and we can provide a measure of estimate uncertainty (Eq. 4.3).

Using the fitted T_1 and M_0 of the alternative linearization as starting values for this signal-versus-angle fit, we can often slightly improve the fit to the data; i.e. the root-mean-square deviation between the fitted curve and the measured data (signal versus angle) decreases. The signal-versus-angle fit only performs well with more than two data points, and well-selected starting values. For the Eurospin example tube (T_1 = 1392 ms) we then find a T_1 of 1659 ± 30 ms (Deoni range applied). For voxel-wise T_1 estimation in the tissue we apply the same fitting routine except for assuming equal (unknown) uncertainty on the measurements. In that case, an estimate of parameter uncertainty can be supplied by estimating σ ($\sigma_i = \sigma$) in Eq. 4.2 from the residuals via

$$\sigma^2 = \frac{\sum_{i=1}^{N}(S_{measured} - S_{modeled})^2}{N-p}, \qquad [4.7]$$

in which N is the number of samples and p the number of free parameters. Subsequently, Eq. 4.3 can be applied and the parameter uncertainty estimate is obtained.

Additional scans for quantification in practice

In practice, it may be hard to cover a flip angle range from 4.7° to 55.5° (corresponding to a repetition time of 25 ms, as described above). It is a large range and, in our experience, large ($\theta > 40°$) and small ($\theta < 3°$) flip angles are difficult to

achieve in practice. Therefore, a repetition time of 25 ms appears as too long. A repetition time of 5 ms, which is frequently used in practice because a short repetition time reduces scan time, appears too short; in that case the flip angle range would be 2.1 – 26.5°, requiring a very small flip angle. For patient scanning we therefore decided to use a repetition time of 10 ms, which corresponds to a flip angle range of 3.0 – 36.8°. The full additional sequence description is then as follows: 3D fast spoiled gradient echo, repetition time / echo time = 10/2.0 ms, θ = 2.5, 5, 10, 15, 20, 25, 30°, NA = 1, acquisition matrix = 376 x 375, pixel spacing = 0.98 mm x 0.98 mm, thickness = 1 mm, spacing = 1 mm. The added value of increasing the repetition time from 5 ms to 10 ms is also an increased signal-to-noise ratio (SNR), as well as a more accurate representation of very long T_1 components. Note that the volunteers were scanned with a repetition time of 5 ms (older data).

Use of reference phantom: flip angle correction factor

The advantage of scanning a reference phantom concurrently with the patient is that we can verify if the variable flip angle T_1-mapping approach produces accurate T_1 values, and – if this is not the case – apply a correction. The main source of error leading to an experimental departure from the theoretical spoiled gradient echo model is due to a non-uniform distribution of flip angles (Brookes et al. 1996). Possible causes are deviations in the flip angle calibration, non-linearity of the RF-amplifier / incomplete RF-spoiling, and imperfect flip angle profiles (Liney et al. 1999, Parker et al. 1997). Especially in 2D acquisitions the flip angle can show significant within-slice variation, which results in location-dependent deviations. In this study we used 3D acquisitions, since this is also the trend in clinical practice. As a first-order flip-angle calibration we propose to apply a single per-slice correction factor to the flip angles. We grant that, even though the acquisitions are in 3D, this leaves some within-slice variation as a potential source of error.

In the signal-versus-angle relationship the Ernst angle (θ_E) defines the position of the peak, as the spoiled gradient echo signal reaches it maximum at

$$\cos\theta_E = e^{-TR/T_1} \rightarrow \theta_E = \cos^{-1} e^{-TR/T_1}. \qquad [4.8]$$

The position of the peak dominantly determines T_1. We therefore need to apply a correction factor to the flip angles that shifts the peak to the right position; i.e. to the position that results in the T_1 estimates that we expect to find in the phantom compartments (gold standard T_1 values from IR experiment). We assume that the correction factor A_l that is applied to flip angles θ_i, with $i = 1, \ldots, N$, depends on position l. Knowing the true T_1 at that position, $T_{1t,l}$, gives the true Ernst angle $\theta_{Et,l}$. We can then use the ratio of the true Ernst angle and the measured Ernst angle to obtain the correction factor

$$A_l = \frac{\theta_{Et,l}}{\theta_{E,l}} = \frac{\cos^{-1} e^{-TR/T_{1t,l}}}{\cos^{-1} e^{-TR/T_{1,l}}}, \qquad [4.9]$$

which we apply to all nominal flip angles $\theta_1 \ldots \theta_N$ to obtain the effective flip angles.

To attain an approximate per-slice correction factor in the tissue, we assume that the correction that holds for position l, holds for a larger region than the confined region of the phantom compartments and can therefore be applied to the signal-versus-angle curves extracted from the breast tissue as well. In case the calculated correction factors display a consistent pattern across phantom compartments (in vertical direction 6 samples, in horizontal direction 2 x 2 samples, see axial scan in Fig. 4.4) we could potentially model the effective flip angle profile (such interpolation could also be applied to the gross B1-field, if available). In this study, we will use a first-order-calibration making use of the mean correction factor found on the inner side of the breasts (more homogeneous than towards the edges of the field of view). The approach presented here is similar to the one proposed by Yang et al. (2006).

4.3.3 Clinical T_{10} quantification: empirical calibration

An alternative to the variable flip angle approach presented above is to calibrate T_1 empirically using the signal intensities measured in the phantom compartments as reference. We will follow the approach as presented in Medved et al. 2004; except that here we will use the phantom as a reference instead of a healthy tissue. We call this approach empirical because the underlying model is very basic. It is assumed that in approximation:

$$S \cdot T_1 \approx constant, \qquad [4.10]$$

therefore it holds

$$\frac{S_{tissue}}{S_{ref}} \approx \frac{T_{1,ref}}{T_{1,tissue}}. \qquad [4.11]$$

As a consequence of using the phantom we do not have to assume an approximate T_1 value for the reference tissue; instead, we use the known T_1 values of the phantom compartments to estimate the constant factor in Eq. 4.10. Moreover, as the phantom contains a range of T_1 values, it can first be tested if this equation holds for the acquisition under study.

In a test experiment this approach was compared to the use of variable flip angle T_1-mapping (Litjens et al. 2009). The Eurospin phantom was scanned (T_1 range: 281 ms – 1384 ms) with the following settings: (i) 3D spoiled gradient echo, repetition time / echo time = 25/1.1 ms, θ = 3, 5, 10, 15, 20, 25, 30, 35, 40°, NA = 4, acquisition matrix = 128 x 129, pixel spacing = 2.60 mm x 2.60 mm, thickness = 4 mm, spacing 4 mm; and (ii) 3D spoiled gradient echo, repetition time / echo time = 25/1.1 ms, θ = 40°, other

settings same as in (i). Variable flip angle T_1-estimation was applied to (i), whereas the reference approach was applied to (ii). In the latter approach, signal intensities measured in 9 tubes were used to estimate T_1 in the remaining tube. With the variable flip angle approach, the average error in T_1 was 5.7% with a standard deviation of 3.8%. With the reference approach the average error was 8.5% with a standard deviation of 6.1%. A two-sided Student's t-test could not demonstrate a statistically significant difference in the performance of the two methods (p = 0.52, N = 10).

Note that in this test experiment there was no difference in proton density between the 'tissue of interest' and the reference material. Therefore, in practice, a proton density correction factor should be obtained before application of this empirical T_1 quantification method. Such a PD factor could be estimated from a single low-angle spoiled gradient echo acquisition, as discussed next.

We can conclude that, provided proper PD-correction, empirical calibration according to Equation 4.10 can be used in practice.

4.4 Methods: tissue proton density mapping

A spoiled gradient echo acquisition acquired with a low flip angle exhibits little T_1-weighting because $cos\,\theta$ in Eq. 4.4 approaches a value of 1, reducing the equation to (Walker-Samuel et al. 2007a):

$$S \approx M_0 \cdot \sin\theta. \qquad [4.12]$$

As all phantom compartments contain the same aqueous solution, in theory they display the same signal intensity in a PD-weighted scan, under the assumption that the presence of the contrast agent does not alter proton density (Parker et al. 1997). With the calibration phantom present in the image we can use the ratio of the signal intensities of the phantom and the tissue to obtain an estimate of relative proton density in the tissue:

$$\frac{S_{tissue}}{S_{phantom}} = \frac{Scanner\ gain \cdot PD_{tissue} \cdot \sin\theta}{Scanner\ gain \cdot PD_{phantom} \cdot \sin\theta} = \frac{PD_{tissue}}{PD_{phantom}}, \qquad [4.13]$$

If we assume the proton density in the phantom compartments to equal that of pure water (100%), we have an absolute measure of proton density in the tissue. We can thereby map proton density with the use of a single low-flip-angle acquisition. Note that the obtained proton density represents the *apparent* proton density, as it is dependent of the applied acquisition sequence.

4.5 Methods: conversion to contrast agent concentration

A common model-based approach to convert signal intensity to contrast agent concentration is via T_1 in combination with Equation 1.1, repeated over here

$$\Delta R_1(t) = R_1(t) - R_{10} = r_1 \cdot C(t), \qquad [4.14]$$

in which r_1 (mM^{-1} s^{-1}) is the longitudinal relaxivity and C (mM) the contrast agent concentration. For this approach it is needed to obtain a precontrast T_1 map ($R_{10} = 1/T_{10}$) for every patient with methods such as discussed in Sections 4.3.2 and 4.3.3. The dynamic $T_1(t)$ can then be derived from the measured signal $S(t)$ under assumption of the spoiled gradient echo model (Haacke et al. 2007):

$$T_1(t) = \frac{-TR}{ln\left(\frac{x-y}{x-y\cdot\cos\theta}\right)}, \qquad [4.15]$$

with $y = S(t)/S_0$ and $x = \frac{1-e^{-TR/T_{10}}\cos\theta}{1-e^{-TR/T_{10}}}$.

Another model-based approach is to use the ratio of the T_1-weighted dynamic series (θ_1) with a PD-weighted precontrast image volume (θ_2). As pointed out in Section 4.4, the spoiled gradient echo signal is PD-weighted in case of a low flip angle. Using the approximation given in Eq. 4.12, this ratio is described by (Walker-Samuel et al. 2007a):

$$R = \frac{S_{\theta_1}}{S_{\theta_2}} = \frac{\sin\theta_1\left(1-e^{-TR/T_1(t)}\right)}{\sin\theta_2\left(1-\cos\theta_1\cdot e^{-TR/T_1(t)}\right)}. \qquad [4.16]$$

As this ratio is solely weighted by T_1 it can be used to derive contrast agent concentration via Eq. 4.14, providing both T_{10} (use of precontrast T_1 -weighted dynamics) and $T_1(t)$:

$$T_1(t) = \frac{-TR}{ln\left(\frac{\sin\theta_1 - R\cdot\sin\theta_2}{\sin\theta_1 - R\cdot\sin\theta_2\cos\theta_1}\right)}, \qquad [4.17]$$

Note that this method thereby also provides a model-based T_{10}-mapping approach. In this study, we did not further investigate this method as we picked the more popular model-based approach, i.e. the variable flip angle method (Section 4.3.2).

Both of the above methods are under the assumption of the spoiled gradient echo model, or in any case a known signal model. However, current T_1-weighted fast dynamic protocols can often not be described with the spoiled gradient echo model. In our case, dynamic data is acquired with a T_1-turbo field echo sequence (eTHRIVE, Philips Healthcare, Best, The Netherlands). This sequence enables time-efficient fat-suppression but cannot be easily described with an equation such as Equation 4.4 because it is a transient (non-steady-state) acquisition. In addition, even if acquisitions are spoiled-gradient-echo-based, there can be a mismatch in practice due to advanced scan and filtering techniques. For this reason, we did not pursue calculation of concentration images under assumption of the spoiled gradient echo model. Therefore, the bottom part of the left branch in Figure 4.1 displays dashed arrows.

In case of no applicable signal model, the use of a reference phantom offers a practical solution: we can calibrate tissue T_1 by making use of the signal intensities measured in the phantom compartments. In the same way as was explained in Section

4.3.3, under assumption of Eq. 4.10, both the pre- and postcontrast $T_1(t)$ can be derived thereby providing a way to quantify the contrast agent concentration (Eq. 4.14):

$$C(t) = \frac{PD_{phantom}}{PD_{tissue}} \cdot \frac{1}{constant \cdot r_1}\left(S_{tissue}(t) - S_{tissue}(0)\right), \qquad [4.18]$$

in which the constant is derived from the signal intensities measured in the phantom compartments. The proton density ratio is estimated from a low-flip angle image volume.

In brief, for quantification of contrast agent concentration in a clinical setting we discussed two main pathways (see Figure 4.1): one model-based pathway requiring several additional scans with different flip angles (~ N = 6, acquired in ~ 7 min for 15 slices); the other making use of the reference phantom to empirically estimate the calibration factor between T_1 and signal intensity, requiring one additional scan with a low flip angle (< 1 min for 15 slices).

4.6 Results: T_{10}-mapping

4.6.1 Gold standard T_{10} quantification: phantom characterization

This experiment was performed to determine gold standard T_1 values for the phantom compartments, as described in Section 4.3.1. The acquisition settings were: (i) repetition time / echo time = 6000/10 ms, inversion time = 50, 100, 200, 400, 800, 1600, 2400, 3200, 4000, 5000 ms, NA = 1, acquisition matrix = 360 x 352, pixel spacing = 0.70 mm x 0.70 mm, thickness = 3 mm, spacing = 3 mm; and (ii) repetition time / echo time = 5000/28 ms, inversion time = 50, 100, 200, 400, 800, 1500, 2500, 3500, 4500 ms, NA = 1, acquisition matrix = 364 x 363, pixel spacing = 0.71 mm x 0.71 mm, thickness = 2 mm, spacing = 2 mm. The former was used to characterize phantom A, the latter to characterize phantoms B1 and B2.

Fitting of the variable inversion time (TI) turbo spin-echo (TSE) acquisitions resulted in the phantom T_1 estimates reported in Table 4.2. For these data, the empirically determined cut-off for inclusion of 'tail' points lies at 15.5% of M_0/s. We determined this value by fitting the curves both with and without these 'tail' points and inspecting the effect on the estimate of T_1 and on its uncertainty. Addition of data points beyond this cut-off did not affect T_1 but increased the uncertainty.

Table 4.2 *Gold standard T_1values in the phantom compartments estimated from TSE IR data.*

Compartment (mM)	Phantom A T_1 (ms)	Phantom B1 T_1 (ms)	Phantom B2 T_1 (ms)
0	2519 ± 40	2487 ± 79	2247 ± 53
0.1	1298 ± 18	1194 ± 24	1235 ± 23
0.2	847 ± 12	834 ± 16	818 ± 19
0.3	648 ± 8	565 ± 11	619 ± 13
0.4	497 ± 7	488 ± 8	487 ± 8
0.5	423 ± 5	392 ± 8	406 ± 6

Assuming a relaxivity value of 4.3 mM^{-1} s^{-1} (Rohrer et al. 2005), we can simulate the expected T_1 as a function of contrast agent concentration in the phantom compartments, using the first estimate (0 mM) as the baseline. For all three sets of phantom compartments, we plotted both the measured as well as the expected T_1 values as a function of contrast agent concentration in Figure 4.9. All measured T_1 values are in close agreement with each other and with the theoretically expected T_1 values. We conclude that we can use these estimates as the gold standard.

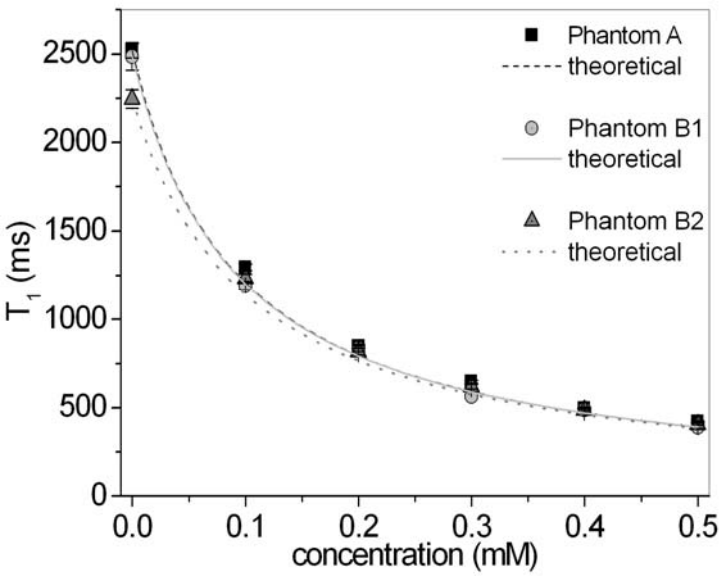

Figure 4.9 *Measured (symbols) as well as theoretically expected (lines) T_1 values as afunction of compartment contrast agent concentration. All measured T_1 values are in close agreement with the theoretically expected values.*

4.6.2 Clinical T_{10} quantification: variable flip angle approach and flip angle correction

Proof of principle

To test if the proposed correction to the flip angles – calibrated with use of the reference phantom – leads to more accurate estimation of T_1 in the tissue, we performed an experiment with test objects representing the breasts. These test objects were part of the above-described TSE IR experiment and therefore their T_1 values are known. In Figure 4.10 we show the setup. The image is acquired with a repetition time of 5 ms and a flip angle of 10°. The tubes are ordered from top to bottom, from low to high concentration (0, 0.1, 0.2, 0.3, 0.4, 0.5 mM). At the right-breast position (left in image) we placed a bottle of non-sparkling drinking water (long T_1), on the other side a standard phantom bottle (short T_1). From the IR recovery experiment we obtained respective gold standard T_1 values of: 1913 ± 42 ms and 334 ± 6 ms.

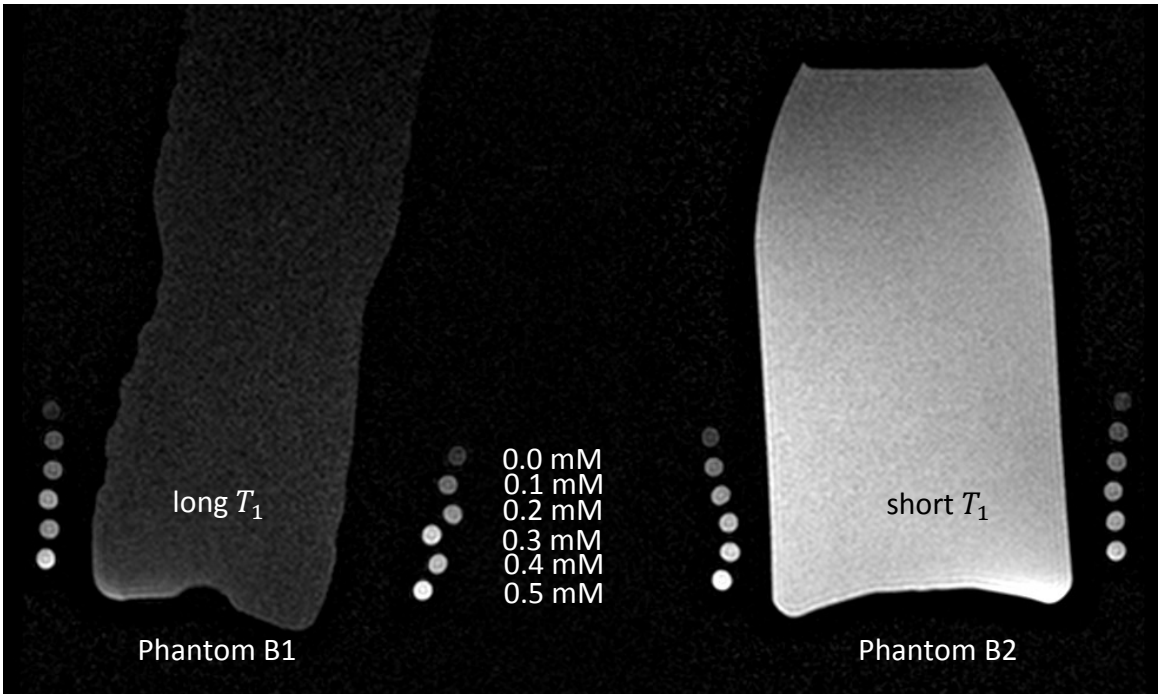

Figure 4.10 *Test experiment with two test objects. The image was acquired with a repetition time of 5 ms and a flip angle of 10°.*

We performed two variable flip angle experiments; one with a repetition time of 5 ms, and one with a repetition time of 25 ms. We did this to find out how much T_1 estimation is influenced by the repetition time, and to see if such a dependency can be corrected for via a correction to the flip angles. The acquisition settings were: (i) repetition time / echo time = 5/1.7 ms, θ = 3, 5, 10, 15, 20, 30°, NA = 3, acquisition matrix = 364 x 365, pixel spacing = 0.71 mm x 0.71 mm, thickness = 2 mm, spacing = 2

mm; and (ii) repetition time / echo time = 25/1.9 ms, θ = 5, 10, 15, 20, 30, 40, 55°, NA = 1, other settings as in (i).

The T_1 estimates in the phantom compartments as well as in the test objects are listed in Table 4.3. We can remark three things: (i) the T_1 estimates obtained with a repetition time of 25 ms are usually higher than those obtained with a repetition time of 5 ms, (ii) for the short-T_1 object this difference is more than a factor of two, and (iii) for the long-T_1 object we obtain an unrealistically large T_1 of about 10 s with a repetition time of 25 ms.

Table 4.3 *Variable flip angle T_1 estimates in phantom compartments and test objects.*

	Repetition time = 5 ms		**Repetition time = 25 ms**	
Compartment (mM)	**Phantom B1 T_1 (ms)**	**Phantom B2 T_1 (ms)**	**Phantom B1 T_1 (ms)**	**Phantom B2 T_1 (ms)**
0	1643 ± 197	2321 ± 259	1879 ± 90	2174 ± 161
0.1	1018 ± 106	932 ± 65	1000 ± 75	1035 ± 69
0.2	593 ± 43	574 ± 42	791 ± 42	793 ± 42
0.3	449 ± 21	433 ± 20	564 ± 27	556 ± 28
0.4	369 ± 22	371 ± 16	447 ± 24	480 ± 23
0.5	328 ± 17	318 ± 17	413 ± 20	391 ± 22
Long-T_1 test object	1776 ± 115	-	10211 ± 563	-
Short-T_1 test object	-	271 ± 7	-	630 ± 12

Looking at the measured curves in the test objects (Figure 4.11), we can see that with a repetition time of 5 ms both objects display a pattern close to model behavior, except for the large-flip-angle measurements of the long-T_1 object. Using the Deoni flip angle range, we can obtain a reasonable fit of the spoiled gradient echo model for both objects. With a repetition time of 25 ms we see a very different pattern; the linear display shows two nonlinear curves. In addition, in the signal-versus-angle display, the measurements for the long-T_1 object appear to start post-peak. These effects result in erroneous fits, even when the flip angles are limited to the Deoni range.

As the true T_1 values of the test objects are, respectively, 1913 ± 42 ms and 334 ± 6 ms (as measured with TSE IR), the Deoni range corresponding to a repetition time of 5 ms equals 1.7° – 23.5°, and the range corresponding to a repetition time of 25 ms equals 3.9° – 49.8°. In both series smaller flip angles could have been included (5 ms: started at 3°, 25 ms: started at 5°), but both acquired series should have been suitable to at least approximate the long and short T_1. It is the unexpected non-model behavior that

hinders us from fitting the data acquired with a repetition time of 25 ms. As this behavior is especially apparent for large flip angles, this may indicate that the larger flip angle pulses are inadequate.

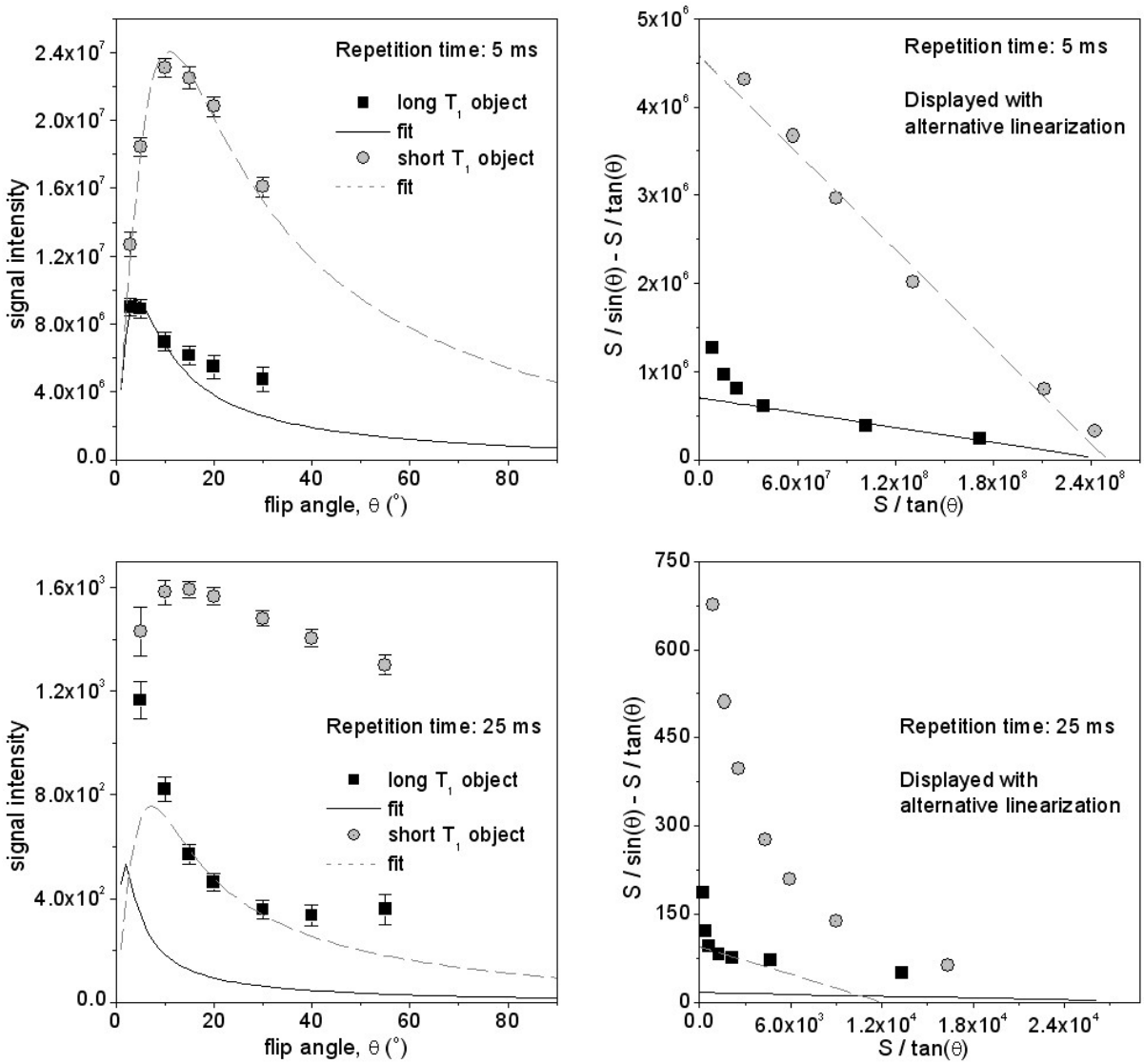

Figure 4.11 *Variable flip angle measurements (symbols) for long-T_1 (left in Figure 4.10) and short-T_1 (right in Figure 4.10) test objects. The fits (lines) are performed making use of the Deoni flip angle range. Top: repetition time of 5 ms, bottom: repetition time of 25 ms. With a repetition time of 25 ms the measurements show a large deviation from model behavior (model behavior would produce a straight line in the right-bottom plot). Here the fitting routine fails.*

In this "Proof of principle" section, the aim is to find out if a flip angle correction calibrated with the use of the reference phantom results in improved T_1 estimates. Because we did not find valid T_1 estimates for the data acquired with a repetition time

of 25 ms, we applied the correction only to the data acquired with a repetition time of 5 ms. We were not able to verify if the repetition-time-dependent bias in T_1 estimates (see Table 4.3, longer repetition time results in higher T_1 estimates) can be corrected for via a correction of the flip angles.

In Figure 4.12 we plotted the variable flip angle T_1 estimates (repetition time: 5 ms) versus the gold standard T_1 values of the phantom compartments. We can see that on average the estimates are too low.

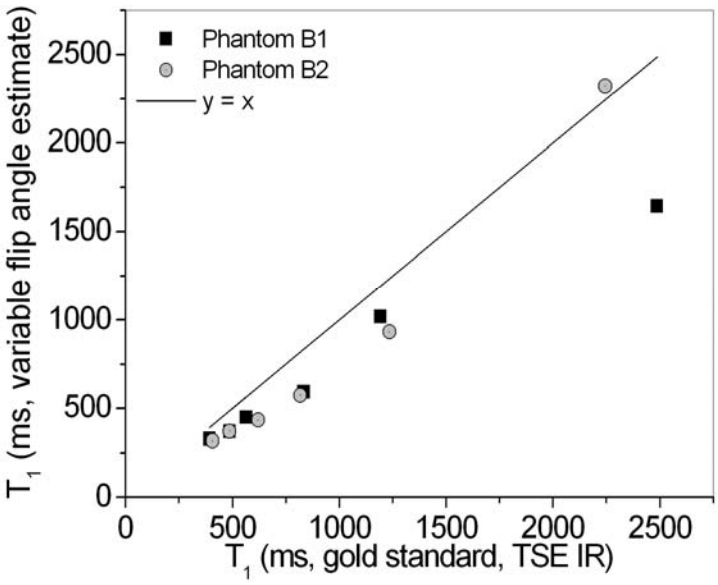

Figure 4.12 *Variable flip angle T_1 estimates (repetition time: 5 ms) versus the gold standard T_1 values. In general the estimated are biased towards lower values.*

We calculated the flip angle correction factor according to Equation 4.9 for each phantom compartment and we obtained the factors as displayed in Table 4.4. The factors are all fairly similar except for a value of 1.02 for the 0 mM compartment of phantom B2. As the T_1 of the 0 mM compartment is hard to estimate because it is relatively long and displays low SNR, this could be due to an error in the measurement / fitting of the corresponding curve. Applying the mean correction factor to the flip angles and re-fitting the measurements of the test objects (using the Deoni range, this time applied to the effective flip angles instead of the nominal flip angles), resulted in a T_1 estimate of 2295 ± 148 ms for the long-T_1 object and of 343 ± 8 ms for the short-T_1 object. As the true values are, 1913 ± 42 ms and 334 ± 6 ms, respectively, and the values before correction were 1776 ± 115 ms and 271 ± 7 ms, the correction introduces a larger deviation from the standard for the long-T_1 object (from 7.2% underestimation to 19.9% overestimation) and a smaller deviation from the standard for the short-T_1 object (from 18.8% underestimation to 2.7% overestimation). Unfortunately, these results are rather

inconclusive and further testing with the use of known test objects is required. Preferably, an intermediate repetition time would be used (e.g. of 10 ms as suggested in Section 4.3.2), and objects defining the range from T_1 ~260 ms to ~1300 ms to mimic breast tissue. However, please note that in determining contrast agent concentration (Eq. 4.14) the scale of $R_1(t)$ is larger than that of R_{10} for long T_{10}. Therefore a 20% error in a long T_{10} estimate has less effect on the calculated contrast agent concentration than a 20% error in a short T_{10} estimate.

Table 4.4 *Flip angle correction factors calculated for the phantom compartments B1 and B2.*

Compartment (mM)	Correction factor (Phantom B1)	Correction factor (Phantom B2)
0 (top)	0.81	1.02
0.1	0.92	0.87
0.2	0.84	0.84
0.3	0.87	0.84
0.4	0.89	0.87
0.5 (bottom)	0.91	0.89
mean ± standard deviation	0.88 ± 0.04	0.89 ± 0.07

Volunteer scans

By scanning the reference phantom concurrently with a patient / volunteer we can verify if the variable flip angle T_1-mapping approach produces accurate T_1 values in the presence of a patient / volunteer. As the above experiment did not provide convincing evidence to advocate the use of the proposed flip angle correction method (introduced in Section 4.3.2), we will limit ourselves to making a comparison between the estimated T_1 values in the phantom compartments – using a variable flip angle method – and the true values (IR gold standard).

Four volunteers (age 24 – 52, no contrast agent injected) were scanned with reference phantom A present in the breast coil. The acquisition settings were: 3D fast spoiled gradient echo, repetition time / echo time = 5.0/1.5 ms, θ = 3, 5, 10, 15, 20, 30°, NA = 3, acquisition matrix = 268 x 267, pixel spacing = 1.30 mm x 1.30 mm, thickness = 1.5 mm, spacing = 1.5 mm. In Figure 4.13 we show example images from the spoiled gradient echo variable flip angle series acquired with an angle of 10°. For volunteers (a) and (c) the compartments were arranged from low to high concentration in the chest-to-nipple direction. In order to be able to distinguish location-dependent effects from concentration-dependent effects, the arrangement was reversed for volunteers (b) and

(d). We can see in the images that the 0 mM compartment has a low SNR and that the tube diameter was fairly small.

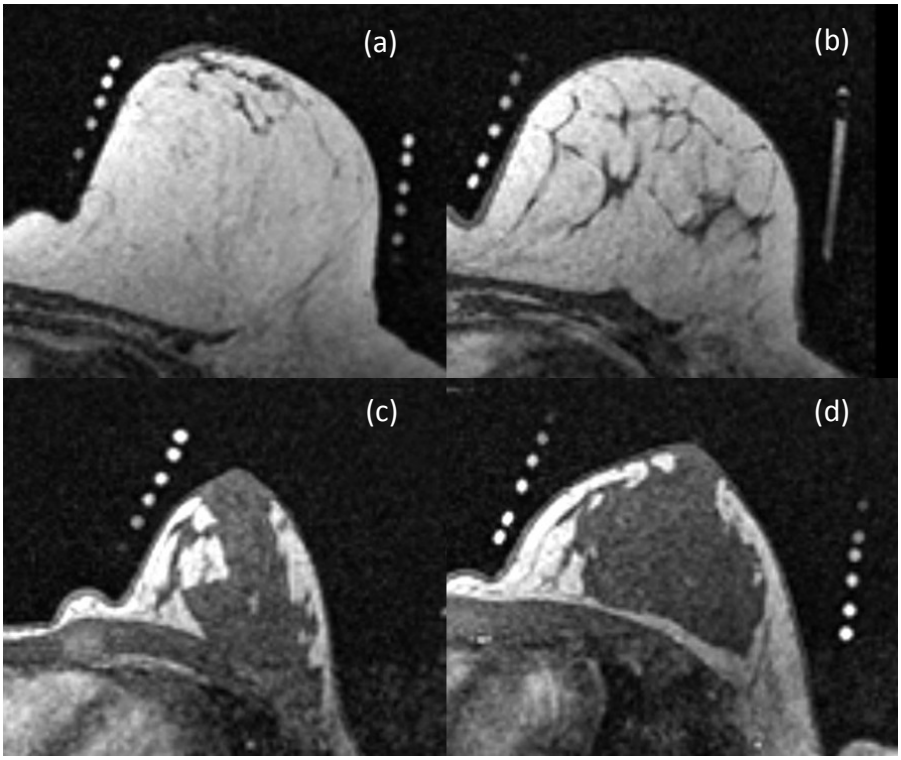

Figure 4.13 *Example images from variable flip angle series, θ = 10°. Volunteers (a) and (c) have the tubes arranged from low to high concentration in the chest-to-nipple direction, while for volunteers (b) and (d) the arrangement is reversed.*

Fitting the signal-versus-angle curves measured in the phantom compartments, we found T_1 estimates as provided in Table 4.5. As the compartments of phantom A were too small to measure the standard deviation of each sample, we fitted the data under the assumption of equal uncertainty on the samples (homoscedasticity), using Eq. 4.7. As the residuals equal zero for a two-point estimate we cannot provide an uncertainty estimate for the T_1 estimates of the 0 mM compartment (Deoni range limited to the two smallest flip angles). We can observe that the variation in found T_1 values between volunteers is rather large. The variation seen in the provided uncertainty estimates is due to the fact that long T_1 values are more difficult to estimate (Haacke et al. 2007), but probably also due to differences in the number of included flip angles (Deoni range).

Table 4.5 *Variable flip angle T_1 estimates in the phantom A compartments as obtained for four volunteers.*

Compartment (mM)	Volunteer (a) T_1 (ms)	Volunteer (b) T_1 (ms)	Volunteer (c) T_1 (ms)	Volunteer (d) T_1 (ms)
0	3097 ± -	2721 ± -	3746 ± -	4077 ± -
0.1	1615 ± 2	1463 ± 24	1599 ± 116	1353 ± 169
0.2	1130 ± 77	1005 ± 25	938 ± 4	845 ± 58
0.3	692 ± 65	795 ± 14	487 ± 5	851 ± 46
0.4	462 ± 7	638 ± 14	486 ± 4	629 ± 17
0.5	635 ± 21	566 ± 8	374 ± 10	478 ± 4

In Figure 4.14 we plotted the variable flip angle T_1 estimates versus the gold standard T_1 values. Considering the scale of the y-axis we again see rather large differences between the volunteers, whereas the trends are similar. This similarity in the trends – volunteers (a) and (c) versus (b) and (d) – indicates that there is no (strong) location-dependent effect. We suspect that the T_1 estimates for the 0 mM compartment are invalid due to insufficient SNR. As such long T_1 values (> 2 s) are not expected in tissue, we can conclude that variable flip angle T_1 estimation works for these data sets, but with limited accuracy; excluding the 0 mM compartment, the mean deviation equals 19%. Interestingly, here we found T_1 values higher than the gold standard values, whereas in the experiment with the test objects we found T_1 values lower than the gold standard. A possible explanation may be the difference in tube size, but it could also be the presence of a volunteer. Loading from the volunteer could have reduced the efficiency with which the receive coil can detect signals and increased spatial variation in B1. There was no difference in scanner or receive coil (Philips 1.5 T Achieva plus 7-channel Invivo phased-array biopsy breast coil).

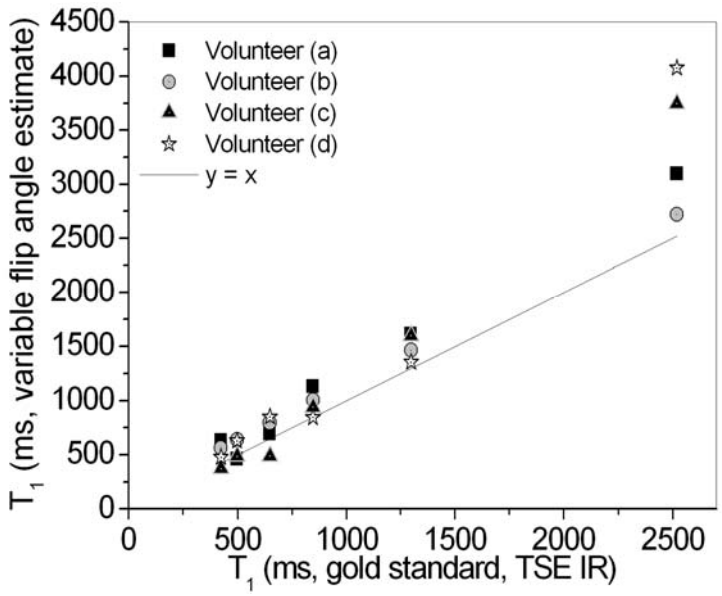

Figure 4.14 *Variable flip angle T_1 estimates for volunteers a-d (phantom A) versus the gold standard values.*

Patient scans

In later experiments we used phantom(s) with larger compartments (B1, B2) and a longer repetition time (10 ms). Both factors should improve variable flip angle T_1 estimation. If we can find accurate estimates in the compartments, the spoiled gradient echo model assumption holds and we can have confidence in the T_1 estimates in the tissue.

Here we present data for two patients: (a) a 55-year old woman and (b) a 50-year old woman. Patient (a) had a small focus in the right breast and had a second-look scan. With this patient only one of the phantom cups was used (B2). Because we could not cover the whole breasts with the variable flip angle series, we did not capture the focus. Patient (b) was scanned in the context of the high-risk screening program. She has a personal history of cancer in the left breast and had had a biopsy in the right breast, that had proved benign. With this patient both phantom cups were in place (B1, B2). The additional scans were as follows: 3D fast spoiled gradient echo, repetition time / echo time = 10/2.0 ms, θ = 2.5, 5, 10, 15, 20, 25, 30°, NA = 1, acquisition matrix = 376 x 375, pixel spacing = 0.98 mm x 0.98 mm, thickness = 1 mm, spacing = 1 mm. These scans were also performed on a Philips 1.5 T Achieva scanner, but with a 16-channel Philips MammoTrak phased-array breast coil, instead of a 7-channel Invivo phased-array biopsy breast coil. The T_1 values as measured on the inner side of both breasts are reported in Table 4.6. In Figure 4.15 we plotted the variable flip angle T_1 estimates against the gold standard. Interestingly, the variable flip angle T_1 estimates are fairly accurate for patient (b), i.e. close to the line $y = x$ (mean deviation with 0 mM compartment excluded:

14%), but for patient (a) we find a deviating trend, i.e. a relatively large overestimation of T_1 (mean deviation with 0 mM compartment excluded: 53%). This may indicate that patient-specific calibration is required (Eliat et al. 2004).

Table 4.6 *Variable flip angle T_1 estimates in the phantom compartments (B1, B2) as obtained for two patients.*

Compartment (mM)	Patient (a), right breast, (Phantom B2) T_1 (ms)	Patient (b), right breast, (Phantom B1) T_1 (ms)	Patient (b), left breast, (Phantom B2) T_1 (ms)
0	5085 ± 746	2589 ± 330	2143 ± 330
0.1	2225 ± 218	1306 ± 96	1283 ± 100
0.2	1170 ± 79	896 ± 61	886 ± 34
0.3	948 ± 58	711 ± 48	686 ± 54
0.4	711 ± 25	558 ± 27	583 ± 37
0.5	578 ± 10	485 ± 21	478 ± 20

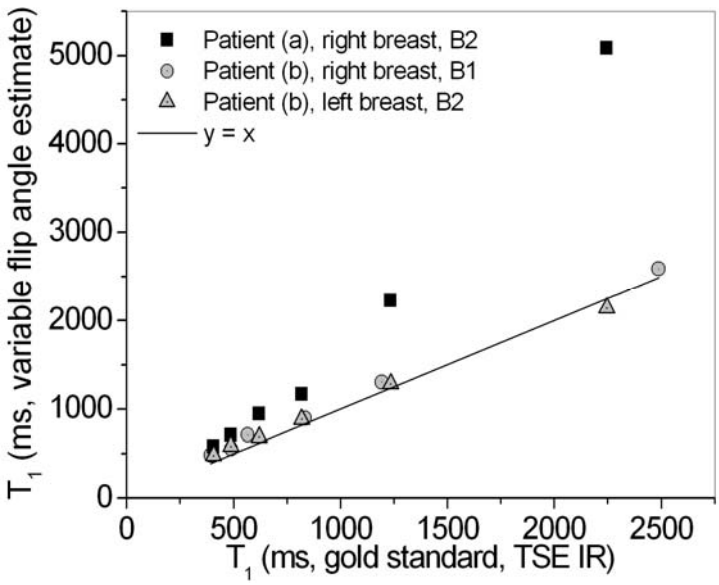

Figure 4.15 *Variable flip angle T_1 estimates for two patients. Patient (a) was scanned in the presence of one phantom (black symbols), patient (b) in the presence of two phantoms (grey symbols).*

For both patients we applied the T_1-mapping procedure to the whole image data. In Figure 4.16 we show the maps for patient (a) with use of all acquired flip angles (top) and with use of the Deoni flip angle range (bottom). Per row the images are the same but we applied different windowing. For patient (b) the same maps are displayed in

Figure 4.17. For patient (a) the breasts appear symmetric (Fig. 4.16), while for patient (b) the right breast displays higher T_1 values than the left breast. Possibly this is due to the earlier-mentioned biopsy she had. If we look at the zoomed-in portion of the breast we see that with the use of selected flip angles (bottom) we obtain a slightly sharper contrast between voxels. In the corresponding histograms we see that the Deoni selection results in a similar width, but shifts the distribution a bit towards lower values. Especially in Figure 4.17 this shift appears a sensible correction, as the T_1 values, fitted with use of all flip angles, are extremely high; i.e. in the range of pure water. As we have extensively inspected the effects of the Deoni flip angle selection with phantom solutions and found it to improve T_1 estimation, we conclude that its use also here improves T_1 mapping. Note that in the tubes we found overestimation of T_1 for patient (a), whereas looking at the tissue it is patient (b) showing very high T_1 values; as mentioned, this could be pathologic.

In the next section, we will derive T_1 maps for these same two patients making use of the empirical approach, as introduced in Section 4.3.3. We will then compare these maps to those presented over here.

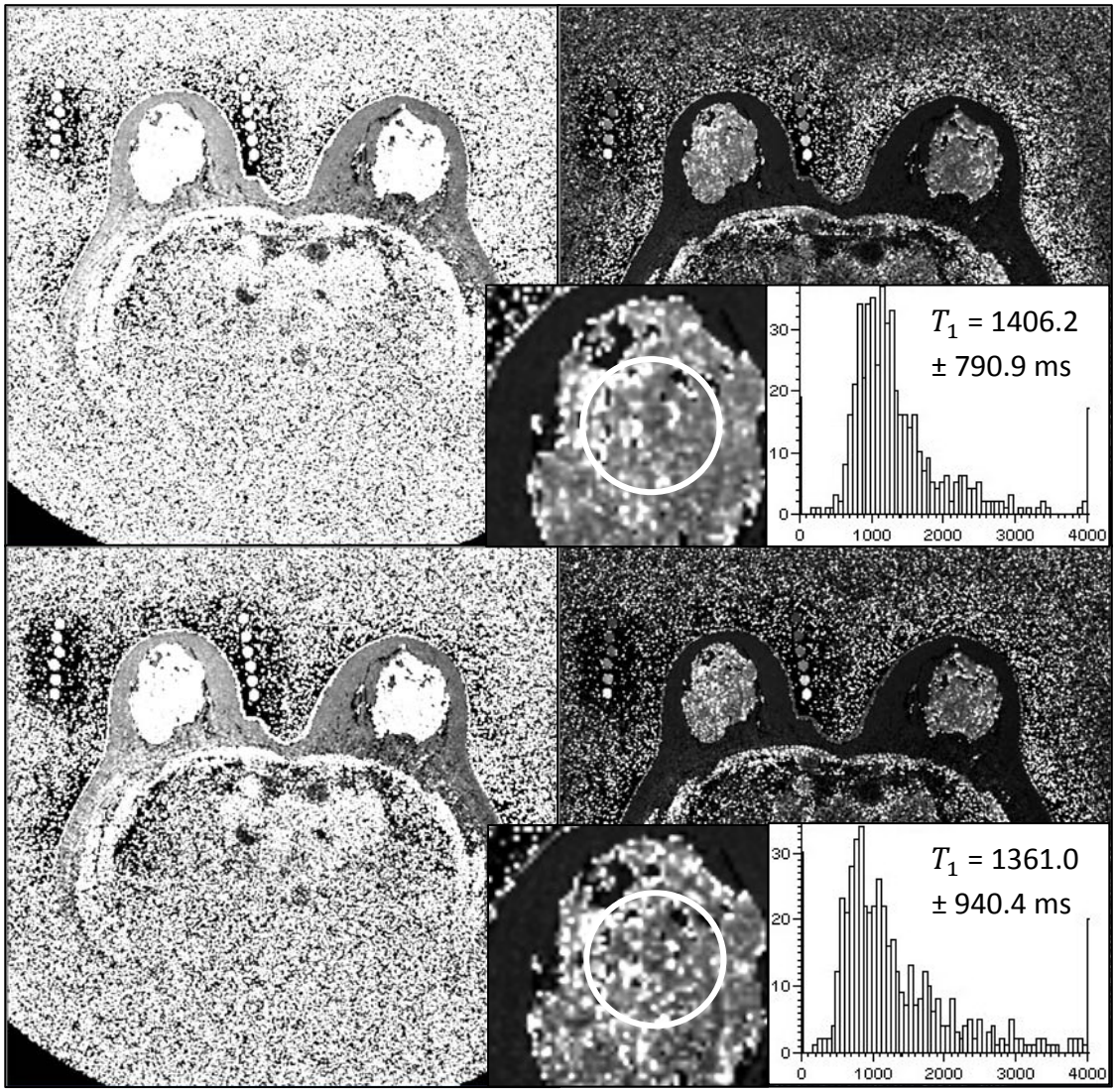

Figure 4.16 *Precontrast variable flip angle T_1 maps for patient (a). Top row: all flip angles are used to fit T_1; the same map is displayed twice with different windowing, on the left the structure in the fatty tissue is emphasized, on the right in parenchymal tissue. Bottom row: Deoni flip angle range is used, windowing is the same as for the top row. The insets show a zoom of healthy parenchyma in the right breast (left in image), as well as a histogram corresponding to the drawn ROI. There is little difference between the methods, except for slightly higher contrast with use of the Deoni selection.*

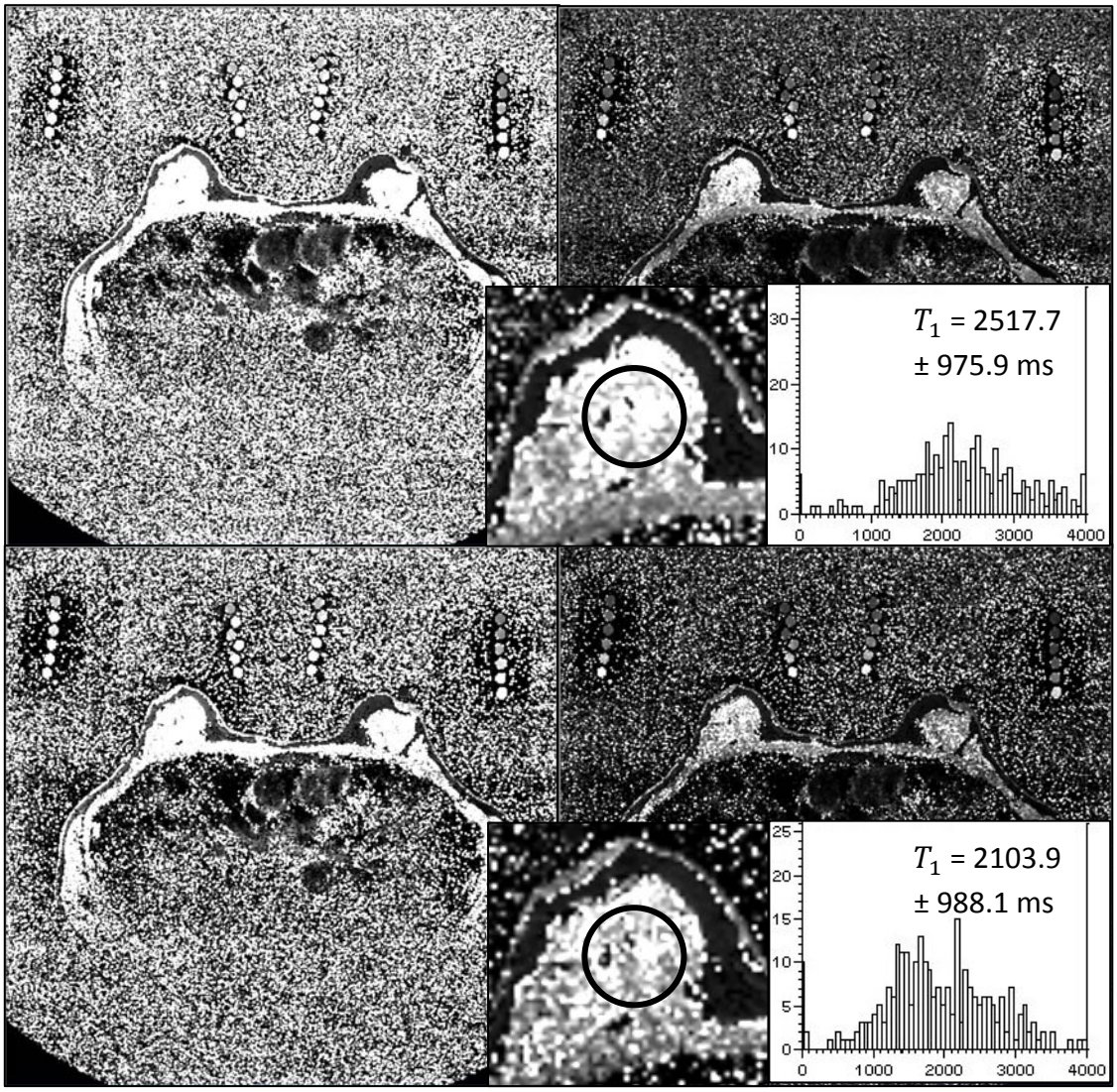

Figure 4.17 *Precontrast variable flip angle T_1 maps for patient (b). Same type of maps as in Figure 4.16. Note that the right breast – that was biopsied – displays a higher T_1 than the left breast; we therefore placed the ROI in this potentially pathologic area. Here the difference between the two methods is more distinct than for patient (a); with the Deoni selection we see more variation in T_1.*

4.6.3 Clinical T_{10} quantification: empirical calibration

Here, we empirically calibrate the relationship between signal intensity and T_1 for the same two patients as in the previous section by making use of the reference phantom. We use a combination of Equations 4.11 and 4.13 to estimate precontrast T_1 in the tissue:

$$T_{1,tissue} = \frac{PD_{tissue}}{PD_{phantom}} \frac{S_{ref} \cdot T_{1,ref}}{S_{tissue}}, \qquad [4.19]$$

in which $PD_{tissue}/PD_{phantom}$ is estimated as a single factor from a low-flip angle acquisition. Its settings were: 3D fast spoiled gradient echo, repetition time / echo time = 10/2.0 ms, θ = 2.5°, NA = 1, acquisition matrix = 376 x 375, pixel spacing = 0.98 mm x 0.98 mm, thickness = 1 mm, spacing = 1 mm (same as in the above patient experiment). The T_1-weighted image that represents a precontrast dynamic was acquired with the same settings except for θ = 20°. In Figure 4.18 we show for both patients the acquired signal versus the contrast agent concentration for both these acquisitions to demonstrate that the low-angle images show little T_1-weighting, whereas the weighting is clearly present in the higher flip angle images. For display purposes we scaled the signals in between 0 and 1 (the PD-weighted images will be shown in the next section). To extract the PD-correction factor ($PD_{tissue}/PD_{phantom}$) from the low-angle image, we used the mean signal in the phantom compartments and a large ROI in one of the breasts. For patients (a) and (b) we found a factor of 0.27 and 0.25, respectively.

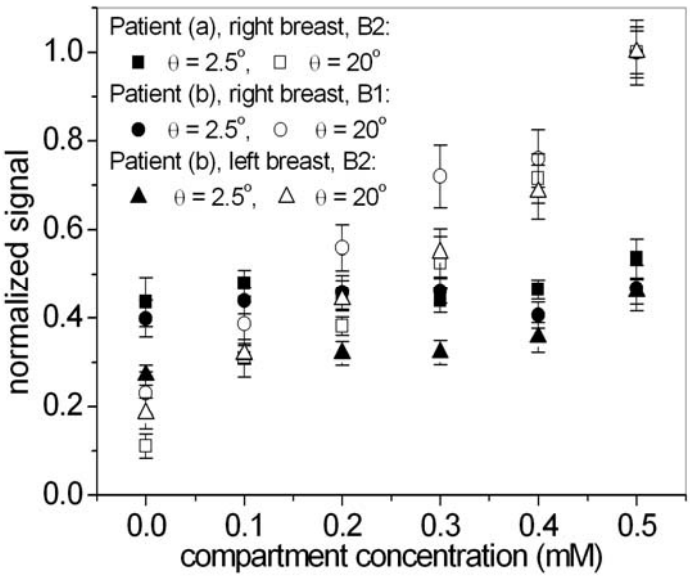

Figure 4.18 *For both patients: low-flip-angle images show litte variation with increasing contrast agent concentration (decreasing T_1), whereas higher flip angle images demonstrate a signal increasing with concentration.*

The main assumption in the proposed empirical calibration of T_1 (Section 4.3.3, Medved et al. 2004) is that we can find a constant that equals $S \cdot T_1$ (Eq. 4.10). In the phantom compartments we found $S \cdot T_1$ to be constant with a standard deviation of 16% (both patients). Deviations did not appear to be a function of T_1. We therefore conclude that Equation 4.19 is applicable.

In Figures 4.19 (patient a) and 4.20 (patient b) we show the obtained T_1 maps. They can be directly compared to Figures 4.16 and 4.17, respectively, as they consider the same patients, the same slices, and are displayed with the same windowing. Comparing the maps obtained for patient (a), we obtain a smoother map with a more narrow distribution and a lower mean value (37% lower compared to Deoni variable flip angle map). For patient (b) we obtain a smoother map as well, but here the T_1 distribution is more similar to the one presented in Fig. 4.17. The narrowing of the distribution can be a sign of less error propagation – the empirical method does not require a fit like the variable flip angle method – but it could also mean a loss of contrast due to the assumption of a constant factor describing $S \cdot T_1$. Note that the distinct asymmetry we saw for patient (b) is no longer present using the empirical calibration.

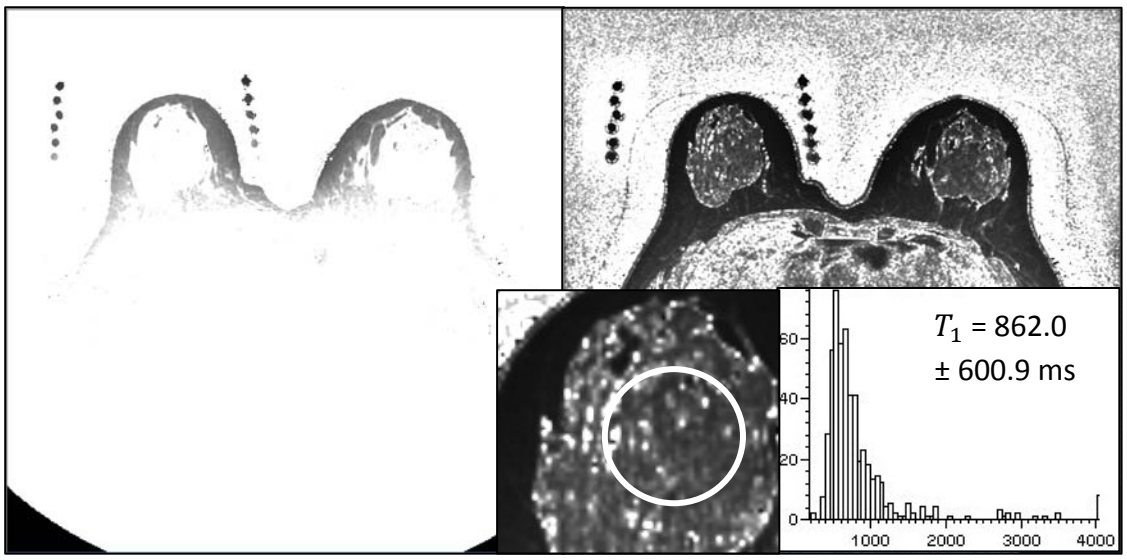

Figure 4.19 *Empirical T_1 map for patient (a). The same map is displayed twice with different windowing, on the left the structure in the fatty tissue is emphasized, on the right in parenchymal tissue. The insets show a zoom of the right breast with the corresponding histogram. The ROI is placed at the same position as in Figure 4.16.*

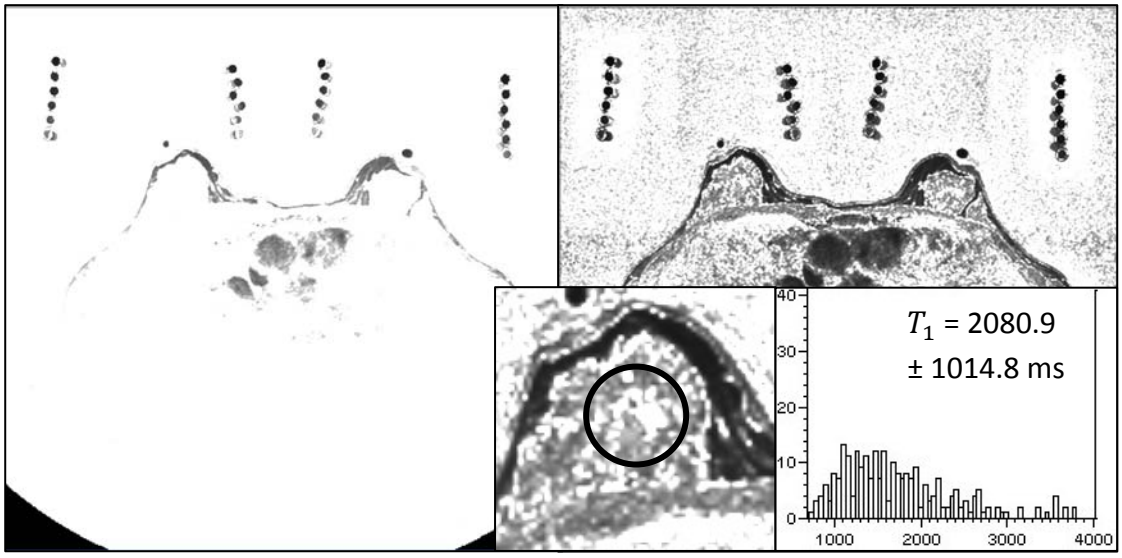

Figure 4.20 *Empirical T_1 map for patient (b). The ROI is placed at the same position as in Figure 4.17.*

As we assumed tissue proton density for the whole image, the signal intensities displayed in the phantom compartments are not representative of their T_1 values. This is because we applied the PD-correction as a single factor, but this could also be done in a voxel-wise manner.

Finally, to enable a comparison of the estimated T_1 values to literature, we listed some references for estimates obtained at 1.5 T in Table 4.7. Looking for instance at the T_1 estimates we obtained for patient (a) in normal parenchyma (focus not present in this slice), with the variable flip angle method the majority of the voxels in the ROI displays a T_1 above 1000 ms, whereas with the empirical approach the majority lies below 1000 ms. In literature T_1 values in normal parenchyma are below 1000 ms (e.g. Merchant et al. 1993 and Liney et al. 1999), so for patient (a) the empirical approach produces T_1 estimates that are more consistent with literature. For patient (b) we found with both approaches a mean T_1 larger than 2 s. Compared to the values listed in Table 4.7, this is extremely high.

Table 4.7 *Breast tissue T_1 values reported in literature.*

Tissue type	T_1 (ms)	Reference
Fibrous breast tissue	932	(Bottomley et al. 1987)
Normal parenchyma	796	(Merchant et al. 1993)
	774	(Liney et al. 1999)
Adipose breast tissue	509	(Bottomley et al. 1987)
	265	(Merchant et al. 1993)
	227	(Liney et al. 1999)
Miscellaneous breast tumors	988	(Bottomley et al. 1987)
Breast carcinoma	961	(Bottomley et al. 1987)
Malignant breast tumor	876	(Merchant et al. 1993)
Fibroadenoma	1093	(Bottomley et al. 1987)
Benign breast tumor	1049	(Merchant et al. 1993)

4.7 Results: tissue proton density mapping

As explained in Section 4.4 and applied in the previous section, we can measure the apparent tissue proton density by extracting the ratio between the tissue signal and the phantom solution signal from a low-flip-angle image (Eq. 4.13). The acquisition settings for the low-flip-angle images for patient (a) and (b) were listed in the previous section. Here, we show the acquired images in Figure 4.21.

As mentioned in the previous section, we found $PD_{tissue}/PD_{phantom}$ ratios of 0.27 and 0.25 for patients (a) and (b), respectively. In other experiments (not reported here) we found consistent values in the range from 0.25 to 0.30 as well. If we assume our phantom compartments to represent pure water proton density, this would mean that the *apparent* mobile water content of breast tissue equals ~30%. This is remarkably low. There is limited literature available, but for instance Stark and Bradley (1999) report 90% proton density for fat and 75% for muscle tissue. This matter therefore requires more investigation. However, if this is what we measure in our setup (i.e. a low *apparent* proton density), the ratio may well be applicable to images acquired with the same setup, even if the ratio is not a correct measure of proton density.

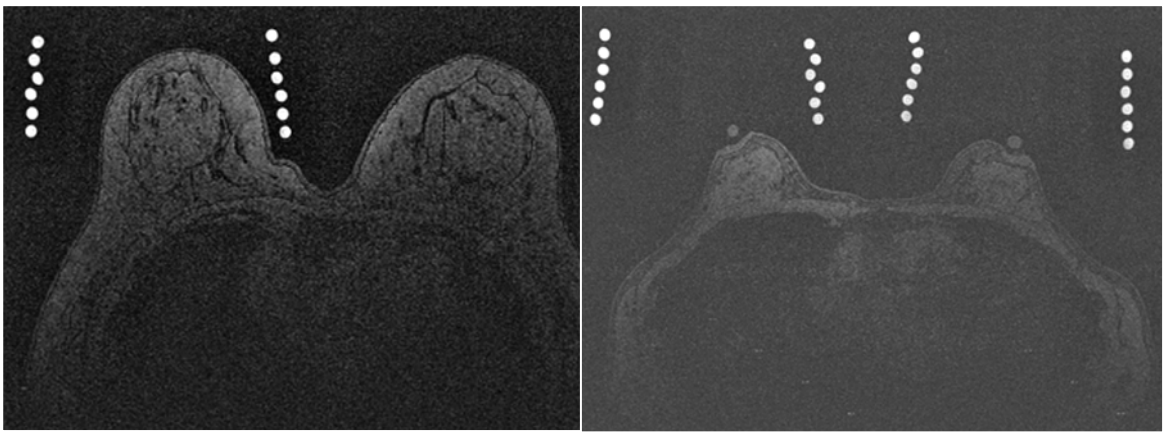

Figure 4.21 *Low-angle image (θ = 2.5°); left for patient (a), right for patient (b). Phantom compartments display similar signal intensities because there is little to no T_1-weighting. There is also little contrast in the tissue.*

4.8 Results: concentration images

To convert the dynamic contrast-enhanced series to contrast agent concentration we make use of the empirical approach as discussed in Section 4.5. As mentioned, the dynamic sequence used in our practice is not purely spoiled-gradient-echo based, and therefore the model-based approach was not pursued. For the same two patients as above, the series was acquired with: 3D fat-suppressed T_1-TFE (turbo field echo, eTHRIVE), repetition time / echo time = 5.5/2.7 ms, θ = 12°, NA = 1, acquisition matrix = 472 x 472, pixel spacing = 0.75 mm x 0.75 mm (patient a) / 0.69 mm x 0.69 mm (patient b), thickness = 2 mm, spacing = 1 mm, number of slices = 200, parallel reduction factor in plane / out of plane = 3/2, temporal resolution ≈ 65 s, 7 dynamics. We used the same proton density ratios as presented in Section 4.6.3 to correct for a difference in proton density between the tissue and the phantom compartments. We analyzed the slices corresponding to the earlier presented spoiled gradient echo data.

To extract a constant for $S \cdot T_1$, here, all volumes of the dynamic series were used, providing a mean estimate. For patient (b), due to the presence of artifacts, this constant was estimated from the phantom compartments in a different slice than the one presented below. In addition, due to the same artifacts, not all phantom compartments could be used (both patients). We will return to this matter in the next section. The signal intensity measurements (as well as the artifacts) demonstrated little variation between dynamics. We found $S \cdot T_1$ to be constant with a standard deviation of 18% (patient a, using compartments: 0, 0.1, 0.2 mM) and 19% (patient b, using compartments: 0.1, 0.2, 0.4 mM). Deviations appeared to show a downward trend with increasing contrast agent concentration (decreasing T_1), but not yet significant. We therefore proceeded under assumption of a constant factor.

The precontrast volume of the dynamic series was used to derive the precontrast T_1 map (in Section 4.6.3 we used a spoiled gradient echo image acquired with θ = 20° to represent a precontrast volume), as presented in Figure 4.22. Note that here the distribution is more narrow than those presented in Figures 4.16 (patient a) / 4.17 (patient b) where we applied variable flip angle T_1-mapping, as well as those presented in Figures 4.19 (patient a) / 4.20 (patient b) where we applied the empirical approach to a spoiled gradient echo image. In addition, the mean value is lower. Due to suppression of the fat component, the T_1 estimates in fatty areas are unreliable.

To recapitulate the different T_1 estimation methods, we listed the means and the standard deviations (std) of the T_1 distributions for patients (a) and (b) in Table 4.8. Here we can also see that with use of the dynamic sequence (turbo field echo) we do not find a distinct difference between the two patients, as was seen with the other approaches. As the T_1 estimates are proportional to $PD_{tissue}/PD_{phantom}$ (Eq. 4.19), the reason for lower values can be due to the fact that the ratio found there (spoiled gradient echo) may not be applicable to the sequence applied over here (turbo field echo). In addition, the estimates are also proportional to $S_{ref} \cdot T_{1,ref}$ (Eq. 4.19). The assumption of a constant value could have led to a more narrow distribution; i.e. in case $S \cdot T_1$ really has a downward relationship with concentration, high T_1 values are underestimated whereas low T_1 values are overestimated. Then again, the mean T_1 values as found in this section are in agreement with those reported in the literature (Table 4.7), so we cannot assume that these outcomes are aberrant, only because they differ from the earlier presented results. Therefore, we continue to use the obtained precontrast T_1 maps (empirical calibration applied to turbo field echo precontrast data) to demonstrate their usage for the conversion to contrast agent concentration.

Table 4.8 *Summary of estimated T_1 distributions for patients (a) and (b) with different approaches.*

T_1 estimation method	Type of date	Patient (a) T_1 (mean ± std ms)	Patient (b) T_1 (mean ± std ms)
Variable flip angle using all angles	T_1-w SPGE	1406 ± 791	2518 ± 976
Variable flip angle using Deoni range	T_1-w SPGE	1361 ± 940	2104 ± 988
Empirical calibration	T_1-w SPGE	862 ± 601	2081 ± 1015
Empirical calibration	T_1-w TFE	655.9 ± 388.9	685 ± 374

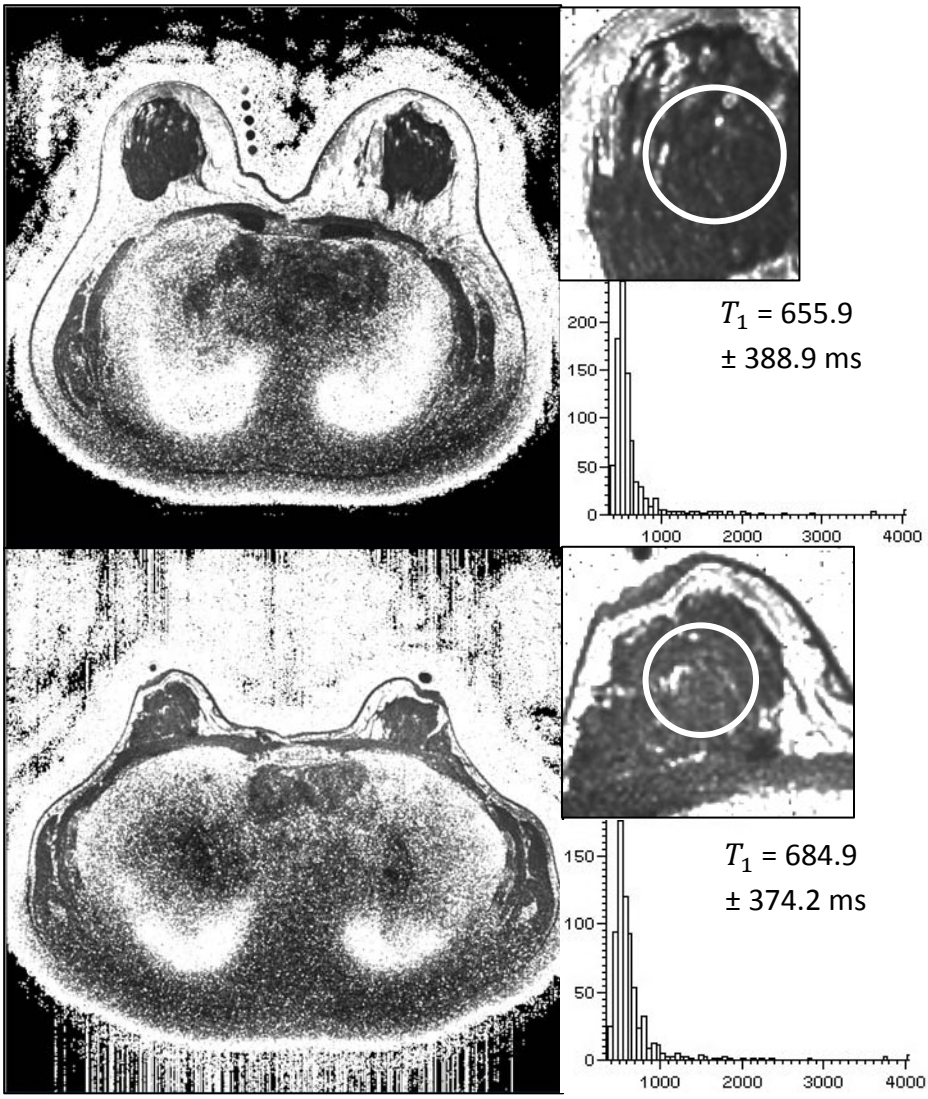

Figure 4.22 *Empirical precontrast T_1 maps derived from the precontrast dynamic volume. Top: patient (a), bottom: patient (b). Note the narrow distribution compared to those presented in Figures 4.16 / 4.17 (variable flip angle approach) and Figures 4.19 / 4.20 (empirical approach applied to spoiled gradient echo image).*

To calculate postcontrast T_1-maps we apply the same equation (4.19) as for the calculation of the precontrast T_1 -maps. Using Equation 4.18 we can derive concentration images making use of both the pre- and postcontrast maps. In Figure 4.23 we display the calculated concentration images for patient (b) side by side with the subtraction images, i.e. $signal(postcontrast) - signal(precontrast)$. The subtraction images are provided to enable a comparison to the current clinical method of assessing enhancement. The first dynamic is shown in signal intensity as the concentration level equals zero at time zero. We see a comparable level of detail between the concentration images and the subtraction images, while the enhancing

structures appear slightly more distinct in the concentration images. The similar (smooth) image quality can be addressed to the fact that the empirical approach does not require fitting of curves. Here we cannot make the comparison – although we see a distinct difference in smoothness in the T_{10} maps – but likely empirically calculated concentration images are more suitable for quantitative morphology than those obtained via a model-based approach, as the latter requires fitting. For (pharmaco-) kinetic analysis the smoothness may be less important.

We have demonstrated an empirical approach to calculation of contrast agent concentration. We conclude that the approach produces high-quality concentration images that can be used for both morphologic and kinetic analysis. The empirical model, i.e. $S \cdot T_1 = constant$, may need adaptation to the specific dynamic sequence, for instance, it could be approximated with a linear or exponential function. Certain suppression or filter techniques can hinder use of the reference phantom for empirical calibration, as discussed next.

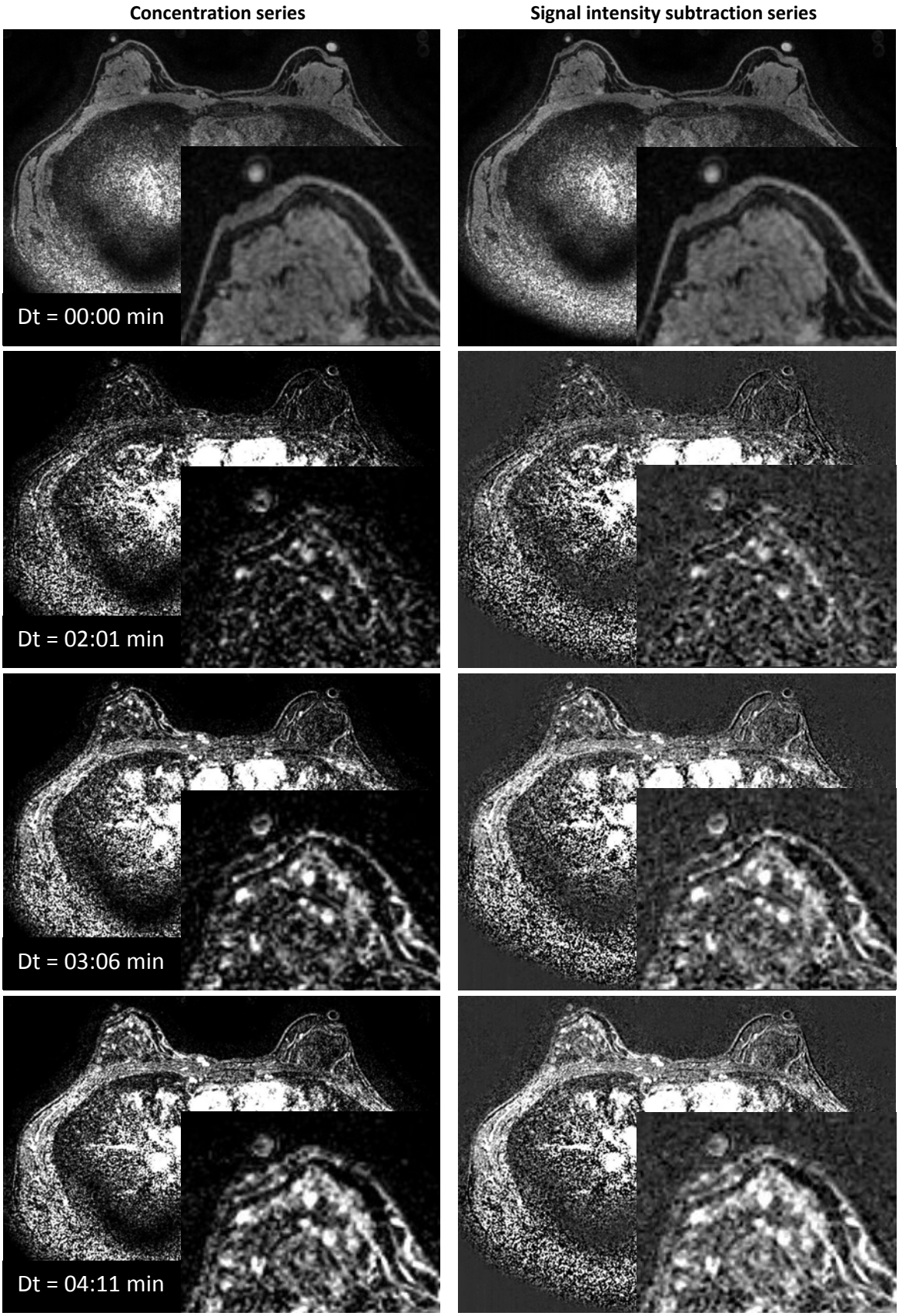
Concentration series
Signal intensity subtraction series
Dt = 00:00 min
Dt = 02:01 min
Dt = 03:06 min
Dt = 04:11 min

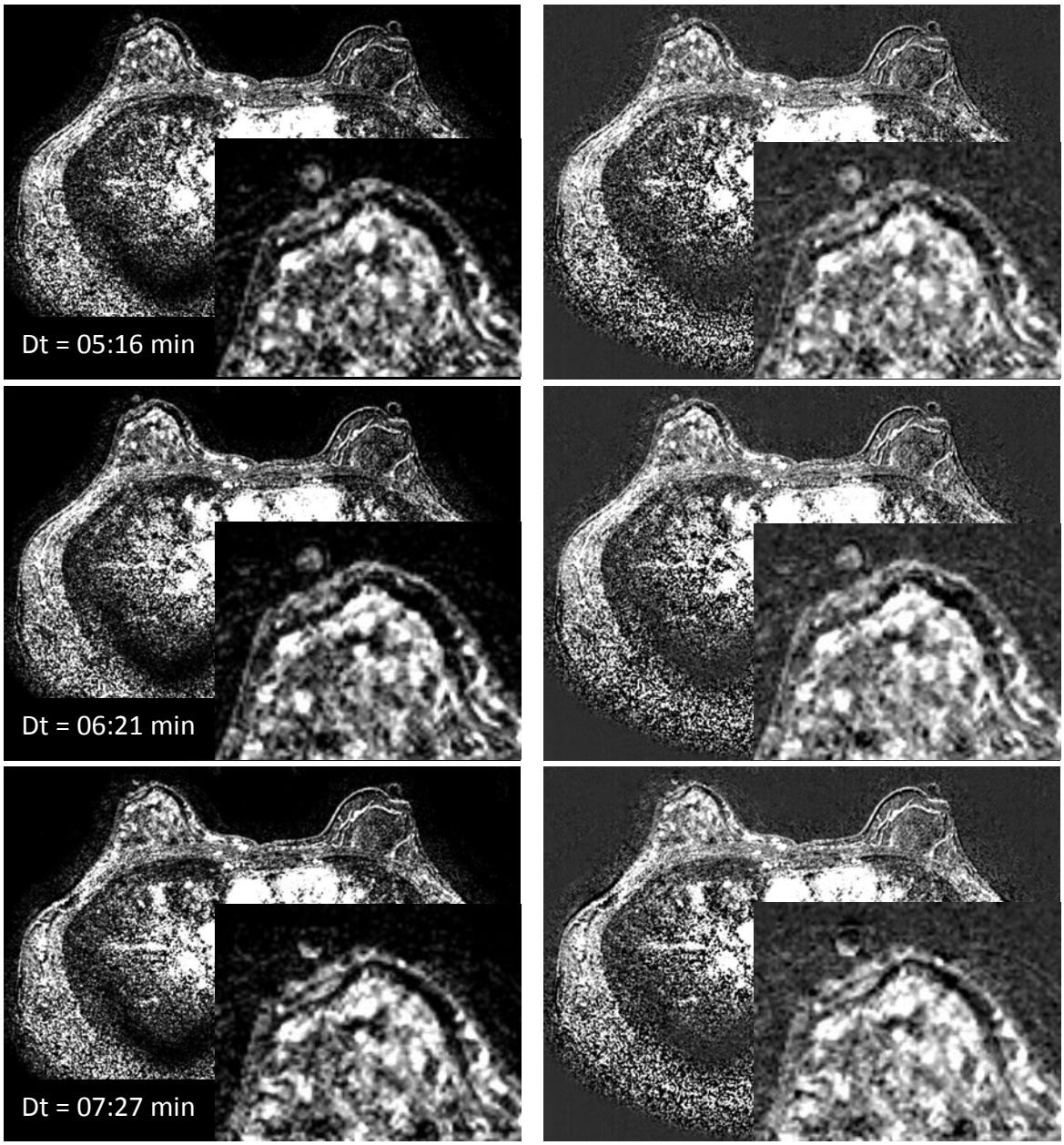

Figure 4.23 *Calculated concentration images (left) and subtraction images for patient (b). The level of detail is comparable. Contrast appears better in the concentration images (less background enhancement).*

4.9 Artifacts arising in DCE-MRI series

As mentioned in the previous section, we could not always perform ROI measurements in the phantom compartments as they were sometimes obscured due to artifacts. We found that compartments situated further away from the body were more often suppressed than those near the body. Probably, approaching the edges of the field of view, inhomogeneity of the B0 field causes the compartment signal to shift into the fat-frequency band that is suppressed. In Figure 4.24 we show two examples, i.e. volunteers (c) and (d) (see Section 4.6.2). For volunteer (c) both the bottom (exceptional) and top compartments are affected, whereas for volunteer (d) the top three compartments are affected, causing ghosting artifacts.

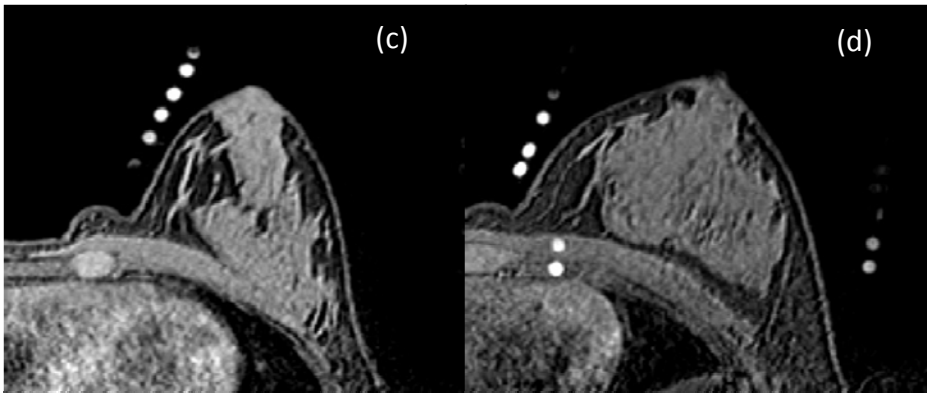

Figure 4.24 *'Precontrast' (no contrast agent was administered) dynamic scans of volunteers (c) and (d) with an acquisition comparable to the one presented in this section.*

It also appears that these artifacts are worse with smaller patients; as the distance between the breasts and the phantoms increases it is more likely that filters suppressing noise outside the breasts act on the phantom signal. In Figure 4.25 we show an extreme case (patient b) for which we investigated the separate roles of fat-suppression and noise-suppression (CLEAR). The images are displayed as with the automatic windowing on the workstation. As you can see, the combination of fat- and noise-suppression can make the phantom compartments practically invisible. Using only fat-suppression we can see the compartments, but they appear 'empty' (we stress that this is the most extreme case we have seen). In case fat-suppression is not applied (bottom row), we obtain useable images. Interestingly though, the balance between the signal intensities in the tissue and in the compartments is very different with or without noise-suppression. Caution for such effects is needed in the application of the empirical approach.

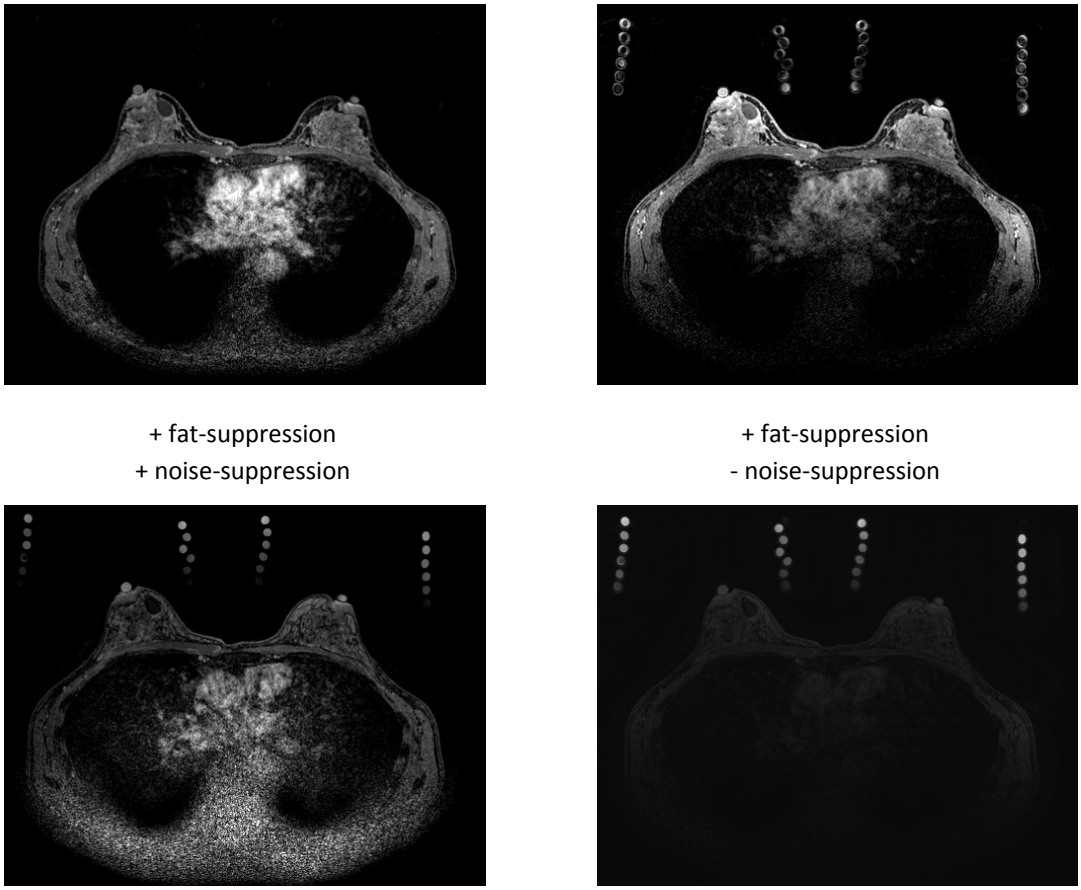

+ fat-suppression
+ noise-suppression

+ fat-suppression
- noise-suppression

- fat-suppression
+ noise-suppression

- fat-suppression
- noise-suppression

Figure 4.25 *Dynamics as acquired for patient (b) (at the end of the true dynamic series), with /without fat-suppression, as well as with / without noise suppression. Especially fat-suppression plays a large role.*

4.10 Discussion

In this chapter we have discussed and demonstrated two main pathways (Figure 4.1) towards quantification of contrast agent concentration. A central role was given to the reference phantom that was developed in-house at the University of Chicago.

4.10.1 Clinical T_{10} quantification

As both the model-based as well as the empirical pathway require precontrast T_1-mapping, we thoroughly investigated the best way to apply a variable flip angle approach, e.g. by flip angle selection and verification / correction with use of the reference phantom, as well as an empirical approach making use of a calibration constant derived from the reference phantom. The methods produced different results: the mean T_1 estimates in the parenchyma were higher with the model-based approach and showed a broader distribution, especially in comparison to the empirical T_1 maps derived from the precontrast dynamic volume (sequence: turbo field echo). At current

time, we do not have the means to assess if one pathway produces more accurate maps than the other.

Selection of flip angle range

In test experiments the flip angle selection method improved T_1 estimation by excluding uncertain or biased samples (samples: flip angles) from the variable flip angle fitting process. We therefore believe that application of the Deoni selection results in improved T_1 estimation in tissue as well. In our data we did not always encounter a clear pattern of increasing uncertainty while moving away from the Ernst angle; more pronounced was the appearance of biased samples. The Deoni selection however also worked well to exclude these biased samples. Their cause is unclear, they occur both in the lower as well as in the higher angle range.

Flip angle correction factor

The variable flip angle correction method did not prove to produce more accurate T_1 estimates, but deserves a closer look as the validation experiment was suboptimal. The presence of the phantom was still useful for variable flip angle T_1 quantification, as it provided a way to assess T_1 accuracy, which varied from patient to patient; e.g. for patient (a) we found a mean error of 53%, whereas for patient (b) we found a mean error of 14%. With a larger group of patients it would be possible to assess the robustness of variable flip angle T_1-estimation making use of the reference phantom. Moreover, it could be studied if a potential (location-dependent) correction factor should be determined per patient (Eliat et al. 2004), or if such a factor translates well from patient to patient. In the latter case, it would not be necessary to scan the phantom with every patient.

Empirical calibration

The empirical approach was inspired by the fact that current clinical DCE-MRI sequences are often not (purely) spoiled-gradient-echo-based. The advantage of an empirical approach is that the theoretical signal model does not need to be known. In literature, phantom calibration is often combined with a signal-model-based approach (De Bazelaire et al. 2005), but, as we have shown here, it does not need to be. As mentioned, the empirical relationship can be adapted to match the specific dynamic sequence. A calibration based on a phantom-only experiment does not account for the presence of the patient and the (semi-)automated shimming procedure, we therefore advocate concurrent scanning of the phantom with the patient. In comparison to the model-based variable flip angle T_1-estimation approach, the empirical approach produces smoother T_1 maps. If the cause for this difference is less noise propagation, the use of empirical T_1 maps in the subsequent calculation of concentration images has the advantage of visually better interpretable concentration images. Because in the

empirical approach we compare signal intensities measured at different locations (i.e. phantom location versus locations within the tissue) it could be beneficial to estimate the sensitivity profile of the breast coil and to use this profile in the calculations.

4.10.2 Concentration images

The concentration images as produced with the empirical approach show the same level of detail as subtraction images, with slightly better perceived contrast between enhancing and non-enhancing structures. Further testing should point out if the concentration images are really of equal quality as the subtraction images. If that is the case they can be used to assess morphology, in addition to kinetics. We propose a multicenter study, where the participants explicitly are not asked to match their DCE-MRI acquisitions, but instead to place the reference phantoms in the breast coil and to add a few (at least one) scans for the purpose of quantification to the clinical protocol. The conversion from signal intensity to contrast agent concentration with use of the reference phantom should result in inter-institute comparable data.

Some studies advocate that there is no need to measure precontrast T_1 for the conversion to contrast agent concentration; that it is sufficient to assume a mean T_1 and use that in the calculation (e.g. Li et al. 2009). However, the often-cited paper by Haacke et al. (2007) clearly mentions that this only holds for relative measures, for instance comparing pre- and post-treatment status. The reason for choosing a fixed T_1 is to save scan time and to reduce error propagation from the fitted variable flip angle T_1 maps. As we have shown in this chapter, empirical calibration may offer an attractive alternative.

4.10.3 Study limitations

A limitation of the final design of the reference phantom is the use of an aqueous solution; ideally air-bubble free agar would be used (Mustafi et al. 2009). This however asks for a design in which the tubes are well-protected, which may take up too much space in the phantom coil. That is in any case a problem; with some patients it is not possible to add a phantom in the coil. A possible solution would be to integrate the phantom with the coil. Another reason to switch to agar is that with agar it would become possible to mimic tissue in more aspects than just T_1, for instance also in the aspect of magnetization transfer between water and macromolecules.

An important limitation of the acquisition protocol was that the scans for quantification consisted usually of only 15 slices. We could therefore not cover the whole breasts. We chose this number of slices to limit the additional scan time to approximately 5 minutes. The applied scans were relatively slow (~ 1 minute per flip angle) because for quantification purposes we wanted to apply very basic sequences (no parallel imaging for instance), to produce data matching the spoiled gradient echo model. To make the protocol applicable for clinical practice the number of slices has to

be increased and the acquisition has to be speeded up. It should however be tested first how this affects signal quantification.

4.10.4 Recommendations

To improve the calculation of contrast agent concentration images, it could be beneficial to correct for receiver coil inhomogeneity, for instance by correcting for the variation in a breast coil / body coil ratio map, which is especially important for the empirical approach. In addition, B1-mapping or use of a multi-transmit coil could help to correct for B1-inhomogeneity.

As mentioned in Jansen et al. 2009b, another factor contributing to the appearance of a contrast uptake curve is the k-space profile ordering of the acquisition. We demonstrated in Heisen et al. 2007b, that different k-space profile orderings lead to differences in descriptive curve type classification (but this just as well holds for pharmacokinetic analysis). The influence of the profile ordering cannot be assessed with a static phantom and therefore remains an open issue to be solved.

4.10.5 Conclusion

In conclusion, we developed a reference phantom that can be used routinely to verify, correct, or calibrate the relationship between contrast agent concentration and the acquired signal intensity. We suggested different approaches, model-based as well as empirical, requiring a few (~ 6) or one additional scan, respectively. With only very limited time available, we would recommend choosing the empirical calibration method over the dual-flip-angle approach. As standardization of the DCE-MRI protocol is unrealistic, the acquired signal should be standardized via a conversion to contrast agent concentration.

4.11 Acknowledgements

This work could not have been performed without the efforts of many people. We would like to thank the following from the University of Chicago: A.M. Wood, B. Peng, F.D. Pineda, D. Mustafi, M. Medved, C. Yang, R. Ladsaria, S. Harris, G.M. Newstead and G.S. Karczmar; from Eindhoven University of Technology: G.J.S. Litjens, and B.M. ter Haar Romeny; and from Philips Healthcare: M. Ivancevic, S. Lobregt, and J. Buurman. We would also like to express our gratitude towards the volunteers and patients that participated in this study.

Chapter 5

The influence of temporal resolution in determining pharmacokinetic parameters from DCE-MRI data

This chapter is based on:

M. Heisen, X. Fan, J. Buurman, N.A.W. van Riel, G.S. Karczmar, B.M. ter Haar Romeny (2010). "The influence of temporal resolution in determining pharmacokinetic parameters from DCE-MRI data" Magn Reson Med, 63, 811-816

M. Heisen, X. Fan, T. Twellmann, J. Buurman, N.A.W. van Riel, G.S. Karczmar, B.M. ter Haar Romeny (2008). "The role of temporal resolution in determining pharmacokinetic parameters from DCE-MR data" Proceedings ISMRM 16, Toronto Canada, 3836

Abstract

We investigated the influence of the temporal resolution of dynamic contrast-enhanced MRI data on pharmacokinetic parameter estimation. Dynamic gadodiamide-enhanced MRI data of implanted prostate tumors on rat hind limb were acquired at 4.7 T, with a temporal resolution of ~5 s. The data were subsequently downsampled to temporal resolutions in the range of 15 s to 85 s, using a strategy that involves a recombination of k-space data. A basic two-compartment model (Tofts) was fit to the contrast agent uptake curves. The results demonstrated that as temporal resolution decreases, the volume transfer constant (K^{trans}) is progressively underestimated (~4% to ~25%), and the fractional extravascular extracellular space (v_e) is progressively overestimated (~1% to ~10%). The proposed downsampling strategy simulates the influence of temporal resolution more realistically than simply downsampling by removing samples.

5.1 Introduction

Dynamic contrast-enhanced magnetic resonance imaging (DCE-MRI) plays an essential role for cancer detection and characterization. Ideally, DCE-MRI data would be acquired with high spatial and high temporal resolution to fully exploit both the morphologic and kinetic information. However, there is always a trade-off between spatial and temporal resolution with currently available equipment and techniques (Kuhl et al. 2005a). Therefore, a wide range of temporal resolutions is encountered for clinical DCE-MRI. For instance, according to the European Society of Breast Imaging (Mann et al. 2008), a sampling time (T_s) of 60 s – 120 s is recommended for high spatial resolution bilateral acquisitions.

A widely used pharmacokinetic model to fit DCE-MRI data and extract physiologic parameters is the basic Tofts model (Tofts et al. 1999). To accurately fit this model to DCE-MRI data, Henderson et al. (1998) recommended that contrast agent uptake in the breast be sampled every 16 s to estimate the volume transfer constant (K^{trans}) and the fraction of extravascular extracellular space (v_e). For the extended model – taking the blood plasma fraction (v_p) into account – their recommendation was to sample every 4 s. The arterial input function (AIF), however, was suggested to be sampled every second. Other work usually did not make a distinction between contrast agent uptake sampling and AIF sampling (Aref et al. 2007, Ramirez et al. 2007) or focused on AIF sampling (Aerts et al. 2008). Most previous studies investigated the effect of low-temporal resolution on pharmacokinetic parameter estimation by downsampling high-temporal-resolution data while assuming an instantaneous collection of k-space data (Aref et al. 2007, El-Khouli et al. 2008, Gal et al. 2007, Henderson et al. 1998); except for Ramirez et al. 2007, who used a sliding temporal window.

The purpose of this study is to investigate the effect of the temporal resolution of DCE-MRI data on pharmacokinetic parameter estimation. Because the contrast agent concentration is changing during a low-temporal-resolution acquisition, the contrast agent uptake observed in the tissue is influenced by the k-space profile ordering. To mimic this effect and simulate DCE-MRI data at different temporal resolutions, a realistic downsampling strategy is introduced that involves a recombination of k-space data. The method is applied to high-temporal-resolution rodent DCE-MRI data acquired with a 4.7 T animal scanner.

5.2 Theory

5.2.1 Downsampling strategy

In our downsampling strategy, the transient effect of contrast agent uptake is incorporated by mimicking an MRI data acquisition. To simulate a linear k-space profile ordering, equal fractions of k-space data are taken from a series of successive high-temporal-resolution k-space images. For instance, using 5 s resolution k-space data to

simulate the first image 'acquired' at a T_s of 15 s, we recombine the first one-third of k-space lines from the 5 s image, the second one-third from the 10 s image, and the third one-third from the 15 s image. The second image at T_s of 15 s is derived from the k-space images acquired at 20 s, 25 s, 30 s, etc. The recombination for the above example is defined as:

$$S_i^d = S_{3i-2}\big(k = 1, \dots, N_\varphi/3\big) + S_{3i-1}\big(k = N_\varphi/3 + 1, \dots, 2\,N_\varphi/3\big) + S_{3i}\big(k = 2\,N_\varphi/3 + 1, \dots, N_\varphi\big), \qquad [5.1]$$

where $S_i^d (i = 1, \dots, N_R/3)$ is the i^{th}downsampled k-space image; N_R is the number of dynamic repetitions; $S_i(k)$ is the kth phase-encoding line of the ith original k-space image; and N_φ is the total number of phase-encoding lines. We call this strategy "k-space-based sampling".

The results obtained with k-space-based sampling are compared to the results of downsampling by omitting intermediate time points of the contrast agent uptake curves, which implies the assumption of instantaneous k-space data collection (Gal et al. 2007, Henderson et al. 1998). This strategy is referred to as "direct sampling" in the remainder of this work.

5.2.2 Pharmacokinetic model

In this study, the basic Tofts model (Tofts et al. 1999) is applied:

$$\frac{dC_t(t)}{dt} = K^{trans}\left(C_p(t) - \frac{C_t(t)}{v_e}\right), \qquad [5.2]$$

where v_e is the fraction of extravascular extracellular space (EES); K^{trans} (min^{-1}) is the volume transfer coefficient between blood plasma and EES; C_p (mM) is the contrast agent concentration in the blood plasma space; and C_t (mM) is the contrast agent concentration in the tissue of interest. We found in Chapter 3 that this model is the only model that is fairly robust against low-temporal resolution.

For the data used in this research, $C_p(t)$ is derived from the contrast agent uptake in skeletal muscle, using the reference tissue approach, assuming literature values for K^{trans} (= 0.11 min^{-1}) and v_e (= 0.20) (Kovar et al. 1998). To minimize noise propagation, the muscle curve was fit with an empiric mathematical model (Fan et al. 2004) prior to this derivation.

To investigate the effect of a varying temporal representation of the contrast agent uptake in tissue as the only changing variable, we exclude the effect of a temporally downsampled AIF in this study (we will return to this matter in Chapter 6). Therefore, the original high-temporal-resolution AIFs are used across all temporal resolutions.

5.3 Materials and methods

5.3.1 Animals and imaging protocol

Copenhagen rats (n = 6) with implanted AT6.1 prostate tumors on the hind limb were used in this study. Multi-slice T_1-weighted gradient echo images (repetition time / echo time = 40/3.5 ms, matrix size = 128 × 128, field of view = 40 mm × 40 mm, flip angle = 30°, k-space profile ordering = linear, slice thickness = 1 mm, number of slices = 3) were acquired through the center of the tumor along the long axis of the leg with a temporal resolution of 5 s at 4.7 T (Bruker, Billerica, MA, USA), before and after gadodiamide (Omniscan, GE Healthcare, Piscataway, NJ, USA) injection, for a total duration of ~10 min. The contrast agent was manually injected as a bolus (duration < 5 s). Each rat received the same amount of contrast agent, i.e. 3.2×10^{-2} mmol, corresponding to a dose of 0.2 mmol kg^{-1} for a weight of 160 g. To account for variations in rat weight, the contrast agent concentration was normalized to this typical dose. The exchange of contrast agent on the microvascular scale was assumed to be similar between rats and humans.

Animals were anesthetized prior to imaging experiments, and anesthesia was maintained during imaging at 1.5% isoflurane. The temperature was maintained at 37 °C with a warm air blower. Heart rate, respiration rate, and temperature were monitored during the MRI experiments. All the data were acquired at the University of Chicago and procedures were carried out in accordance with the institution's Animal Care and Use Committee approval.

5.3.2 Calculation of contrast agent concentration

All data processing was performed in Matlab (Mathworks, Natick, MA, USA). To apply the pharmacokinetic model, DCE-MRI signal intensity curves were converted to contrast agent concentration curves ($C_t(t)$) using a previously published reference method (Medved et al. 2004). The precontrast reference was taken from a user-defined region of interest in muscle (9 x 9 voxels) that was not directly neighboring the tumor. A precontrast T_1 value of 1285 ms for muscle (Marzola et al. 1999) and a relaxivity value of 4.3 mM^{-1} s^{-1} (Furman-Haran et al. 1996) were used in the calculations.

5.3.3 Enhancing tumor segmentation

A single slice, showing most of the tumor area, was selected for further analysis and simulations. A background mask, based on a largest-connected-component and hole-filling algorithm, was first applied. Secondly, an image was constructed consisting of the maximum concentration level encountered in each voxel during the time course of the dynamic series. During the time course of 10 min, necrotic enhancement was not expected. Finally, a semi-automated connected-component algorithm was applied to this image to obtain a contiguous segmentation of the enhancing tumor tissue. The

threshold was manually adjusted to ensure inclusion of most of the enhancing tumor tissue, resulting in a threshold range of 0.034 mM to 0.070 mM.

5.3.4 Fitting routine

To fit the pharmacokinetic model to the data, a golden section search method was implemented (Press et al. 1996, see Chapter 2, Section 2.6.1). The driving force of the golden section search was the minimization of the goodness-of-fit measure R^2. To facilitate the calculation of R^2, the temporal resolution of $C_t(t)$ was increased to the temporal resolution of $C_p(t)$ by linear interpolation; i.e., in the event that $C_t(t)$ had a lower temporal resolution than $C_p(t)$ ($C_p(t)$: T_s = 5 s, $C_t(t)$: T_s = 5 s – 85 s). The starting section for K^{trans} was [0.001 min^{-1} – 1.0 min^{-1}] and for v_e it was [0.01 – 1.0]. The search section was narrowed down for K^{trans} and v_e until the difference between the lower and upper boundary was less than 10^{-3} min^{-1} or less than 10^{-3}, respectively. The fitting routine was applied to voxels with significant contrast agent uptake, i.e., to voxels with a maximum uptake higher than 0.02 mM.

5.4 Results

5.4.1 Enhancing tumor segmentation

Figure 5.1 shows precontrast T_1-weighted images and postcontrast subtraction images for all six cases. The enhancing tumor segmentations are shown in the last column. Except for case 6, all tumors developed a non-enhancing, possibly necrotic, core. Therefore, only the periphery of the tumor was segmented for cases 1 to 5. The enhancement patterns vary from primarily early rim enhancement (case 2) to more global enhancement (case 4).

5.4.2 k-space-based downsampling

The k-space-based sampling strategy (Eq. 5.1) is illustrated in Figure 5.2 for case 1. In this example we demonstrate downsampling from T_s = 5 s to T_s = 15 s. The three consecutive sections of k-space data (top row images) add up to a new k-space image, which is equivalent to a k-space image acquired with T_s = 15 s. Each section of k-space data, as well as the summation of the three, can be Fourier transformed to form an image (bottom row images). As expected, the central part of k-space data (low frequencies) is dominant in determining the overall signal intensity, whereas the outer parts of k-space data (high frequencies) define the details. In an equivalent way, smaller sections were combined to form new data sets at temporal resolutions of 30 s, 45 s, 60 s, and 85 s.

For the same example (case 1), the mean contrast agent uptake curves (all temporal resolutions) for the enhancing tumor segmentation are shown in the plot (Fig. 5.2). As anticipated, low-temporal resolution had more effect on the early phase than on the late phase. The k-space-based sampling strategy demonstrates that low-

temporal-resolution curves do not necessarily consist of points taken from the original curve at regular intervals, as is assumed by direct sampling.

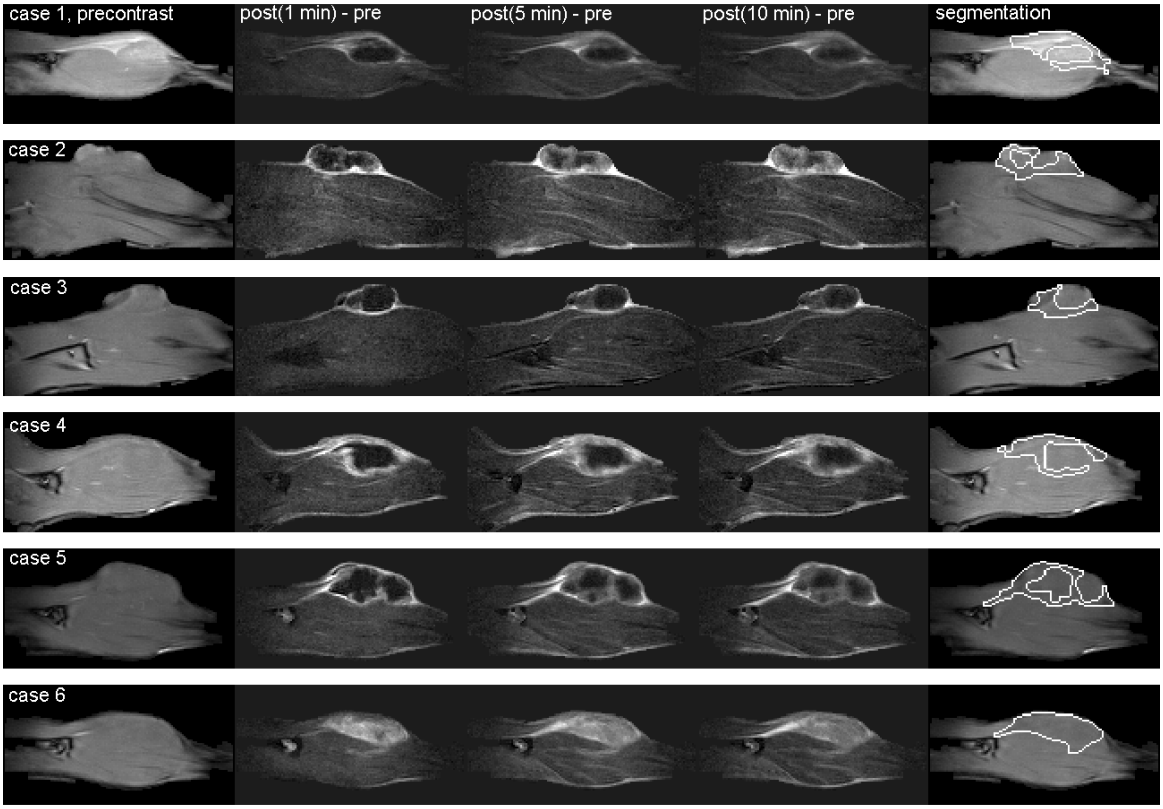

Figure 5.1 *For six cases (rows), from left to right: precontrast image, subtraction image at 1 min, subtraction image at 5 min, subtraction image at 10 min, and the enhancing tumor segmentation. The in-plane resolution is 0.31 mm x 0.31 mm. Images were cropped to a height of ~2.1 cm for display purpose. Except for case 6, all tumors developed a non-enhancing core.*

5.4.3 Pharmacokinetic analysis

The k-space-based and direct sampling strategies were both applied to all six DCE-MRI experiments. The original 5 s and the equivalent lower-temporal-resolution (15 s up to 85 s) contrast agent uptake curves were all fitted with the same pharmacokinetic model to estimate K^{trans} and v_e. Tables 5.1 and 5.2 show the results of fitting the mean contrast agent uptake curves for, respectively, k-space-based and direct sampling. It can be seen (Table 5.1) that the underestimation of K^{trans} as a function of temporal resolution is quite consistent. It varies from ~3% (T_s = 15 s) to ~25% (T_s = 85 s). For v_e, the overestimation varies from ~1% to ~10%.

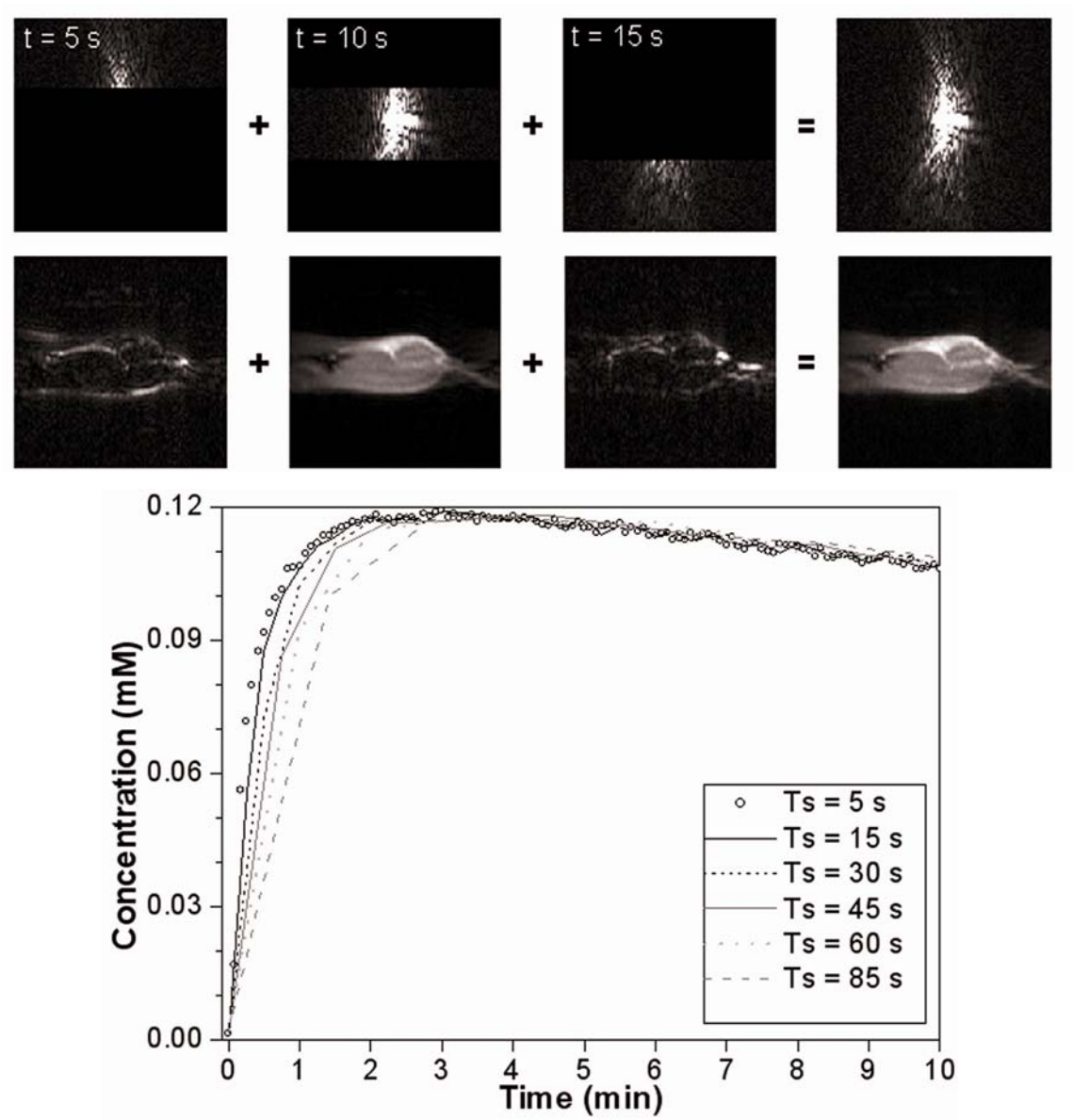

Figure 5.2 *Illustration of the downsampling strategy (from T_s = 5 s to T_s = 15 s) mimicking a linear k-space profile ordering, applied to case 1. First row of images: three consecutive parts of k-space data add up to a new set; second row: the corresponding images. Plot: the mean contrast agent uptake in the enhancing tumor segmentation for case 1 at all temporal resolutions. Especially during the initial phase, the uptake curves do not overlap.*

Although the central k-space portion did not necessarily come from one 5 s k-space image (e.g., at T_s = 30 s), this did not affect the overall tendency of the estimation errors. While direct sampling (Table 5.2) roughly shows underestimation of K^{trans} and overestimation of v_e, the influence of temporal resolution appears smaller than with k-space-based sampling. This implies that the assumption of instantaneous k-space data collection (direct sampling) is inappropriate, as it prevents us from fully simulating the effect of low-temporal resolution. For all fits, R^2-values were within a range of 0.77 – 1.00 (mean R^2 = 0.93 ± 0.05).

Table 5.1 *k-space-based sampling: change in K^{trans} (top) and v_e (bottom) estimated from the mean contrast agent uptake in the enhancing tumor tissue across all temporal resolutions.*

	5 s	**15 s**	**30 s**	**45 s**	**60 s**	**85 s**
Case #	$\boldsymbol{K^{trans}}$ **(min^{-1})**		**Percentage change – $\boldsymbol{K^{trans}}$ (%)**			
1	0.21	-3.4	-9.7	-14.3	-19.5	-27.2
2	0.16	-3.3	-9.7	-13.2	-17.3	-22.8
3	0.15	-3.0	-8.0	-13.0	-16.0	-22.5
4	0.32	-4.0	-9.0	-13.0	-18.0	-26.0
5	0.21	-3.2	-8.6	-13.2	-18.0	-24.9
6	0.23	-4.2	-12.0	-14.8	-20.8	-28.8
	$\boldsymbol{v_e}$		**Percentage change – $\boldsymbol{v_e}$ (%)**			
1	0.54	0.7	2.1	3.4	5.0	8.8
2	0.69	1.4	4.4	6.5	9.1	14.2
3	0.58	0.8	3.0	5.6	8.1	12.8
4	0.83	1.1	2.1	3.2	5.0	8.7
5	0.62	0.8	2.1	3.8	5.4	8.8
6	0.49	0.6	1.7	2.4	4.6	7.1

Table 5.2 *Direct sampling: change in K^{trans} (top) and v_e (bottom) estimated from the mean contrast agent uptake in the enhancing tumor tissue across all temporal resolutions.*

	5 s	**15 s**	**30 s**	**45 s**	**60 s**	**85 s**
Case #	$\boldsymbol{K^{trans}}$ **(min^{-1})**		**Percentage change – $\boldsymbol{K^{trans}}$ (%)**			
1	0.21	-0.6	-3.0	-6.6	-11.8	-19.7
2	0.16	-0.5	-0.5	-1.7	-5.2	-11.8
3	0.15	0.5	-0.6	-4.3	-6.8	-15.8
4	0.32	-0.3	-2.2	-6.4	-12.4	-22.3
5	0.21	-0.6	-3.2	-6.8	-12.1	-19.3
6	0.23	-0.8	-3.1	-6.1	-12.8	-21.4
	$\boldsymbol{v_e}$		**Percentage change – $\boldsymbol{v_e}$ (%)**			
1	0.54	0.1	0.3	0.7	2.3	4.9
2	0.69	0.1	-0.1	0.4	1.9	5.9
3	0.58	-0.3	0.2	1.0	1.7	5.8
4	0.83	0.2	0.3	1.0	2.4	5.0
5	0.62	-0.2	0.3	1.0	2.7	5.0
6	0.49	-0.1	0.5	0.9	2.0	3.4

In addition to the above mean contrast agent uptake analysis for the tumor region of interest, we also performed voxel-wise fitting using data derived with k-space-based sampling. The parametric color maps of K^{trans} and v_e for cases 4 and 6 were selected as examples (see Fig. 5.3) to show the difference between a tumor with (case 4) and without (case 6) a non-enhancing core. At first glance, the estimates of K^{trans} and v_e appear to be quite robust against temporal resolution, especially in muscle. A closer look shows that the 'hot spot' areas present on the original K^{trans} maps become less distinct with decreasing temporal resolution. The location of the tumor, however, remains visible up to a temporal resolution of 85 s. For v_e, there appears to be little influence of temporal resolution. The high v_e values in the tumor rim (case 4) indicate the limitation of the model under study. For these curves, an unrealistically large v_e is required to obtain an accurate fit.

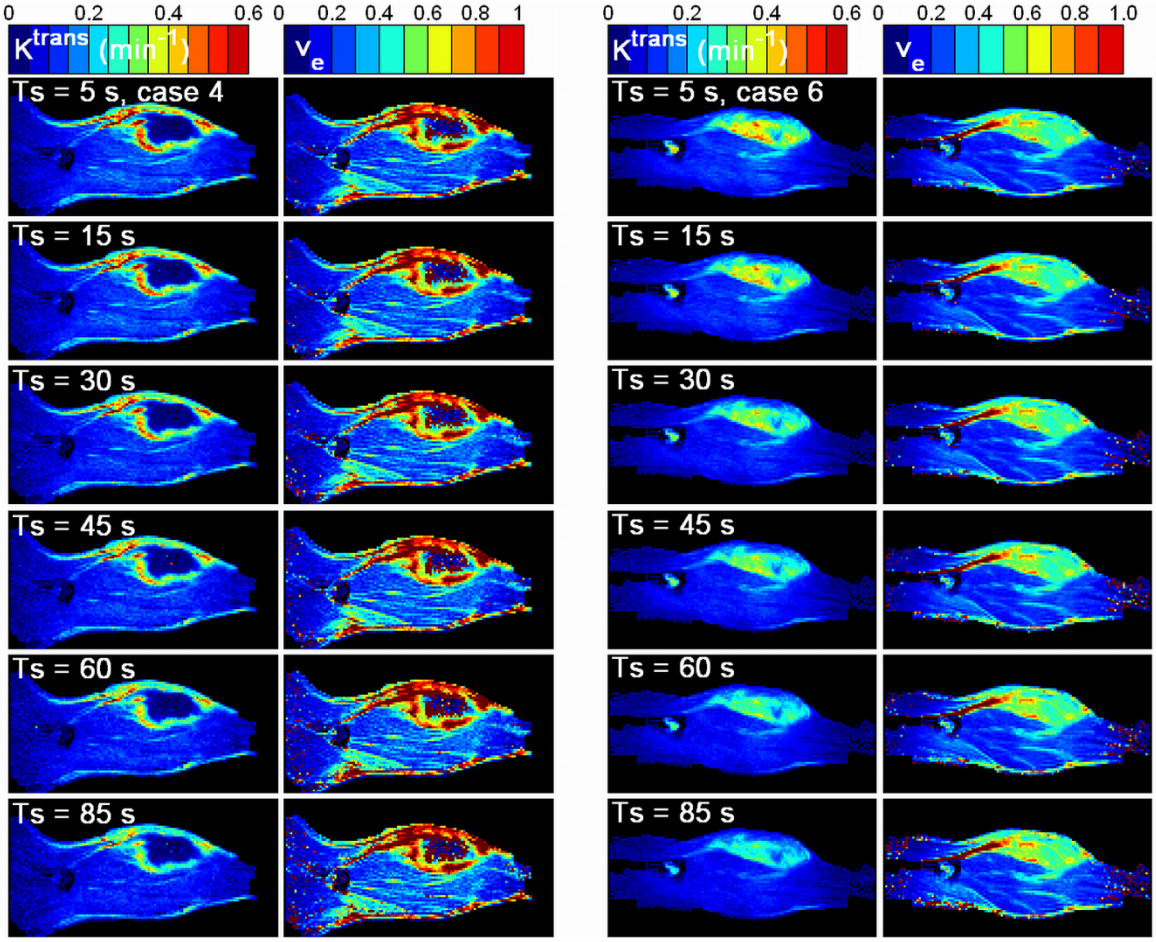

Figure 5.3 *Columns one and two show K^{trans} and v_e for case 4. Columns three and four show K^{trans} and v_e for case 6. From top to bottom temporal resolution decreases (T_s = 5 s, 15 s, 30 s, 45 s, 60 s, and 85 s). These two cases are selected to show the difference between a tumor with and without a non-enhancing core.*

Finally, to see if the observed trends for estimation errors in K^{trans} and v_e (Table 5.1) were statistically significant, one-sided sign tests (Gibbons and Chakraborti 2003) were applied to the parametric difference maps for subsequent T_s: (5 s, 15 s), (15 s, 30 s), (30 s, 45 s), (45 s, 60 s), (60 s, 85 s). For each rat and each combination of subsequent T_s, the null hypotheses that the median of the difference map $K^{trans}(T_{s,2}) - K^{trans}(T_{s,1}) \geq 0$, and the median of the difference map $v_e(T_{s,2}) - v_e(T_{s,1}) \leq 0$ were tested with $T_{s,2} > T_{s,1}$. Both hypotheses were rejected for all tests (P < 0.00001). This means that the progressive underestimation of K^{trans} and the progressive overestimation of v_e are statistically significant.

5.5 Discussion

The influence of the temporal resolution of DCE-MRI data was investigated in the context of the basic two-compartment model, while using a high-temporal-resolution AIF. The original data were downsampled to lower temporal resolutions by making use of a k-space-based recombination technique. The downsampled data, as well as the original data, were fitted with the same pharmacokinetic model. According to both the mean contrast agent uptake curve fitting and the voxel-wise fitting, K^{trans} is progressively underestimated with decreasing temporal resolution, whereas v_e is progressively overestimated. The estimation errors are larger for K^{trans} than for v_e, because the rapid uptake phase is especially affected by a drop in temporal resolution. Even though the 'true' K^{trans} values (at T_s = 5 s) range from 0.15 min^{-1} to 0.32 min^{-1} (Table 5.1), the influence of temporal resolution appears to be consistent across all cases. For v_e, this is less the case.

In comparing k-space-based sampling to direct sampling, the key difference is that the first strategy takes the effect of transient contrast agent uptake into account, while the latter does not. Consequently, the effect of low temporal resolution appears smaller and less consistent with direct sampling than is actually the case. Using direct sampling and the basic two-compartment model, Henderson et al. (1998) found that the required sampling time for the uptake in tissue should be shorter than 16 s to obtain an error smaller than 10% in either K^{trans} or v_e. The sampling time at which we predict the same error level is about twice as large using k-space-based sampling (T_s ≈ 30 s), and about three times as large using direct sampling (T_s ≈ 45 s – 60 s). The discrepancy between the two studies is probably due to the large differences in the experimental setups.

Although we used a more realistic downsampling strategy than the one most commonly used, there are several limitations to this study:

(i) The k-space-based sampling strategy presented in this study mimics a linear k-space profile ordering, thus the conclusions reached here are not valid for other acquisition schemes.

(ii) Temporal resolution was not reduced in exchange for higher image quality and / or larger image volume. In a scanner experiment, a reduction of temporal resolution (while keeping spatial resolution constant) would be expected to lead to an increase in signal-to-noise ratio of each image in the series (more thoroughly discussed in Chapter 6).

(iii) Variations in the relative alignment of the sampling grid (Cheng 2008, Henderson et al. 1998, Laue et al. 2007) were not taken into account.

(iv) The basic two-compartment model does not include a vascular contribution, which could be significant for certain tumors. Its exclusion could have introduced biases on the estimates of K^{trans} and v_e (Buckley 2002b, Harrer et al. 2004).

(v) Emphasis was placed on the temporal resolution of the contrast agent uptake in tissue, and therefore individual high-temporal- resolution AIFs were used. These high-temporal-resolution AIFs would not be available in case of an actual low-temporal-resolution acquisition. The use of individual AIFs extracted from low-temporal-resolution data will be discussed in Chapter 6.

The study was designed to gain insight into estimation errors in K^{trans} and v_e for DCE-MRI data acquired at 'suboptimal' temporal resolutions. It is important to study the modeling of contrast agent uptake at low-temporal resolution because, for instance, clinical DCE-MRI data of the breast are commonly acquired at a temporal resolution of about 60 s to 120 s. Under the applied model assumptions, we estimate that a temporal resolution of 60 s would lead to an error margin of ~18% for K^{trans} and ~6% for v_e. Especially regions with very high K^{trans} are significantly attenuated. However, the blood circulation of rats is about three times faster than that of humans. A similar study should therefore be performed using human DCE-MRI data. As we demonstrated by comparing our k-space-based downsampling strategy to the direct sampling strategy, the impact of the k-space profile ordering on the appearance of contrast agent uptake curves should be considered in both simulation and acquisition methods. In the next chapter, we will use the k-space-based downsampling strategy as introduced in this chapter to investigate if we can decrease the error in the parameter estimates by making use of a reference tissue AIF approach (as was applied in Chapter 3).

5.6 Acknowledgements

We thank T. Twellmann and B.F. Coolen from the Eindhoven University of Technology for fruitful discussions on temporal downsampling; D. Mustafi and M.A. Zamora from the University of Chicago for acquiring the data; C.R. Haney from the University of Chicago for the segmentation algorithm; and T. Akinbiyi from the University of Chicago for consulting on the statistics.

Chapter 6

The use of a reference tissue arterial input function with low-temporal-resolution DCE-MRI data

This chapter is based on:

M. Heisen, X. Fan, J. Buurman, N.A.W. van Riel, G.S. Karczmar, B.M. ter Haar Romeny (2010). "The use of a reference tissue arterial input function with low temporal resolution DCE-MRI data" Phys Med Biol, 55, 4871-4883

M. Heisen, X. Fan, J. Buurman, B.M. ter Haar Romeny (2010). "Effects of reference tissue AIF derived from low temporal resolution DCE-MRI data on pharmacokinetic parameter estimation" Proceedings ISMRM 18, Stockholm, Sweden, 4802

M. Heisen, X. Fan, J. Buurman, B.M. ter Haar Romeny (2009). "The effect of the temporal resolution of the arterial input function (AIF) on pharmacokinetic parameter estimation from dynamic contrast-enhanced (DCE) MRI data" Proceedings RSNA 2009, Chicago, USA, 563

Abstract

Pharmacokinetic modeling is a promising quantitative analysis technique for cancer diagnosis. However, diagnostic dynamic contrast-enhanced magnetic resonance imaging of the breast is commonly performed with low-temporal resolution. This limits its clinical utility. We investigated for a range of temporal resolutions whether pharmacokinetic parameter estimation is impacted by the use of data-derived arterial input functions (AIFs), obtained via analysis of dynamic data from a reference tissue, as opposed to the use of a standard AIF, often obtained from literature. We hypothesized that the first method allows the use of data at lower temporal resolutions than the second method. Test data were obtained by downsampling high-temporal-resolution rodent data via a k-space-based strategy. To fit the basic Tofts model, either the data-derived or the standard AIF was used. The resulting estimates of K^{trans} and v_e were compared with the standard estimates obtained by using the original data. The deviations in K^{trans} and v_e, introduced when lowering temporal resolution, were more modest using data-derived AIFs compared with using a standard AIF. Specifically, lowering the resolution from 5 to 60 s, the respective changes in K^{trans} were 2% (non-significant) and 18% (significant). Extracting the AIF from a reference tissue enables accurate pharmacokinetic parameter estimation for low-temporal-resolution data.

6.1 Introduction

Pharmacokinetic modeling of dynamic contrast-enhanced magnetic resonance imaging (DCE-MRI) data is a quantitative analysis technique employed for a variety of clinical purposes, including cancer diagnosis and therapy assessment. Accurate measurement of pharmacokinetic parameters requires data acquisition with high-temporal resolution, but in the clinical setting this is often not practical because of the need to image large volumes of tissue. Diagnostic DCE-MRI of the breast, for instance, is generally performed with modest temporal resolution (about 1 min) to obtain full bilateral coverage with adequate spatial resolution. Low-temporal resolution presents a challenge; however as recently shown (Planey et al. 2009), it does not prevent application of basic pharmacokinetic models.

Fundamental to pharmacokinetic modeling is the use of an arterial input function (AIF) which describes the bolus of contrast agent passing through the blood circulation, and serves as input to the contrast agent uptake in the tissue of interest. It is difficult to extract an accurate AIF from data acquired with a modest temporal resolution. Direct measurement of the bolus passage in an artery requires a sampling interval of approximately 1 s (Henderson et al. 1998) and is therefore not feasible. A popular alternative is the use of a standard AIF, which is often a population-averaged AIF, derived from data acquired at a relatively high sampling rate; e.g. about 1 sample every 5 s (Parker et al. 2006). Another alternative is the use of a reference tissue AIF method, as introduced into the field of DCE-MRI in 1998 (Kovar et al.). Key to this method is the use of a reference tissue, such as muscle, that has gradual contrast agent uptake, and can be sampled relatively slowly. Under the assumption of known (constant) enhancement parameters for the reference tissue, analysis of its uptake curve can provide a data-derived AIF – even at low temporal resolution.

Derivation of the AIF from a reference tissue shows reasonable repeatability between two DCE-MRI studies of the same subject and the same region of interest (ROI) without repositioning the subject in the scanner (Yankeelov et al. 2006), and reproducibility between two DCE-MRI studies of the same subject at separate occasions (Walker-Samuel et al. 2007b, Yang et al. 2009), as well as good correlation with direct AIF measurement (Kovar et al. 1998, Yankeelov et al. 2007). It has been demonstrated that in diagnostics the use of a data-derived AIF results in a larger area under the receiver operating characteristic (ROC) curve, and thus performs better than the use of a standard AIF (Huisman et al. 2006, Vos et al. 2009). In addition, standard AIFs are commonly applied irrespective of the temporal resolution of the data at hand, and this can lead to, respectively, under- and overestimation in the volume transfer coefficient (K^{trans}) and the distribution fraction (v_e) (Chapter 5, Heisen et al. 2010a). This temporal-resolution-dependent bias cannot be easily accounted for.

Yankeelov et al. (2005) showed that contrast agent uptake measurements in tissue require sampling intervals of 30 s – 60 s. They tested their reference tissue method for its sensitivity to noise and incorrect assignment of reference tissue pharmacokinetic parameter values via simulations at 1 min temporal resolution. More recently, Planey et al. (2009) reported on temporal sampling requirements for pharmacokinetic parameter estimation using reference tissue modeling in human breast cancer. Their simulation study demonstrated a precision within ±15% of the mean up to a sampling interval of 29 s. With downsampled 32.8 s clinical breast data, they obtained parameter estimates that were very similar to those obtained with the native 16.4 s data, whereas downsampled 65.6 s data led to a systematic underestimation in K^{trans}.

Here, we systematically compare the use of a reference tissue AIF extracted from data at various temporal resolutions (data-derived AIFs) with the use of a single standard AIF for data at all temporal resolutions. The study is designed to focus on the role of temporal resolution, i.e. to investigate its effect on pharmacokinetic parameter estimation in isolation. We hypothesize that the use of data-derived AIFs enables accurate parameter estimation at lower temporal resolutions than the use of a standard AIF. Besides comparing the methods, we search for the 'boundary resolution' at which deviations due to low temporal resolution become significant in the pharmacokinetic parameter estimates. Test data are obtained by downsampling high-temporal-resolution (5 s) rodent DCE-MRI data, acquired with a 4.7 T animal scanner, via a k-space-based downsampling strategy to obtain data at a range of temporal resolutions. In this research, we choose to use the reference tissue AIF derived from the original 5 s data as the 'standard' AIF. As a result, the standard AIF is matched to the original data, but is mismatched with the downsampled data in terms of temporal resolution. Other errors that are commonly introduced by the use of a standard AIF, for instance due to variations in systemic circulation and injection protocol, are avoided with this approach. To fit the pharmacokinetic model to the downsampled data, either the data-derived AIF or the standard AIF is used. The resulting parameter estimates are compared with the standard parameter estimates obtained from the original 5 s data.

6.2 Methods

6.2.1 Animals and imaging protocol

Copenhagen rats (n = 6) with implanted AT6.1 prostate tumors on the hind limb were used in this study. Multi-slice T_1-weighted gradient echo images were acquired through the center of the tumor along the long axis of the leg with a temporal resolution of 5 s at 4.7 T (Bruker, Billerica, MA, USA), before and after gadodiamide (Omniscan, GE Healthcare, Piscataway, NJ, USA) injection, for a total duration of ~10 min. The exchange of contrast agent on the microvascular scale was assumed to be similar between rats and humans. All the data were acquired at the University of Chicago and procedures were carried out in accordance with the institution's Animal Care and Use

Committee approval. The detailed description of the acquisition protocol can be found in Chapter 5.

6.2.2 Downsampling strategy

Low-temporal-resolution DCE-MRI data was derived from high-temporal-resolution data via a k-space-based downsampling strategy. Details were presented in a previous study (Chapter 5, Heisen et al. 2010a). Briefly, this strategy incorporates the transient effect of contrast agent uptake by mimicking an MR acquisition with a linear k-space profile ordering. Equal fractions of k-space data taken from a series of successive high-temporal-resolution (5 s) k-space images are combined to form k-space images at a lower temporal resolution. For instance, to simulate the first image 'acquired' at a resolution of 15 s, we recombine the first one-third of k-space lines from the 5 s image, the second one-third from the 10 s image, and the third one-third from the 15 s image. The second image at a resolution of 15 s is derived from the k-space images acquired at 20, 25, 30 s, etc. Using this strategy we simulated low-temporal-resolution data sets at 15, 30, 45, 60, and 85 s resolution. This simulation strategy does not incorporate changes in the signal-to-noise ratio (SNR) of the enhancement patterns due to changes in temporal resolution. For all temporal resolutions, the SNR of the images is comparable to the SNR of the high-temporal-resolution images produced from the original k-space data.

The previous work demonstrated that this realistic simulation strategy reveals a larger influence of temporal resolution than simple downsampling by omitting intermediate time points of a contrast agent uptake curve.

6.2.3 Reference tissue AIF

The reference tissue method introduced by Kovar et al. (1998) was applied with the skeletal muscle of the hind limb as a reference (user-defined ROI: 9 × 9 voxels). The extracted muscle curve ($C_{muscle}(t)$) was fitted with an empirical mathematical model (EMM, Fan et al. 2004) – a single equation with five parameters – to minimize noise propagation, giving

$$\tilde{C}_{muscle}(t) = A \cdot (1 - e^{-\alpha \cdot t})^q \cdot e^{-\beta \cdot t} \cdot \frac{1+e^{-\gamma \cdot t}}{2}, \qquad [6.1]$$

where A (mM) is the upper limit of contrast agent concentration; α (min^{-1}) is the rate of contrast agent uptake; q is related to the slope of early uptake and the curvature of the transition from uptake to washout; and β (min^{-1}) and γ (min^{-1}) are, respectively, the overall and initial rate of contrast agent washout. The EMM-fitted curve ($\tilde{C}_{muscle}(t)$) was used to derive the AIF ($C_p(t)$) via the differential form of the basic Tofts model (Tofts et al. 1999) in combination with assumed literature values of K^{trans} (0.11 min^{-1}) and v_e (0.20) in rat muscle (Kovar et al. 1998) as follows:

$$C_p(t) = 1/K^{trans,muscle} \cdot d\tilde{C}_{muscle}(t)/dt + \tilde{C}_{muscle}(t)/v_{e,muscle}, \qquad [6.2]$$

where C_p (mM) is the contrast agent concentration in the blood plasma space, v_e is the fraction of extravascular extracellular space (EES), and K^{trans} (min^{-1}) is the volume transfer coefficient between blood plasma and EES.

6.2.4 Data analysis

All data processing was performed in Matlab (Mathworks, Natick, MA, USA). A single slice, showing most of the tumor area, was selected for analysis. Signal intensity curves were converted to contrast agent concentration using a previously published calibration method (Medved et al. 2004). The tumor ROI was obtained via a semi-automated connected-component algorithm that resulted in a contiguous segmentation of the enhancing tumor tissue. The basic Tofts model was fitted (2D golden section search method, Press et al. 1996) both voxel-wise and ROI-wise.

A comparison was made between the use of reference tissue AIFs extracted at each specific temporal resolution (data-derived AIF), and the use of a single standard AIF (irrespective of the temporal resolution). For each animal, the standard AIF was derived from the original 5 s data. For both methods (data-derived versus standard AIF) the pharmacokinetic parameter estimates obtained from the original 5 s data were considered as the 'standard'. Parameter estimates were compared with this standard for data derived at 15 s, 30 s, 45 s, 60 s, and 85 s resolution. The regression slopes and the Pearson correlation coefficients (r) were calculated, as well as the percentage of deviation in the mean tumor parameter estimates as a consequence of a drop in temporal resolution.

6.3 Results

Figure 6.1 shows a typical example of contrast agent uptake curves in muscle for all temporal resolutions, and their fits. Most notable is that the reduction in the number of data points results in a decline of the initial uptake slope, as the resolution becomes coarser. Because of the limited number of data points at 85 s resolution, the EMM was fitted as a four-parameter model, fixing q at a value of 2. This value was chosen to prevent the model from fitting with an immediate steep rise that is not supported by the data. The average EMM parameters over all animals are reported for all temporal resolutions in Table 6.1. The large difference in q between the 5 s data (q = 0.82) and the other data sets ($q \approx 2$) indicates that at low temporal resolution there are too few data points on the rising flank of the curve to fit an immediate steep rise. However, an increased value of α (uptake rate) counteracts this effect for the 15 s and 30 s data.

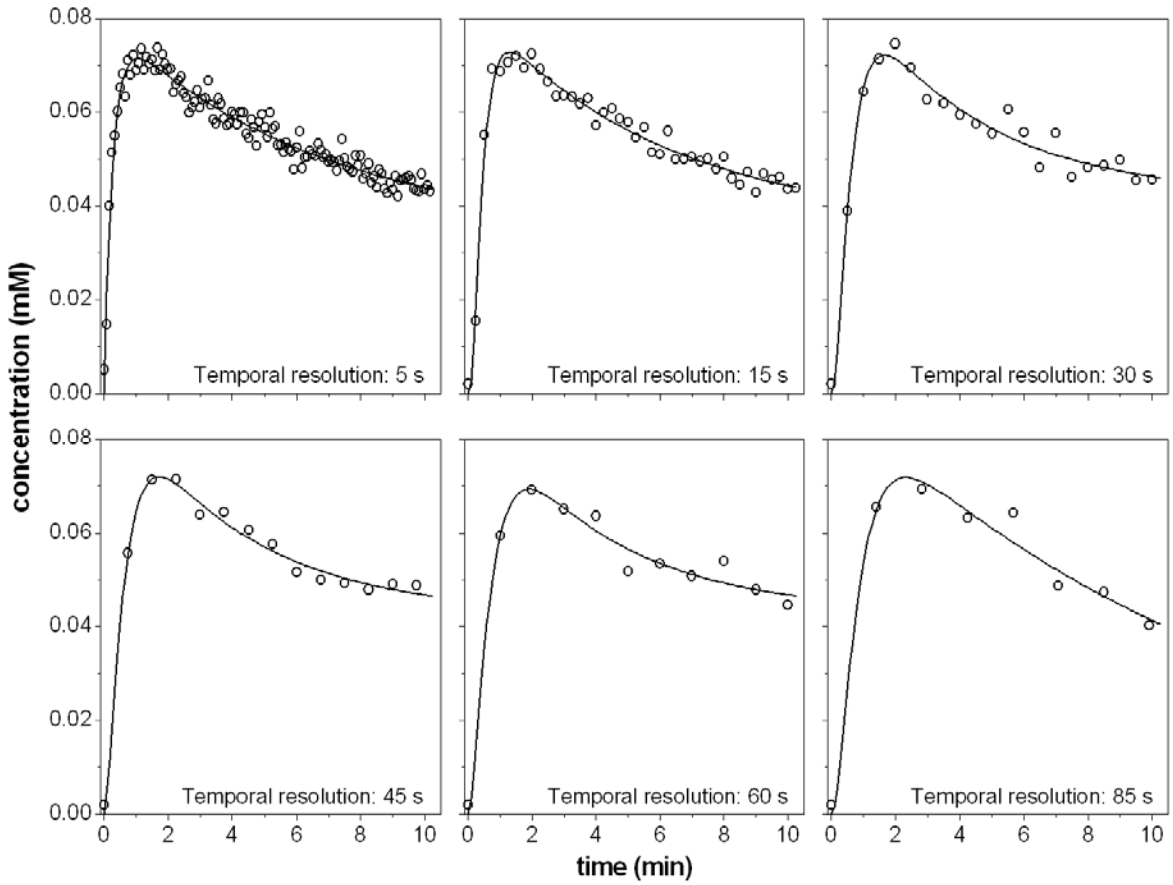

Figure 6.1 *Contrast agent uptake curves in muscle extracted from data at 5 s, 15 s, 30 s, 45 s, 60 s, and 85 s temporal resolution (dots), together with the EMM fits (lines). All curves originate from the same animal and identical ROIs.*

Table 6.1 *Mean empirical mathematical model parameters and their standard deviation obtained by fitting the contrast agent uptake in muscle tissue.*

Temporal resolution (s)	A (mM)	α (min^{-1})	q	β (10^{-2} min^{-1})	γ (min^{-1})
5	0.09 ± 0.02	2.48 ± 1.13	0.82 ± 0.39	1.49 ± 1.02	0.21 ± 0.10
15	0.09 ± 0.02	3.24 ± 0.34	2.07 ± 0.55	1.99 ± 1.33	0.16 ± 0.11
30	0.09 ± 0.02	2.55 ± 0.37	2.23 ± 0.49	1.42 ± 1.09	0.21 ± 0.10
45	0.10 ± 0.02	2.16 ± 0.51	1.80 ± 0.90	1.97 ± 1.82	0.21 ± 0.12
60	0.10 ± 0.02	1.93 ± 0.31	2.12 ± 0.59	1.51 ± 1.33	0.22 ± 0.09
85	0.10 ± 0.02	1.73 ± 0.21	2.00 (fixed)	3.38 ± 2.68	0.15 ± 0.13

Figure 6.2 shows an example (same animal as in Fig. 6.1) of K^{trans} maps obtained at all temporal resolutions with both data-derived AIFs and a single standard AIF. The corresponding AIFs are shown as insets. As expected, the data-derived AIFs became less sharp with decreasing temporal resolution due to a lack of high-frequency information. In comparison to the K^{trans} maps obtained with the original 5 s data, those obtained with data-derived AIFs show less impact of a change in temporal resolution than those obtained with the standard AIF. Use of the standard AIF resulted in a visible loss of K^{trans} 'hot spots' in the tumor rim.

In Figure 6.3, the voxel-wise pharmacokinetic parameter estimates within the tumor ROI obtained with (a) data-derived AIFs and (b) a single standard AIF are plotted versus the 5 s standard parameter values for the same animal as in Figs. 6.1 and 6.2. Temporal resolutions from left to right are: 15 s, 30 s, and 60 s. With the use of data-derived AIFs (Fig. 6.3(a)) the regression slopes (dashed lines) match the lines of identity ($y = x$, solid lines) more closely than with the use of a single standard AIF (Fig. 3(b)); for K^{trans} there is an especially distinct difference.

In Figure 6.4(a), the regression slope data are summarized for all animals. The average tumor ROI size was 544 voxels (range: 311 – 726). All regressions demonstrated significant correlation between the voxel-wise parameter estimates from downsampled data and original data ($P \ll 0.05$). With data-derived AIFs the regression slopes remained closer to 1 with decreasing temporal resolution than with a single standard AIF, both for K^{trans} and v_e. Looking at the whole range of temporal resolutions, there is a significant effect of temporal resolution on the K^{trans} regression slope with both methods, and on the v_e regression slope with the standard AIF method (multiple-comparison ANOVA: $P < 0.05$). Leaving out the 85 s data, the effect of temporal resolution on the K^{trans} regression slope became non-significant with the data-derived AIF method. In Figure 6.4(b), the Pearson correlation coefficient (r) data were summarized for all animals. For both methods (data-derived versus standard AIF), the sharpness of the ellipsoid-shaped cloud of points along the regression line (see also Fig. 6.3) decreased slightly with decreasing temporal resolution. This is reflected in lower r values. This decrease in r is significant for both methods with respect to K^{trans}, and for the standard AIF method with respect to v_e.

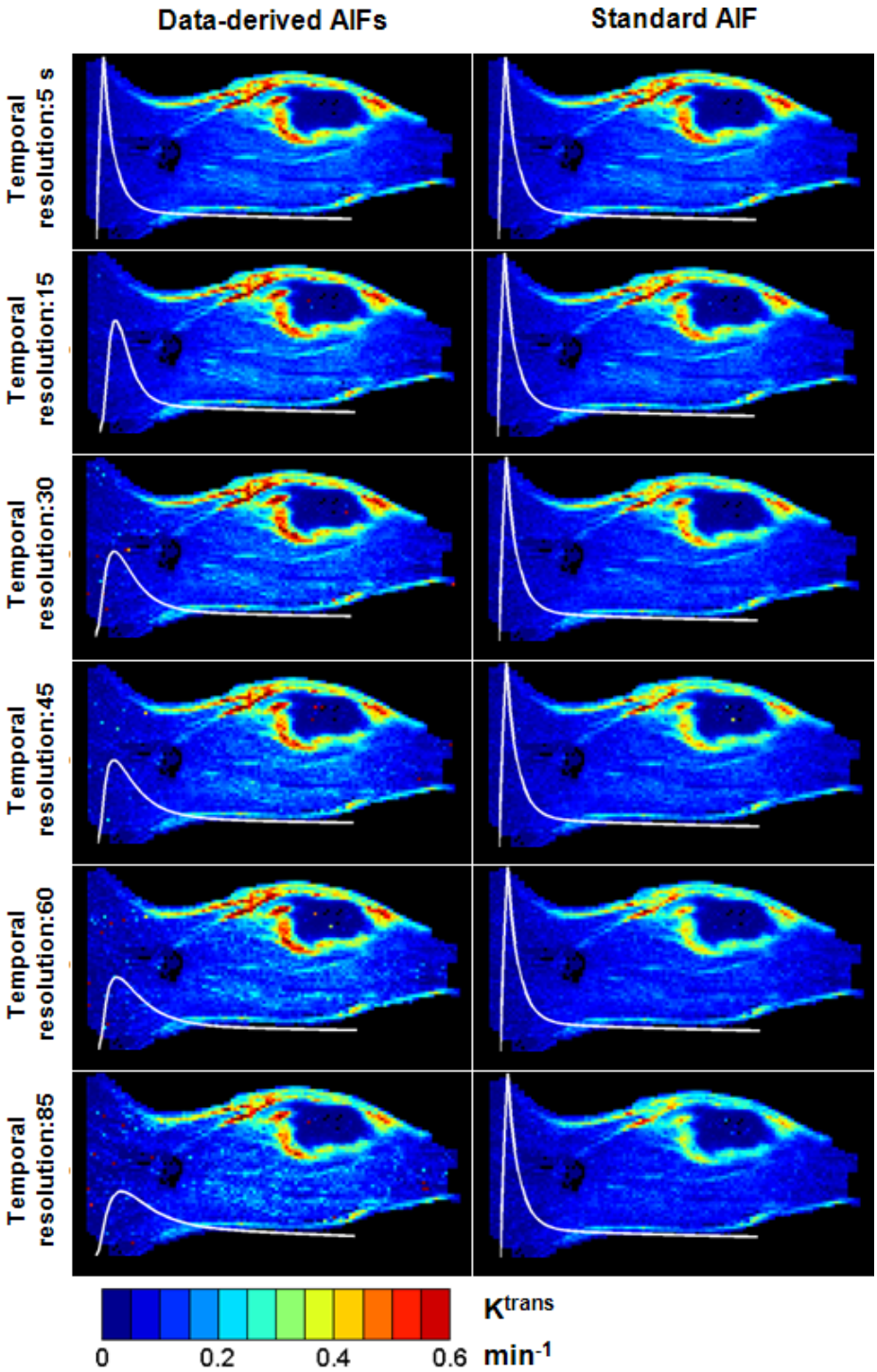

Figure 6.2 *For the same animal as in Fig. 6.1, K^{trans} color maps derived from data at 5 s, 15 s, 30 s, 45 s, 60 s, and 85 s temporal resolution. The first column demonstrates the use of data-derived AIFs, and the second column the use of a single standard AIF. The corresponding AIFs are shown as insets. The influence of temporal resolution, e.g. loss of hot spots, is more distinct with a single standard AIF than with data-derived AIFs.*

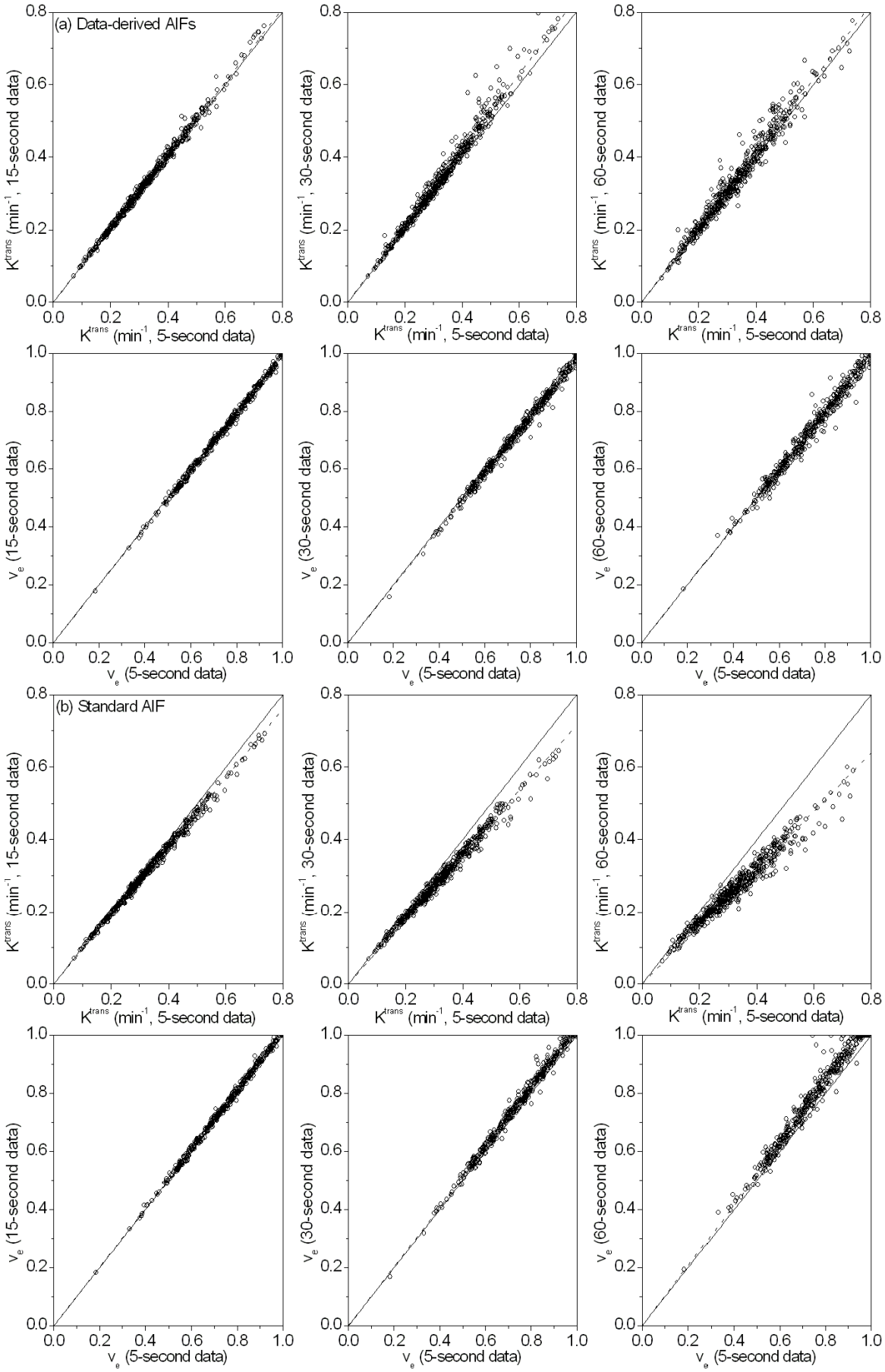
(a) Data-derived AIFs
(b) Standard AIF
K^{trans} (min^{-1}, 15-second data)
K^{trans} (min^{-1}, 30-second data)
K^{trans} (min^{-1}, 60-second data)
K^{trans} (min^{-1}, 5-second data)
v_e (15-second data)
v_e (30-second data)
v_e (60-second data)
v_e (5-second data)

Figure 6.3 (previous page) *Scatter plots of pharmacokinetic parameter estimates obtained from low-temporal-resolution data (y-axis: 15 s, 30 s, and 60 s resolution) versus the standard parameter values set by the 5 s data (x-axis). The line of identity (solid lines) and a straight fit through the data (dashed lines) are included. Only tumor ROI voxels are included. (a) Data-derived AIFs. (b) Single standard AIF. With the use of data-derived AIFs the regression slopes match the line of identity more closely than with the use of a single standard AIF; especially for K^{trans} there is a distinct difference.*

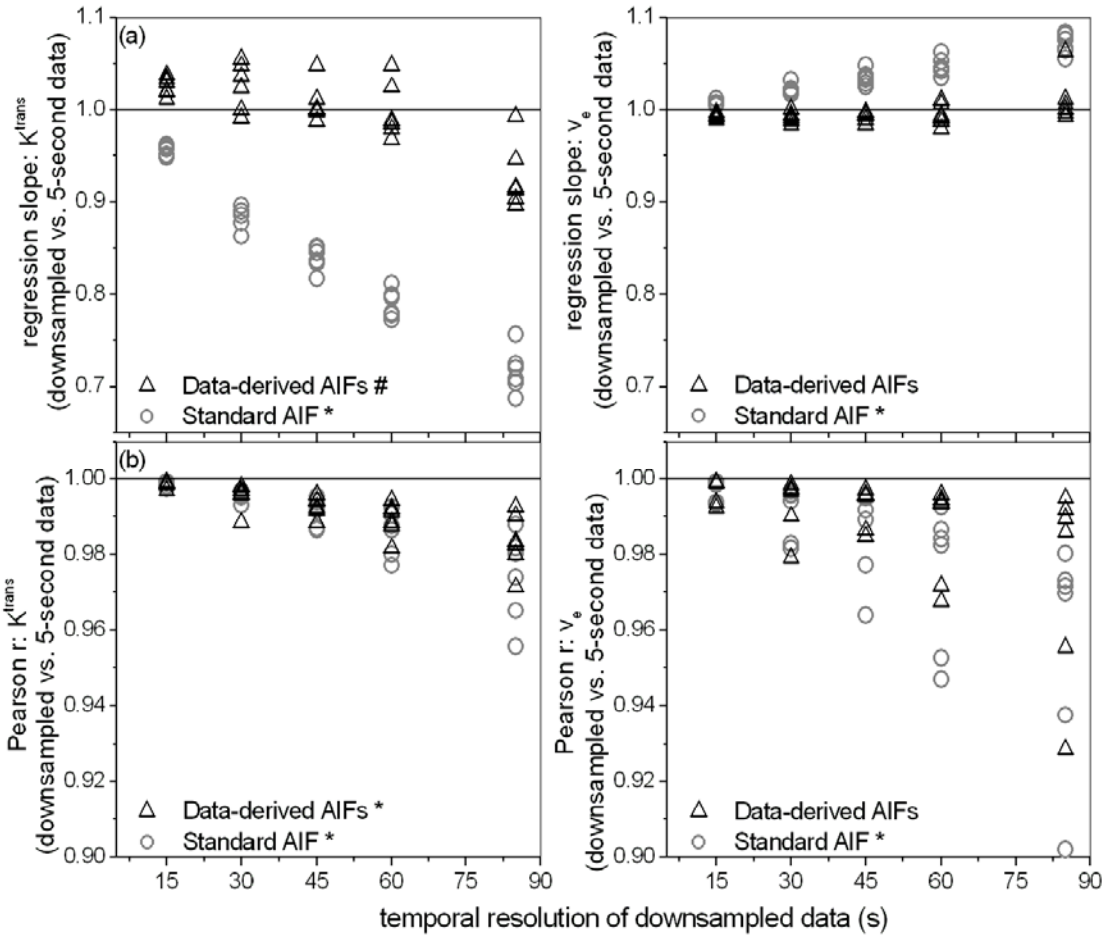

Figure 6.4 *(a) Summary of regression slopes and (b) Pearson correlation coefficients. The triangles represent the data (six animals) fitted with the data-derived AIFs, whereas the circles represent the data (same six animals) fitted with the single standard AIF. The same pattern as in Fig. 6.3 is seen for all animals: with the use of data-derived AIFs the regression slopes are closer to 1 than with the use of a single standard AIF. The Pearson correlation coefficient is high in general, but decreases with decreasing temporal resolution. This pattern is fairly similar for both methods. *Statistically significant influence of temporal resolution (multiple-comparison ANOVA: $p < 0.05$), #statistically significant influence of temporal resolution, but non-significant for the 15 s to 60 s resolution range.*

K^{trans} and v_e values were also calculated for each segmented tumor ROI as a whole, with both methods (data-derived vs. standard AIF). A marked difference was that with the use of a single standard AIF we saw a pattern of progressive under- and overestimation in K^{trans} and v_e, respectively, whereas with the use of data-derived AIFs the pattern was not as consistent. In Figure 6.5, we therefore compared the absolute deviations (mean of six animals) from the standard (5 s resolution data). This figure shows that the use of a standard AIF can introduce large deviations (e.g. mean deviation at 60 s resolution in K^{trans}: 18% in the range 15 – 20%), depending on the temporal resolution of the data at hand. The deviations introduced with the use of data-derived AIFs are more modest (e.g. mean deviation at 60 s resolution in K^{trans}: 2% in the range 1 – 5%).

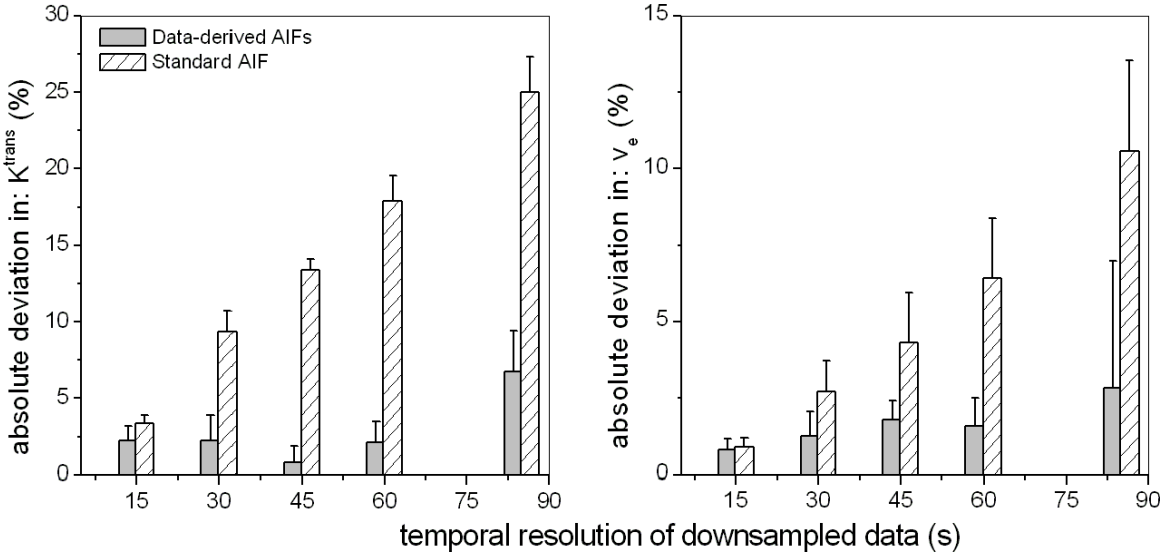

Figure 6.5 *Absolute percentage of deviation (mean taken over all six animals) from the standard in parameter estimates as a function of temporal resolution. In grey: use of data-derived AIFs; hatched: use of a single standard AIF. The standard deviations (six animals) are depicted as well. The use of data-derived AIFs results in a smaller and less temporal-resolution-dependent deviation from the standard than the use of a single standard AIF.*

6.4 Discussion

A comparison was made between K^{trans} and v_e estimates obtained with data-derived AIFs and a single standard AIF. In this experimental design, the standard AIF was mismatched only with the downsampled data sets in terms of temporal resolution. With both methods, good correlation was obtained between the downsampled data and the original 5 s data. However, with the single standard AIF we saw a consistent pattern of increasing under- and overestimation in K^{trans} and v_e, respectively, with decreasing temporal resolution. This was reflected in the regression slopes (see Fig. 6.3) and the

mean absolute deviations from the standard parameter values. This behavior was expected because the slope of the contrast uptake versus time in the tumor cannot be correctly captured at low-temporal resolutions, whereas the input (i.e. the standard AIF) remains the same. Even though this temporal-resolution-dependent bias can be expected, to our knowledge, it is not accounted for in fitting low-temporal-resolution data when using a standard AIF. When the data-derived AIFs were used, there was a significant temporal-resolution-dependent bias for the mean tumor uptake only at 85 s resolution. Probably, this marks the transition to temporal resolutions that are too low for the reference tissue AIF method to work well. For both methods, the Pearson correlation coefficients decreased slightly, yet statistically significantly (except for v_e obtained with data-derived AIFs), with decreasing temporal resolution, resulting in less precision. The use of data-derived AIFs led to more accurate results than the use of a standard AIF. In addition, the use of a standard AIF comes at the price of being non-specific.

It is surprising that, until sampling with a temporal resolution coarser than 60 s, the pharmacokinetic parameter estimates obtained with data-derived AIFs deviate little from the standard. We speculate that this is caused by a compensating effect: the apparent contrast agent uptake rate in muscle (α in the EMM) becomes smaller as temporal resolution decreases. The same happens for the tumor tissue. However, as long as the degrees of underestimation match, the ratio $K^{trans,tumor}/K^{trans,muscle}$ is fairly robust against a reduction in temporal resolution. We can show that this holds by looking at the early phase of contrast agent exchange (t << 1 min), when reflux (K^{trans}/v_e) from the EES to the blood plasma is negligible. During that initial phase, the integral form of the basic Tofts model can be expressed as

$$C_i(t) = K^{trans,i} \int_0^t C_p(\tau) \cdot e^{-K^{trans,i}(t-\tau)/v_{e,i}}\, d\tau \approx K^{trans,i} \int_0^t C_p(\tau) d\tau, \quad \text{for t << 1 min,} \qquad [6.3]$$

where 'i' stands for either 'tumor' or 'muscle'. Using Eq. 6.3, the following equality holds:

$$C_{tumor}(t)/C_{muscle}(t) = K^{trans,tumor}/K^{trans,muscle}, \text{ for t << 1 min.} \qquad [6.4]$$

For tumor tissue exhibiting a very high K^{trans}/v_e – $C_{tumor}(t)$ thereby resembles $C_p(t)$ – the first postcontrast measurement as part of a low-temporal-resolution acquisition may be post-peak. In that case, it is likely that the degrees of underestimation in the uptake rates of tumor and muscle tissue no longer match, and it is not possible to obtain a good estimate of $K^{trans,tumor}$. This 'boundary effect' at high $K^{trans}/v_e$was also described by Planey et al. (2009). Despite this effect, Li et al. (2009) demonstrated statistically significant differences in K^{trans} values between different breast tumor grades using a reference tissue AIF method at 88 s resolution. With our data we might have run into

this boundary at 85 s resolution, because at this resolution we observed a significant bias introduced into the pharmacokinetic parameters. However, the 'unfavorable' combination of large K^{trans} and small v_e did not occur frequently in these data.

With respect to the limitations of this study, we would like to address four themes as follows:

(i) *Simulating low-temporal-resolution data.* The applied downsampling strategy focused on the temporal aspects of enhancement, and did not incorporate changes in the SNR. In a real DCE-MRI scan, a reduction of temporal resolution (while keeping spatial resolution constant) would be expected to lead to an increase in the SNR of each image in the series. The effect of this increase in the SNR of individual images on the precision with which a dynamic process can be sampled is difficult to predict, since the SNR of the dynamic process (i.e. the enhancement of a specific feature) depends on the spatio-temporal pattern of enhancement and the dynamics of the k-space sampling pattern. This complicated issue was not addressed by the present simulations. By keeping the SNR constant for all temporal resolutions, we have calculated the outer bounds on deviations in K^{trans} and v_e. In addition, variations in the alignment of the sampling grid relative to bolus arrival (Henderson et al. 1998, Laue et al. 2007) were not taken into account. The time labels we attached to the downsampled images mark the time in between bolus arrival and completion of the specific image (i.e. full coverage in k-space). Other time labeling strategies could be applied; for instance using labels that mark the time in between bolus arrival and the acquisition of the center of k-space. This practice could however be hard to extrapolate to complicated 3D trajectories in the clinical setting, where time labeling is usually performed irrespective of k-space profile ordering. Because time labeling is closely coupled to AIF alignment and – in a clinical setting – performed without exact knowledge of bolus arrival time, this matter is very relevant with respect to the usage of a standard AIF, but is much less important with respect to the usage of a data-derived AIF. The reference tissue and the tumor tissue are acquired and labeled in the same fashion, therefore automatic alignment is obtained.

(ii) *Reference tissue AIF.* The reference tissue AIF method employed here uses a single reference tissue. AIF accuracy could be improved by using multiple reference tissues (Yang et al. 2007, Yang et al. 2010), or by combining the reference tissue method with a post-peak measurement in an artery (Fan et al. 2010b). An inherent assumption of the reference tissue method is that the AIF is the same for the reference tissue as for the tumor. This is not necessarily true, although the reference tissue is usually nearer to the tumor tissue than the 'feeding' artery (for breast this is often the aorta) in which a direct AIF measurement can be performed. In addition, recent research has demonstrated that the reference tissue AIF can be adjusted to produce a local tumor AIF (Fan and Karczmar 2009). In the present work, fixed literature values were assigned to

K^{trans} and v_e in the reference tissue, whereas in reality there is a natural range (for human skeletal muscle, see Padhani et al. 2002). This assignment is not a necessity; but, additional degrees of freedom in the fitting routine entail a greater potential variability. The method fails in the instance that there is no reference tissue available, and needs sensible constraints based on *a priori* knowledge about the expected shape of the contrast uptake at very low temporal resolution, owing to a lack of data to define the upslope.

(iii) *Pharmacokinetic model*. The basic Tofts model is assumed to model the contrast agent uptake in muscle as well as in tumor. Inclusion of the vascular fraction in the model (i.e. the extended Tofts model) would have required high-temporal resolution (Chapter 3, Faranesh and Yankeelov 2008), but its exclusion could have led to biases in K^{trans} and v_e. In addition, the model is applied under assumption of the fast exchange limit.

(iv) *Animal model*. The animal model used here has a systemic circulation time that is approximately three times shorter than in humans, which likely makes low temporal resolution more of a challenge for the analysis of rat data than of human data. It is unlikely that this difference in systemic circulation affects K^{trans} and $v_{e,}$ because they describe tissue properties on the micro scale. The used tumor model, however, only reflects a small portion of the large variety in tumor types.

The comparison between the use of data-derived AIFs and a single standard AIF demonstrated a large difference in impact of a change in temporal resolution. The pharmacokinetic parameter estimates for the mean tumor curve obtained with data-derived AIFs were not biased as long as temporal resolution was 60 s or better, whereas this was not the case for estimates obtained with a single standard AIF. The present study was based on data acquired from model tumors in rodents, and therefore it remains to demonstrate whether the conclusions hold for studies of patients. Nevertheless, these preliminary results are promising, and show that it is advisable to extract the AIF from a reference tissue when working with low-temporal-resolution data.

Relating these results to those presented in Chapter 3, we find that indeed, for this type of tumor, we can apply the basic Tofts model to data acquired with sampling times longer than 20 s, as was already speculated. This suggests that for pharmacokinetic analysis of diagnostic DCE-MRI breast data, the use of a reference tissue AIF will result in more accurate parameter estimates than the use of a standard AIF.

6.5 Acknowledgements

We would like to thank the following from the University of Chicago: D. Mustafi and M.A. Zamora for acquiring the data; C.R. Haney for fruitful discussions on data fitting; and E. Hipp for proofreading the manuscript. We would also like to thank Markus van Almsick from Eindhoven University of Technology for his mathematical modeling insights. This work was partly funded by NIH grant R33CA100996-02 and NIH grant P50 CA125183-01 (SPORE).

Chapter 7

Multi-parametric assessment of the anti-angiogenic effects of liposomal glucocorticoids

This chapter is based on:

E. Kluza, M. Heisen (co-first author), S. Schmid, D.W.J. van der Schaft, R.M. Schiffelers, G. Storm, B.M. ter Haar Romeny, G.J. Strijkers, K. Nicolay (submitted). "Multi-parametric assessment of the anti-angiogenic effects of liposomal glucocorticoids"

Abstract

Inflammation plays a prominent role in tumor growth propagation. Anti-inflammatory drugs have therefore been proposed as potential anti-cancer therapeutics. To reduce the high daily doses required for tumor growth inhibition and to reduce the adverse side effects of the therapy with free drug, glucocorticoids have been encapsulated in long-circulating liposomes. In the current study, we determined the anti-angiogenic activity of a single dose of liposomal prednisolone phosphate (PLP-L), by monitoring the tumor vascular functioning and tissue viability over a period of one week.

C57BL/6 mice were subcutaneously inoculated with B16F10 murine melanoma cells. Six animals were PLP-L-treated, whereas six served as control. *In vivo* tumor tissue properties were probed using MRI before and at three time points after treatment. Dynamic contrast-enhanced MRI data were used to provide measures of K^{trans}, v_e, time-to-peak, initial slope, and the fraction of non-enhancing pixels. Moreover, the values of the apparent diffusion coefficient (ADC) and T_2, as well as tumor size were assessed with MRI. After one week, tumor tissue was histologically examined for microvessel density and vessel wall characteristics.

Treatment with PLP-L resulted in significantly smaller tumor volumes compared to the control group. Vascular effects of PLP-L were manifested by a significant drop in tumor K^{trans} 48 h post-treatment, which was maintained until one week after drug administration. However, this effect was not large enough to significantly distinguish the treated from the non-treated animals. Therapy did not affect tumor tissue viability but did prevent the increase in cellular density that was observed in the control group as deduced from measurements of the ADC parameter. No evidence for PLP-L-induced tumor vessel normalization was found.

We demonstrated that treatment with PLP-L alters tumour vascular function. However, our results suggest that angiogenesis-related parameters are not sufficient to reveal the therapeutic response to PLP-L.

7.1 Introduction

Inflammation is a common feature of the tumor microenvironment, which, according to recent findings, plays a prominent role in tumor growth propagation (Coussens and Werb 2002, Mantovani et al. 2008). The close relationship between cancer and inflammatory processes prompted the idea of silencing tumor-associated inflammation for therapeutic purposes (Schiffelers and De Visser 2009). Consequently, anti-inflammatory drugs, widely used in clinical practice, have been proposed as potential anti-cancer therapeutics. One of these agents, celecoxib, has recently entered clinical trials, promising a valuable contribution of anti-inflammatory therapy to cancer prevention and treatment (Bhatt et al. 2010, Debucquoy et al. 2009, Mantovani et al. 2010, Sooriakumaran et al. 2009).

The anti-tumor activity of glucocorticoids (GCs), known as steroid anti-inflammatory agents, has been demonstrated in mouse tumor models (Folkman et al. 1983, Penhaligon and Camplejohn 1985). However adverse effects, caused by high daily doses necessary to achieve tumor growth inhibition, were found to be a major limitation. Recently, encapsulation into long-circulating liposomes was demonstrated to be an effective strategy to enhance intratumoral GC concentration (Schiffelers et al. 2005), as a result of favorable pharmacokinetic properties of liposomes (Drummond et al. 1999, Drummond et al. 2008) and the enhanced permeability and retention effect present in tumor tissue (Greish 2010). Importantly, the employment of the liposomal drug delivery system dramatically decreased the therapeutic dose and the dosing frequency compared to that of the free drug. For prednisolone phosphate (PLP), which was found to have the most favorable therapeutic index among investigated liposome-encapsulated GCs (Banciu et al. 2008a), a single intravenous injection of 20 mg PLP/kg/week was sufficient to significantly inhibit tumor growth in B16F10 melanoma and C26 colon carcinoma (Schiffelers et al. 2005).

Inhibition of angiogenesis was proposed to be a key effect of liposomal-GC therapy, leading to tumor growth delay (Schiffelers et al. 2005). Findings that support this hypothesis include a decreased expression of multiple pro-angiogenic factors (Banciu et al. 2006) and the inhibition of macrophage activity in the tumor (Banciu et al. 2008b), both of which play an important role in the process of neovascularisation. In addition, anti-proliferative effects of liposomal GC on endothelial cells were observed *in vitro* (Banciu et al. 2006, Banciu et al. 2008a). However, the influence of liposomal GC on the structure and the functioning of the tumor vasculature has not yet been investigated. The evaluation of the tumor vascular response is essential to fully characterize the anti-angiogenic activity of liposomal GC and to provide better understanding of the anti-tumor mechanism.

In this study, we therefore aimed to determine the anti-angiogenic potency of liposomal prednisolone phosphate (PLP-L) by studying its effect on the tumor

vasculature. The efficiency of a single dose of PLP-L (20 mg PLP/kg) was investigated in B16F10 murine melanoma during one week. For comprehensive characterization of the vascular status, both *in vivo* magnetic resonance imaging (MRI) and histological analyses were performed.

In vivo evaluation of the vascular changes induced by PLP-L was done using dynamic contrast-enhanced MRI (DCE-MRI). This method enables non-invasive characterization of the vessel functioning, based on the pharmacokinetics of a low-molecular-weight gadolinium chelate (Jackson et al. 2007). Due to their sensitivity to changes in vascular density and permeability, DCE-MRI-derived parameters, such as the endothelial transfer coefficient K^{trans}, serve as valuable *in vivo* markers of anti-angiogenic effects (O'Connor et al. 2007).

Furthermore, we investigated the effect of PLP-L on the tumor viability, since the expected vascular suppression may lead to cell death by limiting the availability of oxygen and nutrients to the rapidly multiplying tumor cells. For characterization of tissue viability, we used two DCE-MRI-derived parameters, i.e. the fraction of extravascular extracellular space (v_e) and the fraction of non-enhancing pixels; the former a measure of cellular density, the latter identifying areas of poor perfusion. Moreover, we assessed the apparent diffusion coefficient (ADC) and the transverse relaxation time (T_2), which are valuable complementary MR indicators of changes in the cellular density and the occurrence of local hemorrhages (Carano et al. 2004, Moffat et al. 2004).

As a final step of the vascular response assessment, we performed immunohistochemical examination of tumor tissues after the *in vivo* measurements, at the end of the study. Two aspects related to the anti-angiogenic activity of PLP-L were investigated. First, we determined the microvessel density (MVD), which is the most-established histological marker of the vascular status and response to anti-angiogenic therapy (Bertolini et al. 2007, Weidner et al. 1991). Secondly, we investigated whether PLP-L treatment induced tumor vessel normalization, an effect previously described for anti-angiogenic agents (Jain 2005). As a marker of vessel normalization / maturation we considered the presence of a smooth muscle layer around the vascular endothelium.

7.2 Materials and methods

7.2.1 Preparation and characterization of PLP-L

PLP-L were prepared as described previously (Metselaar et al. 2003). In short, DPPC (1,2-dipalmitoyl-*sn*-glycero-3-phosphocholine), cholesterol, and PEG2000-DSPE (1,2-distearoyl-*sn*-glycero-3-phosphoethanolamine-N-[methoxy(polyethylene glycol)-2000]), obtained from Avanti Polar Lipids (Albaster, AL, USA), were mixed at a molar ratio of 1.85/1/0.15. Subsequently, the lipids were dissolved in chloroform / methanol 1:1 (v/v) and dried by rotary evaporation. The dry lipid film was hydrated in an aqueous

solution of 100 mg/mL of prednisolone phosphate (PLP) (Fagron, Nieuwerkerk a/d IJssel, The Netherlands). The resulting multilamellar lipid vesicles were extruded (Lipofast Extruder, Avestin, Toronto, Canada) 6 times through polycarbonate membrane filters with a pore diameter of 200 nm and 100 nm (Costar, Cambridge, MA, USA) at 55° C. Non-encapsulated PLP was removed using dialysis in HEPES buffered saline (pH 7.4) (Sigma-Aldrich, St. Louis, MO, USA). A dialysis membrane with a molecular weight cut-off between 12 kDa and 14 kDa (Spectrum Laboratories Inc., CA, USA) was used. During 24 h of dialysis the buffer was repeatedly replenished. The final PLP-L preparation was stored at 4° C.

The mean diameter and size distribution of the liposomes were determined with dynamic light scattering (Zetasizer Nano, Malvern, UK) at 25° C. The phospholipid content in the liposome suspensions was assessed using phosphate analysis according to Rouser et al. 1970 and the concentration of liposome-encapsulated prednisolone phosphate was analyzed with high-performance liquid chromatography (Banciu et al. 2006). A mean diameter of 100 nm and a narrow size distribution (polydispersity index = 0.1) were determined for the prepared liposomes. The drug and the lipid concentrations were 5 mg/mL and 60 µmol/mL, respectively.

7.2.2 Murine tumor model

B16F10 murine melanoma cells were cultured as a monolayer at 37° C and 5% CO_2, in DMEM medium (1 g glucose/L) (Invitrogen, Breda, The Netherlands), supplemented with 10% fetal bovine serum (Greiner Bio-One, Alphen a/d Rijn, The Netherlands), 2 mmol/L L-glutamine (Lonza Bioscience, Basel, Switzerland), and 50 U/mL penicillin / streptomycin (Lonza Bioscience). The cell line originates from American Type Culture Collection (CRL-6475).

Six to eight week-old C57BL/6 mice (Charles River, Maastricht, The Netherlands) were subcutaneously inoculated with 1×10^6 B16F10 cells in the right flank. Between day 7 and 9 after inoculation, the tumors became palpable in all mice. The animal experiments were approved by the Institutional Ethical Review Committee for animal experiments of Maastricht University (The Netherlands).

7.2.3 Study timeline

The timeline of the study is presented in Figure 7.1(a). The pre-treatment MRI examination was performed on the day that tumors became palpable (Day 0). After the pre-treatment MRI scans were acquired, the animals received a single intravenous dose of either PLP-L (20 mg PLP/kg) (n = 6, PLP-L-treated group) or a corresponding volume of saline (n = 6, control group). The post-treatment MRI examinations were performed on Day 2, Day 4 and Day 6. The time frame of our study was chosen in view of the one-week-long therapeutic efficacy of PLP-L (Schiffelers et al. 2005) and the fast growth of B16F10 tumors. After MRI measurements on Day 6, the mice were sacrificed and the dissected tumors were immunohistochemically analyzed.

7.2.4 MRI acquisition

MRI measurements were performed with a 6.3 T scanner (Bruker, Biospin, Ettlingen, Germany), using a 3 cm birdcage coil (Rapid Biomedical, Rimpar, Germany). The mice were anesthetized with isoflurane and placed in a cradle equipped with a mask for anesthetic gas and a warm water pad. An infusion line filled with contrast agent was placed in the tail vein to enable injection during the MRI experiment. Respiration was monitored with a balloon sensor connected to an ECG / respiratory unit (Rapid Biomedical). The imaging protocol included a fat-suppressed multi-slice T_2-weighted spin-echo sequence (repetition time / echo time = 4200/35 ms, number of averages (NA) = 4) and a multi-slice diffusion-weighted spin-echo sequence (repetition time / echo time = 2000/35 ms, number of directions = 3, b-value = 0, 400 s/mm^2, NA = 2). Quantitative T_2 maps were obtained using a multi-echo method, consisting of a series of T_2-weighted spin-echo images with 16 different echo times varying from 9 ms to 144 ms (repetition time = 2000 ms, NA = 2). T_1-weighted dynamic contrast-enhanced series (radio-frequency-spoiled gradient echo, repetition time / echo time = 80/3.0 ms, flip angle = 50°, number of slices = 8) were acquired for a duration of 25 min with NA = 2 (n = 100, sampling time = 15.36 s), or NA = 1 (n = 200, sampling time = 7.68 s). A dose of 0.3 mmol/kg of Gadoteridol (Prohance, Bracco Diagnostics, Princeton, NJ, USA) was manually injected as a bolus in the tail vein 80 s after the start of acquisition. All acquired images had a matrix size of 128 × 128, field of view of 3 cm × 3 cm and 1 mm slice thickness. The image iso-center and orientation were the same for all scans.

7.2.5 MRI data analysis

Analysis of T_2- and diffusion-weighted images was performed in Mathematica 6.0 (Wolfram Research Inc., Champaign, IL, USA). Regions of interest (ROIs) were manually defined by drawing contours around the tumor area in every diffusion-weighted image slice in which the tumor was visible. T_2-weighted images served as an additional reference. Tumor volumes were calculated by multiplying the number of pixels in the tumor ROIs with the pixel volume. ADC maps were generated from fitting diffusion-weighted imaging data according to the equation

$$ADC = -1/b \, ln(S/S_0) \, , \qquad [7.1]$$

where S and S_0 are the respective signals at b = 400 s/mm^2 and b = 0 s/mm^2 (Stejskal and Tanner 1965). T_2 maps were calculated in each slice from mono-exponential-decay fitting of the multi-echo data.

DCE-MRI data processing was performed in Matlab (Mathworks, Natick, MA, USA). The analysis included those pixels within the tumor ROI that showed significant signal enhancement, i.e. enhancement equal to or greater than 5 times the noise level. The standard deviation of the noise was determined in air and corrected for the Rician distribution (Kaufman et al. 1989). The fraction of non-enhancing pixels in the total tumor area was quantified and used as a tissue-viability parameter.

The DCE-MRI signal intensity curves were converted to contrast agent concentration curves ($C_t(t)$) using a previously published reference method (Medved et al. 2004). The pre-contrast reference was taken from a user-defined ROI in muscle (5 x 5 voxels). A pre-contrast T_1 value of 1285 ms for muscle (Marzola et al. 1999) and a relaxivity value of 3.7 mM^{-1} s^{-1} for Gadoteridol (measured at 6.3 T at 20° C) were used in the calculations.

The $C_t(t)$ curves of the selected pixels of the tumor ROI were first analyzed by applying the basic two-compartment model by Tofts et al. (1999):

$$\frac{dC_t(t)}{dt} = K^{trans}\left(C_p(t) - \frac{C_t(t)}{v_e}\right), \qquad [7.2]$$

where v_e is the fraction of extravascular extracellular space (EES); K^{trans} (min^{-1}) is the volume transfer coefficient between blood plasma and EES; C_p (mM) is the contrast agent concentration in the blood plasma space, and C_t (mM) is the contrast agent concentration in the tissue of interest. The input function $C_p(t)$ was derived from the contrast agent uptake in skeletal muscle using the reference tissue approach (Kovar et al. 1998), assuming literature values for K^{trans} (0.11 min^{-1}) and v_e (0.20) (Kovar et al. 1998). To minimize noise propagation, the muscle curve was fitted with an empirical mathematical model (Fan et al. 2004) prior to this derivation. We used the first 5 min of the DCE-MRI scan. The fitting was performed with a golden section search method, by minimizing the goodness-of-fit measure R^2 (Press et al. 1996, see Chapter 2, Section 2.6.1). In addition to the applied enhancement threshold (enhancement ≥ 5 times the noise level), we excluded erroneous fits by discarding pixels with a v_e value equal to or greater than 0.95.

Secondly, the descriptive parameters time-to-peak (T_{peak}) and initial slope ($Slope_i$) were derived from the $C_t(t)$ curves (Szabo et al. 2003). T_{peak} (min) is the time elapsed between the start of enhancement and the time point at which the contrast agent concentration reached its maximum ($C_{t,peak}$). $Slope_i$ (mM/min) approximates the upslope of $C_t(t)$:

$$Slope_i = C_{t,peak}/T_{peak}. \qquad [7.3]$$

For consistency, also here only data acquired in the first 5 min were taken into account.

7.2.6 Immunohistochemical analysis of tumor tissues

Tumors were snap-frozen in isopentane and stored at -80° C. Five-µm-thick sections were cut and fixed with ice-cold acetone for 5 min. In order to assess microvessel density (MVD), endothelial cells were stained with rat anti-mouse CD31 primary antibody (BioLegend, San Diego, CA, USA). FITC-conjugated rabbit anti-rat IgG (Dako, Glostrup, Denmark) was used as a secondary antibody. For nuclear staining, DAPI (4,6'-diamidino-2-phenylindole, Molecular Probes, Eugene, Oregon, USA) was applied.

The tissue samples were examined with fluorescence microscopy (Zeiss, Sliedrecht, The Netherlands). MVD was assessed according to the method described by Weidner et al. (1991), i.e. by counting the number of vessels in five vascular regions of a section at 200× magnification. We also stained for smooth muscle cells, which are often lacking around tumorous vessels, to investigate vessel normalization. Staining was done with monoclonal anti-actin, α-smooth muscle-FITC antibody (Sigma-Aldrich). Co-staining was done with rat anti-mouse CD31 antibody (BioLegend) and Alexa Fluor 350-conjugated goat anti-rat IgG (Molecular Probes). The presence of normalized vessels was examined using fluorescence microscopy (Zeiss).

7.2.7 Statistical analysis

All data are reported as mean ± one standard deviation (SD). Statistical analysis was performed in SPSS 16.0 (SPSS Inc., Chicago, Illinois, USA). A t-test was used to assess the difference between tumor volumes of PLP-L-treated and control mice at different study time points. Statistical analysis of DCE-MRI data was performed on median, 25th, 75th, 95th percentile values and interquartile distance (distance between 25th and 75th percentile values), determined from histograms of K^{trans}, v_e, T_{peak} and $Slope_i$ for each data set (Furman-Haran et al. 2005). The comparison between the results obtained at different time points after drug or saline administration and the baseline readout was done using a paired t-test. The comparison of the longitudinal data obtained for both treated and control animals was done using mixed-factors ANOVA for repeated measures, where the within-subject factor was time and the between-subject factor was treatment. For this analysis, we used the relative change in the parameter with respect to its baseline value. The fraction of non-enhancing pixels, as well as ADC and T_2 data were tested using the same statistical methods as described above for the DCE-MRI-derived kinetic parameters. For ADC and T_2, the median was used as comparison parameter. The analysis of the MVD data was done using a t-test. In all analyses, the difference was considered significant at $P < 0.05$.

7.3 Results

7.3.1 Effects of PLP-L on tumor growth

To evaluate the effect of PLP-L on tumor growth we monitored lesion size over time, using high resolution MRI measurements. Tumor growth curves, which represent summarized data obtained for the PLP-L-treated and the control group, are presented in Figure 7.1(b). During the first days after PLP-L administration (Day 2 and 4), tumor volumes were not significantly affected by the treatment. The growth-inhibiting effect of PLP-L became evident on Day 6, which corresponds to previous findings (Banciu et al. 2008a, Schiffelers et al. 2005). At this time point, tumors of PLP-L-treated mice were on average a factor of two smaller than those of the control group.

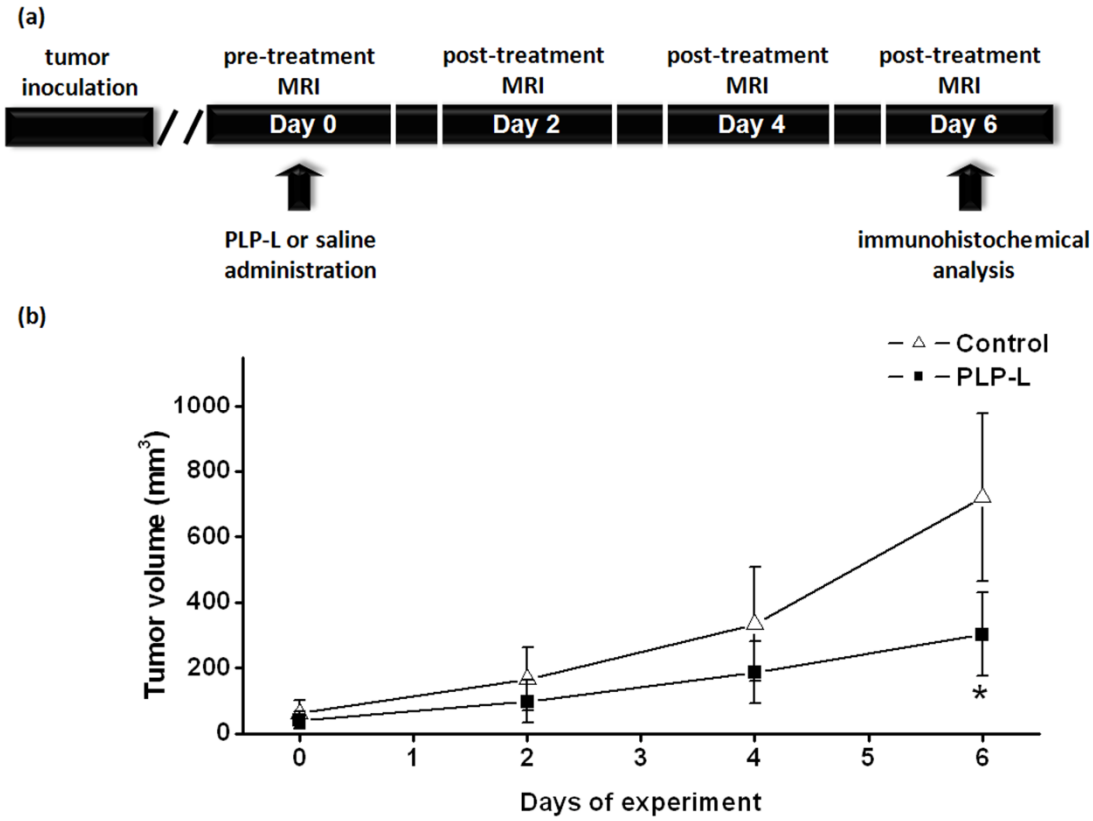

Figure 7.1 *(a) Timeline of the study, (b) tumor growth curves for PLP-L-treated and saline-treated mice (control) (mean ± SD, n = 6). *Significant difference in tumor volumes between PLP-L treated and control mice on Day 6.*

7.3.2 Evaluation of anti-angiogenic effects of PLP-L with DCE-MRI

As markers of vascular functioning we used K^{trans}, T_{peak} and $Slope_i$, estimated via mathematical modeling of dynamic contrast-enhanced data. Because v_e is a measure of cellular density rather than vessel functioning, it is discussed in the next section. All assessed parameters are summarized in Table 7.1, whereas representative MR images and K^{trans} maps obtained for PLP-L and control mice are presented in Figure 7.2. Large variability in DCE-MRI parameters was observed already in the pre-treatment measurements (Figure 7.3, Table 7.1), indicating natural inter-tumor differences in vascular functioning. Therefore, we used baseline measurements as a reference for the assessment of vascular effects.

Table 7.1 (next page) *Summary of the parameters obtained from the analysis of DCE-MRI data, expressed as mean ± SD (n = 6). *Significant change compared to baseline (Day 0) ($P < 0.05$).*

	PLP-L-treated K^{trans} (min^{-1})					Control K^{trans} (min^{-1})				
	median	25th percentile	75th percentile	95th percentile	interquartile distance	median	25th percentile	75th percentile	95th percentile	interquartile distance
Day 0	0.25±0.05	0.17±0.08	0.31±0.09	0.47±0.14	0.14±0.03	0.25±0.07	0.18±0.05	0.33±0.09	0.49±0.12	0.15±0.06
Day 2	0.19±0.04*	0.14±0.03*	0.25±0.05*	0.37±0.09	0.11±0.03*	0.22±0.07	0.15±0.05	0.30±0.09	0.44±0.16	0.15±0.05
Day 4	0.16±0.07*	0.11±0.06*	0.21±0.08*	0.35±0.11	0.09±0.03*	0.26±0.14	0.17±0.09	0.33±0.17	0.48±0.27*	0.16±0.09
Day 6	0.14 ± 0.02*	0.08±0.03*	0.22±0.04*	0.42±0.09	0.14±0.06	0.17±0.08*	0.10±0.06*	0.24±0.11*	0.39±0.14*	0.14±0.06
	v_e					v_e				
Day 0	0.31±0.10	0.22±0.09	0.45±0.14	0.73±0.15	0.23±0.10	0.38±0.09	0.29±0.07	0.52±0.13	0.76±0.13	0.23±0.11
Day 2	0.35±0.04	0.28±0.04	0.44±0.05	0.70±0.05	0.17±0.02	0.36±0.06	0.29±0.05	0.48±0.05	0.74±0.06	0.19±0.04
Day 4	0.34±0.14	0.26±0.13	0.46±0.13	0.74±0.08	0.20±0.03	0.41±0.04	0.32±0.02	0.52±0.06	0.77±0.07	0.21±0.06
Day 6	0.29±0.04	0.19±0.08	0.40±0.06	0.70±0.07	0.21±0.10	0.30±0.07	0.23±0.06	0.40±0.08	0.67±0.07	0.16±0.03
	T_{peak} (min)					T_{peak} (min)				
Day 0	1.63±0.60	0.99±0.39	2.83±0.65	3.91±0.21	1.84±0.54	2.03±0.64	1.07±0.43	3.26±0.34	3.86±0.13	2.20±0.37
Day 2	2.30±0.40	1.30±0.34	3.41±0.15	3.92±0.13	2.11±0.30	2.03±0.51	1.22±0.27	3.33±0.18	3.99±0.13*	2.11±0.28
Day 4	2.43±0.36*	1.34±0.32*	3.48±0.13*	3.92±0.13	2.13±0.26	2.00±0.74	1.15±0.54	3.22±0.46	3.86±0.13	2.07±0.48
Day 6	2.73±0.19*	1.51±0.25*	3.54±0.17*	3.86±0.13	2.03±0.13	2.39±0.83	1.41±0.64	3.33±0.31	3.84±0.16	1.92±0.44
	$Slope_i$ (mM/min)					$Slope_i$ (mM/min)				
Day 0	0.13±0.05	0.07±0.03	0.23±0.07	0.46±0.17	0.16±0.05	0.13±0.05	0.07±0.02	0.23±0.08	0.50±0.16	0.16±0.06
Day 2	0.09±0.02	0.06±0.01	0.18±0.04	0.38±0.09	0.12±0.03	0.12±0.04	0.06±0.03	0.21±0.08	0.45±0.21	0.15±0.06
Day 4	0.09±0.06	0.05±0.03	0.18±0.13	0.43±0.27	0.13±0.10	0.14±0.10	0.07±0.05	0.28±0.18	0.61±0.32	0.20±0.14
Day 6	0.06±0.01*	0.04±0.01	0.12±0.01*	0.40±0.17	0.08±0.01*	0.08±0.04*	0.04±0.01*	0.15±0.08*	0.35±0.12*	0.11±0.07*

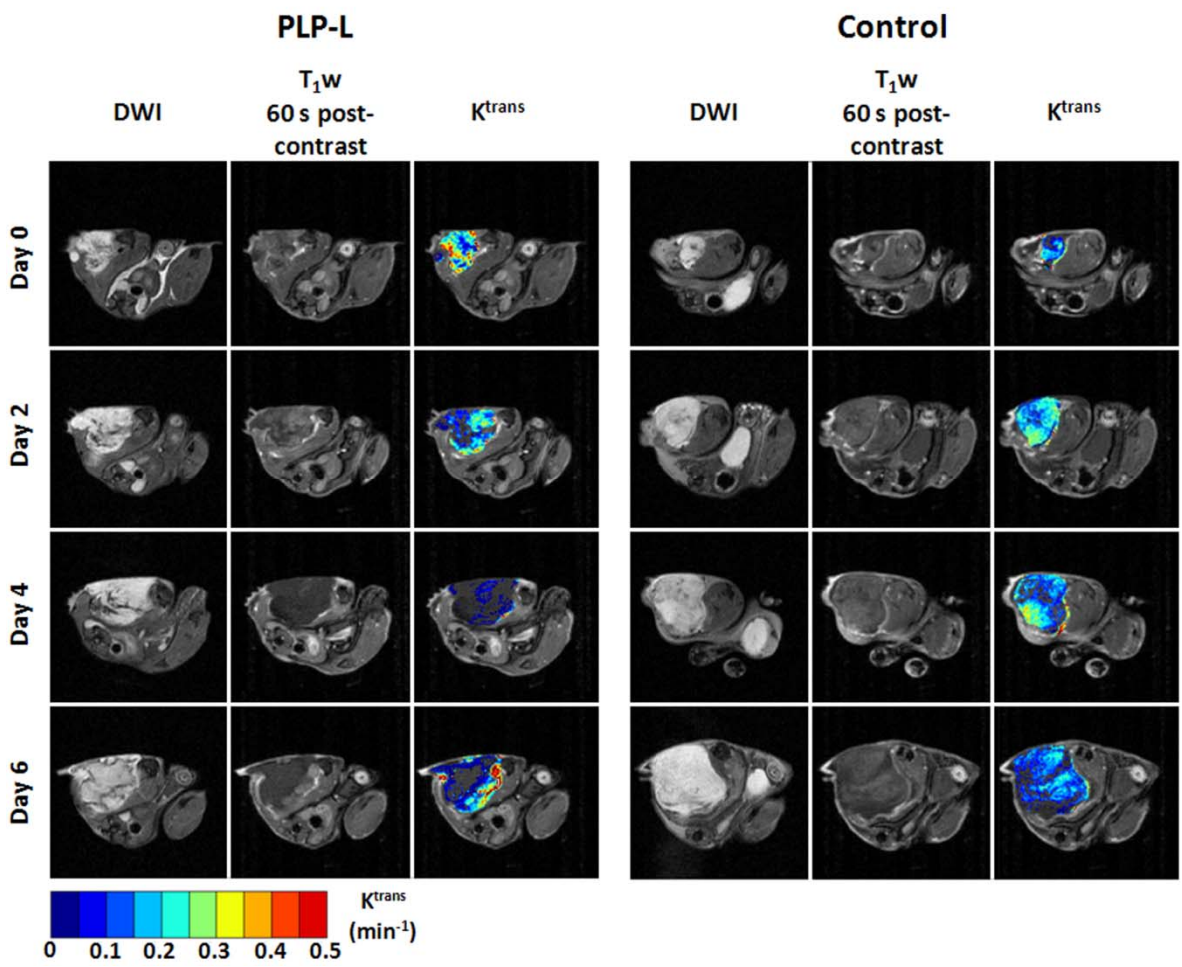

Figure 7.2 *Representative diffusion-weighted images (DWI), T_1-weighted images (T_1w) 60 s after start of enhancement, and corresponding K^{trans} maps obtained for a PLP-L-treated (left) and a control mouse (right) before (Day 0) and at different time points after PLP-L or saline (Control) administration.*

Within-group comparison

In all PLP-L-treated tumors, the first post-treatment examination revealed a reduced median K^{trans} (27 ± 14%) compared to the pre-treatment state (Figure 7.3(a)). A significant drop in median K^{trans} continued on Day 4 and 6, resulting, on average, in a 40% and 45% decrease, respectively. The same trend was observed for the 25th and 75th K^{trans} percentiles (Table 7.1). For the 95th percentile, which reflects the fraction of K^{trans} 'hot spots' often associated with intensive tumor growth (De Lussanet et al. 2005), no change was found at any time point (Table 7.1). Interestingly, the interquartile range was significantly decreased on Day 2 (25 ± 15%) and 4 (33 ± 25%), which indicates a more homogeneous distribution of K^{trans} values throughout the enhancing tumor area (Table 7.1). Apparently, a large portion of the tumor is affected in a positive sense, except for the 'hot spot' areas. However, as these high-K^{trans} areas

are often aggressive, therapeutic success could stand or fall by the permanence of these areas.

Time-to-peak (T_{peak}) was also clearly affected by the therapy: after an initial increase of 60% on Day 2, it was maintained at approximately the same level (Figure 7.3(c)). A significant therapy-induced drop in $Slope_i$ was observed only on Day 6. In contrast, in the control group, no significant change in any of the DCE-MRI parameters was observed, neither on Day 2 nor on Day 4 (Figure 7.3, Table 7.1). Surprisingly, on the last measurement day (Day 6) a decrease in median K^{trans} (40 ± 18%) and median $Slope_i$ (48 ± 18%) became apparent in the control group (Figure 7.3(a), (d)).

Between-groups comparison

To test whether the assessed kinetic parameters could serve as non-invasive imaging markers to distinguish responders from non-responders, we performed a statistical comparison between the longitudinal data obtained for the PLP-L-treated and the control group. The analysis revealed no significant influence of the PLP-L treatment on DCE-MRI-based markers compared to the control. This result refers to all assessed parameters, indicating that, under the present experimental conditions, DCE-MRI failed to distinguish the response to PLP-L treatment from the normal tumor development.

7.3.3 Evaluation of the tumor viability

The effect of PLP-L treatment on the tumor tissue viability was characterized by means of four MR parameters, i.e. v_e, the fraction of non-enhancing pixels, ADC, and T_2.

Within-group comparison

Both DCE-MRI-derived markers, i.e. v_e and the fraction of non-enhancing pixels, did not change significantly after administration of PLP-L (Figure 7.3(b), Table 7.1). Similarly, in the control group they remained stable over time. The results of ADC and T_2 measurements are summarized in Figure 7.4. Neither ADC nor T_2 were significantly affected by the treatment with PLP-L. The constant median values of ADC and T_2 of approximately 0.83×10^{-3} mm^2/s and 62 ms, respectively, throughout the investigation suggest that therapy did not cause necrotic changes in the tumor. Interestingly, for the control group we observed a decrease in median ADC over time (Figure 7.4(a)). A significant drop compared to the starting point was noted already on Day 2. The trend of decreasing ADC observed throughout the experiment suggests that the normal tumor growth is accompanied by an increase in cellular density. On the other hand, T_2 remained relatively stable (Figure 7.4(b)).

Between-groups comparison

For neither of the aforementioned viability parameters we found a significant influence of the PLP-L treatment compared to the control.

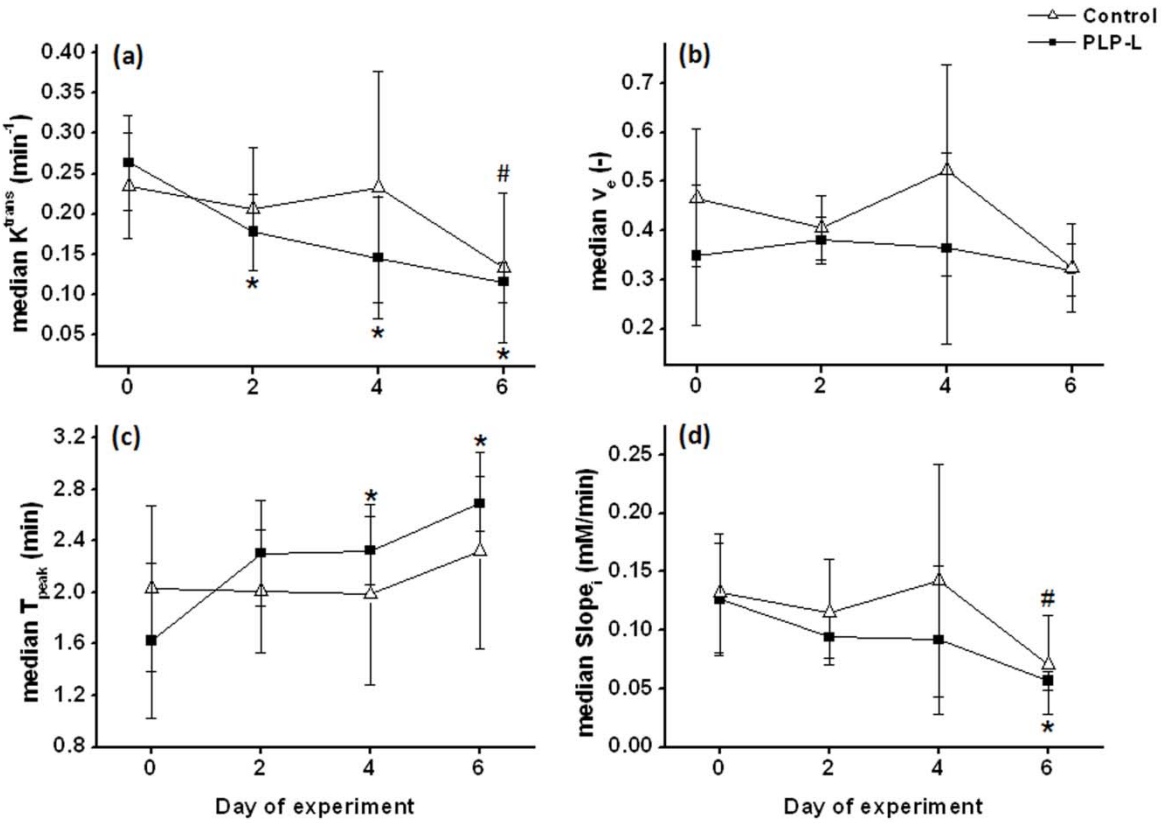

Figure 7.3 *Influence of PLP-L treatment on median (a) K^{trans}, (b) v_e, (c) T_{peak}, and (d) Slope$_i$ in the tumor, compared to the control (mean ± SD, n = 6). *Significant difference compared to baseline (Day 0) for PLP-L; #significant difference compared to baseline for control group (P < 0.05).*

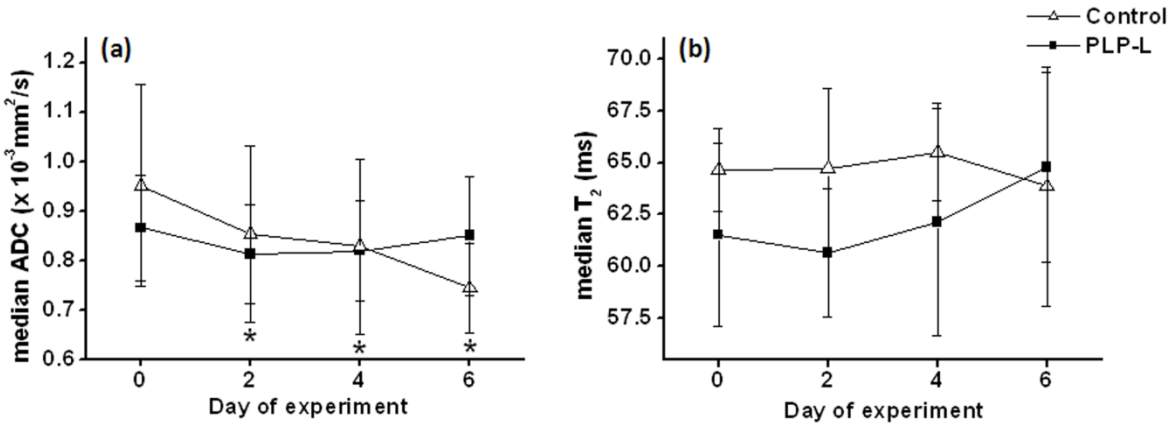

Figure 7.4 *Effect of PLP-L on median (a) apparent diffusion coefficient (ADC) and (b) transverse relaxation time (T_2) in the tumor compared to the control (mean ± SD, n = 6). *Significantly decreased median ADC values compared to baseline measurements for control.*

7.3.4 Microvessel density and vessel normalization

Ex vivo analysis of tumor tissues was performed after MRI experiments, thus, one week after administration of PLP-L or saline. First, we assessed the microvessel density (MVD). The summarized results of this analysis are presented in Figure 7.5. The average MVD of 34 vessels/mm^2 assessed in PLP-L-treated tumors was lower compared to 58 vessels/mm^2 in the control group. Nevertheless, statistical analysis did not confirm a significant difference in MVD. In addition, we investigated the correlation between MVD and K^{trans}, being important *ex vivo* and *in vivo* markers of the vascular status, respectively. However, we did not find a significant correlation (r^2 = 0.23).

To investigate vascular maturation, tumor sections were examined for the presence of a smooth muscle layer around the endothelium of tumor vessels. Both PLP-L- and control tumor sections were analyzed and compared to normal muscle tissue, which was used as a reference. In Figure 7.6(a), a normal vessel of the muscle is presented. It is characterized by a continuous rim of smooth muscle cells around the endothelium. We did not observe such well-formed vessels in both PLP-L-treated and control tumors (Figure 7.6(b), (c)). Predominantly, tumor vessel walls were composed of a bare endothelial cell layer. If smooth muscle staining was present in the tumor tissue, it appeared to be disturbed and poorly defined (Figure 7.6(c)). This observation refers to both the PLP-L-treated and the control group, which suggests that this is not a therapy-induced effect.

Figure 7.5 (next page) *(a) Representative fluorescence microscopy images of tumor sections from control and PLP-L-treated mice. CD31-stained endothelial cells are shown in green and cell nuclei in blue (DAPI). (b) Microvessel density (MVD) assessed for control (white bar) and PLP-L-treated (grey bar) tumors. Bars represent mean ± SD (n = 6).*

Figure7.6 (next page) *Representative fluorescence microscopy images of the tumor and surrounding muscle tissue. Anti-α-SMA staining for smooth muscle cells is shown in green and CD31 staining of endothelial cells in blue. (a) An example of a mature vessel in skeletal muscle, showing a ring of smooth muscle cells around the endothelium. (b) The border region between the tumor and the normal muscle tissue, containing anti-α-SMA-negative vessels (tumor) and multiple vessels with pronounced anti-α-SMA staining (indicated with white arrows in muscle tissue). (c) Tumor vasculature, among which a single vessel was found to have a discontinuous smooth muscle layer (indicated with white arrow and shown in a higher magnification in the inset).*

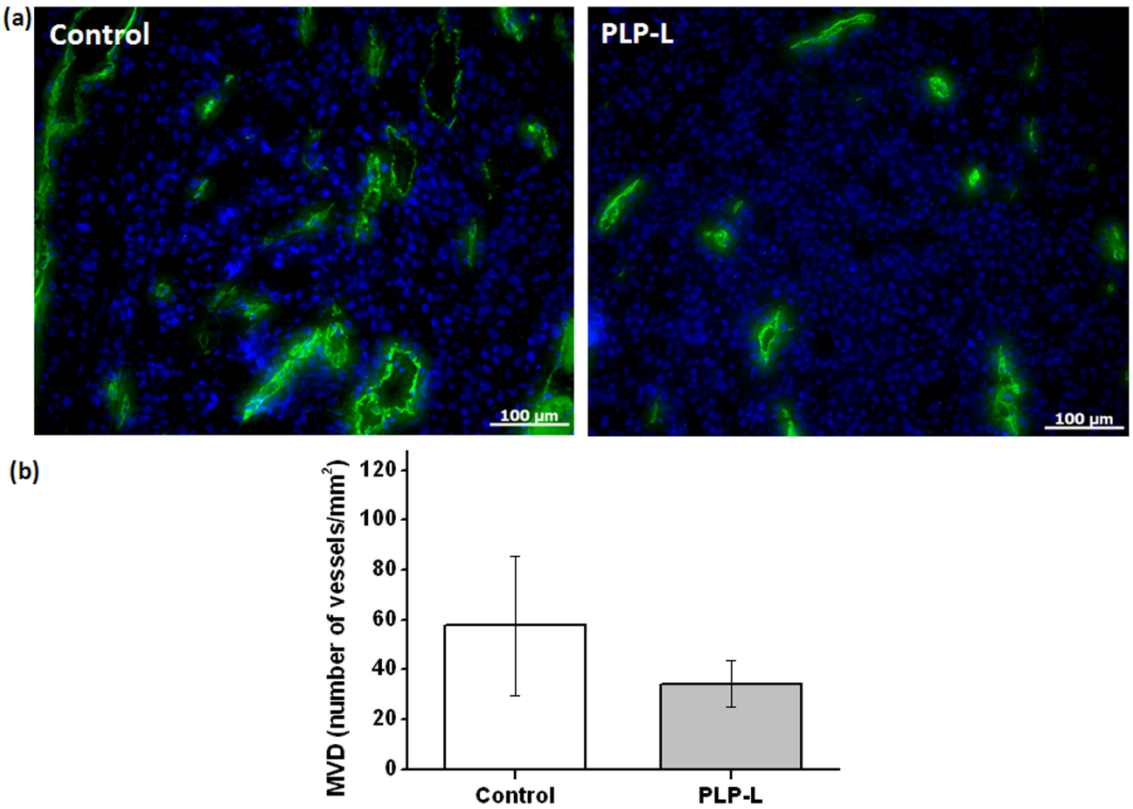

Figure 7.5

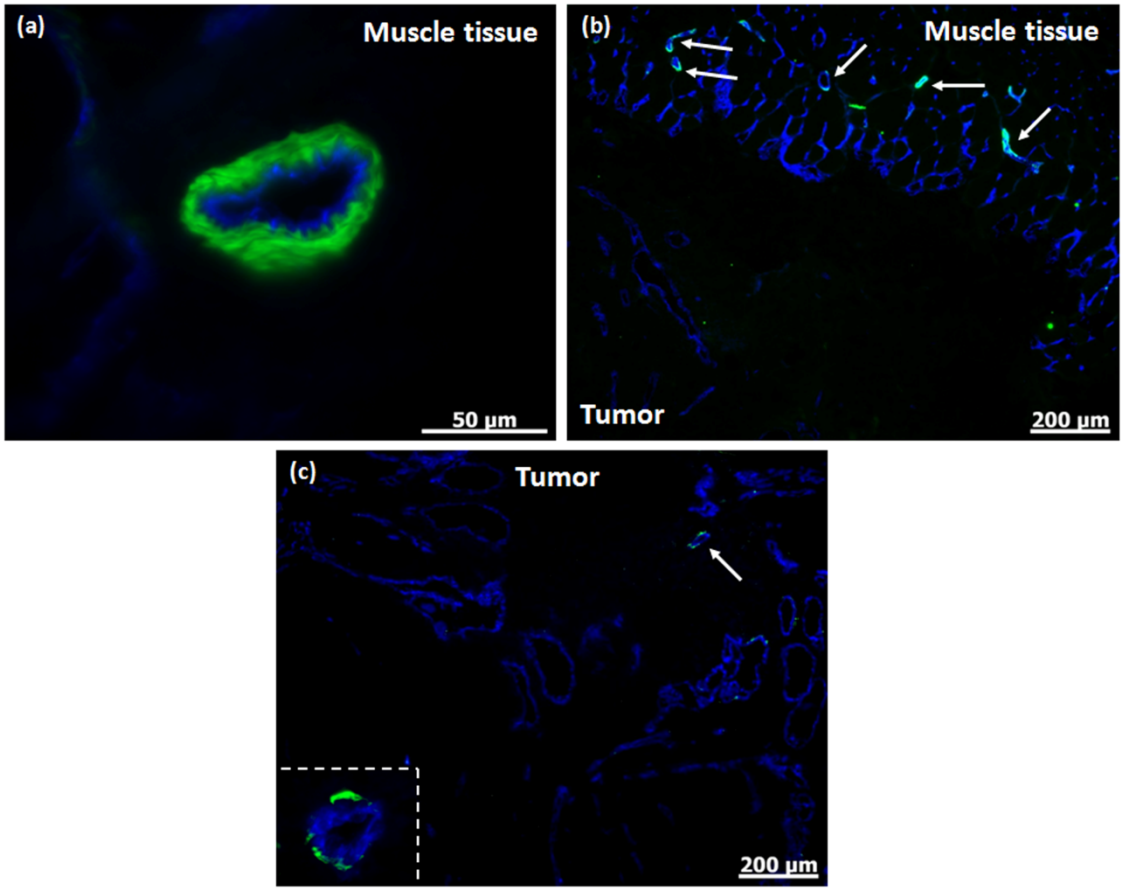

Figure7.6

7.4 Discussion

In the current study, we evaluated the response of tumor vasculature to PLP-L treatment using *in vivo* MRI and immunohistochemical analyses. DCE-MRI monitoring revealed therapy-induced vascular alterations that were manifested by a significant decrease in K^{trans} and concomitant increase in T_{peak}. At the same time, the treatment did not influence any of the MR parameters related to the tumor tissue viability. Interestingly, PLP-L administration prevented a drop in ADC values over time, which was observed in non-treated tumors. Surprisingly, the tumor growth in the control group was also accompanied by a significant decrease in K^{trans} and $Slope_i$ one week after the start of the experiment. Moreover, at this time point, neither a statistically important difference in MVD between the PLP-L-treated and the control group, nor signs of therapy-induced tumor vessel normalization were found. The current findings provide a rather complex picture of the vascular effects of PLP-L. On one hand, the DCE-MRI results support the thesis on angiogenesis inhibition underlying tumor growth suppression by PLP-L. However, we did not find a significant difference in vascular parameters between PLP-L-treated and control tumors, which we attribute to high inter-tumor variability and vascular alterations that accompany normal tumor development. These results underline the importance of an experimental setup with both a treatment and a control group.

In this study, we confirmed the previously reported inhibitory effect of PLP-L on the growth of B16F10 melanoma. The mechanisms underlying this effect may involve the complex interaction of the drug with the tumor microenvironment. Therefore, versatile techniques, such as MRI, which provide extensive morphological and functional information, are especially attractive for therapy evaluation. Moreover, the application of non-invasive methods facilitates translation from the preclinical to the clinical setting.

7.4.1 Evaluation of anti-angiogenic effects of PLP-L

To monitor the response of the tumor vasculature to therapy with PLP-L, we used DCE-MRI, which is currently the leading *in vivo* method for the assessment of anti-angiogenic effects (Leach et al. 2005b, O'Connor et al. 2007). Generally, we observed a large variability between individuals, starting already at the pre-treatment state. By using baseline measurements as a reference, we found significantly reduced median K^{trans} after the PLP-L treatment. Moreover, a decreased interquartile distance of K^{trans} distribution on Day 2 and 4 indicated a more homogenous tumor vascular functioning in PLP-L-treated mice. The suppressive effect on tumor vasculature was further supported by significantly increased T_{peak}. However, when the summarized data of the PLP-L-treated and the control mice were compared, no clear anti-angiogenic effect of PLP-L was detected. We believe that this is due to the aforementioned inter-tumor variability of vessel functioning, observed throughout the course of the experiment. Moreover, we found that non-treated tumors followed eventually the same trend of changes in vascular parameters as PLP-treated lesions. This occurred later

in time, on Day 6, indicating tumor growth-dependent factors as a source of the decreased vascular functioning in the control group. We avoided the interference of necrotic regions with these results, as non-enhancing pixels were excluded from DCE-MRI analysis. However, another important tumor tissue property, the interstitial fluid pressure, which is known to increase with tumor growth (Sevick and Jain 1989), could have played a role in the observed effect. Interestingly, on Day 6, we also did not find a significant difference in MVD between the PLP-L-treated and the control group. At the same time, MVD did not correlate with median K^{trans} assessed on Day 6. The dissociation between MRI-based and histopathological parameters can be explained by the different character of these measures (de Lussanet et al. 2005). Despite that, both DCE-MRI and histological readout led to the same conclusion that PLP-L did not affect the vasculature significantly compared to the control.

With the use of more complex pharmacokinetic modeling, the extraction of separate estimates of blood flow and permeability, as well as the vascular fraction v_p, might provide additional insights into the vascular effects of PLP-L (Donaldson et al. 2010). The basic Tofts model, as applied in this study, does not incorporate v_p as a model parameter. According to Henderson et al. (1998), for human data, that would require a temporal resolution of at least 4 s; and according to Chapter 3, at least 2 s (reference tissue AIF approach in common with current study). Separate estimates of flow and permeability instead of K^{trans} require an even higher temporal resolution; e.g. in Henderson et al. 2000, a temporal resolution of 0.5 s is used.

7.4.2 Evaluation of the tumor viability

As supportive parameters we used those related to the tumor tissue viability, i.e. v_e, the fraction of non-enhancing pixels, ADC, and T_2. We found that the PLP-L treatment did not result in significant changes in either of the aforementioned parameters, indicating undisturbed tumor-cell density and stable necrotic fraction. Interestingly, we reported a consistent decay of the tumor ADC over time in the control group. Since this was not observed after PLP-L administration, we can conclude that the treatment does not only affect the tumor size but also prevents an increase of tumor-cell density.

7.4.3 Reported effects of glucocorticoid treatment measured with MRI

The effects of GC therapy have been previously assessed in brain tumors with MR measurements, showing a significantly reduced mean diffusivity in peritumoral edematous brain and ADC in the tumor, as well as a reduced blood-tumor-barrier permeability after dexamethasone treatment (Bastin et al. 1999, Minamikawa et al. 2004). Armitage et al. (2007) observed significantly reduced K^{trans}, v_e, and v_p (the fractional plasma volume) 48-72 h post-treatment in glioblastoma, however not in meningioma and intracranial metastatic carcinoma, after treatment with the same drug. The use of a low-molecular-weight contrast agent may be more advantageous in

studying brain tumors than in studying tumors outside the brain, because of the much more limited permeability in healthy brain tissue. In the study by Crokart et al. (2007) a rapid-clearance blood pool agent P792 (Vistarem) was used instead; finding a significantly lower fraction of perfused pixels 30 min after hydrocortisone administration compared to the control. However, neither K^{trans}, v_p nor the redistribution rate constant k_{ep} were affected.

7.4.4 Distinction between responders and non-responders

An important aim of our investigation was to determine whether angiogenesis-related parameters are suitable markers of the therapeutic efficacy of PLP-L. Previous studies on the anti-angiogenic effects of PLP-L focused predominantly on molecular markers of angiogenesis. Banciu et al. (2006) reported a significantly reduced expression of the basic fibroblast growth factor and a wide range of inflammatory mediators involved in the process of angiogenesis. At the same time, the vascular endothelial growth factor was not affected by the treatment. We hypothesized that the diagnostic criteria used for angiogenesis inhibitors can be also applied for PLP-L. However, we found that neither MR nor histopathological vascular markers were capable of differentiating between the PLP-L-treated and the control tumors. This was surprising, since the PLP-L treatment resulted in an over 40% decrease in median K^{trans}, which is often considered a true positive response to the anti-angiogenic treatment (O'Connor et al. 2007). However, this was also observed for the control group on Day 6. Therefore, the assessed vascular parameters appear to be of limited value as biomarkers of the response to liposomal GC. Ideally, the biological endpoint should relate specifically to the mechanism of the therapeutic action. However, due to a broad spectrum of GC activities, the identification of a specific therapeutic marker might be very challenging. Considering the previous findings (Banciu et al. 2006, Banciu et al. 2008b), the most promising markers appear to be those related to the silencing effects of GC on the tumor-associated inflammation. The non-invasive assessment of this type of information requires the use of cellular and molecular imaging techniques.

7.4.5 Conclusion

We provided evidence that treatment with PLP-L suppresses the functioning of the tumor vasculature, which can subsequently lead to tumor growth inhibition. The anti-angiogenic effects of PLP-L were manifested by a significant drop in tumor K^{trans} 48 h post-treatment, which was maintained until one week after drug administration. However, we also observed naturally occurring vascular alterations in the control group. The obtained results suggest that angiogenesis monitoring does not provide sufficient information on the therapeutic efficacy of PLP-L. Therefore, more specific markers of the anti-tumor activity of liposomal glucocorticoids are desired. Among the potential candidates are those directly related to the suppression of inflammatory processes in the tumor.

7.5 Glucocorticoids as anti-cancer therapy: an ongoing debate

Glucocorticoids (GCs) are among the most effective anti-inflammatory and immunosuppressive agents (Franchimont 2004). In clinical oncology, they are included in all therapeutic regimes of lymphatic tissue malignancies (Coleman 1992). Moreover, they are used as a part of endocrine therapy in breast and prostate cancer, and as anti-edema agents in brain tumors (Coleman 1992, Herr and Pfitzenmaier 2006). GCs are also widely applied in prevention and treatment of chemotherapy-associated side effects, such as nausea and allergic reactions. However, the influence of GC on the growth of solid tumors is a topic of ongoing scientific debate. This is due to the unclear role of the glucocorticoid receptor in the regulation of malignant cells and the still controversial idea of anti-immune therapy as anti-cancer strategy (Coleman 1992, Herr and Pfitzenmaier 2006). Nevertheless, the broad spectrum of GC activities, including anti-inflammatory, anti-angiogenic, anti-edema, necrotic and apoptotic actions, appears to be very attractive for the treatment of such a complex disease as cancer. In contrast, other pre-clinical and, to some extent, clinical data suggest that GCs induce resistance to chemo- and radio-therapy and increase metastatic potential (Herr and Pfitzenmaier 2006). From the current study we can confirm that GCs suppress the functioning of the tumor vasculature, possibly leading to growth inhibition. However, as therapy did not result in a significant difference in vascular markers between the treated and control group, the significant effect of the PLP-L therapy on tumor growth suggests that the agent acts through other pathways as well.

7.6 Acknowledgements

This study was partly funded by the BSIK project entitled Molecular Imaging of Ischemic Heart Disease (project number BSIK03033), European Network of Excellence Diagnostic Molecular Imaging (DIMI, LSHB-CT-2005-512146), and the Integrated European Union Project Targeted Delivery of Nanomedicine (MEDITRANS, FP6-2004-NMP-NI-4/IP 026668-2). This study was performed in the framework of the European Cooperation in Science and Technology (COST) D38 Action Metal-Based Systems for Molecular Imaging Applications. We thank Louis van Bloois from Utrecht University for HPLC measurements.

Chapter 8

General discussion

In this work we provided a thorough discussion of the theoretical framework of quantitative analysis of DCE-MRI data, as well as practical guidance for its use. Although the application of the discussed models and methods is not limited to the context of DCE-MRI of the breast, we performed our investigation with that perspective in mind. In doing so, we focused on common clinical practice. A general discussion on issues that were not addressed in the preceding chapters will be given here, including future perspectives.

8.1 Standardization of quantitative analysis

As has been stressed previously, a wide-scale introduction of pharmacokinetic analysis into clinical practice will require more standardization in the field. It is somewhat ironic that pharmacokinetic modeling should be an answer to lacking standardization in acquisition techniques, but suffers from limited standardization itself as well. In addition, there is skepticism about the added value of pharmacokinetic analysis to current diagnostic practice; which could be related to its limited standardization. More research is needed to provide a larger body of evidence that pharmacokinetic assessment can or cannot improve diagnostics in combination with morphologic assessment. In this context it would be very interesting to (further) investigate the kinetics of non-mass-like enhancement, because the current descriptive curve-type modeling does not appear appropriate to assess such lesions.

8.2 Reference tissue AIF

From our work in Chapter 6 we conclude that with low-temporal-resolution data the AIF should be derived from a reference tissue. In DCE-MRI of the breast, the pectoralis muscles are the most likely candidates. However, the signal-to-noise ratio in the muscle tissue is often low. This could hinder its use as a reference tissue. As the muscle tissue is not of main interest, this aspect is usually not considered in the design of acquisition sequences and the choice of acquisition parameter settings. We think it should be.

8.3 Bolus arrival time

An under-exposed research topic in pharmacokinetic analysis is the bolus arrival time (Henderson et al. 1998, Kershaw and Buckley 2006, Laue et al. 2007). Especially with data at low-temporal resolution, a good estimate of bolus arrival time could improve pharmacokinetic parameter estimation. As it is likely that contrast agent will be arriving at the tissue of interest while acquiring for instance a 1 min image volume, bolus arrival time will usually not coincide with the start of a new dynamic volume. Intermediate readings of k-space, so before the full volume is acquired, could provide more detailed information about bolus arrival time.

8.4 Combining high-spatial and high-temporal resolution

To settle the 'battle' between spatial and temporal resolution, acquisition protocols incorporating both by use of smart k-space sampling schemes, like time-resolved imaging of contrast kinetics, or smart alternation between high / low spatial / temporal resolution should be considered. However, with partial k-space sampling it should be thoroughly tested what the implications are of low-temporal-resolution sampling of outer k-space in combination with high-temporal-resolution scanning of central k-space. Indeed, most information lies in the center of k-space, but not all information. Failure to detect enhancement in smaller structures such as foci or tumor rim could affect diagnostics.

8.5 Representative curve and kinetic maps

In this work we computed pharmacokinetic parameter values per voxel, as well as per region-of-interest using the mean uptake curve. The exception is Chapter 7, in which we investigated different measures derived from the histograms of the parameter distributions per lesion to assess treatment response. We however did not discuss how to find a summary measure of tumor kinetics for diagnostics. Especially a heterogeneous tumor will display many different contrast agent uptake patterns for different voxels within the tumor. So, how to represent tumor kinetics with a single descriptor in such a case? The BI-RADS guidelines (American College of Radiology 2003) recommend to place a region-of-interest (at least 3 pixels) on the most suspicious part of the tumor. As there is no consensus on whether this is the area with fastest enhancement or strongest wash-out, both are allowed. Some workstations will have software to provide a color-coded map of the three descriptive curve types, each type represented with a color and the color intensity reflecting the degree of initial enhancement. With such software an ROI can often be interrogated for statistics of kinetics. The step of manual ROI placement is likely to introduce inter-observer variability in the final diagnostic outcome. However, Baltzer et al. (2009) could not improve diagnostic performance by making use of computer-aided selection of the most-suspicious curve.

The use of pharmacokinetic analysis software is not (yet) wide-spread. With the automatic generation of pharmacokinetic maps, the radiologist may be confronted with several color-coded images, one for each model parameter. Probably, few radiologists have enough experience with pharmacokinetic modeling to combine the information from the different maps in their minds and use it for radiological assessment. An intuitive and user-friendly way of providing pharmacokinetic information will be necessary to enable wide-scale clinical use of such kinetic analysis techniques.

8.6 Motion artifacts

We did not address the correction of motion artifacts in this work. However, the absence / correction of motion during the acquisition of the dynamic contrast-enhanced

series is crucial for kinetic analysis. With motion, possibly many pixels will display erroneous enhancement patterns that could be mistakenly assessed as malignant / benign. Of course, pixel-wise kinetic mapping will suffer more from motion artifacts than ROI-wise interrogation of kinetics.

8.7 Quantitative morphologic assessment

We mentioned in the introduction that quantitative analysis is not necessarily restricted to kinetic analysis. The assessment of morphologic features using concentration images instead of signal intensity images would be interesting to pursue further. Such a study could be performed with a radiologist assessing the images or with automated calculation of morphologic features.

8.8 Signal calibration: model versus practice

In most literature, DCE-MRI signal quantification appears a 'done deal'. Usually a precontrast T_1 map is obtained making use of a variable flip angle approach and the spoiled gradient echo model is used to convert signal intensity to $T_1(t)$. In our view, there is however a large discrepancy between literature and clinical practice; many current dynamic acquisition protocols cannot be described with the spoiled gradient echo model. This issue is under-exposed in literature. Even if in theory the acquisition should be spoiled-gradient-echo based, likely there is a mismatch in practice because of advanced scan and filtering techniques. In most work it is not verified if the assumed signal model truly applies to the acquired data. This is also why we pursued the use of a calibration phantom; with such a phantom the theoretical signal model can be corrected, or the signal can be calibrated empirically.

8.9 Contrast agent relaxivity

To convert $T_1(t)$ to contrast agent concentration we make use of the relaxivity of the contrast agent. By using a fixed value, we assume that the effect of the contrast agent is the same on all protons regardless of their environment. However, it has been demonstrated that the relaxivity is affected by the concentration of macromolecules (Stanisz and Henkelman 2000), which can differ between different tissues / modeling compartments. Likely, the relaxivity in the calibration phantom compartments (Chapter 4) also differs from the relaxivity in tissue. In addition, magnetization transfer effects are also different in the presence of macromolecules. Both effects should be further investigated.

Despite the neglect of inter-tissue differences in relaxivity, the use of a fixed value could provide a certain level of standardization. However there is another issue, i.e., varying relaxivity values are reported for the same agents at the same field strength. Take gadodiamide (Gd-DTPA-BMA) as an example. Although the GE web pages (Omniscan, GE Healthcare, Piscataway, NJ, USA, product monograph) report that the relative image contrast was found to be independent of the applied field strength in the

range from 0.15 T up to 1.5 T (no relaxivity values reported), Rohrer et al. (2005) found significant dependency of gadodiamide (among other agents) relaxivity on the field strength and solvents. In water (37°C), they measured a relaxivity of 3.5 mM^{-1} s^{-1} at 0.47 T, of 3.3 mM^{-1} s^{-1} at 1.5 T, and of 3.2 mM^{-1} s^{-1} at 3 T. Comparing water to other solvents at 1.5 T, they found a relaxivity of 4.3 mM^{-1} s^{-1} in plasma (37°C), and of 4.6 mM^{-1} s^{-1} in blood (37°C). Examples of other reported relaxivity values for gadodiamide are: 4.5 mM^{-1} s^{-1} at 1.5 T (Yang et al. 2010), 3.9 mM^{-1} s^{-1} at 1.0 T (www.mr-tip.com), 3.3 mM^{-1} s^{-1} at 1.5 T (Park et al. 2008). For gadopentetate dimeglumine (Gd-DTPA, Magnevist, Berlex, Fairfield, NJ, USA), Donahue et al. (1994) reported no significant influence of different solvents (saline, plasma, cartilage) on the relaxivity at 8.45 T. The mean value was 4.0 mM^{-1} s^{-1}. However, Rohrer et al. (2005) reported a significant dependency on the field strength and solvents for this contrast agent as well. A more standardized use of relaxivity values could improve reproducibility and inter-institute comparisons.

8.10 Contrast agent size

One of the tissue properties probed with DCE-MRI is capillary vessel wall permeability. Permeability is a function of the wall pore size as well as the size of the contrast agent. The agent is most sensitive to permeability differences if the size of the agent closely matches the pore size (Henderson et al. 2000). Common gadolinium-based contrast agents are on the smaller end of the spectrum (< 1 kDa). Several preclinical studies have indicated that in tissues outside the brain larger contrast agents (~10-100 kDa, i.e. blood pool agents) are more effective to detect differences in vessel wall permeability (Adam et al. 1996, Brasch and Turetschek 2000, Daldrup et al. 1998). In this work, we studied DCE-MRI as performed in current practice, i.e. with a low-molecular-weight contrast agent. According to the above, this may mean that we did not use the most sensitive technique.

An additional advantage of the use of larger contrast agents would be less strict temporal sampling requirements, although the duration of the dynamic acquisition has to be increased (Jaspers et al. 2009). At present, there is only limited approval for the use of blood pool agents, but their use could potentially boost diagnostics. With these new agents the applicability of pharmacokinetic models has to be reinvestigated.

In studying the distribution of circulating low-molecular-weight drugs, conventional contrast agents are ideal, because they match the drugs in size (Brix et al. 2004). This is of particular interest for drug delivery to solid tumors as the systemically administered drug often cannot reach all target cells due to for instance poor perfusion and high interstitial pressure, which forms a major challenge for anti-cancer drug therapy (Jain 1997).

8.11 Assessment of treatment effects

In the assessment of treatment response, especially in case anti-vascular / anti-angiogenic agents are used, the common use of the basic Tofts model is probably not justified (Donaldson et al. 2010). In this model, the vascular contribution to the signal is ignored as well as the mean transit time. As it is the vascularity that the agents act upon, the data should be acquired in such a way that at least the extended Tofts model can be applied, providing a measure of the capillary fraction v_p. Moreover, to understand the mechanisms through which the vasculature is affected, it may be important to distinguish perfusion from permeability (Brix et al. 2010). With the use of higher temporal resolution data and an extended pharmacokinetic model we possibly could have found more clues about the mechanisms of the anti-inflammatory drug investigated in Chapter 7.

8.12 Use of animal data

In Chapters 5, 6, and 7 we made use of preclinical animal data. The rat data used in Chapters 5 and 6 were acquired for a study that assessed the anti-angiogenic effect of green tea (Fan et al. 2010a). The protocol was approved by the Animal Care and Use Committee of The University of Chicago. As in the current work these data were used in a simulation experiment to study the effect of low-temporal resolution which is not directly beneficial to patients – but provides a valuable indication that at low-temporal resolution the use of a reference tissue AIF method enables pharmacokinetic analysis – we consider it justifiable to 'recycle' data that were acquired for the assessment of an anti-cancer therapeutic. The therapeutic could be directly beneficial to patients, especially since green tea is widely available. By deriving simulated data at lower temporal resolutions from the original high-temporal-resolution data, there was no need for additional animal experiments.

In Chapter 7 we used mouse data to establish the best imaging markers for early evaluation of anti-cancer therapy with liposomal prednisolone phosphate. The protocol was approved by the Institutional Ethical Review Committee for animal experiments of Maastricht University. As cancer drug resistance is a severe problem in oncology and the novel therapeutic under study has already demonstrated to inhibit tumor growth, we think it important to study the mechanisms underlying this effect. As cell-stromal interaction is crucial for angiogenesis, these mechanisms cannot be studied in an *in vitro* environment. MRI allows for painless therapy monitoring and the use of *in vivo* imaging markers greatly reduced the number of animals necessary to perform a longitudinal study. Because such therapy monitoring with MRI is applicable to humans, it could be directly beneficial to patients. In a clinical setting these markers are important to distinguish responders from non-responders at an early time, preventing unnecessary treatment, resulting in a tailored therapy.

8.13 Concluding remarks

Challenges to arrive at meaningful clinical application of quantitative DCE-MRI of the breast are in particular:

- customized application of pharmacokinetic models, which is dictated by the quality of the data and the specifics of the pathology,
- standardization of pharmacokinetic parameter estimation methods,
- facilitation of reference tissue AIF methods,
- validated signal calibration,
- intuitive representation of the estimated tissue properties.

In this work we studied many aspects of DCE-MRI in great detail, in order to pave the road towards further clinical application. The presented results call for further testing in practice. We believe that pharmacokinetic analysis of common DCE-MRI breast data is achievable, and will improve diagnostic accuracy. The next step would be to demonstrate its added value to morphologic analysis as an alternative for descriptive kinetic analysis. Quantitative analysis will improve the much needed standardization, so we can provide all women undergoing DCE-MRI of the breast with an adequate and consistent diagnosis.

References

Adam G, Muhler A, Spuntrup E, Neuerburg J M, Kilbinger M, Bauer H, Fucezi L, Kupper W, and Gunther R W (1996). “Differentiation of spontaneous canine breast tumors using dynamic magnetic resonance imaging with 24-Gadolinium-DTPA-cascade-polymer, a new blood-pool agent. Preliminary experience” Invest Radiol, 31, 267-274

Aerts H J, van Riel N A, and Backes W H (2008). “System identification theory in pharmacokinetic modeling of dynamic contrast-enhanced MRI: influence of contrast injection” Magn Reson Med, 59, 1111-1119

American College of Radiology (2003). “Breast imaging reporting and data system: breast imaging atlas (BI-RADS), Magnetic resonance imaging” Fourth edition, Reston, USA, American College of Radiology

Aref M, Handbury J D, Xiuquan J J, Aref S, and Wiener E C (2007). “Spatial and temporal resolution effects on dynamic contrast-enhanced magnetic resonance mammography” Magn Reson Imaging, 25**,** 14-34

Armitage P A, Schwindack C, Bastin M E, and Whittle I R (2007). “Quantitative assessment of intracranial tumor response to dexamethasone using diffusion, perfusion and permeability magnetic resonance imaging” Magn Reson Imaging, 25, 303-310

Bains L J, Naish J H, and Buckley D L (2010). “Arterial input function correction and its impact on quantitative DCE-MRI: a comparison with DCE-CT” Proceedings ISMRM 18, Stockholm, Sweden, 3147

Baltzer P A, Freiberg C, Beger S, Vag T, Dietzel M, Herzog A B, Gajda M, Camara O, and Kaiser W A (2009). “Clinical MR-mammography: are computer-assisted methods superior to visual or manual measurements for curve type analysis? A systematic approach” Acad Radiol, 16, 1070-1076

Balvay D, Frouin F, Calmon G, Bessoud B, Kahn E, Siauve N, Clement O, and Cuenod C A (2005). “New criteria for assessing fit quality in dynamic contrast-enhanced T1-weighted MRI for perfusion and permeability imaging” Magn Reson Med, 54, 868-877

Banciu M, Fens M H, Storm G, and Schiffelers R M (2008a). “Antitumor activity and tumor localization of liposomal glucocorticoids in B16 melanoma-bearing mice” J Control Release, 127, 131-136

Banciu M, Metselaar J M, Schiffelers R M, and Storm G (2008b). “Antitumor activity of liposomal prednisolone phosphate depends on the presence of functional tumor-associated macrophages in tumor tissue” Neoplasia, 10, 108-117

Banciu M, Schiffelers R M, Fens M H, Metselaar J M, and Storm G (2006). “Anti-angiogenic effects of liposomal prednisolone phosphate on B16 melanoma in mice” J Control Release, 113, 1-8

Bastin M E, Delgado M, Whittle I R, Cannon J, and Wardlaw J M (1999). “The use of diffusion tensor imaging in quantifying the effect of dexamethasone on brain tumours” Neuroreport, 10, 1385-1391

Berg W A (2009). “Tailored supplemental screening for breast cancer: what now and what next?” Am J Roentgenol, 192, 390-399

Bertolini F, Mancuso P, Shaked Y, and Kerbel R S (2007). “Molecular and cellular biomarkers for angiogenesis in clinical oncology” Drug Discov Today, 12, 806-812

Bevington P R and Robinson D K (2003). “Data reduction and error analysis for the physical sciences” Third edition, New York, USA, Mc Graw Hill

Bhatt R S, Merchan J, Parker R, Wu H K, Zhang L, Seery V, Heymach J V, Atkins M B, McDermott D, and Sukhatme V P (2010). “A phase 2 pilot trial of low-dose, continuous infusion, or "metronomic" paclitaxel and oral celecoxib in patients with metastatic melanoma” Cancer, 116, 1751-1756

Bluemke D A et al. (2004). “Magnetic resonance imaging of the breast prior to biopsy” JAMA, 292, 2735-2742

Bonate P L (2006). “Pharmacokinetic-pharmacodynamic modeling and simulation” Second edition, New York, USA, Springer

Bottomley P A, Hardy C J, Argersinger R E, and len-Moore G (1987). “A review of 1H nuclear magnetic resonance relaxation in pathology: are T1 and T2 diagnostic?” Med Phys, 14, 1-37

Brasch R and Turetschek K (2000). “MRI characterization of tumors and grading angiogenesis using macromolecular contrast media: status report” Eur J Radiol., 34, 148-155

Brix G, Bahner M L, Hoffmann U, Horvath A, and Schreiber W (1999). “Regional blood flow, capillary permeability, and compartmental volumes: measurement with dynamic CT-initial experience” Radiology, 210, 269-276

Brix G, Griebel J, Kiessling F, and Wenz F (2010). “Tracer kinetic modelling of tumour angiogenesis based on dynamic contrast-enhanced CT and MRI measurements” Eur J Nucl Med Mol Imaging, 37, Suppl 1, S30-S51

Brix G, Kiessling F, Lucht R, Darai S, Wasser K, Delorme S, and Griebel J (2004). “Microcirculation and microvasculature in breast tumors: pharmacokinetic analysis of dynamic MR image series” Magn Reson Med, 52, 420-429

Brix G, Semmler W, Port R, Schad L R, Layer G, and Lorenz W J (1991). “Pharmacokinetic parameters in CNS Gd-DTPA enhanced MR imaging” J Comput Assist Tomogr, 15, 621-628

Brix G, Zwick S, Kiessling F, and Griebel J (2009). “Pharmacokinetic analysis of tissue microcirculation using nested models: multimodel inference and parameter identifiability” Med Phys, 36, 2923-2933

Brookes J A, Redpath T W, Gilbert F J, Needham G, and Murray A D (1996). “Measurement of spin-lattice relaxation times with FLASH for dynamic MRI of the breast” Br J Radiol, 69, 206-214

Buckley D L (2002a). “Transcytolemmal water exchange and its affect on the determination of contrast agent concentration in vivo” Magn Reson Med, 47, 420-424

Buckley D L (2002b). “Uncertainty in the analysis of tracer kinetics using dynamic contrast-enhanced

T1-weighted MRI" Magn Reson Med, 47, 601-606

Buckley D L (2010a). "Modeling and Quantitative Analysis: from Simple to Complex" Proceedings ISMRM 18, Stockholm, Sweden, A22

Buckley D L (2010b). "Multimodality imaging of tumor angiogenesis:perfusion modeling for tumor angiogenesis" Proceedings ISMRM 18, Stockholm, Sweden, E09

Buckley D L, Kershaw L E, and Stanisz G J (2008). "Cellular-interstitial water exchange and its effect on the determination of contrast agent concentration in vivo: dynamic contrast-enhanced MRI of human internal obturator muscle" Magn Reson Med, 60, 1011-1019

Buckley D L, Roberts C, Parker G J, Logue J P, and Hutchinson C E (2004). "Prostate cancer: evaluation of vascular characteristics with dynamic contrast-enhanced T1-weighted MR imaging – initial experience" Radiology, 233, 709-715

Cao Y, Brown S L, Knight R A, Fenstermacher J D, and Ewing J R (2005). "Effect of intravascular-to-extravascular water exchange on the determination of blood-to-tissue transfer constant by magnetic resonance imaging" Magn Reson Med, 53, 282-293

Carano R A, Ross A L, Ross J, Williams S P, Koeppen H, Schwall R H, and Van B N (2004). "Quantification of tumor tissue populations by multispectral analysis" Magn Reson Med, 51, 542-551

Cheng H L (2008). "Investigation and optimization of parameter accuracy in dynamic contrast-enhanced MRI" J Magn Reson Imaging, 28, 736-743

Choyke P L, Dwyer A J, and Knopp M V (2003). "Functional tumor imaging with dynamic contrast-enhanced magnetic resonance imaging" J Magn Reson Imaging, 17, 509-520

Coleman R E (1992). "Glucocorticoids in cancer therapy" Biotherapy, 4, 37-44

Coleman T F and Li Y (1992). "A reflective Newton method for minimizing a quadratic function subject to bounds on some of the variables" Technical Report (TR92-1315), Ithaca, New York, USA, Cornell University

Conover W J (1980). "Practical nonparametric statistics" Second edition, New York, USA, John Wiley and Sons

Coussens L M and Werb Z (2002). "Inflammation and cancer" Nature, 420, 860-867

Crokart N et al. (2007). "Glucocorticoids modulate tumor radiation response through a decrease in tumor oxygen consumption" Clin Cancer Res, 13, 630-635

Crone C (1963). "The permeability of capillaries in various organs as determined by use of the 'indicator diffusion' method" Acta Physiol Scand, 58, 292-305

Daldrup H, Shames D M, Wendland M, Okuhata Y, Link T M, Rosenau W, Lu Y, and Brasch R C (1998). "Correlation of dynamic contrast-enhanced MR imaging with histologic tumor grade: comparison of macromolecular and small-molecular contrast media" AJR Am J Roentgenol, 171, 941-949

Damen A A H (2003). "Physiological processes and parameter estimation, 5Q240, Eindhoven, The

Netherlands, Measurement and control group, department of electrical engineering, Eindhoven University of Technology

De Bazelaire C, Siauve N, Fournier L, Frouin F, Robert P, Clement O, de K E, and Cuenod C A (2005). “Comprehensive model for simultaneous MRI determination of perfusion and permeability using a blood-pool agent in rats rhabdomyosarcoma” Eur Radiol, 15, 2497-2505

De Lussanet Q G, Backes W H, Griffioen A W, Padhani A R, Baeten C I, van B A, Lambin P, Beets G L, van Engelshoven J M, and Beets-Tan R G (2005). “Dynamic contrast-enhanced magnetic resonance imaging of radiation therapy-induced microcirculation changes in rectal cancer” Int J Radiat Oncol Biol Phys, 63, 1309-1315

Debucquoy A, Roels S, Goethals L, Libbrecht L, Van C E, Geboes K, Penninckx F, D'Hoore A, McBride W H, and Haustermans K (2009). “Double blind randomized phase II study with radiation+5-fluorouracil+/-celecoxib for resectable rectal cancer” Radiother Oncol, 93, 273-278

Deoni S C, Rutt B K, and Peters T M (2003). “Rapid combined T1 and T2 mapping using gradient recalled acquisition in the steady state” Magn Reson Med, 49, 515-526

Di Giovanni P, Azlan C A, Ahearn T S, Semple S I, Gilbert F J, and Redpath T W (2010). “The accuracy of pharmacokinetic parameter measurement in DCE-MRI of the breast at 3 T” Phys Med Biol, 55, 121-132

Donahue K M, Burstein D, Manning W J, and Gray M L (1994). “Studies of Gd-DTPA relaxivity and proton exchange rates in tissue” Magn Reson Med, 32, 66-76

Donahue K M, Weisskoff R M, and Burstein D (1997). “Water diffusion and exchange as they influence contrast enhancement” J Magn Reson Imaging, 7, 102-110

Donahue K M, Weisskoff R M, Chesler D A, Kwong K K, Bogdanov A A, Jr., Mandeville J B, and Rosen B R (1996). “Improving MR quantification of regional blood volume with intravascular T1 contrast agents: accuracy, precision, and water exchange” Magn Reson Med, 36, 858-867

Donaldson S B, West C M, Davidson S E, Carrington B M, Hutchison G, Jones A P, Sourbron S P, and Buckley D L (2010). “A comparison of tracer kinetic models for T1-weighted dynamic contrast-enhanced MRI: application in carcinoma of the cervix” Magn Reson Med, 63, 691-700

Drummond D C, Meyer O, Hong K, Kirpotin D B, and Papahadjopoulos D (1999). “Optimizing liposomes for delivery of chemotherapeutic agents to solid tumors” Pharmacol Rev, 51, 691-743

Drummond D C, Noble C O, Hayes M E, Park J W, and Kirpotin D B (2008). “Pharmacokinetics and in vivo drug release rates in liposomal nanocarrier development” J Pharm Sci, 97, 4696-4740

Eliat P A et al. (2004). “Magnetic resonance imaging contrast-enhanced relaxometry of breast tumors: an MRI multicenter investigation concerning 100 patients” Magn Reson Imaging, 22, 475-481

El Khouli R H, Macura K J, Barker P B, Habba M R, Jacobs M A, and Bluemke D A (2009). “Relationship of temporal resolution to diagnostic performance for dynamic contrast enhanced MRI of the breast” J Magn Reson Imaging, 30, 999-1004

El Khouli R, Jacobs M, Wei J, Barker P, Macura K, and Bluemke D (2008). “Dynamic Contrast Enhanced

MRI of the Breast: Kinetic curve analysis to determine the optimal temporal resolution" Proceedings ISMRM 16, Toronto, Canada, 3751

Fan X, Mustafi D, Zamora M, River J N, Foxley S, Karczmar G S (2010a). "Can DCEMRI assess the effect of green tea on the angiogenic properties of rodent prostate tumors?" Phys Med, 26, 111-6

Fan X, Haney C R, Mustafi D, Zamora M, Markiewicz E J, and Karczmar G S (2010b). "Use of a reference tissue and blood vessel to measure the arterial input function in DCEMRI" Magn Reson Med, n/a doi: 10.1002/mrm.22551

Fan X and Karczmar G S (2009). "A new approach to analysis of the impulse response function (IRF) in dynamic contrast-enhanced MRI (DCEMRI): a simulation study" Magn Reson Med, 62, 229-239

Fan X, Medved M, Karczmar G S, Yang C, Foxley S, Arkani S, Recant W, Zamora M A, Abe H, and Newstead G M (2007). "Diagnosis of suspicious breast lesions using an empirical mathematical model for dynamic contrast-enhanced MRI" Magn Reson Imaging, 25, 593-603

Fan X, Medved M, River J N, Zamora M, Corot C, Robert P, Bourrinet P, Lipton M, Culp R M, and Karczmar G S (2004). "New model for analysis of dynamic contrast-enhanced MRI data distinguishes metastatic from nonmetastatic transplanted rodent prostate tumors" Magn Reson Med, 51, 487-494

Faranesh A Z and Yankeelov T E (2008). "Incorporating a vascular term into a reference region model for the analysis of DCE-MRI data: a simulation study" Phys Med Biol, 53, 2617-2631

Faranesh A Z, Kraitchman D L, and McVeigh E R (2006). "Measurement of kinetic parameters in skeletal muscle by magnetic resonance imaging with an intravascular agent" Magn Reson Med, 55, 1114-1123

Flannery B P and Teukolsky S A (1992). "Numerical recipes in C, The art of scientific computing" Second edition, New York, USA, Cambridge University Press

Folkman J, Langer R, Linhardt R J, Haudenschild C, and Taylor S (1983). "Angiogenesis inhibition and tumor regression caused by heparin or a heparin fragment in the presence of cortisone" Science, 221, 719-725

Fram E K, Herfkens R J, Johnson G A, Glover G H, Karis J P, Shimakawa A, Perkins T G, and Pelc N J (1987). "Rapid calculation of T1 using variable flip angle gradient refocused imaging" Magn Reson Imaging, 5, 201-208

Franchimont D (2004). "Overview of the actions of glucocorticoids on the immune response: a good model to characterize new pathways of immunosuppression for new treatment strategies" Ann NY Acad Sci, 1024, 124-137

Fritz-Hansen T, Rostrup E, Larsson H B, Sondergaard L, Ring P, and Henriksen O (1996). "Measurement of the arterial concentration of Gd-DTPA using MRI: a step toward quantitative perfusion imaging" Magn Reson Med, 36, 225-231

Furman-Haran E, Margalit R, Grobgeld D, and Degani H (1996). "Dynamic contrast-enhanced magnetic resonance imaging reveals stress-induced angiogenesis in MCF7 human breast tumors" Proc Natl

Acad Sci USA, 93, 6247-6251

Furman-Haran E, Schechtman E, Kelcz F, Kirshenbaum K, and Degani H (2005). “Magnetic resonance imaging reveals functional diversity of the vasculature in benign and malignant breast lesions” Cancer, 104, 708-718

Gal Y, Mehnert A, Bradley A, McMahon K, and Crozier S (2007). “An evaluation of four parametric models of contrast enhancement for dynamic magnetic resonance imaging of the breast” Conf Proc IEEE Eng Med Biol Soc 2007, 71-74

Galbraith S M (2006). “MR in oncology drug development” NMR Biomed, 19, 681-689

Galbraith S M, Lodge M A, Taylor N J, Rustin G J, Bentzen S, Stirling J J, and Padhani A R (2002). “Reproducibility of dynamic contrast-enhanced MRI in human muscle and tumours: comparison of quantitative and semi-quantitative analysis” NMR Biomed, 15, 132-142

Garpebring A, Ostlund N, and Karlsson M (2009). “A novel estimation method for physiological parameters in dynamic contrast-enhanced MRI: application of a distributed parameter model using Fourier-domain calculations” IEEE Trans Med Imaging, 28, 1375-1383

Gibbons J D and Chakraborti S (2003). “Nonparametric Statistical Inference” Fourth edition, New York, USA, Dekker M.

Gilhuijs K G, Deurloo E E, Muller S H, Peterse J L, and Schultze Kool L J (2002). “Breast MR imaging in women at increased lifetime risk of breast cancer: clinical system for computerized assessment of breast lesions initial results” Radiology, 225, 907-916

Gjedde A (1995). “Tracer kinetics” Second edition, Philadelphia, USA, Saunders, “Principles of nuclear medicine” 451-461

Greish K (2010). “Enhanced permeability and retention (EPR) effect for anticancer nanomedicine drug targeting” Methods Mol Biol, 624, 25-37

Haacke E M et al. (2007). “New algorithm for quantifying vascular changes in dynamic contrast-enhanced MRI independent of absolute T1 values” Magn Reson Med, 58, 463-472

Hamilton W F et al. (1948). “Comparison of the Fick and dye injection methods of measuring the cardiac output in man” Am J Physiol, 153, 309-321

Harmatz J S and Greenblatt D J (1987). “A simplex procedure for fitting nonlinear pharmacokinetic models” Comput Biol Med, 17, 199-208

Harrer J U, Parker G J, Haroon H A, Buckley D L, Embelton K, Roberts C, Baleriaux D, and Jackson A (2004). “Comparative study of methods for determining vascular permeability and blood volume in human gliomas” J Magn Reson Imaging, 20, 748-757

Heilmann M, Kiessling F, Enderlin M, and Schad L R (2006). “Determination of pharmacokinetic parameters in DCE MRI: Consequence of nonlinearity between contrast agent concentration and signal intensity” Invest Radiol, 41, 536-543

Heisen M, Buurman J, Vilanova A, Twellmann T, and Gerritsen F A (2007). “Impact of the arterial input

function on the classification of contrast-agent uptake curves in dynamic contrast-enhanced (DCE) MR images based on heuristic shape modeling" Proceedings ECR 2007, Vienna, Austria.

Heisen M, Fan X, Buurman J, van Riel N A, Karczmar G S, and ter Haar Romeny B M (2010a). "The influence of temporal resolution in determining pharmacokinetic parameters from DCE-MRI data" Magn Reson Med, 63, 811-816

Heisen M, Fan X, Buurman J, van Riel N A W, Karczmar G S, and ter Haar Romeny B M (2010b). "The use of a reference tissue arterial input function with low-temporal-resolution DCE-MRI data" Phys Med Biol, 55, 4871-4883

Heisen M, Twellmann T, Buurman J, Vilanova A, Gerritsen F A, and ter Haar Romeny B M (2007). "The influence of temporal resolution and phase-encoding order on shape-based classification of dynamic contrast enhanced (DCE) MRI uptake curves in the breast" ISMRM 15, Berlin, Germany, 133

Henderson E, Rutt B K, and Lee T Y (1998). "Temporal sampling requirements for the tracer kinetics modeling of breast disease" Magn Reson Imaging, 16, 1057-1073

Henderson E, Sykes J, Drost D, Weinmann H J, Rutt B K, and Lee T Y (2000). "Simultaneous MRI measurement of blood flow, blood volume, and capillary permeability in mammary tumors using two different contrast agents" J Magn Reson Imaging, 12, 991-1003

Herr I and Pfitzenmaier J (2006). "Glucocorticoid use in prostate cancer and other solid tumours: implications for effectiveness of cytotoxic treatment and metastases" Lancet Oncol, 7, 425-430

Heywang S H, Wolf A, Pruss E, Hilbertz T, Eiermann W, and Permanetter W (1989). "MR imaging of the breast with Gd-DTPA: use and limitations" Radiology, 171, 95-103

Heywang-Kobrunner S H et al. (2001). "International investigation of breast MRI: results of a multicentre study (11 sites) concerning diagnostic parameters for contrast-enhanced MRI based on 519 histopathologically correlated lesions" Eur Radiol, 11, 531-546

Hittmair K, Gomiscek G, Langenberger K, Recht M, Imhof H, and Kramer J (1994). "Method for the quantitative assessment of contrast agent uptake in dynamic contrast-enhanced MRI" Magn Reson Med, 31, 567-571

Hoffmann U, Brix G, Knopp M V, Hess T, and Lorenz W J (1995). "Pharmacokinetic mapping of the breast: a new method for dynamic MR mammography" Magn Reson Med, 33, 506-514

Houssami N, Ciatto S, Macaskill P, Lord S J, Warren R M, Dixon J M, and Irwig L (2008). "Accuracy and surgical impact of magnetic resonance imaging in breast cancer staging: systematic review and meta-analysis in detection of multifocal and multicentric cancer" J Clin Oncol, 26, 3248-3258

Huang W et al. (2010). "Approaching Complete Separation of Benign and Malignant Breast Lesions by DCE-MRI: Impact on Healthcare Costs" Proceedings ISMRM 18, Stockholm, Sweden, 368

Huang W, Li X, Morris E A, Tudorica L A, Seshan V E, Rooney W D, Tagge I, Wang Y, Xu J, and Springer C S (2008). "The magnetic resonance shutter speed discriminates vascular properties of malignant

and benign breast tumors in vivo" Proc Natl Acad Sci USA, 105, 17943-17948

Huisman H J, Veltman J, Karssemeijer N, Boetes C, Blickman J G, and Barentsz J O (2006). "Computer-aided diagnosis of breast MRI using pharmacokinetic modeling" Proceedings RSNA 2006, Chicago, USA, SSC17-09

Hulka C A, Smith B L, Sgroi D C, Tan L, Edmister W B, Semple J P, Campbell T, Kopans D B, Brady T J, and Weisskoff R M (1995). "Benign and malignant breast lesions: differentiation with echo-planar MR imaging" Radiology, 197, 33-38

Iman R L, Helton J C, and Campbell J E (1981). "An Approach to Sensitivity Analysis of Computer-Models. 1. Introduction, Input Variable Selection and Preliminary Variable Assessment" Journal of Quality Technology, 13, 174-183

Jackson A, Buckley D L, and Parker G J M (2005). "Dynamic Contrast-Enhanced Magnetic Resonance Imaging in Oncology" First edition, Berlin-Heidelberg, Germany, Springer-Verlag

Jackson A, O'Connor J P, Parker G J, and Jayson G C (2007). "Imaging tumor vascular heterogeneity and angiogenesis using dynamic contrast-enhanced magnetic resonance imaging" Clin Cancer Res, 13, 3449-3459

Jain R K (1997). "The Eugene M. Landis Award Lecture 1996. Delivery of molecular and cellular medicine to solid tumors" Microcirculation, 4, 1-23

Jain R K (2005). "Normalization of tumor vasculature: an emerging concept in antiangiogenic therapy" Science, 307, 58-62

Jansen S A, Newstead G M, Abe H, Shimauchi A, Schmidt R A, and Karczmar G S (2007). "Pure ductal carcinoma in situ: kinetic and morphologic MR characteristics compared with mammographic appearance and nuclear grade" Radiology, 245, 684-691

Jansen S A, Paunesku T, Fan X, Woloschak G E, Vogt S, Conzen S D, Krausz T, Newstead G M, and Karczmar G S (2009). "Ductal carcinoma in situ: X-ray fluorescence microscopy and dynamic contrast-enhanced MR imaging reveals gadolinium uptake within neoplastic mammary ducts in a murine model" Radiology, 253, 399-406

Jansen S A, Shimauchi A, Zak L, Fan X, Wood A M, Karczmar G S, and Newstead G M (2009). "Kinetic curves of malignant lesions are not consistent across MRI systems: need for improved standardization of breast dynamic contrast-enhanced MRI acquisition" AJR Am J Roentgenol, 193, 832-839

Jaspers K, Aerts H J, Leiner T, Oostendorp M, van Riel N A, Post M J, and Backes W H (2009). "Reliability of pharmacokinetic parameters: small vs. medium-sized contrast agents" Magn Reson Med, 62, 779-787

Johnson J A and Wilson T A (1966). "A model for capillary exchange" Am J Physiol, 210, 1299-1303

Kaiser W A and Zeitler E (1989). "MR imaging of the breast: fast imaging sequences with and without Gd-DTPA. Preliminary observations" Radiology, 170, 681-686

Kaufman L, Kramer D M, Crooks L E, and Ortendahl D A (1989). "Measuring signal-to-noise ratios in MR

imaging" Radiology, 173, 265-267

Kershaw L E and Buckley D L (2006). "Precision in measurements of perfusion and microvascular permeability with T1-weighted dynamic contrast-enhanced MRI" Magn Reson Med, 56, 986-992

Kershaw L E, Hutchinson C E, and Buckley D L (2009). "Benign prostatic hyperplasia: evaluation of T1, T2, and microvascular characteristics with T1-weighted dynamic contrast-enhanced MRI" J Magn Reson Imaging, 29, 641-648

Kety S S (1951). "The theory and applications of the exchange of inert gas at the lungs and tissues" Pharmacol Rev, 3, 1-41

Kim S, Quon H, Loevner L A, Rosen M A, Dougherty L, Kilger A M, Glickson J D, and Poptani H (2007). "Transcytolemmal water exchange in pharmacokinetic analysis of dynamic contrast-enhanced MRI data in squamous cell carcinoma of the head and neck" J Magn Reson Imaging, 26, 1607-1617

Kim Y R, Rebro K J, and Schmainda K M (2002). "Water exchange and inflow affect the accuracy of T1-GRE blood volume measurements: implications for the evaluation of tumor angiogenesis" Magn Reson Med, 47, 1110-1120

Kirkup L (2002). "Data analysis with Excel: An introduction for physical scientists" First edition, Cambridge USA, Cambridge University Press

Koh T S, Zeman V, Darko J, Lee T Y, Milosevic M F, Haider M, Warde P, and Yeung I W (2001). "The inclusion of capillary distribution in the adiabatic tissue homogeneity model of blood flow" Phys Med Biol, 46, 1519-1538

Kose U, Buurman J, Zak L, Newstead G M, and Morsch K (2010). "Inter-observer agreement in the use of MR BI-RADS descriptors: A retrospective study" Proceedings RSNA 2010, Chicago, USA, n/a

Kovar D A, Lewis M, and Karczmar G S (1998). "A new method for imaging perfusion and contrast extraction fraction: input functions derived from reference tissues" J Magn Reson Imaging, 8, 1126-1134

Kuhl C K (2007a). "Breast MR imaging at 3T" Magn Reson Imaging Clin N Am, 15, 315-20, vi

Kuhl C K (2007b). "The current status of breast MR imaging. Part I. Choice of technique, image interpretation, diagnostic accuracy, and transfer to clinical practice" Radiology, 244, 356-378

Kuhl C K, Kuhn W, Braun M, and Schild H (2007). "Pre-operative staging of breast cancer with breast MRI: one step forward, two steps back?" Breast, 16, Suppl 2, S34-S44

Kuhl C K, Mielcareck P, Klaschik S, Leutner C, Wardelmann E, Gieseke J, and Schild H H (1999). "Dynamic breast MR imaging: are signal intensity time course data useful for differential diagnosis of enhancing lesions?" Radiology, 211, 101-110

Kuhl C K, Schild H H, and Morakkabati N (2005a). "Dynamic bilateral contrast-enhanced MR imaging of the breast: trade-off between spatial and temporal resolution" Radiology, 236, 789-800

Kuhl C K, Schrading S, Leutner C C, Morakkabati-Spitz N, Wardelmann E, Fimmers R, Kuhn W, and Schild H H (2005b). “Mammography, breast ultrasound, and magnetic resonance imaging for surveillance of women at high familial risk for breast cancer” J Clin Oncol, 23, 8469-8476

Lammertsma A A, Brooks D J, Beaney R P, Turton D R, Kensett M J, Heather J D, Marshall J, and Jones T (1984). “In vivo measurement of regional cerebral haematocrit using positron emission tomography” J Cereb Blood Flow Metab, 4, 317-322

Landis C S, Li X, Telang F W, Coderre J A, Micca P L, Rooney W D, Latour L L, Vetek G, Palyka I, and Springer C S, Jr. (2000). “Determination of the MRI contrast agent concentration time course in vivo following bolus injection: effect of equilibrium transcytolemmal water exchange” Magn Reson Med, 44, 563-574

Landis C S, Li X, Telang F W, Molina P E, Palyka I, Vetek G, and Springer C S, Jr. (1999). “Equilibrium transcytolemmal water-exchange kinetics in skeletal muscle in vivo” Magn Reson Med, 42, 467-478

Larsson H B and Tofts P S (1992). “Measurement of blood-brain barrier permeability using dynamic Gd-DTPA scanning--a comparison of methods” Magn Reson Med, 24, 174-176

Larsson H B, Stubgaard M, Frederiksen J L, Jensen M, Henriksen O, and Paulson O B (1990). “Quantitation of blood-brain barrier defect by magnetic resonance imaging and gadolinium-DTPA in patients with multiple sclerosis and brain tumors” Magn Reson Med, 16, 117-131

Laue H O, Althaus M, Behrens S, Hahn H K, and Peitgen H-O (2007). “Dependency of parameter estimates for the Tofts model on temporal sampling rate and on bolus arrival time” Proceedings ISMRM 15, Berlin, Germany, 1722

Leach M O et al. (2005a). “Screening with magnetic resonance imaging and mammography of a UK population at high familial risk of breast cancer: a prospective multicentre cohort study (MARIBS)” Lancet, 365, 1769-1778

Leach M O et al. (2005b). “The assessment of antiangiogenic and antivascular therapies in early-stage clinical trials using magnetic resonance imaging: issues and recommendations” Br J Cancer, 92, 1599-1610

Lehman C D et al. (2005). “Screening women at high risk for breast cancer with mammography and magnetic resonance imaging” Cancer, 103, 1898-1905

Lerski R A and de Certaines J D (1993). “Performance assessment and quality control in MRI by Eurospin test objects and protocols” Magn Reson Imaging, 11, 817-833

Li J, Yu Y, Zhang Y, Bao S, Wu C, Wang X, Li J, Zhang X, and Hu J (2009). “A clinically feasible method to estimate pharmacokinetic parameters in breast cancer” Med Phys, 36, 3786-3794

Li K L, Zhu X P, Waterton J, and Jackson A (2000). “Improved 3D quantitative mapping of blood volume and endothelial permeability in brain tumors” J Magn Reson Imaging, 12, 347-357

Li X, Rooney W D, and Springer C S, Jr. (2005). “A unified magnetic resonance imaging pharmacokinetic theory: intravascular and extracellular contrast reagents” Magn Reson Med, 54, 1351-1359

Liney G P, Gibbs P, Hayes C, Leach M O, and Turnbull L W (1999). “Dynamic contrast-enhanced MRI in the differentiation of breast tumors: user-defined versus semi-automated region-of-interest analysis” J Magn Reson Imaging, 10, 945-949

Litjens G J S, Heisen M, Buurman J, and ter Haar Romeny B M (2010). “Pharmacokinetic models in clinical practice: What model to use for DCE-MRI of the breast?” Proceedings IEEE International Symposium on Biomedical Imaging 2010, Rotterdam, The Netherlands, 185-188

Litjens G J S, Heisen M, Buurman J, Wood A M, Medved M, Karczmar G S, and ter Haar Romeny B M (2009). “T1 quantification: Variable flip angle method vs. use of reference phantom” RSNA 2009, Chicago, USA, 422

Lopata R G, Backes W H, van den Bosch P P, and van Riel N A (2007). “On the identifiability of pharmacokinetic parameters in dynamic contrast-enhanced imaging” Magn Reson Med, 58, 425-429

Lord S J, Lei W, Craft P, Cawson J N, Morris I, Walleser S, Griffiths A, Parker S, and Houssami N (2007). “A systematic review of the effectiveness of magnetic resonance imaging (MRI) as an addition to mammography and ultrasound in screening young women at high risk of breast cancer” Eur J Cancer, 43, 1905-1917

Mann R M, Kuhl C K, Kinkel K, and Boetes C (2008). “Breast MRI: guidelines from the European Society of Breast Imaging” Eur Radiol, 18, 1307-1318

Mantovani A, Allavena P, Sica A, and Balkwill F (2008). “Cancer-related inflammation” Nature, 454, 436-444

Mantovani G, Maccio A, Madeddu C, Serpe R, Antoni G, Massa E, Dessi M, and Panzone F (2010). “Phase II nonrandomized study of the efficacy and safety of COX-2 inhibitor celecoxib on patients with cancer cachexia” J Mol Med, 88, 85-92

Marzola P, Mocchegiani E, Nicolato E, Tibaldi A, Sbarbati A, and Osculati F (1999). “Chemical shift imaging at 4.7 tesla of thymus in young and old mice” J Magn Reson Imaging, 10, 97-101

Mattheij R and Molenaar J (2002). “Ordinary differential equations in theory and practice” Second edition, Philadelphia, USA, SIAM Classics in applied mathematics, 43

McDonald D M and Choyke P L (2003). “Imaging of angiogenesis: from microscope to clinic” Nat Med, 9, 713-725

Medved M, Karczmar G, Yang C, Dignam J, Gajewski T F, Kindler H, Vokes E, MacEneany P, Mitchell M T, and Stadler W M (2004). “Semiquantitative analysis of dynamic contrast enhanced MRI in cancer patients: Variability and changes in tumor tissue over time” J Magn Reson Imaging, 20, 122-128

Merchant T E, Thelissen G R, de Graaf P W, Nieuwenhuizen C W, Kievit H C, and Den O W (1993). “Application of a mixed imaging sequence for MR imaging characterization of human breast disease” Acta Radiol, 34, 356-361

Metselaar J M, Wauben M H, Wagenaar-Hilbers J P, Boerman O C, and Storm G (2003). “Complete

remission of experimental arthritis by joint targeting of glucocorticoids with long-circulating liposomes" Arthritis Rheum, 48, 2059-2066

Minamikawa S, Kono K, Nakayama K, Yokote H, Tashiro T, Nishio A, Hara M, and Inoue Y (2004). "Glucocorticoid treatment of brain tumor patients: changes of apparent diffusion coefficient values measured by MR diffusion imaging" Neuroradiology, 46, 805-811

Moffat B A, Hall D E, Stojanovska J, McConville P J, Moody J B, Chenevert T L, Rehemtulla A, and Ross B D (2004). "Diffusion imaging for evaluation of tumor therapies in preclinical animal models" MAGMA, 17, 249-259

Morales M F and Smith R E (1948). "On the theory of blood-tissue exchange of inert gases; validity of approximate uptake expressions" Bull Math Biophys, 10, 191-200

Mustafi D, Peng B, Heisen M, Wood A M, Buurman J, and Karczmar G (2009). "World of phantoms: Reference standards for bench to breast MRI" ISMRM 17, Honolulu, USA, 2104

Nelder J A and Mead R (1965). "A Simplex-Method for Function Minimization" Computer Journal, 7, 308-313

Newell D, Nie K, Chen J H, Hsu C C, Yu H J, Nalcioglu O, and Su M Y (2010). "Selection of diagnostic features on breast MRI to differentiate between malignant and benign lesions using computer-aided diagnosis: differences in lesions presenting as mass and non-mass-like enhancement" Eur Radiol, 20, 771-781

O'Connor J P, Jackson A, Parker G J, and Jayson G C (2007). "DCE-MRI biomarkers in the clinical evaluation of antiangiogenic and vascular disrupting agents" Br J Cancer, 96, 189-195

Orton M R, d'Arcy J A, Walker-Samuel S, Hawkes D J, Atkinson D, Collins D J, and Leach M O (2008). "Computationally efficient vascular input function models for quantitative kinetic modelling using DCE-MRI" Phys Med Biol, 53, 1225-1239

Padhani A R, Hayes C, Landau S, and Leach M O (2002). "Reproducibility of quantitative dynamic MRI of normal human tissues" NMR Biomed, 15, 143-153

Park J A, Reddy P A, Kim H K, Kim I S, Kim G C, Chang Y, and Kim T J (2008). "Gold nanoparticles functionalised by Gd-complex of DTPA-bis(amide) conjugate of glutathione as an MRI contrast agent" Bioorg Med Chem Lett, 18, 6135-6137

Parker G J and Tofts P S (1999). "Pharmacokinetic analysis of neoplasms using contrast-enhanced dynamic magnetic resonance imaging" Top Magn Reson Imaging, 10, 130-142

Parker G J, Roberts C, Macdonald A, Buonaccorsi G A, Cheung S, Buckley D L, Jackson A, Watson Y, Davies K, and Jayson G C (2006). "Experimentally-derived functional form for a population-averaged high-temporal-resolution arterial input function for dynamic contrast-enhanced MRI" Magn Reson Med, 56, 993-1000

Parker G J, Suckling J, Tanner S F, Padhani A R, Revell P B, Husband J E, and Leach M O (1997). "Probing tumor microvascularity by measurement, analysis and display of contrast agent uptake kinetics" J Magn Reson Imaging, 7, 564-574

Partridge S C, DeMartini W B, Kurland B F, Eby P R, White S W, and Lehman C D (2009). “Quantitative diffusion-weighted imaging as an adjunct to conventional breast MRI for improved positive predictive value” Am J Roentgenol, 193, 1716-1722

Patlak C S, Blasberg R G, and Fenstermacher J D (1983). “Graphical evaluation of blood-to-brain transfer constants from multiple-time uptake data” J Cereb Blood Flow Metab, 3, 1-7

Penhaligon M and Camplejohn R S (1985). “Combination heparin plus cortisone treatment of two transplanted tumors in C3H/He mice” J Natl Cancer Inst, 74, 869-873

Peters A M (1998). “Fundamentals of tracer kinetics for radiologists” Br J Radiol, 71, 1116-1129

Planey C R et al. (2009). “Temporal sampling requirements for reference region modeling of DCE-MRI data in human breast cancer” J Magn Reson Imaging, 30, 121-134

Port R E, Knopp M V, and Brix G (2001). “Dynamic contrast-enhanced MRI using Gd-DTPA: interindividual variability of the arterial input function and consequences for the assessment of kinetics in tumors” Magn Reson Med, 45, 1030-1038

Pradel C et al. (2003). “Reduced capillary perfusion and permeability in human tumour xenografts treated with the VEGF signalling inhibitor ZD4190: an in vivo assessment using dynamic MR imaging and macromolecular contrast media” Magn Reson Imaging, 21, 845-851

Press W H, Teukolsky S A, Vetterling W T, and Flannery B P (1996). “Numerical Recipes in Fortran 77: The Art of Scientific Computing” Second edition, New York, USA, Cambridge University Press

Press W H, Teukolsky S A, Vetterling W T, and Flannery B P (2007). “Numerical recipes, The art of scientific computing” Third edition, New York, Cambridge University Press

Ramirez M S, Ragan D K, Kundra V, and Bankson J A (2007). “Feasibility of multiple-mouse dynamic contrast-enhanced MRI” Magn Reson Med, 58, 610-615

Raue A, Kreutz C, Maiwald T, Bachmann J, Schilling M, Klingmüller U, Timmer J (2009). “Structural and practical identifiability analysis of partially observed dynamical models by exploiting the profile likelihood” Bioinformatics, 25, 1923-1929

Renkin E M (1959). “Transport of potassium-42 from blood to tissue in isolated mammalian skeletal muscles” Am J Physiol, 197, 1205-1210

Rescigno A and Beck J S (1972). “Compartments”, First edition, New York, USA, Academic Press, “Foundations of mathematical biology” 255-322

Rijpkema M, Kaanders J H, Joosten F B, van der Kogel A J, and Heerschap A (2001). “Method for quantitative mapping of dynamic MRI contrast agent uptake in human tumors” J Magn Reson Imaging, 14, 457-463

Rohrer M, Bauer H, Mintorovitch J, Requardt M, and Weinmann H J (2005). “Comparison of magnetic properties of MRI contrast media solutions at different magnetic field strengths” Invest Radiol, 40, 715-724

Rouser G, Fkeischer S, and Yamamoto A (1970). “Two dimensional then layer chromatographic separation of polar lipids and determination of phospholipids by phosphorus analysis of spots” Lipids, 5, 494-496

Sardanelli F et al. (2007). “Multicenter comparative multimodality surveillance of women at genetic-familial high risk for breast cancer (HIBCRIT study): interim results” Radiology, 242, 698-715

Saslow D et al. (2007). “American Cancer Society guidelines for breast screening with MRI as an adjunct to mammography” CA Cancer J Clin, 57, 75-89

Schabel M C, Morrell G R, Oh K Y, Walczak C A, Barlow R B, and Neumayer L A (2010). “Pharmacokinetic mapping for lesion classification in dynamic breast MRI” J Magn Reson Imaging, 31, 1371-1378

Schiffelers R M and de Visser K E (2009). “Inflammation as target for pharmaceutical intervention in cancer” Curr Pharm Des, 15, 1822-1824

Schiffelers R M, Metselaar J M, Fens M H, Janssen A P, Molema G, and Storm G (2005). “Liposome-encapsulated prednisolone phosphate inhibits growth of established tumors in mice” Neoplasia, 7, 118-127

Schorn C, Fischer U, Luftner-Nagel S, and Grabbe E (1999). “Diagnostic potential of ultrafast contrast-enhanced MRI of the breast in hypervascularized lesions: are there advantages in comparison with standard dynamic MRI?” J Comput Assist Tomogr, 23, 118-122

Sevick E M and Jain R K (1989). “Geometric resistance to blood flow in solid tumors perfused ex vivo: effects of tumor size and perfusion pressure” Cancer Res, 49, 3506-3512

Simonetti A W, Hoogenraad F G, and van Muiswinkel A M (2007). “Automatic arterial input function selection using spatial information and feature space reduction” Proceedings ISMRM 15, Berlin, Germany, 2820

Sooriakumaran P, Coley H M, Fox S B, anas-Pirard P, Lovell D P, Henderson A, Eden C G, Miller P D, Langley S E, and Laing R W (2009). “A randomized controlled trial investigating the effects of celecoxib in patients with localized prostate cancer” Anticancer Res, 29, 1483-1488

Sourbron S, Ingrisch M, Siefert A, Reiser M, and Herrmann K (2009). “Quantification of cerebral blood flow, cerebral blood volume, and blood-brain-barrier leakage with DCE-MRI” Magn Reson Med, 62, 205-217

St Lawrence K S and Lee T Y (1998). “An adiabatic approximation to the tissue homogeneity model for water exchange in the brain: I. Theoretical derivation” J Cereb Blood Flow Metab, 18, 1365-1377

Stanisz G J and Henkelman R M (2000). “Gd-DTPA relaxivity depends on macromolecular content” Magn Reson Med, 44, 665-667

Stark D D and Bradley W G (1999). “Magnetic resonance imaging” Third edition, Volume III, St. Louis, USA, Mosby

Starmer C F and Clark D O (1970). “Computer computations of cardiac output using the gamma

function" J Appl Physiol, 28, 219-220

Stejskal E O and Tanner J E (1965). "Spin Diffusion Measurements: Spin Echoes in the Presence of A Time-Dependent Field Gradient" J Chem Phys, 42, 288-292

Szabo B K, Aspelin P, Wiberg M K, and Bone B (2003). "Dynamic MR imaging of the breast. Analysis of kinetic and morphologic diagnostic criteria" Acta Radiol, 44, 379-386

Taylor J S, Tofts P S, Port R, Evelhoch J L, Knopp M, Reddick W E, Runge V M, and Mayr N (1999). "MR imaging of tumor microcirculation: promise for the new millennium" J Magn Reson Imaging, 10, 903-907

Tofts P S (1997). "Modeling tracer kinetics in dynamic Gd-DTPA MR imaging" J Magn Reson Imaging, 7, 91-101

Tofts P S (2003). "Quantitative MRI of the brain: measuring changes caused by disease" First edition, Chichester, UK, John Wiley and Sons Ltd

Tofts P S and Kermode A G (1991). "Measurement of the blood-brain barrier permeability and leakage space using dynamic MR imaging. 1. Fundamental concepts" Magn Reson Med, 17, 357-367

Tofts P S et al. (1999). "Estimating kinetic parameters from dynamic contrast-enhanced T(1)-weighted MRI of a diffusable tracer: standardized quantities and symbols" J Magn Reson Imaging, 10, 223-232

Tofts P S, Berkowitz B, and Schnall M D (1995). "Quantitative analysis of dynamic Gd-DTPA enhancement in breast tumors using a permeability model" Magn Reson Med, 33, 564-568

Veltman J, Stoutjesdijk M, Mann R, Huisman H J, Barentsz J O, Blickman J G, and Boetes C (2008). "Contrast-enhanced magnetic resonance imaging of the breast: the value of pharmacokinetic parameters derived from fast dynamic imaging during initial enhancement in classifying lesions" Eur Radiol, 18, 1123-1133

Vincensini D, Dedieu V, Eliat P A, Vincent C, Bailly C, de C J, and Joffre F (2007). "Magnetic resonance imaging measurements of vascular permeability and extracellular volume fraction of breast tumors by dynamic Gd-DTPA-enhanced relaxometry" Magn Reson Imaging, 25, 293-302

Vonken E P, van Osch M J, Bakker C J, and Viergever M A (2000). "Simultaneous quantitative cerebral perfusion and Gd-DTPA extravasation measurement with dual-echo dynamic susceptibility contrast MRI" Magn Reson Med, 43, 820-827

Vos P C, Hambrock T, Barentsz J O, and Huisman H J (2009). "Automated calibration for computerized analysis of prostate lesions using pharmacokinetic magnetic resonance images" Proceedings MICCAI 2009, London, UK, Volume 5761/2009, 836-843

Vos P C, Hambrock T, Hulsbergen-van de Kaa CA, Futterer J J, Barentsz J O, and Huisman H J (2008). "Computerized analysis of prostate lesions in the peripheral zone using dynamic contrast enhanced MRI" Med Phys, 35, 888-899

Wade O L and Bishop J M (1962). "Cardiac output and regional blood flow" First edition, Philadelphia,

USA, F.A. Davis Co

Walker-Samuel S, Leach M O, and Collins D J (2006). “Evaluation of response to treatment using DCE-MRI: the relationship between initial area under the gadolinium curve (IAUGC) and quantitative pharmacokinetic analysis” Phys Med Biol, 51, 3593-3602

Walker-Samuel S, Leach M O, and Collins D J (2007). “Reference tissue quantification of DCE-MRI data without a contrast agent calibration” Phys Med Biol, 52, 589-601

Walker-Samuel S, Parker C C, Leach M O, and Collins D J (2007). “Reproducibility of reference tissue quantification of dynamic contrast-enhanced data: comparison with a fixed vascular input function” Phys Med Biol, 52, 75-89

Wang H Z, Riederer S J, and Lee J N (1987). “Optimizing the precision in T1 relaxation estimation using limited flip angles” Magn Reson Med, 5, 399-416

Warner E et al. (2004). “Surveillance of BRCA1 and BRCA2 mutation carriers with magnetic resonance imaging, ultrasound, mammography, and clinical breast examination” JAMA, 292, 1317-1325

Weidner N, Semple J P, Welch W R, and Folkman J (1991). “Tumor angiogenesis and metastasis-correlation in invasive breast carcinoma” N Engl J Med, 324, 1-8

Weinmann H J, Laniado M, and Mutzel W (1984). “Pharmacokinetics of GdDTPA/dimeglumine after intravenous injection into healthy volunteers” Physiol Chem Phys Med NMR, 16, 167-172

Yabuuchi H et al. (2010). “Non-mass-like enhancement on contrast-enhanced breast MR imaging: lesion characterization using combination of dynamic contrast-enhanced and diffusion-weighted MR images” Eur J Radiol, 75, e126-e132

Yang C, Karczmar G S, Medved M, and Stadler W M (2004). “Estimating the arterial input function using two reference tissues in dynamic contrast-enhanced MRI studies: fundamental concepts and simulations” Magn Reson Med, 52, 1110-1117

Yang C, Karczmar G S, Medved M, and Stadler W M (2007). “Multiple reference tissue method for contrast agent arterial input function estimation” Magn Reson Med, 58, 1266-1275

Yang C, Karczmar G S, Medved M, Oto A, Zamora M, and Stadler W M (2009). “Reproducibility assessment of a multiple reference tissue method for quantitative dynamic contrast enhanced-MRI analysis” Magn Reson Med, 61, 851-859

Yang C, Stadler W M, Karczmar G S, Milosevic M, Yeung I, and Haider M A (2010). “Comparison of quantitative parameters in cervix cancer measured by dynamic contrast-enhanced MRI and CT” Magn Reson Med, 63, 1601-1609

Yang C, Wolf G L, Karczmar G S, and Stadler W M (2006). “Improved T1 estimation with spoiled gradient recalled echo (SPGR) images using a modified variable flip angle method” ISMRM 14, Seattle, USA, 2499

Yankeelov T E, Cron G O, Addison C L, Wallace J C, Wilkins R C, Pappas B A, Santyr G E, and Gore J C (2007). “Comparison of a reference region model with direct measurement of an AIF in the

analysis of DCE-MRI data" Magn Reson Med, 57, 353-361

Yankeelov T E, DeBusk L M, Billheimer D D, Luci J J, Lin P C, Price R R, and Gore J C (2006). "Repeatability of a reference region model for analysis of murine DCE-MRI data at 7T" J Magn Reson Imaging, 24, 1140-1147

Yankeelov T E, Luci J J, DeBusk L M, Lin P C, and Gore J C (2008). "Incorporating the effects of transcytolemmal water exchange in a reference region model for DCE-MRI analysis: theory, simulations, and experimental results" Magn Reson Med, 59, 326-335

Yankeelov T E, Luci J J, Lepage M, Li R, Debusk L, Lin P C, Price R R, and Gore J C (2005). "Quantitative pharmacokinetic analysis of DCE-MRI data without an arterial input function: a reference region model" Magn Reson Imaging, 23, 519-529

Yankeelov T E, Rooney W D, Li X, and Springer C S, Jr. (2003). "Variation of the relaxographic "shutter-speed" for transcytolemmal water exchange affects the CR bolus-tracking curve shape" Magn Reson Med, 50, 1151-1169

Zhang J L, Rusinek H, Bokacheva L, Chen Q, Storey P, and Lee V S (2009). "Use of cardiac output to improve measurement of input function in quantitative dynamic contrast-enhanced MRI" J Magn Reson Imaging, 30, 656-665

Zwick S, Brix G, Tofts P S, Strecker R, Kopp-Schneider A, Laue H, Semmler W, and Kiessling F (2010). "Simulation-based comparison of two approaches frequently used for dynamic contrast-enhanced MRI" Eur Radiol, 20, 432-442

Samenvatting

Borstkanker is een ziekte waar één op de acht vrouwen in geïndustrialiseerde landen mee te maken krijgt. Sinds 2001 neemt het aantal nieuwe gevallen in een land als de Verenigde Staten gestaag af. En, sinds 1990, neemt ook het aantal sterfgevallen ten gevolge van borstkanker af. Deze laatste daling wordt deels aan vroegtijdige detectie en deels aan betere behandelingen toegeschreven. Nog steeds is de impact van deze ziekte op de samenleving groot. Dit proefschrift gaat over vroegtijdige detectie van borstkanker door MRI beelden op een kwantitatieve wijze te analyseren (MRI: magnetic resonance imaging).

Preventief screenen (bevolkingsonderzoek) en ook het stellen van een diagnose gebeurt in het algemeen met behulp van röntgen-mammografie. MRI is een alternatieve beeldvormende techniek die steeds belangrijker wordt, bijvoorbeeld voor het screenen van vrouwen die een erfelijke aanleg voor borstkanker hebben. Ook kan het voorkomen dat röntgen-mammografie niet in een duidelijke uitslag resulteert. In dat geval kan MRI uitkomst bieden. MRI is ook een veelgebruikte techniek om de effecten van een behandeling tegen kanker te meten. Een MRI onderzoek van de borst bestaat onder andere uit een dynamische serie beelden: een contrastmiddel wordt geïnjecteerd en vervolgens enkele minuten gevolgd door een 'filmpje' van de borst op te nemen. Het opnemen en analyseren van de dynamische MRI-serie zijn uitvoerig onderzocht in dit proefschrift.

In de dynamische data kan voor een stukje weefsel een T_1-gewogen curve worden gemeten (T_1: weefseleigenschap die verschillend is voor elk type weefsel). Meestal bekijkt de radioloog – naast een aantal andere weefseleigenschappen – het verloop van deze curve om in te schatten of het weefsel gezond is of niet. Bijvoorbeeld: als het contrastmiddel eerst snel wordt opgenomen om vervolgens ook weer snel 'uit te spoelen' dan is dat een teken van kwaadaardigheid; dit in tegenstelling tot een langzame opname zonder 'uitspoeling', wat een teken is van goedaardigheid. Dit verschil in contrastopname-curve komt voort uit fysiologische veranderingen die het weefsel ondergaat wanneer er zich een tumor ontwikkelt. Dit verschil is gebleken in de klinische praktijk door grote aantallen patiënten te bestuderen; deze manier van curve-type classificatie is niet gebaseerd op *kennis* van de fysiologie.

Een andere manier om deze contrastopname-curves te analyseren komt voort uit de farmacokinetische modellering. De contrastopname wordt met deze methode beschreven in fysiologische termen. Dit schept de mogelijkheid om niet alleen vast te stellen dat het weefsel pathologisch is, maar ook om vast te stellen wat er dan precies anders is in vergelijking met gezond weefsel. Ook zorgt gebruik van deze methode

ervoor dat ongewenste invloeden geen effect hebben op het karakteriseren van de contrastopname-curves.

In dit proefschrift hebben we de fysiologische modelaannames van verschillende farmacokinetische modellen uitvoerig besproken en vergeleken. Ook hebben we een aantal praktische aspecten bekeken zoals het verkrijgen van een arteriële input-functie (beschrijving van hoe het contrastmiddel wordt 'aangeboden' aan het weefsel) en het schatten van modelparameters. In een simulatiestudie hebben we gekeken naar wat een beperkte tijdsresolutie of een hoog ruisniveau betekent voor de toepassing van een drietal farmacokinetische modellen (verschillend in complexiteit). Slechts één van deze modellen (basic Tofts) bleek toepasbaar te zijn op dynamische MRI-data zoals die van de borst wordt opgenomen. Omdat de beperkte tijdsresolutie van dergelijke borstdata (vaak duurt de opname van één beeldvolume 1 minuut of langer) een belemmering vormt voor de toepassing van farmacokinetische modellering, hebben we het tijdsaspect nog verder onderzocht. Hieruit volgde dat farmacokinetische modellering toegepast kan worden op data met een tijdsresolutie van ongeveer 1 minuut, mits de arteriële input-functie op een slimme manier verkregen wordt; namelijk indirect afgeleid uit de contrastopname-curve gemeten in een gezond weefsel.

Een belangrijke voorwaarde voor het betekenisvol toepassen van farmacokinetische modellering is dat de contrastopname-curves de concentratie van het contrastmiddel in de tijd weergeven. De gemeten signaalintensiteit is namelijk afhankelijk van allerlei instellingen en daarom op zichzelf niet betekenisvol en moeilijk te vergelijken. Wat het omrekenen van gemeten signaalintensiteit naar concentratie moeilijk maakt is dat een verandering in signaalintensiteit een indirect effect is van de contrastmiddelconcentratie in het weefsel. Het is dus noodzakelijk om ofwel een theorie aan te nemen die het verband tussen de concentratie en de gemeten intensiteit beschrijft, ofwel een empirische kalibratie uit te voeren. Beide hebben wij onderzocht, gebruikmakend van een kalibratie-object ontwikkeld aan The University of Chicago. Dit object is zo ontworpen dat het met de patiënt meegescand kan worden en omsluit als een 'bakje' de borst.

Naast het gebruik van farmacokinetische modellering voor diagnostiek, hebben we in een dierstudie ook gekeken naar het kwantificeren van het effect van een nieuwe therapie. We hebben gekeken hoe een ontstekingsremmer ervoor kan zorgen dat een tumor langzamer groeit.

Het in dit proefschrift gepresenteerde onderzoek draagt bij aan een betekenisvolle toepassing en interpretatie van kwantitatieve dynamische MRI borstdata.

Dankwoord

Na 4 jaar eenzaam ploeteren pas weer je donkere kantoortje uitkomen? Niets bleek minder waar… Samenwerken was de sleutel tot dit proefschrift en ik heb met veel plezier mijn rol hierin vervuld. Ik wil dan ook graag een aantal mensen hartelijk bedanken voor hun bijdragen aan de totstandkoming van dit proefschrift. Bart, bedankt dat je me hebt gestimuleerd om voorbij de horizon te kijken, om een tijd in Chicago te werken en om mezelf tot een all-round onderzoeker te ontwikkelen. Jouw belangstelling voor niet alleen de onderzoeker maar ook de mens achter de onderzoeker is hartverwarmend. Hans, jij hebt me alle ruimte gegeven om een eigen draai aan mijn onderzoek te geven. Met jouw kritische houding wist je me steeds op de medische praktijk te attenderen: "Ok, heel interessant, maar wat heeft de patiënt hier aan?" Ook heb ik de kunst van het 'beïnvloeden' een beetje van je kunnen afkijken. Natal, jouw kennis van systeemtheorie en signaalanalyse in combinatie met dit vakgebied heeft tot uiterst nuttige inzichten geleid. Je enthousiasme is aanstekelijk. Greg, your 'brainstorm-way-of-life' has been very inspiring and led to many new research questions as well as solutions. When I asked you to discuss the focus of my project, your answer was: "You want to talk about *focus*? With *me*?" Need I say more? Luckily, Fan was there assuring that I actually produced material. Hearing every morning: "Marieke, did you finish your paper?" was a surprisingly effective way to help me focus on what really mattered. I would like to thank you both for receiving me at The University of Chicago and for providing guidance during the project. Not to mention the many laughs we had, it was great to be part of your team. Ik wil ook graag Klaas Nicolay, Jelle Barentsz en Kenneth Gilhuijs hartelijk danken voor het plaatsnemen in mijn commissie.

Over de jaren heen heb ik aan een tiental bureaus gezeten. Ik dank hier dan ook in één keer al mijn kamergenoten en collega's voor een mooie tijd (I thank all my office mates and colleagues for a great time!). Frans, dank je voor een rustige plek bij jou op de kamer die ik tegen het eind goed kon gebruiken! Geert, ik kijk met veel plezier terug op onze samenwerking. Ik viel met mijn neus in de boter met jou als Master student. Zonder jouw werk waren de hoofdstukken 2 en 3 niet geworden tot wat ze nu zijn. Thorsten, thank you for your help and continuing interest. I hope you'll be pleasantly surprised by the end result. Ewelina, it was great working with you. The combination of our very different writing styles led to a paper we can be proud of. Alessandro, thanks for being so funny and making me rethink the Dutch way of organizing everyone and everything… Ellen en Roy, bedankt voor alle gezelligheid, stoom-afblaas-gelegenheden en plezier. Justus, nooit eerder kreeg iemand me zo gek om Hollandse Nieuwe te eten! Dat Barts groep een heel bijzondere plek is om te werken blijkt ook steeds tijdens de onvergetelijke Ardennenweekendjes, bedankt allemaal!

Ook bij Philips Healthcare wil ik al mijn collega's bedanken voor de fijne en open sfeer. Frans, ik heb veel geleerd van jouw stiltes die steevast gevolgd werden door een zeer terechte kritische vraag. Arjan, bedankt voor je input en enthousiasme! Steven, op de valreep heb jij nog een belangrijke rol gespeeld voor het werk beschreven in hoofdstuk 4. Na: "Zeg, ik heb daar nog eens naar gekeken", volgde meestal een belangrijke optimalisatie van onze methoden. Bedankt! Iwo, dank je voor je hulp bij last-minute klussen. Ursula, het was gezellig om in Chicago met een 'Nederlandse' collega op te trekken. Marcel, bedankt voor goede raad.

Of course, I'd also like to thank my dear colleagues in Chicago. A big thank you to Abbie, Liz, and Fred, whose contributions to chapter 4 are invaluable. It has been great working with you guys! Dev, Chad, Cheng, Liz, Milica, Sunny, Marta, Sean, Erica, Jim, and John, thanks to all of you I had an incredible time in Greg's lab. Liz, you are the most environmentally-friendly American I've ever met! Milica, I enjoyed exchanging 'European' (= sarcastic) jokes with you. Abbie, I'll miss our chats at the scanner console. Gillian, your interest in this research has been an important motivation, thank you. Marko, I've always highly appreciated your input into this research.

Buiten mijn werk prijs ik me zeer gelukkig met mijn vrienden waarmee ik honderduit klets en veel lol mee beleef. Bedankt voor alle steun en afleiding, Jennifer, Gaby, Hanneke, Arend, José, Carola, Mirjam, Marian, Jutta, Evelinda, Marloes, Renske, Kim, Bram en Marleen. Ellen en Renske, geweldig dat jullie mijn paranimfen zijn! Douwe en Evelinda, bedankt voor jullie spectaculaire design van het omslag. I'd also like to thank my dear friends that I met in Chicago, Tayo, Van, Christina, and Ellen. I hope to see you again.

Beste schoonfamilie, ik vind het geweldig dat jullie zoveel interesse tonen! Pap, mam, Job, Vivian, Janneke, Harrie, Elly, bedankt voor jullie onvoorwaardelijke steun! Het is jullie Marie (snel uitgesproken: 'MRI', grapje van pa) toch maar mooi gelukt… Lieve Jürgen, dankzij jou was het laatste jaar ook het mooiste jaar. Jij wist op de juiste momenten een adempauze in te lassen, maar me ook liefdevol doch resoluut uit bed te duwen wanneer ik op een zondag geen zin meer had me te houden aan de goede voornemens van de vorige avond: "dat maak ik morgenvroeg nog wel even af…". Die spreekwoordelijke laatste loodjes hadden zonder jouw steun veel zwaarder gewogen. Terecht kun je zeggen: "*Wij* hebben het af!"

Curriculum vitae

Marieke Heisen was born February 10, 1982, in Nijmegen, The Netherlands. She graduated from secondary school at the Stedelijk Gymnasium Nijmegen in 2000. In that year she started studying Biomedical Engineering at Eindhoven University of Technology, from which she obtained her Master of Science degree cum laude in 2006. During her studies she carried out an internship in the Laboratoire Imagerie Moléculaire et Fonctionelle at Université Victor Segalen Bordeaux II in France. Here, she worked on modeling of the influence of tissue heterogeneity on electrical and thermal conductivity during radiofrequency ablation of the liver guided by thermometer MRI. She performed her Master's project in a collaboration between the Biomedical Image Analysis group at Eindhoven University of Technology and the Clinical Science & Advanced Development group at Philips Healthcare in Best. Her Master's thesis concerned pharmacokinetic analysis of dynamic contrast-enhanced (DCE) MRI data of the breast to detect and characterize cancer. She continued to pursue her interest in this field and started in 2006 with a PhD project at the same university, again in close collaboration with Philips Healthcare. During her PhD project, Marieke also worked with the department of Radiology at The University of Chicago, where she spent one year in total. The result is this dissertation entitled "Understanding quantitative DCE-MRI of the breast: Towards meaningful clinical application".

List of publications

Journal publications

M. Heisen, X. Fan, J. Buurman, N.A.W. van Riel, G.S. Karczmar, B.M. ter Haar Romeny (2010). "The use of a reference tissue arterial input function with low temporal resolution DCE-MRI data" Phys Med Biol, 55, 4871-4883

M. Heisen, X. Fan, J. Buurman, N.A.W. van Riel, G.S. Karczmar, B.M. ter Haar Romeny (2010). "The influence of temporal resolution in determining pharmacokinetic parameters from DCE-MRI data" Magn Reson Med, 63, 811-816

E. Kluza, M. Heisen (co-first author), S. Schmid, D.W.J. van der Schaft, R.M. Schiffelers, G. Storm, B.M. ter Haar Romeny, G.J. Strijkers, K. Nicolay (submitted). "Multi-parametric assessment of the anti-angiogenic effects of liposomal glucocorticoids"

G.J.S. Litjens, M. Heisen, J. Buurman, B.M. ter Haar Romeny (submitted). "Data-imposed limitations on pharmacokinetic models for DCE-MRI of the breast"

Conference proceedings

M. Heisen, B. Peng, A.M. Wood, D. Mustafi, J. Buurman, G.M. Newstead, G.S. Karczmar (2010). "Patient-specific calibration for breast MRI: breast-coil insertable reference phantom" Proceedings ISMRM 18, Stockholm, Sweden, 2493

M. Heisen, X. Fan, J. Buurman, B.M. ter Haar Romeny (2010). "Effects of reference tissue AIF derived from low temporal resolution DCE-MRI data on pharmacokinetic parameter estimation" Proceedings ISMRM 18, Stockholm, Sweden, 4802

G.J.S. Litjens, M.Heisen, J. Buurman, B.M. ter Haar Romeny (2010). "Pharmacokinetic models in clinical practice: What model to use for DCE-MRI of the breast?" Proceedings IEEE ISBI 2010, Rotterdam, The Netherlands, 1727

M. Heisen, A.M. Wood, J. Buurman, D. Mustafi, B. Peng, G.M. Newstead, C. Yang, M.K. Ivancevic, G.S. Karczmar (2009). "Standardization and calibration for breast MRI: The use of a unique air bubble free agar phantom" Proceedings RSNA 2009, Chicago, USA, 421

M. Heisen, X. Fan, J. Buurman, B.M. ter Haar Romeny (2009). "The effect of the temporal resolution of the arterial input function (AIF) on pharmacokinetic parameter estimation from dynamic contrast-enhanced (DCE) MRI data" Proceedings RSNA 2009, Chicago, USA, 563

G.J.S. Litjens, M. Heisen, J. Buurman, A.M. Wood, M. Medved, G.S. Karczmar, B.M. ter Haar Romeny (2009). "T_1 quantification: Variable flip angle method vs. use of reference phantom" Proceedings RSNA 2009, Chicago, USA, 422

D. Mustafi, B. Peng, M. Heisen, A.M. Wood, J. Buurman, G.S. Karczmar (2009). "World of phantoms: Reference standards for bench to breast MRI" Proceedings ISMRM 17, Honolulu, USA, 2104

M. Heisen, X. Fan, T. Twellmann, J. Buurman, N.A.W. van Riel, G.S. Karczmar, B.M. ter Haar Romeny (2008). "The role of temporal resolution in determining pharmacokinetic parameters from DCE-MR data" Proceedings ISMRM 16, Toronto Canada, 3836

M. Heisen, T. Twellmann, J. Buurman, A. Vilanova, F.A. Gerritsen, B.M. ter Haar Romeny (2007). "The influence of temporal resolution and phase-encoding order on shape-based classification of dynamic contrast enhanced (DCE) MRI uptake curves in the breast" Proceedings ISMRM 15, Berlin, Germany, 133

M. Heisen, J. Buurman, A. Vilanova, T. Twellmann, F.A. Gerritsen (2007). "Impact of the arterial input function on the classification of contrast-agent uptake curves in dynamic contrast-enhanced (DCE) MR images based on heuristic shape modeling" Proceedings ECR 2007, Vienna, Austria, 284